Mesoporous carbonaceous materials (Starbon®) for metal adsorption and energy storage

Andrea Muñoz García

Doctor of Philosophy

University of York
Chemistry

August 2017

Abstract

Humankind heavily rely on electrical and electronic devices which require precious metals and energy, the latter typically derived from fossil fuels. Increasing concern for the environment has led to the search for renewable sources of energy (i.e. solar, wind) and sustainable ways to utilise metals. Porous carbons have been widely used as adsorbents to recover metals from waste streams, and as electrodes for energy storage devices (i.e. electrochemical double layer capacitors).

Starbon® are mesoporous carbonaceous materials derived from starch. A method for the preparation of Starbon® monoliths has been developed. In turn, the potential of Starbon® for the adsorption and recovery of precious metals from solution was investigated. Starbon® were capable of adsorbing Pd, Pt and Au, reaching adsorption capacities of up to 600 $mg \cdot g^{-1}$ for Au. The adsorption was very rapid (equilibrium reached after 10 min) and led to the formation of Au nanoparticles. The application of Starbon® to complex mixtures of metal waste showed preferential adsorption of Au, leaving the other metals (i.e. Cu, Fe, Ni) in solution. In addition, monoliths allowed for the adsorption of gold in flow regimes.

A method for the preparation of Starbon®-graphite composites was also developed. These materials combined the good porosity of Starbon® and the high conductivity of graphite. These composites were shaped as small discs which allowed them to be tested as electrochemical double layer capacitors. The electrochemical characterisation showed the good performance of these Starbon®-graphite composite capacitors, reaching capacitance values of 205.4 $F \cdot g^{-1}$. Graphite concentrations of ~ 1% led to an optimal porous and conductive structure which enhanced the diffusion properties and thus, the performance of the devices. The composites were shaped as discs without the need of a binder, which can negatively affect the properties of the material.

Contents

List of Figures

.

List of Tables

Acknowledgments

First, I would like to thank James for giving me the opportunity to course my PhD in this outstanding centre under his supervision. I also would like to thank Andy for being a wonderful supervisor and friend. Thanks to Vitaly and Helen for their support and advise. Thank you as well to everyone at the ICTP-CSIC for making me feel so welcome during the time I spent in their lab, specially to Peter, Enrique and Gary for their support and contributions throughout this PhD. I would like to thank Paul Elliot for his constant help in the lab and the rest of the technical team: Charlotte, Hannah and a special mention to Maria for helping me with the furnace and everything else. Thank you as well to Darren, for his help with ICP. Also, thank you to all the people that is or has worked at the GCCE for your help and for making the working environment so enjoyable, especially: Lucie, Tom(s), Katie, Sasha, Jennie, Eddie, Stefan, Javier, Jimmy, Duncan, Rob, Leyre, Camille, Mark, Andy, Saumye, Yixin, Michael. A big thanks to Konstantina for coming back and being such a great friend. Thank you as well to my new colleagues at the NNFCC for their support during my last months of writing up.

I would also like to thank my friends for those uncountable but awesome hours of study that brought me here – Leyre, Merche, Maria Jesús, César, Rafa, Diego, Marcos, Minerva – and for those friendships that stay strong beyond distance and time – Zina, Carla, Julia, Elena, Izaskun. A huge thank you to my one and only 'Modern family' for making me feel close in the distance. An infinite thanks to my parents, Blanca and Pepa, as their love and support have brought me where I am today. Thank you to 'La Troupe' and Kitty for helping me every step of the way from the very beginning. A big thank you to my wonderful grandparents and specially to Luis, who passed me the passion for chemistry without even noticing, and to Santiago, for teaching me that knowledge is a weightless luggage. Thank you to Juncal for your constant support and for understanding so well what is like to be abroad and at home in one place.

And of course, the biggest thank you goes to Fergal. We started this PhD together and we are finishing it together, only you know how rewarding and challenging has been, and how much, beyond chemistry, I have learned from it. Thank you for showing me that I was capable to do this PhD by myself, it has been an absolute pleasure to share this adventure with you. I am looking forward the next one!

Declaration

I declare that this thesis is a presentation of original work and I am the sole author. This work has not previously been presented for an award at this, or any other, University. All sources are acknowledged as References. All Starbon® synthesis, data analysis and the majority of characterisation was carried out by me. The work in this thesis that was carried out by, or in collaboration with, other workers is fully acknowledged in the text.

Part of the work disclosed herein has been published in the following article.

Starch-derived carbonaceous mesoporous materials (Starbon®) for the selective adsorption and recovery of critical metals
A. Muñoz García, A. J. Hunt, V. L. Budarin, H. L. Parker, P. S. Shuttleworth, G. J. Ellis, J. H. Clark, Green Chemistry 2015, 17, 2146-2149

Monolithic mesoporous graphitic composites as super capacitors: from Starbons to Starenes®
A. Muñoz García, V.L. Budarin, Y. Zhou, A. J. Hunt, L. Lari, V. K. Lazarov, H. J. Salavagione, E. Morales, G. J. Ellis, J. H. Clark, P. S. Shuttleworth, Journal of Materials Chemistry A, 2018.

Introduction

Chapter 1

1 Introduction

1.1 Scope of the project

The aim of the present work is to develop a method for the preparation of monolithic carbons that avoids the use of binding agents, which generally weaken some material's properties (i.e. conductivity) (Chapter 2).

The ability of such materials to adsorb and recover precious metals from solution is also investigated through batch experimentation (Chapter 2) and in flow regime (Chapter 3).

Chapter 4 describes a method to produce conductive monoliths by combining bio-derived porous carbon (Starbon®) with a good electrical conductor (i.e. graphite) in order to prepare electrodes for electrochemical double-layer capacitors which serve as energy storage devices (Chapter 5).

The overall aim of this project is to develop sustainable materials that contribute towards the creation of efficient and innovative pathways to drive our economy, overcoming the current environmental challenges.

1.2 Green Chemistry

Green chemistry was first defined by Paul Anastas as "the design of chemical products and processes to reduce the use and generation of hazardous substances".[1] A series of twelve principles were stablished as guiding rules to achieve sustainability in a process or product.[2, 3] The Twelve Principles of Green Chemistry are:

1. *Waste prevention*. Avoiding the production of waste is preferred to subsequent treatment and cleaning.

2. *Atom economy*. The product includes as many atoms from the reactant as possible to optimise the use of raw materials.

3. *Synthesis of less hazardous chemicals*. The hazards of all raw materials, products and reaction pathways need to be considered and assessed.

4. *Design of safer chemicals*. Modelling the properties and potential toxicity of a product is strongly advised before its synthesis.

5. *Safer solvents and auxiliaries*. If the use of solvent cannot be avoided, non-hazardous options need to be used (i.e. water or supercritical fluids).

6. *Design for energy efficiency*. This involves the reduction of the energy barrier associated with a reaction, and the creation of devices capable of retrieving and storing energy from renewable sources.

7. *Use of renewable feedstocks*. The substitution of fossil fuels for renewable feedstocks to produce chemicals and fuel is required.

8. *Reduction of derivatives*. Minimisation of the number of chemical transformations involved in process.

9. *Catalysis*. The use of catalytic compounds may lead to lower energy and feedstock requirements as well as the reduction of waste generation.

10. *Design for degradation*. Substitution of persistent functional groups such as amines or halogenated moieties for more bio-degradable groups (i.e. esters or amides) when possible.

11. *Real-time analysis for pollution prevention*. Developing analytical techniques that allow real-time control of processes that produce hazardous substances.

12. *Inherently safer chemistry for accident prevention*. Addressing a wide spectrum of hazards to prevent industrial accidents.

The development of bio-based carbons and their application for metal recovery and energy storage applies the criteria established by the Green Chemistry Principles. The carbons described in this thesis were prepared from starch which agrees well with the 'renewable feedstock' principle, as well as the 'waste prevention' principle as starch can be obtained from waste sources such as potato peelings.[4] The preparation method

avoided the utilisation of templates to create the porous structure, and hazardous chemicals, enhancing the atom economy and safety of the process as suggested by the twelve principles. In addition, the application of these bio-based carbons for metal recovery to purify contaminated streams, yielded recovered metals that can be used as a starting material in other processes. The utilisation of Starbon® as energy storage devices also agrees well with the 'design for energy' principle.

1.3 Recovery of precious metals

1.3.1 Importance of precious metals

Precious metals (PMs) such as gold, palladium and platinum have become essential to sustain the 21st century lifestyle, as they are present in electronic gadgets, used as catalysts by the chemical industry and within active compounds in medical treatments (Figure 1.1).[5-7]

1.3.1.1 Catalysis

In catalysis, PMs play a key role in gas purification and in the formation of commodity compounds, including plastics, synthetic fibres and bulk chemicals.[8] The ability of PMs to act as active sites in catalysts is in part due to their ability to adsorb and dissociate H_2 and O_2 molecules, good acid and thermal stability and resistance to oxidation.[8] Palladium catalysts are used in the preparation of several polymers, including polyvinyl chloride (PVC) used to fabricate pipes, electric wires and housing material, and methyl methacrylate (MMA) employed as glass substitute.[8] As an example, during production of vinyl chloride, catalytic amounts of supported palladium are required to remove acetylene impurities from the hydrogen chloride stream.[8, 9] In addition, a range of platinum catalysts are widely used in petroleum refineries, to obtain high quality gasoline.[10, 11] Both palladium and platinum are also used as catalysts in the preparation of synthetic fibres and the purification of gases.[8] For example, Pd and Pt supported on carbonaceous surfaces are involved in the preparation of Nylon-6, a well-known synthetic

fabric used to manufacture clothing.[8] Pd and Pt-based catalyst are also used to purify, H_2, N_2 and CO_2 streams.[12, 13] This ability to purify gas streams is also applied in the arguably, best-known application of PM catalysts, in autocatalytic converters for automobiles which are capable of transforming hydrocarbons, carbon monoxide (CO) and nitrogen oxides (NO_x) from the exhaust gases into innocuous water vapour, nitrogen (N_2) and carbon dioxide (CO_2).[14] Gold is used industrially as a catalyst in the formation of the monomer vinyl acetate, a precursor of common polymers, such as polyvinyl acetate that is widely used as glue.[15] A variety of gold catalysed processes have been patented recently with applications in gas purification, fuel cells and olefin and polymer production.[16] As an example, Johnson Matthey recently developed a supported gold catalyst for the hydrochlorination of acetylene, a key process for the preparation of the vinyl chloride monomer (VCM), precursor of PVC.[17]

Main applications of precious metals			
Metal	Catalysis	Medical care	Electronics
Gold	Production of VCM, polymer precursor. Patented for many other reactions	Drug delivery, including gene therapy Bio-sensing (monitoring tumours)	Contacts, connectors Wire bonding Prevent heat damage
Palladium	Production of polymers (PVC, MMA) Preparation of synthetic fibres	Internal radiation source (radiotherapy) Anticancer treatment	Control flow of electric current Plating to yield conductive connectors
Platinum	Gas purification (catalytic converters) Petroleum refineries to obtain gasoline	Electrode in glucose-meters Implantable devices (pacemakers)	Adding thermal stability to magnetic storage layer of hard disks

Figure 1.1 Selected applications of gold, palladium and platinum in the fields of catalysis, medicine and electronics.[5, 8, 14].

1.3.1.2 Electronics

Currently, a large fraction of PMs is set aside for the fabrication of electronic devices. Phones, personal computers (PCs), laptops and tablets require PMs in their circuit boards.[6] Gold is employed to produce bonding wires that connect the circuit board with the lead-frame.[18] Gold is also used in contacts and connectors due to its high electrical conductivity and resistance to corrosion.[18] The good thermal conductivity of gold prevents damage in silicon chips that generate large amounts of heat.[18] Platinum is used to improve the stability of the magnetic storage layer in hard disks.[14] Ceramic capacitors incorporate palladium to control the electric current flow, and to stabilise metallic silver in hybrid integrated circuits.[14] As with gold, palladium coatings are used in the production of conductive connectors.[14]

Although only very small amounts of precious metals are used in electronic devices (Table 1.1), consumption is counted by the tonne, due to the high demand of electronic gadgets.[6, 19] For instance, the number of mobile phones produced worldwide was just below the 1000 million mark in 2008.[20] The same year, 300 million PCs and laptops were also manufactured. The production of mobile phones, PCs and laptops in 2008 resulted in the consumption of 100 tonnes of gold and 36 tonnes of palladium.[21]

Table 1.1 Content (mg) of precious metals in electronic devices.[6]

Metal	Amount of precious metals (mg)		
	Phones	PCs	Flat screens
Au	26.1	169	161
Pd	11.6	39.9	42.2

Some medical applications for PMs are mentioned in Figure 1.1. However, a more in-depth discussion of the role of PMs for such applications is out of the scope of the present project.

1.3.2 Challenges associated to precious metals

The number of electronic devices produced worldwide has increased dramatically over the last two decades (10 times more sells in 2009 compared to 1997).[20] In addition, low-carbon technologies are being built around the outstanding properties displayed by PMs.[22] As a result, demand for PMs has done nothing but increase, triggering an escalation of prices and putting huge pressure on natural ores.[14] Overexploitation of metal reserves has caused serious environmental damage.[23] Additionally, the relatively short life span of electronic devices is causing enormous amounts of waste electrical and electronic equipment (WEEE).[24]

1.3.2.1 Problems derived from the extraction process

Mine waste includes a complex mixture of discarded rock, processing chemicals and ashes.[25] It represents one of the world's largest streams of waste.[25] The major footprint is derived from discarded rock, as only small fractions of metals are extracted per tonne of excavated rock.[26]

Extraction from metal ores generally involves hydrometallurgical processing (leaching metals from the rock) and cyanides were traditionally used as leaching agents.[27] Although cyanides have since been substituted for non-toxic compounds, there are still many tailing ponds containing high concentrations of cyanides around the world that present a threat to the environment.[25] Particularly worrying is the ability of cyanides to form very soluble complexes with some heavy metals, as these keep the toxic elements in solution for longer periods of time, expanding their damaging area.[28]

Some tailing sludges are highly acidic, which could be harmful if accidentally released to soils and water streams.[29] In addition, leaching processes may mobilise other metals from the rock. As an example, arsenic can be released from gold deposits during weathering, posing a serious threat in the environment due to the toxicity of arsenic.[29]

1.3.2.2 Problems derived from usage of precious metals

Discarded electronic devices are grouped under the name of WEEE.[30] This category includes any discarded equipment that uses electricity.[31] On the other hand, the term E-waste only includes electronic devices such as mobile phones or computers.[31] If not disposed of appropriately, some of WEEE and E-waste components could be released to the environment (i.e. heavy metals), seriously threating entire ecosystems.[30] Burning WEEE to obtain metal-containing ashes is not an optimal solution either, as compounds toxic to humans and harmful for the environment may be generated (i.e. dioxins, polyaromatic hydrocarbons).[31] Dealing with WEEE is especially problematic due to the volumes generated yearly; as mentioned above, the demand of electronic devices has exponentially increased in the last two decades, leading to the production of almost 1000 million phones in 2008 alone.[20] In turn, life span of electronic devices has significantly shortened.[31] The life span of mobile phones and flat screens have been estimated as 3 and 6 years respectively.[6] However, these values are optimistic, short innovation cycles and advertising from manufacturers encourages society to replace electronic devices ever more often.[24, 31] This has resulted in the production of enormous amounts of E-waste, mainly from Europe and the United States. Estimated at 20-50 million tonnes a year worldwide in 2006, E-waste production rates were expected to increase during the present decade, as Latin America, China and Eastern Europe start to significantly contribute to it.[31]

1.3.3 Elemental sustainability

If extraction rates follow the current growing trend, global reserves of gold and platinum will be depleted in the next 50 years (100 years in the case of palladium).[22] Clearly, current consumption rates are not driven by the 'elemental sustainability' concept which classifies a metal as sustainable if its use by the present generation does not compromise the ability of future generations to exploit this element.[22] Thus, the recycling of PMs has become crucial to sustain humanity's existing lifestyle without compromising future

generations. Currently, only 60% of PMs are recycled.[32] While metals from jewellery and supported catalyst are mostly recovered, large amounts of PMs from electronic devices and autocatalytic converters are still not recycled.[33] Recovery and recycling can be encouraged by raising awareness among the population through advertisements, outreach events and social media. In addition, legislation can play a key role in stimulating the recovery and recycling WEEE.[34] As an example, the European Union put in place a Directive in 2003 to create free of charge collection schemes for electronic devices.[30]

Non-recycled PMs are not destroyed, but dispersed as part of landfill.[35] Both recovered WEEE and disseminated PMs present potential as secondary metal ores due to their relatively large amounts of PMs overall.

1.3.3.1 Secondary ores for precious metals

Recovering metals from different types of waste can be more energetically and economically efficient and present lower environmental impact than extraction from natural ores.[22, 33] As a result, a variety of waste systems have been assessed as potential secondary sources of PMs (Figure 1.2).[36]

- *Mine waste*. Over a tonne of waste (even more in some cases) is produced per tonne of metal extracted from primary ores.[26] In the surrounding areas of a mine it is possible to find waste rock that has been discarded after metal leaching, and waste ponds containing liquid waste with metal concentrations below historical economically viable threshold (ppm range).[25] However, the increasing demand for PMs, and associated price rise, has forced the reconsideration of the potential value of such waste as a secondary source of PMs.[37]
- *Municipal solid waste (MSW).* This combines a wide variety of components, including plastics, glass, organic matter and electronics.[38] The presence of electric and electronic devices combined with the vast production of MSW, over 255 million tonnes in Europe every year,[39] turns MSW into a potential secondary

source of PMs. As an example, it has been shown that the MSW/underground reserves ratio of platinum group metals is 3.6%.[40] The percentage increases up to 16.3% in the case of gold.[40] Clearly, pre-separation of WEEE to avoid its combination with MSW is essential and can offer an enriched secondary source of PMs. However, pre-separation still needs to be further encouraged, as the amount of WEEE in MSW can be as high as 8% in developed countries.[41]

- *WEEE*. This includes different types of discarded electric devices.[31] Nevertheless, electronic devices such as mobile phones and computers are main contributors to WEEE.[31] Enormous amounts of WEEE have been generated in the last decades; Europe alone was set for disposal of 8.3-9.1 million tonnes of electronic devices in 2005.[42] These values are expected to reach 12.3 million tonnes a year in 2020.[42] Globally, the estimation is 40-50 million tonnes of WEEE generated every year.[36] Concentrations of PMs in WEEE well exceed those in natural ores. For example, a tonne of motherboard scrap contains 25 times more gold than a tonne of natural ore.[34] These values increase up to 35 times for mobile phone handsets.[34] The exorbitant production of electronic waste combined with its high concentration of PMs make WEEE a vast and potentially attractive secondary source for PMs.
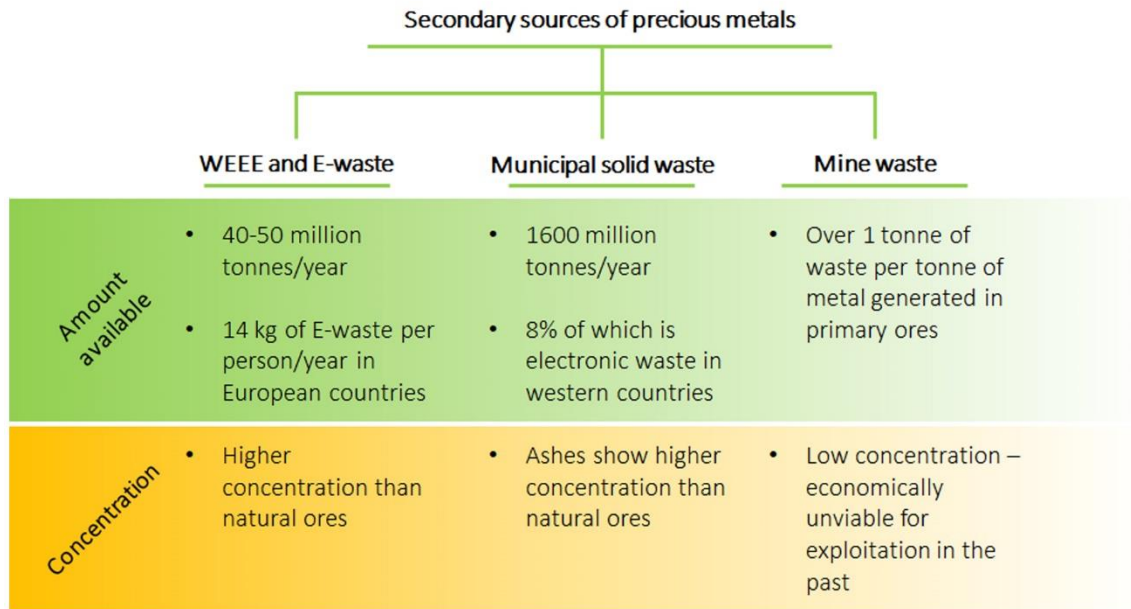
Figure 1.2 Major secondary sources of precious metals, their availability (green) and concentration (yellow).[36]

1.3.3.2 Techniques to recover precious metals from secondary ores

Several techniques can be employed to obtain PMs from secondary sources:

- *Pyrometallurgical operations*. Waste containing PMs is crushed and smelted in a high temperature furnace to yield metals.[27, 43] However, pyrometallurgy requires large amounts of energy due to the high temperatures used in the process.[44] In addition, burning certain types of metal-containing waste may release toxic compounds such as dioxins and polycyclic aromatic hydrocarbons from plastics.[31]

- *Hydrometallurgical/leaching operations*. This involves the dissolution of all soluble metals to produce a metal-containing liquor.[27, 43] Cyanide was traditionally used as leaching agent.[45] However, as explained in Section 1.3.2.1, it presented a serious threat to the environment if accidentally released from the storing pools.[28] Cyanides have been substituted by Cl_2 and aqua regia (3:1 mixture of concentrated HCl and HNO_3), addressing the environmental risk embodied by cyanides.[45] Environmental concerns settled, hydrometallurgy has become a popular method to extract metals from secondary ores, due to its low cost and

simplicity of operation.[45] After solubilisation, metals can be then recovered from solution using different techniques, including chemical precipitation, ion exchange, electrochemical processes and adsorption.[43] Despite their ease of operation, these techniques present some drawbacks. For example, chemical precipitation is not efficient for low concentration solutions and produce large amounts of sludge.[46] Ion exchange, although selective, presents low adsorption capacity and is expensive.[46] Electrochemical techniques are also quite costly.[47] Activated carbons (AC) have been widely used as adsorbents due to their high efficiency, even at very low concentrations of metals.[48] However, commercial AC are expensive and difficult to regenerate.[49] Bio-adsorbents present similar adsorption capabilities and are in turn inexpensive and reusable.[48]

1.3.4 Bio-adsorbents

Non-living, bio-derived materials capable of removing substances from solution are known as bio-adsorbents.[50] The advantages of bio-adsorbents are many, including renewability, minimal production of sludge, ease of handling, high adsorption capacities and potential for regeneration and reusability.[51] The term bio-adsorbent encloses a wide range of materials, from fungi to bacteria and agricultural waste, among many others.[50] As the focus of the present work is starch-based materials for PM adsorption, polysaccharide-derived materials used for the adsorption of gold, platinum and palladium are the main topic of the following sections.

1.3.4.1 Non-polysaccharide derived bio-adsorbents for the adsorption of precious metals

A class of non-polysaccharide bio-adsorbent compounds that perform well in the recovery of PMs are polyphenols.[52] Polyphenols are secondary metabolites in plants and can be found in many food products including fruits, vegetables and beverages.[53] Polyphenolic compounds such as tannins displayed PM adsorption capacities of 1500 mg·g^{-1}.[52] Despite this excellent performance as bio-adsorbents, the future for large scale

PM adsorption using bio-derived polyphenols is not as promising as that of polysaccharides because their concentrations in agricultural and food waste are relatively low, in the order of mg polyphenol per kg of waste.[53]

1.3.4.2 Polysaccharide-derived bio-adsorbents for the adsorption of precious metals

Polysaccharide-derived bio-adsorbents have previously been used to investigate the adsorption of heavy metals.[54-56] However, the number of studies focused on PMs adsorption is limited. Table 1.2 lists the available literature on polysaccharide-based materials for the bio-adsorption of Au, Pt and Pd and Figure 1.3 summarises this information in a graphical way. In all cases, the number of studies on Au adsorption surpasses those for Pd and Pt, due to the high value of this metal (Pt 974 $/oz, Au 1319 $/oz and Pd 1099 $/oz).[57, 58]

Table 1.2 Polysaccharide-derived bio-adsorbents for the recovery of gold, palladium and platinum described on the literature.

Polysaccharide	Description of adsorbent	Adsorption capacity ($mg \cdot g^{-1}$)	Ref.
Chitosan	Glutaraldehyde crosslinked chitosan	(Au^{3+}) 590	[59]
	Crosslinked hexamethylene di-isocyanate chitosan	(Au^{3+}) 720	[59]
	Sulphur derived chitosan	(Au^{3+}) 620	[59]
	Sulphur derived crosslinked hexamethylene diisocyanate chitosan	(Au^{3+}) 600	[59]
	Chemically modified chitosan resin	(Au^{3+}) 709	[60]
	L-lysine crossedlinked modified chitosan	(Au^{3+}) 70.3	[61]
	Glycine modified crosslinked chitosan resin	(Au^{3+}) 170	[62]
	4-amino,4'-nitro azobencene chitosan	(Au^{3+}) 70.0	[63]
	Unmodified chitosan	(Au^{3+}) 650	[64]
	Glutaraldehyde crosslinked chitosan	(Pt^{4+}) 300	[65]
	Glutaraldehyde crosslinked chitosan	(Pt^{4+}) 351	[66]
	Polyethyleneimine modied chitosan	(Pt^{4+}) 585	[66]
	Thiourea modified chitosan	(Pt^{4+}) 507	[66]

	Glutaraldehyde crosslinked chitosan	(Pd^{2+}) 260	[67]
	Thiourea modified chitosan	(Pd^{2+}) 270	[67]
	Rubeanic acid derived chitosan	(Pd^{2+}) 345	[67]
	4-amino,4'-nitro azobencene chitosan	(Pd^{2+}) 58.6	[63]
	Glutaraldehyde crosslinked chitosan	(Pd^{2+}) 213	[66]
	Polyethyleneimine modied chitosan	(Pd^{2+}) 372	[66]
	Thiourea modified chitosan	(Pd^{2+}) 362	[66]
Alginic acid	*Chllorella vulgaris*	(Au^{3+}) 98.5	[68]
	Ascophyllum nodosum	(Au^{3+}) 30.0	[69]
	Sargassum natans	(Au^{3+}) 420	[69]
	Fucus vesiculosus	(Au^{3+}) 74.8	[70]
	Crosslinked alginic acid	(Au^{3+}) 1100	[71]
	Calcium alginate beads	(Au^{3+}) 290	[72]
Cellulose	De-alginated seaweed waste	(Au^{3+}) 197	[73]
	Crosslinked cellulose	(Au^{3+}) 1490	[71]
	Crosslinked cotton cellulose	(Au^{3+}) 1223	[74]
	Crosslinked paper gel	(Au^{3+}) 994	[75]
	N-aminoguanidine crosslinked cellulose	(Au^{3+}) 1813	[76]
	p-aminobenzoic paper gel	(Au^{3+}) 1004	[77]
	Medicago sativa (alfalfa) shoots	(Au^{3+}) 36.0	[78]
	Lemmon peel	(Au^{3+}) 1280	[79]
	Buckwheat hulls	(Au^{3+}) 297	[80]
	Durio Zibthinus husk	(Au^{3+}) 339	[81]
	Banana peel carbon	(Au^{3+}) 802	[82]
	Rice husk carbon	(Au^{3+}) 150	[83]
	Barley straw carbon	(Au^{3+}) 289	[83]
	Apricot stone carbon	(Au^{3+}) 6.4	[84]
	Bagasse ashes	(Au^{3+}) 324	[85]
	N-aminoguanidine crosslinked cellulose	(Pt^{4+}) 123	[76]
	p-aminobenzoic paper gel	(Pt^{4+}) 98	[77]
	N-aminoguanidine crosslinked cellulose	(Pd^{2+}) 119	[76]
	p-aminobenzoic paper gel	(Pd^{2+}) 160	[77]
	Racomitrium lanuginosum (moss)	(Pd^{2+}) 37.2	[86]
Pectin	Crosslinked pectin	(Au^{3+}) 945	[71]
Starch	Starch-based hydrothermal carbon spherules	(Au^{3+}) 591	[87]
	Carbonised expanded starch	(Au^{3+}) 600	Present work
	Carbonised expanded starch	(Pt^{2+}) 21.5	
	Carbonised expanded starch	(Pd^{2+}) 73.2	

Polysaccharide-derived bio-adsorbents		Number of studies
Chitosan Require crosslinking to improve acid and thermal stabilities N-groups active role in adsorption Adsorption mechanisms: electrostatic attraction, ion exchange or chelation	**Cellulose** Require crosslinking to improve physical stability Reduction of metal ions to form nanoparticles and oxidation of the bio-adsorbent surface Ion exchange mechanism if N-groups were added	**Per type of polysaccharide** Cellulose 39% Chitosan 39% Alginic acid 12% Pectin 2% Starch 8%
Alginic acid Including non-living algae and alginate derivates Reduction of metal ions to form nanoparticles Oxidation of the bio-adsorbent surface (hydroxyl and carboxylic groups)	**Pectin** Reduction of metal ions and oxidation of the bio-adsorbent Very limited literature **Starch** Reduction of metal ions and oxidation of the bio-adsorbent Limited literature (includes present work)	**Per type of precious metal** Pd 21% Pt 14% Au 65%

Figure 1.3 Characteristics of polysaccharide-derived bio-adsorbents and the number of studies per type of metal and polysaccharide.[56, 59-62, 64-85, 87, 88]

1.3.4.2.1 Cellulose

Cellulose is formed by repeating β-D-glucopyranose units, with every second anhydrous glucose unit rotated 180 ° (Figure 1.4).[89] Cellulose is a major constituent of plant cell walls, which makes it the most abundant polysaccharide in the world. Its natural generation rate (through photosynthesis) is estimated at 10 billion tonnes a year.[89] Its renewable character, wide availability and low-cost make cellulose an attractive bio-adsorbent.[90] In contrast, cellulose requires chemical treatment before being used for adsorption applications to improve its physical properties (thermal resistance, hydrophobic and hydrophilic character, elasticity).[88] Crosslinking and conversion to AC can improve the physical properties of cellulose.[88, 91] Cellulosic agricultural waste offers a renewable source of AC, opposite to its fossil derived counterpart produced from coal.[92] Additionally, conversion to AC adds economic value to the cellulosic waste.[92]

1.3.4.2.2 Chitosan

Chitin and chitosan are random co-polymers of 2-acetamide-2deoxy-β-D-glucose and 2-amino-2-deoxy-β-D-glucose (Figure 1.4).[93] Chitosan is obtained by deacetylation of chitin, one of the most abundant polysaccharides, which can be found in the shell of crustaceans and is, therefore, a waste product of the seafood processing industry.[49, 56] It has been shown that untreated chitosan may dissolve in acidic media.[49] Therefore, it requires pre-treatment (generally crosslinking) to overcome its low acid and thermal stability, and poor porosity.[56]

1.3.4.2.3 Alginic acid

Alginic acid is formed by non-regular repetitions of 1,4-β-D-mannuronic and α-L-guluronic acid units (Figure 1.4).[94] Alginic acid can be obtained from brown algae in which this polysaccharide accounts for 10-40% of its dry weight[95]. 1.6 million tonnes of algae were harvested in 2015 alone, making alginic acid a widely available polysaccharide.[96] De-alginated seaweed is a by-product of alginate production and the main component is cellulose,[97] therefore, de-alginated bio-adsorbents have been grouped with cellulosic materials.

1.3.4.2.4 Pectin

Pectin is constituted by D-galacturonic acid units, with a minor presence of a neutral sugar, rhamnose (Figure 1.4).[98] Commercial pectin is extracted from fruit peels, mainly apple and citrus, that are by-products of the food industry (juice and cider production).[99] It can also be extracted from sugar beet pulp which is a by-product of the sugar industry and presents high pectin content.[100] Wide availability and waste valorisation through its application as bio-adsorbent make pectin a potentially good candidate for PM recovery. However, very limited studies have been carried out in this area.
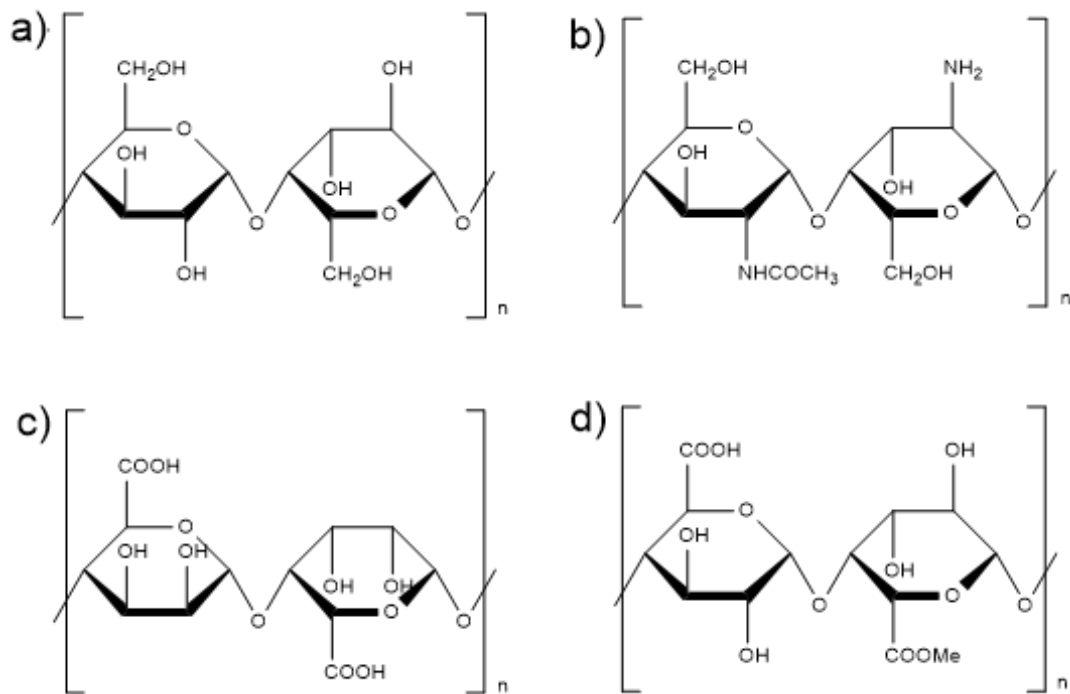
Figure 1.4 Chemical structures of a) cellulose, b) chitosan, c) alginic acid and d) pectin.

1.3.4.2.5 Starch

Starch is an energy storing polysaccharide in plants, and the major source of carbohydrates in the human diet.[101] Plants use starch to store the glucose produced during photosynthesis.[102]

23.6 million tonnes of agricultural crops were used to produced 10.7 million tonnes of starch in 2016 in the European Union alone.[103] Worldwide, it was estimated that 71 million tonnes of starch were used in 2011.[104] Besides the traditional commercial sources, starch can be recovered from waste streams, which could be potentially used as starting material for the preparation of chemicals.[105] This not only adds economic value to the waste stream, but help reducing the environmental impact of the starch processing. As an example, industrial potato peeling generates significant amount of waste: 90 kg per tonne of raw material processed, a third of which is starch.[4]

Starch is formed by two types of glucan chains, amylose and amylopectin (Figure 1.5).[49] Both consist of glucose molecules connected by α (1-4) glycosidic linkages.[106] The key differences between them are in the degree of branching in the polymer; whereas amylose is linear, amylopectin presents α (1-6) glycosidic linkages.[106] 'Cooking' starch in an excess of water is known as gelation or gelatinisation.[106] During this process, starch loses its crystallinity and amylose leaches out the granules which irreversibly swell, yielding a porous gel.[106] When the resulting gel is cooled down, it hardens to form a three-dimensional network due to partial recovery of crystallinity. It is noteworthy that amylose is responsible for recrystallization in the short term, however, the crystalline regions in the original starch granules were formed by amylopectin chains.[106]
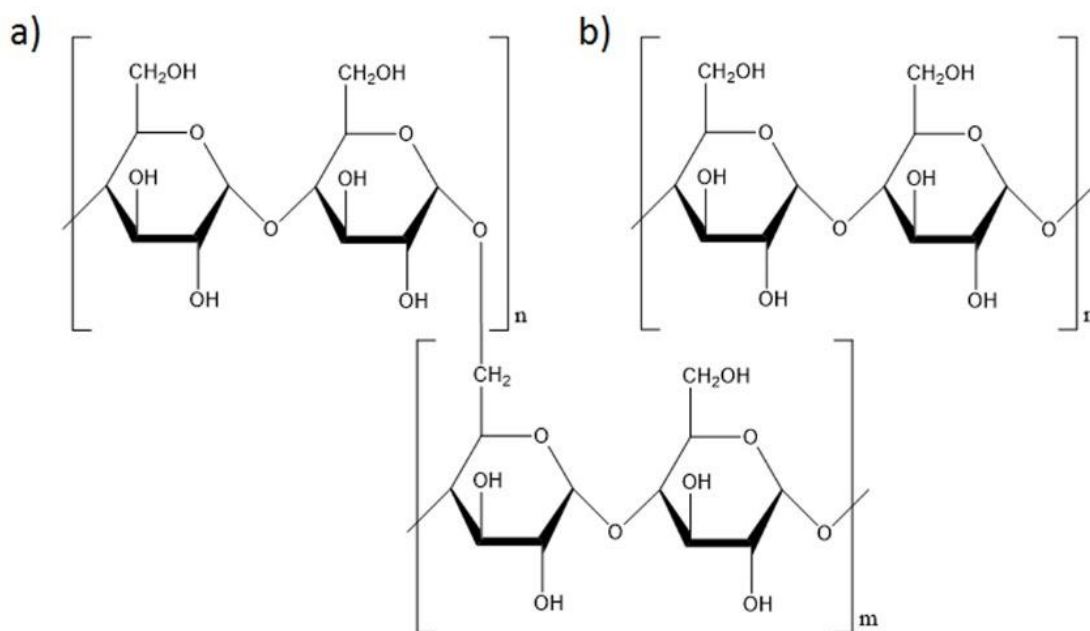
Figure 1.5 Chemical structure of a) amylopectin and b) amylose.

The relative content of amylose and amylopectin varies within botanical sources from waxy starches with less than 2% of amylose to amylo-starches, with over 70% of amylose.[107] Variation of the ratio of amylose to amylopectin strongly affects the properties of starch and its potential uses.[108] High-amylose starches contain over 50% and sometimes up to 70% of amylose, and are commercially used for candies and as coatings

for deep fried foods due to strong gel formation on heating in water.[109] As mention above, the recovery of crystallinity during retrogradation primarily involved amylose.[106] Thus, high-amylose starches retrograde to a greater extend generating stronger gels. Hylon VII is one of the commercially available high-amylose starches and it has been used for the preparation of Starbon®.[110] These materials will be described in detail in Section 1.3.5.

Research about the utilisation of starch-derived materials as bio-adsorbents is limited despite of being one of the most abundant polysaccharide produced by plants (after cellulose).[49] In addition, it has been recently shown that modified starch (gelled and subsequently carbonised) is highly porous and has been successfully employed in the adsorption of organic compounds.[111, 112] Therefore, modified starch can potentially become a good bio-adsorbent for the recovery of PMs.

1.3.4.3 Adsorption mechanism of polysaccharide-based bio-adsorbents

PMs can be adsorbed onto bio-adsorbents through different mechanisms which can be classified into:[113]

- Chemical mechanisms including chelation, complexation and reduction.
- Physical mechanisms which include electrostatic interactions and ion exchange.

Chemical mechanisms include donation or exchange of electrons. The mechanism of complexation involves the donation of an electron pair from a ligand to a metal centre.[114] Chelation is a type of complexation in which the ligand is polydentate and can form a ring with the metal as the closing element.[115] In the reduction mechanism, metals get reduced to their metallic form while the adsorbent oxidises.[116]

On the other hand, physical mechanisms do not involve electron movements, instead they rely on electrostatic forces. In the ion exchange mechanism, an ion is removed from solution and is replaced by a similar ion originating from the adsorbent material, whereas in an electrostatic mechanism there is no exchange of ions.[117]

The adsorption mechanism changes with the characteristics of bio-adsorbents (i.e. functional groups present) and solution conditions (i.e. pH), suggesting that the mechanism is heavily dependent on the biomass properties and case-by-case studies are required.[118] Nevertheless, general trends can be observed. For example, most of the studies on PM adsorption by chitosan showed that electrostatic interactions were responsible for the adsorption at low pH.[60, 61, 66] On the other hand, PMs where chelated if the adsorption took place at neutral pH.[59] This phenomenon can be explained by the protonation of amine groups under acidic conditions. Protonated groups are positively charged and are capable of electrostatically binding PM anions (Precious metals in acidic HCl solution form the following complexes: $AuCl_4^-$, $PdCl_4^-$ and $PtCl_4^-$). At neutral pH, amine groups have a lone pare of electrons that can be used to chelate cations in solution.[114] As most of the studies were carried at low pH due to better solubility of PMs, the favoured mechanism for chitosan was electrostatic interactions. Some studies showed the reduction of PM ions to its metallic form when other bio-adsorbents such as cellulose and alginic acid were used.[70, 71, 74, 75]. Pectin and starch-derived materials also showed evidence of reduction, however there is only a small number of studies available.[71,87]

1.3.4.4 Recovering metals from bio-adsorbents

Retrieving the metals from the bio-adsorbent surface after the adsorption process is essential for reusability and recycling.[50] Two methods have been widely studied to recover metals from adsorbents:

- *Desorption*. A series of compounds are used to leach the metals back into solution.[119] Several organic and inorganic solvents have been tested in metal desorption, including acetone, ethanol, hydrochloric acid and thiourea among others.[61, 84] Solvents need to efficiently solubilise metals without damaging the structure of the bio-adsorbent (to allow for reusability), as well as not be harmful for the environment and cost efficient.[120] Research commonly focuses on the first two premises.[62,84] However, the environmental impact and price rise derived from

mining activities, and high metal demand were the primary reason the exploitation of secondary sources and therefore need to be considered. Desorption allows the recovery and re-use of the bio-adsorbent, reducing the dependency upon the biomass supply.[120]

- *Incineration*. The metal-loaded bio-adsorbent is burnt, yielding ashes rich in a specific metal and silica.[83] Ashes are usually treated to remove silica in order to purify the obtained metal.[83] However, the bio-adsorbent cannot be re-used because it is lost during the process.[50]

Both methods have been used to recover precious metals from metal-loaded bio-adsorbents.[61, 75, 83, 84] Interestingly, a correlation between the adsorption mechanism and the recovery method employed can be observed; when PMs were adsorbed in their ionic forms (i.e. chelation and ion exchange mechanisms) metals were retrieved by solvent desorption.[60, 62, 66] In contrast, PM nanoparticles (NPs) formed as a result of a reduction mechanism were mostly recovered by incineration.[75, 83, 85]

Recently, a third option is being considered: *in-situ* use of metal-loaded bio-adsorbent for different applications.[50] This pathway avoids consuming significant amounts of solvent and energy to free the metals and contributes to close the loop of circular economy.[50] Only a few examples have been described in the literature, and all focus on heavy metals (the literature considers heavy metals those elements with densities over 5 g·cm^{-3}).[121] For example, the metal-loaded compound, formed when Ni was recovered by sawdust bio-adsorbents, was used to catalyse the decomposition of phenolic toxic compounds in water streams.[122] Fir sawdust was also used to adsorb Cu and the metal-loaded complex was subsequently used as a catalyst in the fast pyrolysis process to convert the bio-adsorbent into bio-oil.[123]

The applications of carbon supported PMs are broad, especially in the field of catalysis where carbon supported PMs can be used to catalyse many reactions including hydrogenations,[124] oxidations,[125, 126] reductions[127] and polymerizations.[128] Thus, PM-

loaded polysaccharide-derived bio-adsorbents are good candidates to catalyse a wide range of industrial reactions.

1.3.5 Starbon®

Starbon® are starch-based mesoporous carbonaceous materials that were developed at the Green Chemistry Centre of Excellence in York.[110,129]

1.3.5.1 Starbon® properties

Starbon® materials are prepared by a simple 4-step methodology that includes gelation, solvent exchange, drying and carbonisation.[110] The physical and chemical properties displayed by Starbon® can be tuned to perform well in a broad range of applications.[110]

- *Porosity*. Starbon® are highly mesoporous materials, with significantly less micropores than other commercially available porous carbons (i.e. activated carbon).[110] The presence of mesopores can be advantageous for some applications. For example, in contrast to micropores, mesopores can lead to reversible adsorption of different compounds.[130] Applications like chromatography or substance recovery usually require materials able to eventually desorb the targeted compounds.[130] Energy storage devices such as supercapacitors also benefit from the presence of mesopores, as they enable better dispersion of the electrolyte.[131]

  The preparation of Starbon® do not require the use mesoporous templates or hazardous chemicals to create the porous network because Starbon® porosity arises from the gelation of polysaccharides.[110]

- *Chemical functionalities*. Starbon® surface can display a wide range of functional moieties, from polysaccharide-like (i.e. hydroxyl and ether groups) to graphitic (i.e. aromatic groups).[110] The surface chemistry of Starbon® can be easily modified by varying the carbonisation temperature during preparation; while low temperatures yield hydrophilic materials, carbonisation at high temperatures

leads to more hydrophobic structures.[110,132] As the graphite layers' present in high temperature Starbon® are not fully organised, Starbon® are well described as turbostratic materials.[133]

- *Shape*. Starbon® have been traditionally prepared as a powder.[110] However, as a result of the present work, Starbon® monoliths have been developed, which significantly expands the range of potential applications for these materials.[134]

1.3.5.2 Starbon® applications

Since its creation a decade ago, Starbon® have been used in a wide variety of applications including catalysts, nanoparticle support, adsorption and isomer separation (Figure 1.6).

- *Catalysis.* It has been shown that Starbon® perform well as a catalyst in several organic reactions that are key for industrial processes. As an example, sulfonated Starbon® were up to ten times more active than other porous carbon in the esterification of succinic acid.[135-137] The resulting esters can be used as solvents or as intermediates for other chemical compounds.[138]

  The formation of amide bonds is essential in the pharmaceutical industry.[139] Sulfonated Starbon® were successfully used as a catalyst in the N-acylation reaction between amines and carboxylic acids to obtain amides.[140] Similarly, good performance was also observed when sulfonated Starbon® were used to catalyse the Ritter reaction between nitriles and epoxides to yield substituted amide groups.[141]

  Starbon®-derived materials also performed well in the alkylation of phenol with cyclohexane and the acetylation of 5-acetyl methyl salicylate with acetic anhydride.[142] Both types of reactions are intermediates in the preparation of fine chemical and pharmaceutical products.[143]

- *Support for nanoparticles*. Metal NPs are demanded for many applications because of their large surface to volume ratio.[144] Adding a support surface to the nanoparticles aids the control of NP size and clustering.[145] Starbon® have been

successfully employed to support platinum group metal NPs (i.e. Ru, Rh, Pt and Pd) which were subsequently used as catalysts for the hydrogenation of succinic acid.[146] This type of reaction traditionally involved high energies and pressures.[147] However, metal-supported Starbon® catalyst allowed this reaction to proceed in an aqueous media and under mild conditions.[146] Hydrogenation reactions are widely used at an industrial level by food and petrochemical companies.[8] These materials were also used in the hydrogenation of levulinic acid to eventually yield 2-methyl tetrahydrofuran, a potential biofuel and sustainable solvent.[148-150] Sulfonated Starbon® with attached Pd NPs also showed improved conversion and selectivity in different reactions using glycerol as starting material.[151] Glycerol transformation into products with high-added value has become of interest because glycerol is currently obtained in large amounts as by-product of biodiesel preparation.[151] The resulting products can be employed as fuel additives,[152] and emulsifiers in food, pharmaceutical and personal care products.[153, 154]

Transition metal-containing Starbon® aerogels have also been synthesised by simply adding the metal salts during the preparation process.[155]

- *Adsorption*. Starbon® have shown higher and more selective adsorption of CO_2 than other commercial activated carbon.[156] Therefore, Starbon® materials present potential for gas purification.

Starbon® have also been applied to the recovery of various organic substances from solution.[111, 112] For example, Starbon® perform well in the adsorption of a range of phenols, displaying adsorption capacities over 100 mg·g^{-1}, comparable to other available adsorbents.[112] Recovery of phenols from the waste streams of many industries (i.e. steel, herbicides) is of vital importance, as they are toxic and carcinogenic.[112]

Starbon® also showed improved adsorption capacity in comparison to NORIT®, a commercially available AC, for the adsorption of the dye methylene blue.[111] Dyes are found in the waste streams of many industries, including textile and paper

companies.[157] As phenols, dyes need to be recovered due to their toxicity, persistence in the environment and negative health effects.[158]

Starbon® have not been used previously to recover metals from waste waters. However, the ability of Starbon® to support metal nanoparticles and its good adsorption capabilities for organic compounds suggested that Starbon® could be a potentially good bio-adsorbent for PMs, as is explored in this Thesis.
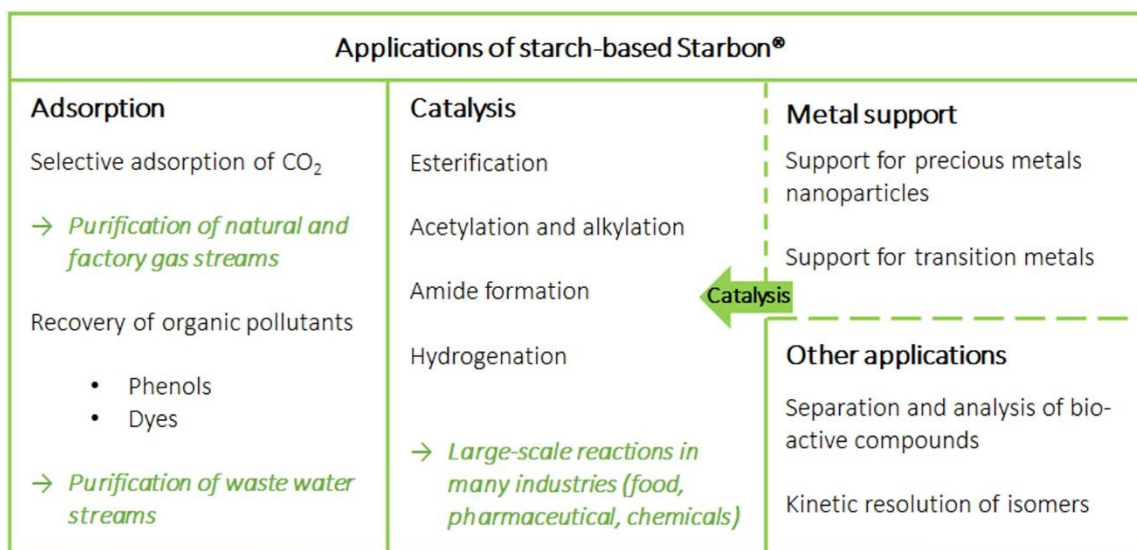
Figure 1.6 Range of applications in which of starch-based Starbon® have been tested.[111, 112, 135-137, 142, 151, 156]

1.4 Carbon materials for energy storage

1.4.1 Energy in today's world

Primary energy is the energy contained in coal, natural gas, crude oil, nuclear and bio-renewable sources which has not been subjected to any transformation. 73% of Europe's primary energy relies on fossil fuels and nuclear resources which generate greenhouse gases (GHGs) and radioactive waste respectively.[159] This value increases up to 91% in the USA.[160] The consumption of fossil fuels entails the release of billions of tonnes of CO_2 to the atmosphere every year, which has already caused an increase of 1 °C in the temperature of the planet, with dramatic consequences to entire ecosystems.[161, 162] In

addition, the energy demand increases every year worldwide, despite the decrease observed in Europe for the last decade.[163] The increasing concern for the environment and the realisation that fossil fuel reserves are depleting has enhanced the interest in renewable sources of energy.

1.4.2   Renewable sources of energy

A source of energy is considered renewable when is constantly replenished by nature.[164] The most common renewable energies are: hydroelectricity, solar power, wind power, geothermal heat and biomass (Figure 1.7).[165] Renewable sources of energy contribute to the reduction of GHG and waste, and are widely available.[164] Nevertheless, it is noteworthy that the 'sustainability' of hydroelectricity has been questioned, as some studies showed that the organic matter covered by the water eventually decays. Such decomposition generates GHGs.[166]

Theoretically, renewable energy sources can provide over 3000 times the current global demands and their use has significantly grown in the last few years with a net increase of 14% on its use for power generation in 2016.[167, 168] However, renewable energies are still far from leading the primary energy production, with a current share of 25.5% in Europe.[159] One of their major limitations is the lack of stability in production rates which significantly vary throughout a day or a season.[169] Storing energy to be used upon demand later is essential for the success of renewable sources of energy.[170]
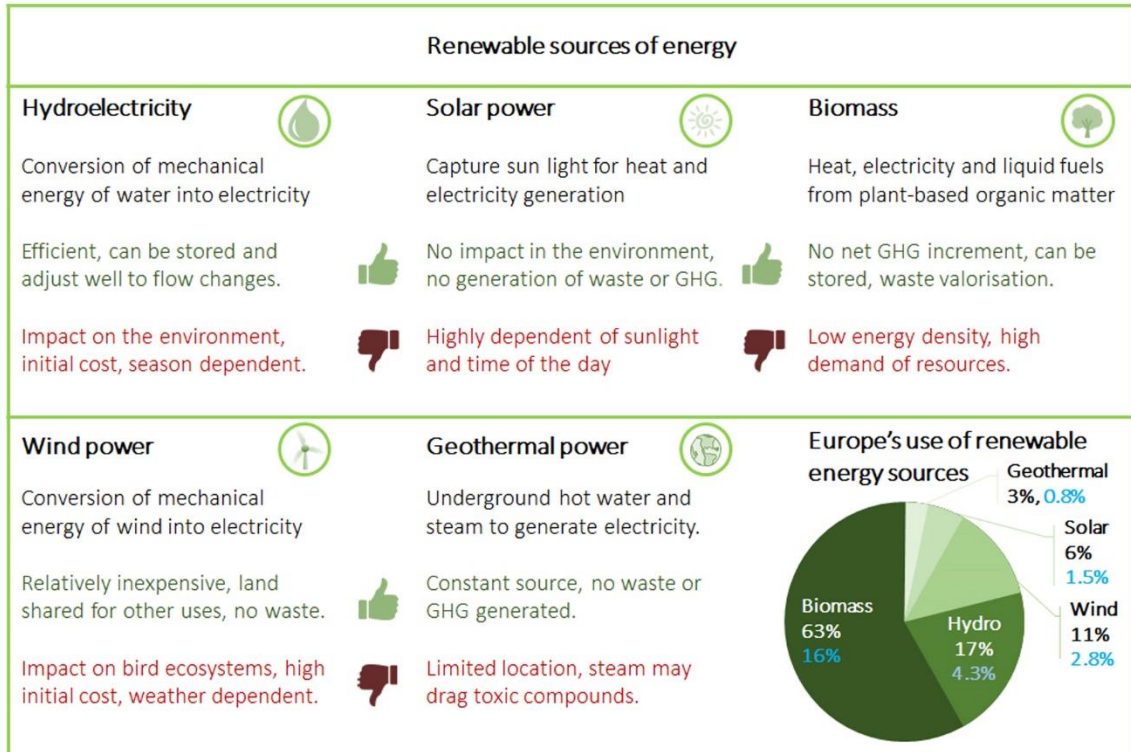
Figure 1.7 Strengths and weaknesses of most significant sources of renewable energy and its share in the European renewable market. Highlighted in blue is the contribution to the total primary energy generated in Europe.[159, 160, 164]

1.4.3 Energy storage (ES)

Storing the excess of energy produced overnight or during off-peak times is extremely important to deal with daily minute-hour peaks and other short-term fluctuations in electrical demand.[169] Storing technologies can also provide energy during brief power outages and contribute to the reduction of sags and surges.[169] ES commonly refers to storing electricity, which cannot be stored directly and therefore requires its transformation to other forms of energy.[171] A variety of techniques and devices for ES have been developed, each of which presents different characteristics and of these energy or power density are the most important.[169, 172-174] Energy density refers to the amount of energy that can be stored, and power density reflects how fast such energy can be released.[175] The representation of energy vs power density is known as a Ragone plot and this offers a clear summary of the state of the art of ES (Figure 1.8).[174]
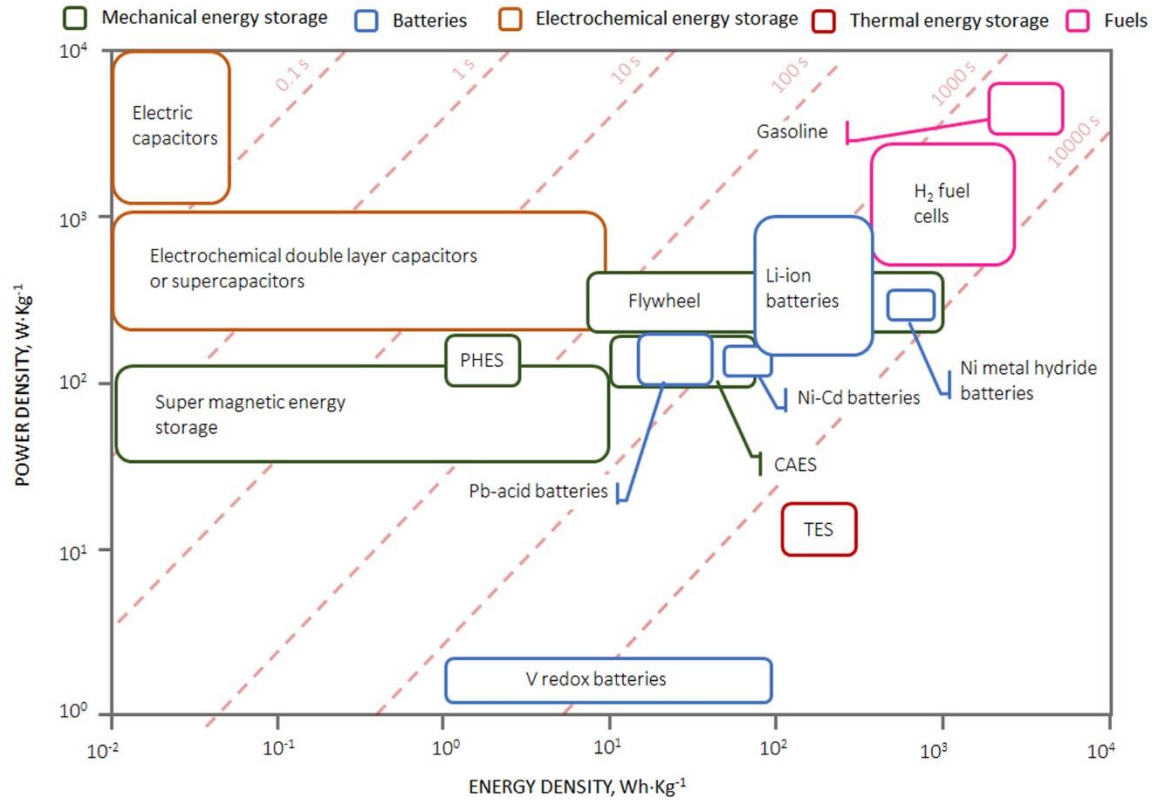
Figure 1.8 Ragone plot including a wide range of energy storage technologies, and fuels for comparative purposes. The diagonal lines indicate the time required to release the energy stored in the device.[173, 174, 176]

ES technologies can be classified by the type of energy used for storage into five main categories: thermal, mechanical, electromagnetic, chemical and electrochemical storing (Figure 1.9).[169, 172] However, the first four are outside the scope of the present work and are not discussed in detail. Electrochemical energy storage systems are described in the following sections.

Types of energy storage	
Thermal 🌡️ Transformation of energy into heat Sensible heat Heating up a substance with high specific heat (i.e. water) Latent heat Heating up a substance that undergoes a phase change (i.e. inorganic salts) Thermochemical energy Energy is applied to endothermic reactions that can be reversed with a catalyst	**Mechanical** ⚙️ Transformation into kinetic or potential energy Pump hydro-storage Water is pumped up at low-peak times and release back down to move a turbine when energy is needed Compressed air Energy is applied to compress air, which moves a turbine during depressurisation. Flywheel Energy is used to accelerate a rotor which produce energy during deceleration

Electrochemical 🔋	**Chemical** 🌿	**Electromagnetic** 🧲
Energy is store in an electrochemical cell and energy is retrieve when the electric circuit is closed	Energy is applied to the preparation of a compound (H_2, MeOH, EtOH) which is burned to retrieve the energy	Energy is stored in an electromagnetic field created by direct current flowing through a superconductive coil

Figure 1.9 Classification and brief description of most relevant types of energy storage.[177,178]

1.4.3.1 Batteries

A battery is an electrochemical device capable of storing electricity as chemical energy which can be released upon demand.[173] Batteries are a succession of one or more electrochemical cells formed by two electrodes that are connected through an external electric circuit and an electrolyte.[173] It is possible to distinguish two types of batteries: primary batteries which cannot be recharged and secondary or rechargeable batteries.[179]

Batteries can be used in a wide range of applications, including as regulators in the electric grid, in hybrid electric vehicles, portable electronic devices and wireless network systems.[171, 180]

In rechargeable batteries, the reaction between the anode and the cathode generates a flow of electrons through the external circuit that discharge the battery.[173] During this

process, the anode oxidises, causing the reduction of the cathode.[173] To recharge the battery, an external voltage is applied to reverse the chemical reaction (Figure 1.10).
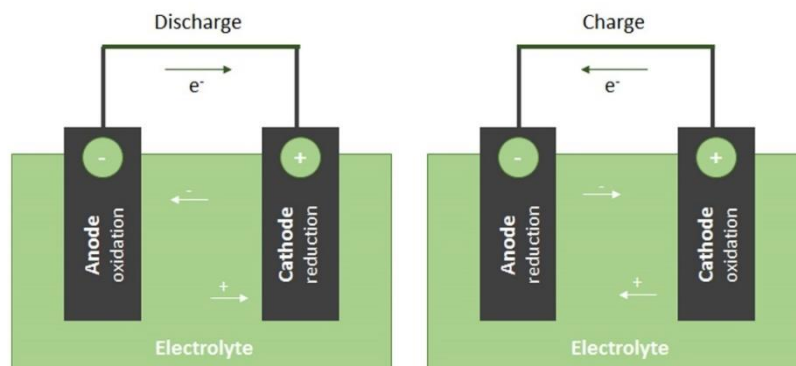
Figure 1.10 Schematic representation of the charge-discharge process occurring in a secondary battery.[173]

Batteries present relatively high energy density. Storage is derived from their ability to store energy in the bulk of a substance.[181] On the other hand, the charge-discharge process is slow.[181] On average, the efficiency of batteries ranges between 60 and 80%.[182] However, a wide range of batteries are available commercially, which differ from each other in the composition of the electrodes and therefore their properties.[180, 183-186] Lead-acid batteries have been widely used in automobiles during the 20th century.[174] Despite being mature devices with long-life cycles, lead-acid batteries are being replaced by others with larger energy density such as Ni-Cd batteries.[187] The cost, and the concerns about using heavy metals have encouraged their substitution.[174] Li-ion batteries have received much attention in the last years because they are light, small and powerful.[178, 188] They are currently used in some hybrid and electric vehicles and portable electronic devices, and demand is rapidly increasing.[180, 189, 190] As a result, concerns about over-exploitation and depletion of Li ores, as well as cost, have promoted research into sodium batteries.[190] In addition, high energy densities displayed by Li-ion batteries can result in overcharging for which they require a protection circuit.[191] Sodium has a very similar reduction potential to lithium, but is a significantly more abundant element.[180, 190]

1.4.3.2 Supercapacitors

Capacitors are energy storage devices that are formed by two conducting surfaces separated by an insulator.[181] In opposition to batteries, energy is accumulated by a physical process that does not involve chemical reactions.[181] During the charging process, a voltage is applied and electric charges separate and accumulate in opposite sides of the insulator (Figure 1.11).[181]

Supercapacitors are a particular type of capacitor that have received much attention in the last years as they can store more energy than traditional capacitors and release it faster than batteries.[192, 193] In supercapacitors the insulating material is replaced by an electrolyte.[181] Supercapacitors can be subsequently categorised as electrochemical double-layer capacitors (EDLCs) or faradaic supercapacitors.[194] In EDLCs the charge is stored between the electrode and the electrolyte due to the formation of the so called 'double-layer' (capacitive behaviour).[181] As shown in Figure 1.11, when voltage is applied, the ions in the electrolyte are attracted to the charged surface of the electrode, charging the supercapacitor.[181, 194] On the other hand, Faradaic supercapacitors combine the double-layer mechanism with highly reversible and rapid redox reactions occurring at the surface of the electrodes (pseudo-capacitive behaviour).[195]
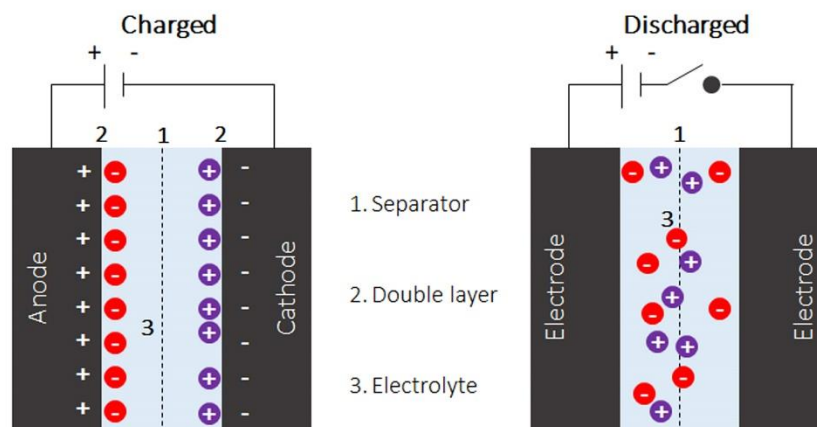
Figure 1.11 Schematic representation of the charge-discharge process occurring in an EDLC supercapacitor.[181]

Supercapacitors have found applications in specialised markets when short duration storage is required.[179, 196] For example, they are used for a rapid release of energy during power outage to feed back-up systems and avoid losing data.[192] Supercapacitors are also installed to protect adjustable-speed drivers for voltage sags that can otherwise stop entire production lines.[197] Supercapacitors can also be used in association with batteries to complement the latter. For instance, in electric vehicles peak energy demands required to go up a hill or accelerate are covered by supercapacitors.[198] They are particularly successful in trash hauling vehicles that need to break every few meters, as supercapacitors can store the energy released during breaking.[199] In hybrid vehicles supercapacitors extend the life of the battery and ease starting under cold weather.[194] Supercapacitors are also used to relieve batteries from high-power and pulsed currents which can damage the battery.[200] Nevertheless, it has been suggested that the breakthrough of supercapacitors in the broader market requires competing with batteries in terms of applications.[179]

EDLCs present many advantages over batteries, such us rapid release of energy (Table 1.3). As the process is not limited by the kinetics of a chemical reaction, energy can be released rapidly.[181] In addition, the physical storing mechanism employed by supercapacitors results in better reversibility and lower energy losses, allowing for thousands of extra cycles to be completed.[181] The human and environmental risk associated to supercapacitors is negligible compared to batteries that used toxic heavy metals (Pd-acid and Ni-Cd) or can be overloaded (Li-ion).[191] On the other hand, batteries present significantly larger energy densities, which can be explained by the 'location' of energy in both cases; whereas batteries stored energy in the bulk of the chemical compounds, supercapacitors are only able to use the surface of the electrodes.[181]

Table 1.3 Comparison of the properties of Li-ion batteries and EDLC supercapacitors.[173, 174, 178, 181, 201]

Properties	Supercapacitors	Batteries
Power density	1-10 kW·kg^{-1} Release energy in seconds	0.15 kW·kg^{-1} Release energy in hours
Energy density	5 Wh·kg^{-1} (3-4 in commercial devices)	> 50 Wh·kg^{-1}
Efficiency	95%	60-80%
Life expectancy	1 million cycles 30 years	1000-10000 cycles 5-10 years
Self-discharge rate	10-40% per day	5% per month
Shelf life	No degradation over time	Degrade over time
Temperature of operation	-40 to 70 °C	Close to RT
Cost	300-2000 $·kWh^{-1}	600-2500 $·kWh^{-1}
Effects on environment	Non-toxic	Li mining
Safety	Not known	Li-ion batteries can overload

1.4.3.2.1 Materials for supercapacitor electrodes

In the last years, much research has focused on the search of optimal materials for supercapacitors.[194, 202, 203] Three groups of materials are widely used in the production of electrodes for supercapacitors: carbons, metal oxides and conductive polymers.[202]

Carbon is the sixth element of the periodic table and it can be organised in different allotropes.[203] Allotropy is not exclusive for carbon, as it is also observed in other elements of the p group.[204] However, the number of allotropes in carbon is unusual and leads to a wide range of materials and properties.[205] Diamond and graphite are the two natural crystalline allotropes of graphite;[203] in diamond, the carbon atoms present sp^3 hybridization and are laid in tetrahedral conformation.[204] In graphite, the carbon atoms shoe a sp^2 hybridisation and are arranged forming hexagonal rings within a planar sheet.[204, 205] These sheets are parallelly orientated and linked to each other by weak bonds.[204] There are also carbon materials, usually known as engineered carbons, that

present two or three types of hybridisation such as carbon nanotubes (CNTs) and amorphous carbons respectively and these constitute the majority of commercial carbons.[203, 204] A significant fraction of engineered carbons are developed by heat treatment in inert atmosphere (carbonisation) of carbon-rich precursors.[203] During carbonisation, the precursor decomposes leading to the formation of the highly carbonaceous material, and water, CO_2 and CO that are lost as part of dehydration, decarboxylation and decarbonylation reactions.[206] The carbonisation process is generally followed by an activation step. T overall process yields highly porous materials.[203] This activation step consists on thermal activation (controlled gasification in the presence of oxidising gases to modify the carbon) or chemical activation (heating at lower temperatures in the presence of dehydrating agents). Carbons present several advantages including relatively low cost, wide availability and non-toxicity.[194, 195] High surface area and good conductivity is what makes a carbon ideal for EDLC applications.[207] As mentioned above, the charge is stored in the surface of the supercapacitor's electrode which indicates that the surface area of an electrode plays an important role in ES.[181] Nevertheless, it is noteworthy that the relation between surface area and capacitance is not linear and very much depends on the accessibility of the pores.[131, 198]

A wide range of carbon materials have been used to prepare EDLC electrodes.[195, 202, 203]

- *Activated carbon*. Their high surface area and relatively low cost make AC the most widely used materials for EDLC applications,[207] and AC-based supercapacitors have been reviewed by several authors.[195, 202] The capacitance of these electrode can reach 120 and 300 $F \cdot g^{-1}$ in organic and aqueous electrolytes respectively.[207] The major drawback of AC is the difficulty to control the pore structure and pore size distribution during preparation.[195]
- *Carbon nanotubes*. Despite their unique pore structure that favours ion transportation,[195] and excellent electric, thermal and mechanical properties, CNTs show a relatively poor performance as EDLCs (20-80 $F \cdot g^{-1}$) due to their reduced surface area.[203, 208]

- *Graphene*. As with CNTs, graphene presents good electric, thermal and mechanical properties.[209] The combination of these properties with the large surface area makes graphene an excellent candidate for EDLC applications.[202] Unfortunately, research on graphene-based supercapacitors is very recent and some drawbacks have not yet been overcome. The major problem is its tendency to re-stack, which significantly decreases the capacitance of the material.[202]

- *Templated carbons*. The use of a template such as mesoporous silica allows one to tailor the number and size of the pores, which usually include a large proportion of mesopores as it has been shown that this type of pore facilitates the mobility of the electrolyte, increasing the material's capacitance.[195] However, the preparation is relatively costly and requires hazardous chemicals to eliminate the template.[210]

- *Carbon aerogels*. These mesoporous materials do not require binding agents to be shaped as electrodes, which can increase the internal resistance of the carbon, as they can be produced as monoliths.[195, 203, 211] Nevertheless, the lack of micropores significantly reduces its capacitance.[195]

- *Activated carbon fibres (ACFs)*. These materials present high surface area and allow for good control of the pore characteristics.[203] However, ACFs are more expensive than ACs.[195, 203]

- *Carbide-derived carbons (CDCs)*. Carbon produced by extraction of metals from metal carbides is known as carbide-derived carbon. Chlorination of carbides results in the formation of a highly porous carbon structure.[212] The pore size distribution can be accurately controlled by adjusting the chlorination temperature.[213] These characteristics make carbides good candidates for supercapacitor applications.[214]

Metal oxides have received much attention in the last years for the preparation of faradaic supercapacitors, as it has been shown that these materials offer 10 times higher capacitance compared to EDLCs due to most of the energy being stored in rapid redox reactions (up to 1000 $F \cdot g^{-1}$ for RuO_2).[215] RuO_2 has been extensively studied due to its

favourable properties including three oxidation states within a 1.2 V window that can be interchanged through highly reversible redox reactions, good metallic and proton conductivity and long cycle life.[207, 216] However, the high economic and environmental costs of RuO_2-derived electrodes have limited their use to military and aerospace applications.[202, 215] Other metal oxides with similar electrochemical performance but more cost effective and with environmentally friendly properties that are under investigation include MnO_2, NiO, Fe_3O_4 and V_2O_5.[194]

Conductive polymers can also be used to prepare faradaic supercapacitors as they present high electric conductivity in a doped state, a wide voltage window and high storage capacitance.[217,218] In addition, these materials tend to be low cost, with minimal environmental impact. However, conductive polymers display swelling and shrinking during charge discharge cycles which decreases their electrochemical performance and accelerates their degradation so they cannot achieve thousands of cycles.[194]

1.4.3.2.2 The need for composite materials

As mention above, ACs are the most widely used materials to produce EDLC electrodes due to high porosity, availability and relatively low cost.[207] However, high porosity generally implies poor high internal resistance or poor conductivity that can reduce the capacitance of the device.[203] One of the strategies followed to improve the conductivity of the electrode is the preparation of composites materials.[219-225] The resulting materials present enhanced electrochemical properties (i.e. capacitance). For example, highly dispersed CNTs were added to ACs to yield a composite with enhanced energy and power density compared to the untreated AC.[219]

CNTs have also been used to improve the conductivity of carbon aerogels [220, 221] and graphene electrodes, where CNTs are applied to reduce the characteristic re-stacking of graphene.[222-224] Graphene was in turn used to enhance conductivity and capacitance of AC.[225] Although the application of high-tech carbons such as CNTs and graphene improve

the capacitance of the electrodes, it is important to consider that the production of these materials is expensive and therefore may increase the overall cost of the device.

The aim of the present work is to develop alternative and cost-effective carbon-carbon composites that combine the advantageous porosity of ACs or carbon aerogels with high conductivity. Thus, it is believed that the addition of the non-expensive and highly conductive graphite to mesoporous Starbon® can result in porous conductive carbons with the potential to be used for EDLC.

1.5 Conclusion

Our current lifestyle significantly relies in the production and consumption of energy. Humankind has traditionally entirely relied on fossil fuels to produce such energy. However, an increasing concern for the environment has led to:

- A need for renewable sources of energy (i.e. solar, wind) that reduce or avoid the GHGs emissions. However, it is not possible to obtain a constant supply of energy from these sources which emphasise the importance of energy storage techniques that allow to keep the energy generated and use it upon demand.
- Alternative 'low-carbon' technologies which heavily rely on precious metals. This place huge pressure on metal natural ores and significantly raise the prices of the elements. As a result, the need for metal recovery and recycling has been emphasised, especially from sources such as WEEE, which amounts increase yearly, and contains significant amounts of valuable metals.

The aim of the present work is the preparation of monolithic carbon materials that can be used to recover precious metals from waste streams, and to store energy as electrodes in supercapacitor devices. These materials are prepared under the guidelines of the 12 Green Chemistry Principles defined by Anastas, including the utilisation of renewable and non-hazardous materials.

Preparation and characterisation of Starbon® monoliths and their application in precious metal adsorption

Chapter 2

2 Preparation and characterisation of Starbon® monoliths and their application in precious metal adsorption

2.1 Introduction

Precious metals (i.e. gold, platinum and palladium) are used in many applications: from electronics to chemical catalysts, including jewellery and medical treatments, among others.[5-7] Their use in printed circuit boards (PCBs) of electronic devices has increased greatly the demand of these metals and, in turn, their prices.[14, 19, 226] Fast consumption rates of PMs (in electronics, chemical reactions or medicine) are causing depletion of natural ores and generation of thousands of million tonnes of environmentally threatening mine waste.[14, 23] Efforts are currently focused on secondary metal sources, including mine tailings and WEEE.[36] Using secondary metal ores reduces the rate of exploitation of natural sources and not only minimises the amount of waste generated but also re-uses the current waste.[22, 33]

Chitosan, cellulosic materials and ACs, have gained much attention in the last few years as potential bio-adsorbents, because of their low cost, wide availability, ease of action, biodegradability and benignity to the environment.[51] ACs have been widely used as adsorbents by industry to recover heavy metals from waste streams due to their high efficiency even at very low concentrations.[48] However, the majority of the pores found in AC are micropores which present high surface energy that can lead to irreversible adsorption, making desorption more challenging.[130] Alternatively, mesoporous carbonaceous materials can selectively and reversibly adsorb different metals, although the cost of preparation has limited their applicability.[227]

Starbon® are carbonaceous mesoporous materials derived from polysaccharides (i.e. starch) that can be prepared in a low-cost process that does not require hazardous chemicals or templates to create the pores.[110] Starbon® have previously been used for the recovery of dyes from aqueous solutions and as support surface for metal NPs.[111, 146] The good adsorption properties combined with its ability to support NPs make Starbon® a potentially good candidate for the adsorption of metals. As its surface can be easily tuned during preparation, Starbon® present a range of functionalities that can be tailored to achieve selective adsorption.[110, 111]

Starbon® can be shaped as monoliths during the preparation process without the use of binding agents that may affect the properties of the material.[134] Monolithic shape allows to carry out work in flow regimes, including the recovery of metals from waste streams, faster and more efficiently than batch experiments.

2.1.1 Aims of the work

- Developing a method for the preparation of Starbon® monoliths and subsequent characterisation of the materials.
- To determine optimal Starbon® properties for the adsorption of precious metals.
- To establish the adsorption mechanism by which platinum, palladium and gold get adsorbed onto the Starbon® surface.

2.2 Results and Discussion

2.2.1 Preparation of Starbon® monoliths

A new method to prepare Starbon® monoliths, was developed by adjusting the process described by Budarin *et al.*[110] The method consists of five steps: 1) gelation, 2) solvent exchange, 3) drying, 4) addition of acid catalyst and 5) final carbonisation.[110] An exhaustive description of the preparation of Starbon® has been detailed in the PhD thesis of Parker *et al.* and , and therefore it is out the scope of this work.[105]

The variations introduced in the process consisted on minor changes to obtain and preserve the monolithic shape. First, after gelation the gel was poured into a cylindrical mould. Second, the p-toluenesulfonic acid (p-TSA) was applied by adding the monolith to an acetone solution containing the p-TSA. Two separated compartments were designed in order to separate the stir bar and the monolith, to prevent the monolith from breaking due to the constant impact of the stir bar (Figure 2.1). Finally, the carbonisation programme was adapted to avoid fast heating ramps that could cause fractures on the structure of the monolith (see experimental description in Chapter 6).

Figure 2.1 System used to apply the p-TSA solution to the Starbon® aerogel.

2.2.2 Physical characterisation of Starbon® monoliths

2.2.2.1 Appearance of Starbon® monoliths

The appearance of the Starbon® monolith significantly changed during the process (i.e. density, colour, texture). Along with appearance, the size and mass of the monolith changed throughout the preparation process.

Starch powder was initially mixed with water prior gelation. This mixture was a very runny and white suspension. Such solution turned very viscous during gelation due to the leaching of the amylose out of the granules.[106] This viscous gel hardened during retrogradation and adopted the shape of the container (in this case, cylindrical, to yield a

monolith). Such material was flexible and heavy due to the presence of water within its structure. During drying, the solvent was evaporated, and the material became rigid. Such material was very light (displaying a density of 0.33 $g \cdot cm^{-3}$) and resembled chalk. Finally, carbonisation turned the material black, denser (0.45 $g \cdot cm^{-3}$) and rigid, but brittle (Figure 2.2). In spite of these changes in appearance throughout the process, the monolithic structure was retained, and no fractures nor fissures were observed.
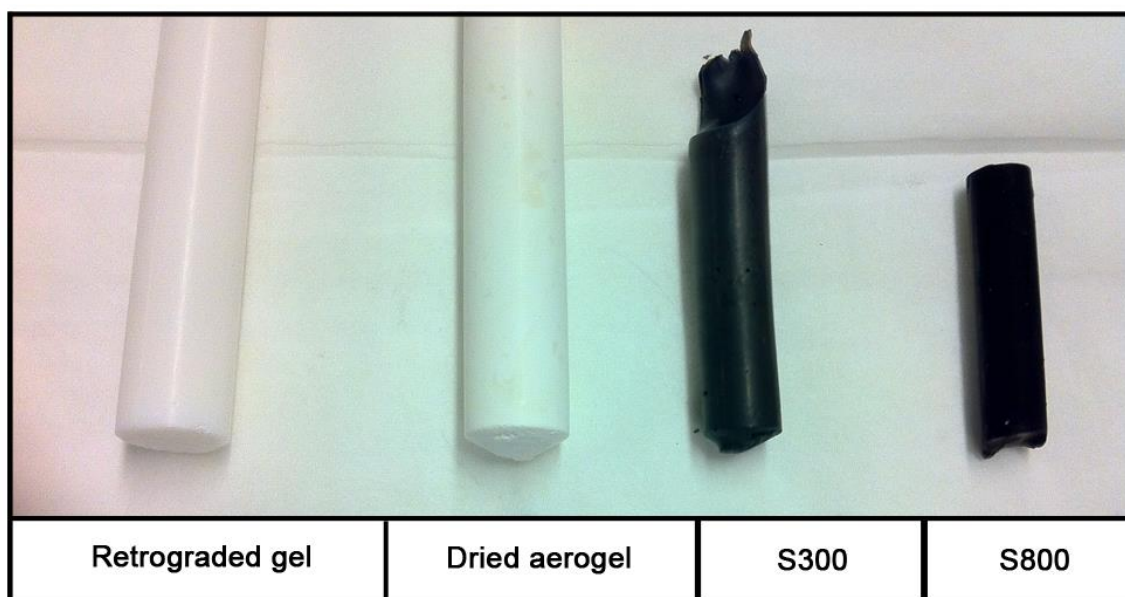
Figure 2.2 Appearance of Starbon® monoliths at different stages of the preparation process. From left to right: retrograded gel (after retrogradation), dried aerogel (after supercritical CO_2 drying), S300 and S800 (after carbonisation at 300 and 800 ºC respectively)

The initial monolithic diameter, 14.2 mm, corresponded to the width of the cylindrical mould employed and was reduced during the process (yielding 8.0 mm after carbonisation at 800 °C). Reduction was mainly caused by two steps: drying and carbonisation.

Two methods of drying were tested. The contraction occurred during drying was significantly less pronounced using supercritical carbon dioxide (scCO$_2$) (9.2%) compared to vacuum drying (51%), as shown in Figure 2.3. Using scCO$_2$ contributed to preserve the monolithic structure, which significantly and irreversibly contracted during vacuum

drying. In addition, scCO$_2$ drying contributed to improve the textural properties, as shown by White *et al.* in a previous study.[228]

Figure 2.3 Starbon® aerogel dried under vacuum (left) and using scCO$_2$ (right).

Carbonisation was responsible for the other 34% reduction in diameter that was observed. In order to determine the temperature at which diameter reduction was most significant, width was measured at different stages of carbonisation. At 300 and 450 °C diameter was 31 and 41% lower respectively, reaching a maximum reduction of 44% at 800 °C. Reduction was, therefore, non-linear as it showed a plateau at high temperature indicating that width reduction mainly occurred at low carbonisation temperatures (see Figure 2.4). Other AC monoliths described in the literature displayed lower diameter reduction during the preparation process suggesting that the shrinkage depended on the nature of the original material.[229]

The mass of a monolith also decreased during preparation. In this case, mass of the dried aerogel was used as reference to calculate mass loss during carbonisation because the presence of solvent impeded the use of the gel mass as a reference point. After carbonisation at 300 °C and 450 °C, 50 and 65% of the mass was lost respectively. On further heating to 800 °C 71% of the mass was lost. As for the diameter reduction, a

plateau was also observed as for the mass loss (Figure 2.4). This plateau is a consequence of the chemical processes taking place during carbonisation; major mass loss occurred below 500 °C (> 65%) as H_2O, CO_2 and CO are lost as part of dehydration, decarboxylation and decarbonylation reactions.[206] At higher temperatures, most processes taking place were rearrangement reactions that did not produce net mass loss (only 6% reduction observed from 450 to 800 °C).[132, 206]
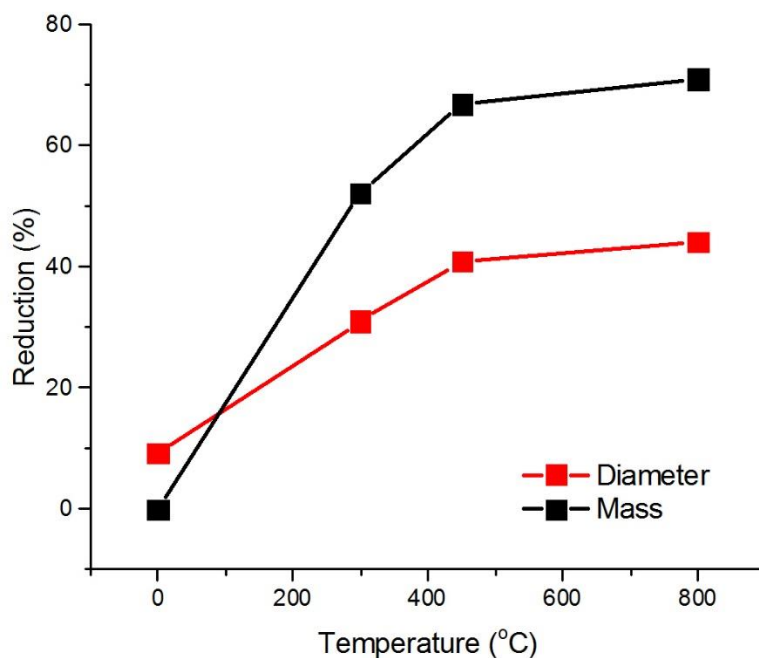
Figure 2.4 Relation between diameter (red) and mass reduction (black) of Starbon® monoliths with increasing carbonisation temperature.

2.2.2.2 Scanning Electron Microscopy (SEM)

Images of the surface and the bulk of the monoliths were generated by SEM. The lateral surface of the monolith presented a very different texture compared to the inner section for both the aerogel and carbonised monoliths (Figure 2.5). The surface was flat, smooth, and non-porous. This smooth surface was also observed during preparation of powder Starbon® after the retrogradation stage, however it has never been analysed before.

Some pores were observed in the external film of the carbonised material, probably formed during carbonisation (Figure 2.5 (c-d)). In contrast, the inner material presented high degree of porosity, as shown in Figure 2.5 (e). The aerogel presented a highly porous and fibrous structure, consistent with the data obtained in previous work.[105, 230] This material showed wide pores and channels (Figure 2.5 (b)) whilst carbonised material offered a denser and more compact structure with narrower pores (Figure 2.5 (e)), in agreement with porosimetry results detailed in the following section.

Starbon® monoliths were ground to a powder to enable certain analytical techniques to be applied (i.e. N_2 adsorption porosimetry, infrared spectroscopy) and the batch metal adsorption experiments. Figure 2.5 (f) shows that the porous structure of Starbon® changed from fibrous to more sponge-like after grinding. SEM analysis was conducted in collaboration with Ms Meg Stark at the Technology Facility in the Department of Biology of the University of York, UK.
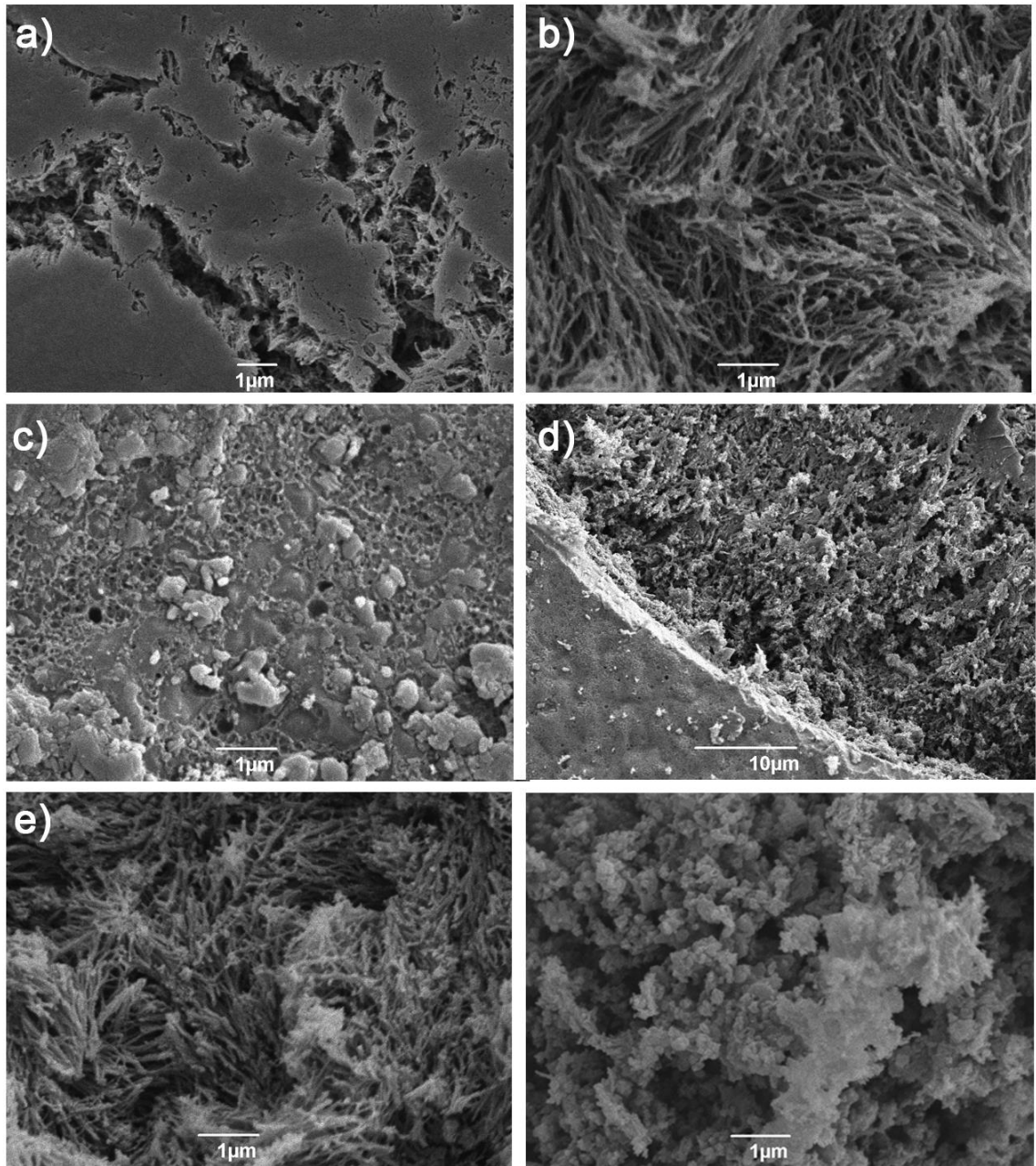
Figure 2.5 SEM images of a) aerogel surface, b) aerogel inner core, c) surface of S800, d) boundary between core and surface of S800, and e) core of S800 and f) S800 powder after grinding.

2.2.2.3 N$_2$ adsorption analysis

N$_2$ adsorption porosimetry was employed to measure textural properties of both aerogel and carbonised samples of Starbon®. Figure 2.6 shows the N$_2$ adsorption isotherms, and all four curves can be grouped as type IV isotherms. Type IV is characteristic of

mesoporous compounds (i.e. Starbon®) and presents a hysteresis loop due to capillary condensation (the strength of the adsorbate-adsorbate interactions increases during the adsorption process, making desorption slower).[231] Type IV isotherms can present four kinds of hysteresis loops depending on the pore shape.[232] Both aerogel and carbonised Starbon® presented type H3 hysteresis loop indicative of slit-shaped pores which was in agreement with previous work involving Starbon®.[105] The point at which the hysteresis loop closes is generally determined by the gas used for analysis.[232] Nevertheless, some authors have suggested that an onset of capillary condensation shifted to larger relative pressures was indicative of larger mesopores.[228] In agreement with this hypothesis, the relative pressure at which the onset appeared for Starbon® decreased with increasing carbonisation temperature indicating smaller mesopores. It is also possible to observe that the hysteresis loop for S300 did not close completely. This has been attributed to the swelling of non-rigid porous.[232] Such types of pores may be found in S300 as this was a key temperature for the transformations occurring during carbonisation and therefore could suffer swelling during the porosimetry analysis. Another plausible explanation for this phenomenon is the presence of small micropores;[232] the diffusion rate of N_2 in those pores is very slow, increasing the time required to reach the equilibrium pressure. If such equilibrium pressure is not reached, the resulting isotherm can present an open hysteresis loop.

At low relative pressures, the inflexion point known as point B marked the moment at which monolayer adsorption was complete and multilayer adsorption started.[232]
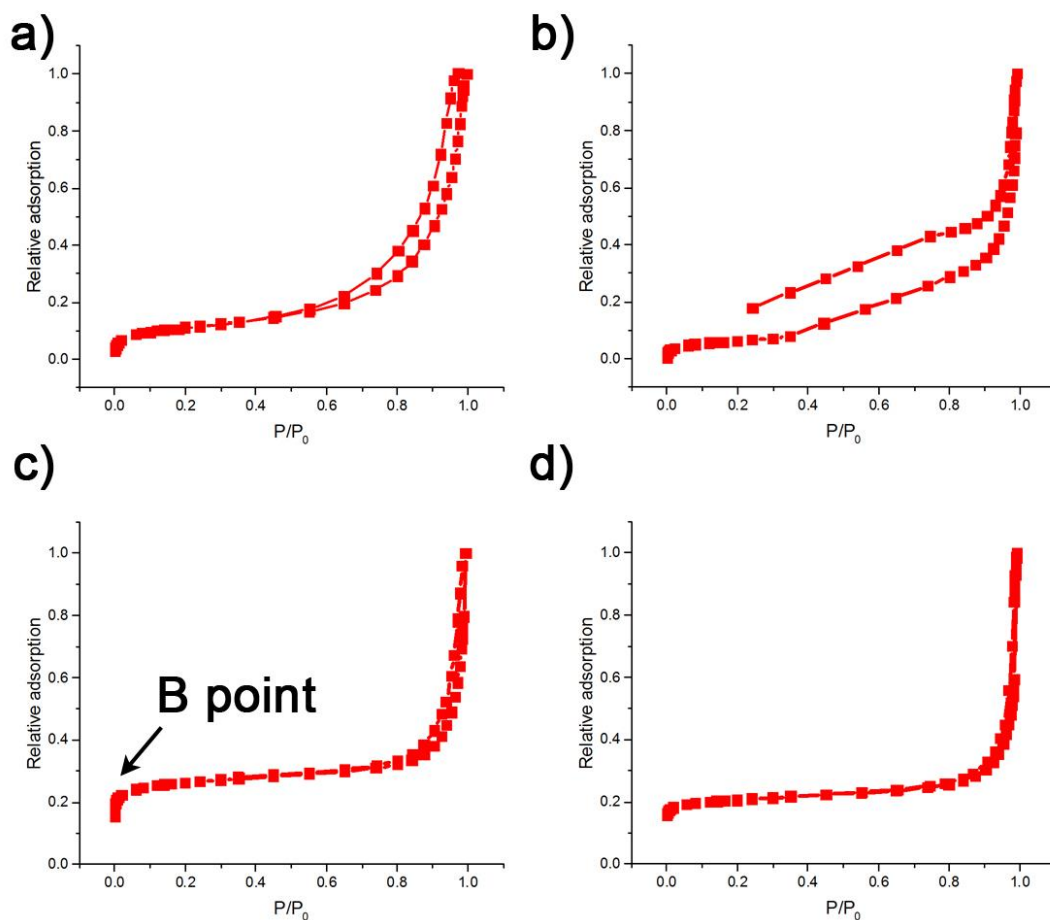
Figure 2.6 N₂ adsorption isotherms of a) Starbon® aerogel, b) S300, c) S450 and d) S800.

Textural properties are summarised in Table 2.1. Data obtained for the aerogel compares well with previous studies of Starbon®.[228] The pore volume was larger than that observed for starch aerogels produced by a similar methodology but using an autoclave instead of microwave heating.[233] In both cases, these variations can be caused by the different starch/water ratios employed to prepare the materials.

For the carbonised materials, surface area increased with carbonisation temperature. This was related to micropore formation, which first appeared at 300 °C.[132] Consequently, the micropore volume was also larger for high temperature Starbon®, and became as high as 25% of the total pore volume at 800 °C. On the other hand, changes in total pore

volume were almost negligible. Some carbonaceous monoliths described in the literature presented similar or larger surface areas, which could be related to their high degree of microporosity (91%).[234] Other carbonaceous monoliths presented a higher fraction of mesopores but required two heating processes at high temperatures, for carbonisation and subsequent activation, which increased significantly the cost of the process.[235]

As shown previously, surface energy is usually higher for highly microporous materials due to the small distance between pore walls in such pores.[110, 130] Starbon® displayed larger values of surface energy at increasing carbonisation temperatures in good agreement with the increasing microporosity of the material.

The effect of carbonisation temperature in the textural properties is in good agreement with previous work carried out by Shuttleworth *et al.* and Budarin *et al.*[132, 210]

Table 2.1 Textural properties of Starbon® materials, analysed by N_2 adsorption porosimetry. BET model was applied to obtain the surface area. Total and mesopore volumes were calculated from the BJH model. D-R model was used to obtain the micropore volumes.

Material	S_{BET} $(m^2 \cdot g^{-1})$	V_{tot} $(cm^3 \cdot g^{-1})$	V_{meso} $(cm^3 \cdot g^{-1})$	V_{micro} $(cm^3 \cdot g^{-1})$	Micro porosity (%)	E $(kJ \cdot mol^{-1})$
Aerogel	177	0.68	0.62	0.06	8.8	12.4
S300	175	1.20	1.13	0.07	5.8	11.5
S450	363	1.07	0.81	0.25	23.4	26.4
S800	706	1.20	0.90	0.30	25.0	28.0

Pore size distribution (PSD) showed that the majority of pores were contained within the mesopore and low macropore domains for carbonised materials, with an average pore radius (APR) of 40 nm (Figure 2.7). In contrast, Starbon® aerogel showed larger macropores with an average radius for meso- and macropores of 30 and 110 nm respectively. APR values were larger than those described in previous Starbon® work.[210] This could be related to the amount of starch in water employed to prepare the monoliths as White *et al.* showed that increasing concentration of starch led to larger number of

macropores that appeared as a result of foaming during gelation.[228] The presence of water dissipated the microwave energy; therefore, low concentrations of water favoured the heating of the bulk of starch, which promoted foaming and large macropores.[228,236]

Even though the presence of micropores was expected for S450 and S800, as shown in Table 2.1, it was not possible to observe them in the PSD as the analysis did not include the microporous region.
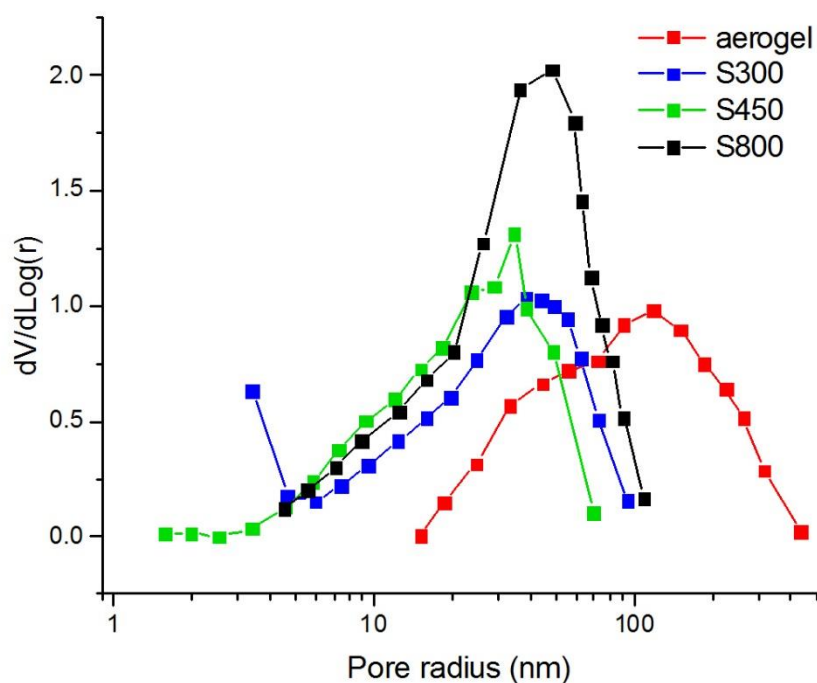
Figure 2.7 Pore size distribution of Starbon® materials at different temperatures of carbonisation.

2.2.3 Chemical properties of Starbon®

The chemical composition of Starbon® underwent significant changes during carbonisation. The nature of these changes has been investigated by analytical techniques such as thermal gravimetric analysis (TGA), infrared spectroscopy (IR) and X-ray photoelectron spectroscopy (XPS).

2.2.3.1 Thermal gravimetric analysis (TGA)

Thermal decomposition of polysaccharides has been previously described in depth by Moldoveanu et al.[206] In addition, the thermal decomposition of starch to yield Starbon® has also been studied in previous work.[132]

TGA measures the mass loss occurring during carbonisation and the first derivate of this curve highlights the critical temperatures at which decomposition and chemical transformations took place. The largest mass drops were observed at 140 and 280 °C (Figure 2.8). Mass loss at low temperature (small peak at ~80 °C) was caused by the loss of adsorbed water and was not considered part of the carbonisation. Below 200 °C the first chemical transformations are known to occur, these are crosslinking or dehydration of the hydroxyl groups.[132] Such elimination reactions lead to the formation of C=C and C=O bonds.[206] These transformations were therefore related to the peak observed at 140 °C. Decarboxylation occurs at later stages of carbonisation, at temperatures between 200-400 °C, when some oxygen functional groups 'leave' as CO_2, causing the peak observed at 280 °C.[237] The relatively small peak observed at 430 °C could be caused by the decomposition of weak acidic functionalities such as lactones or anhydrides .[237] The mass loss observed at higher temperatures was less significant and is attributed to decarbonylation of groups such as phenols or hydroquinones.[237] Aromatisation also occurred at high temperatures.[206] Aromatisation was not associated with significant mass loss, as it primarily involves rearrangement of the remaining functionalities into aromatic groups [206] The observations made by TGA were in good agreement with the results of IR and XPS results. In addition, the main decomposition peak observed at ~140 °C agreed well with the observations made by Budarin et al. in previous work with Starbon®, where the decomposition peak of acid-doped starch was also observed around that temperature (~180 °C).[110] In the earlier study, Budarin et al showed that the decomposition peak appeared at higher temperatures (310 °C) when starch was not doped with acid. The small peak observed in Figure 2.8 around that temperature could also be due to the p-TSA not

reaching the inner core of the monolith and therefore, part of the material presented a delayed decomposition.
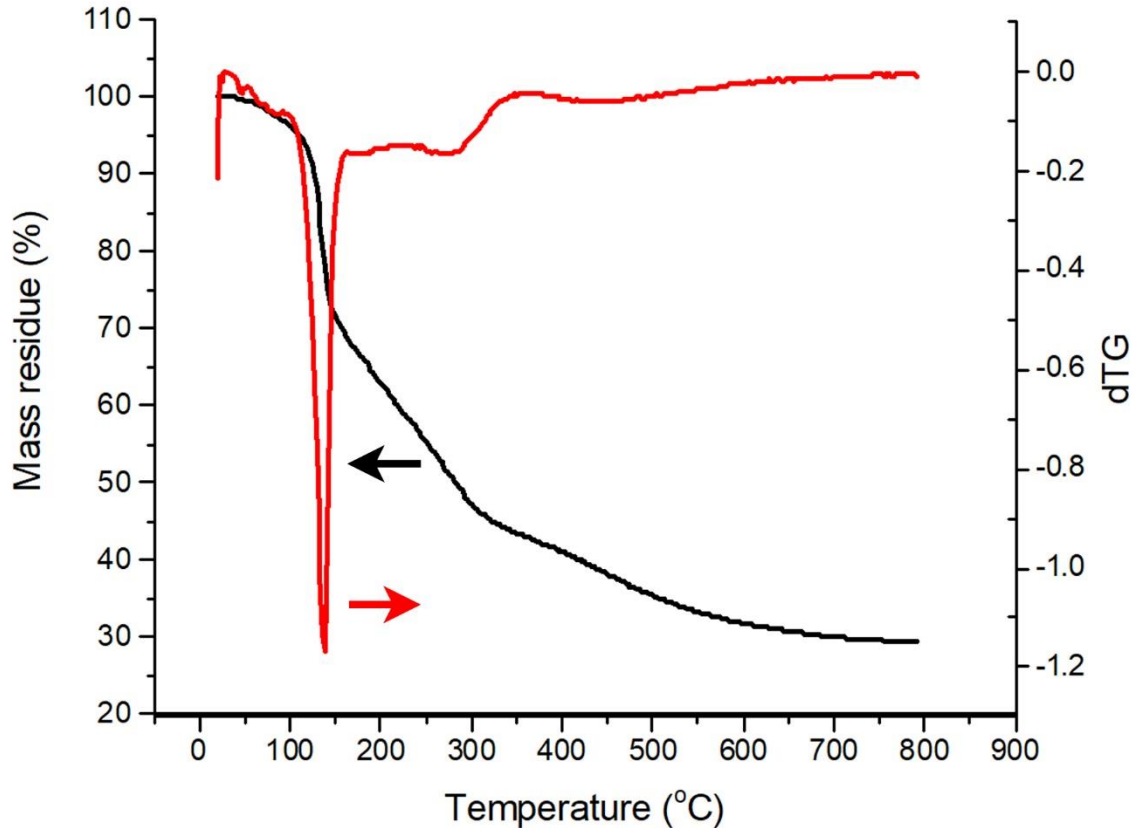
Figure 2.8 Thermal gravimetric decomposition pattern (black) of Starbon® aerogel at a heating rate of 1 °C·min⁻¹ and the first derivate of the decomposition pattern (red) highlighting the temperatures at which the mass loss was most prominent.

2.2.3.2 Infrared spectroscopy

IR shows the functional groups present in a specific sample. Figure 2.9 displays the IR spectra for starch aerogel, S300 and S450. Unfortunately, data for S800 could not be obtained due to its high absorbance, which made impossible to resolve the spectra.

Starbon® aerogel showed the characteristic functional groups of starch: a broad band between 3658 and 3009 cm^{-1} represented hydroxyl groups (-CH_2OH), the peak at 2938 cm^{-1} was caused by sp^3 carbons (-CH_3) and C-O-C groups were characterised by a strong

81

peak at 1018 cm^{-1}.[238] Upon carbonisation, hydroxyl groups were transformed into carbonyl groups (-C=O) denoted by a sharp peak at 1718 cm^{-1}, and double bonds (-CH=CH) (peak at 1618 cm^{-1}).[132] This was in good agreement with the observations made in previous studies with Starbon®.[110] The peak for carbon double bonds usually appears between 1650-1690 cm^{-1}, however, conjugated systems reduce the wavenumber of this peak.[238] Low intensity bands seen in S300 and S450 between 1300 and 1200 cm^{-1} may be related to C(sp$_2$)-O-C(sp$_3$) groups, that could be formed during carbonisation.[206]
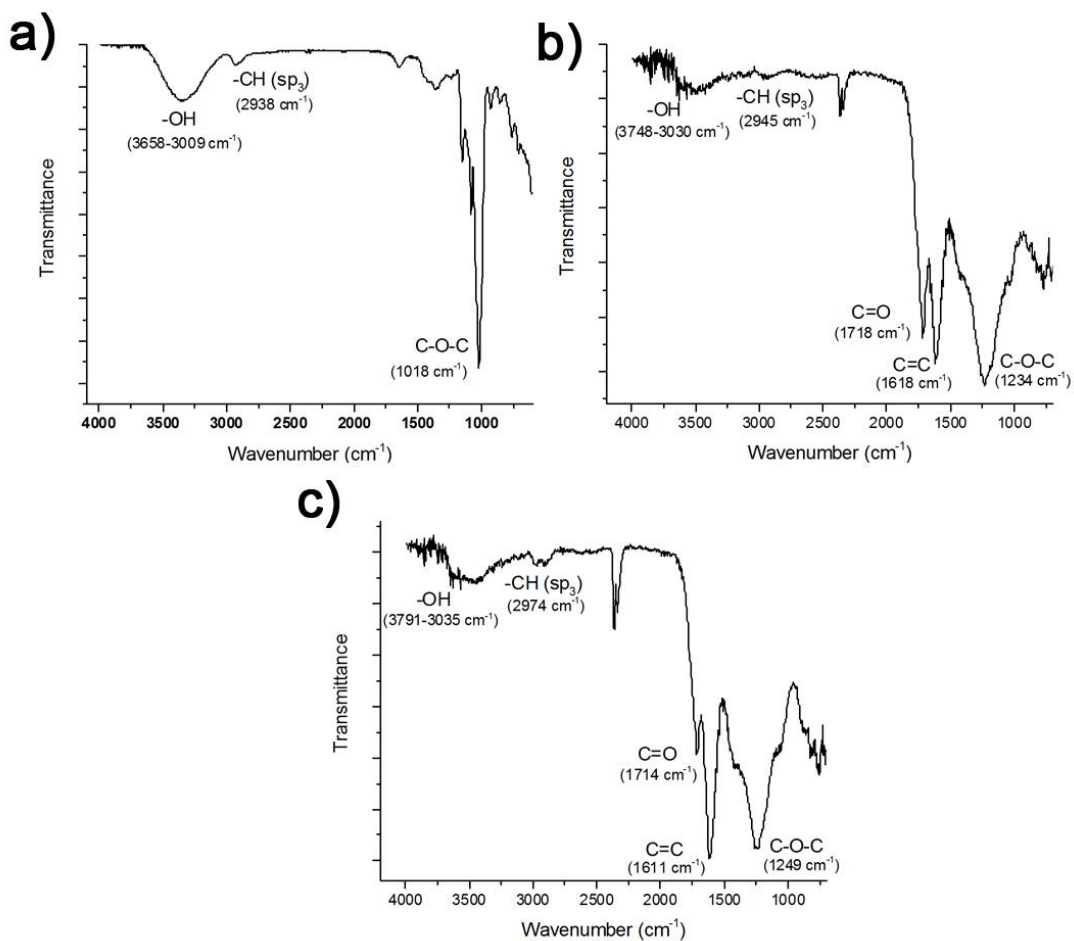
Figure 2.9 Infrared spectra of a) Starbon® aerogel, b) S300 and c) S450.

2.2.3.3 X-ray photoelectron spectroscopy

XPS can measure the atomic composition and chemical state of the elements present at the surface of a solid. The elemental composition of carbonised Starbon® included C, O and S and has been summarised in Table 2.2. The XPS analysis shown throughout this chapter was carried by the team of the National EPSRC XPS Users' Service facility at Newcastle University (UK). The analysis of the data was carried out by the author. The traces of sulphur detected were the residue of the p-TSA added to catalyse carbonisation. The concentration is lower in S450 and S800 compared S300 showing that the p-TSA decompose at increasing temperatures. The slight increase in sulphur concentration observed for S800 was probably caused by the small amounts present, which prevented precise analysis.

Table 2.2 Elemental composition and C/O ratio of carbonised Starbon® as obtained by XPS analysis.

Material	C (%)		O (%)		S (%)		C/O ratio
	Mean	SD	Mean	SD	Mean	SD	
S300	80.9	0.2	18.6	0.1	0.5	0.1	4.3
S450	86.8	0.0	13.1	0.1	0.1	0.1	6.6
S800	94.9	0.1	4.8	0.1	0.2	0.0	19.8

The C/O ratio increased in correlation with the carbonisation temperature. The initial 1.2 ratio expected for starch aerogel (Figure 2.10) increased up to 4.3, 6.6 and 19.8 upon carbonisation at 300, 450 and 800 °C respectively. These values were in good agreement with the data obtained by Budarin *et al.*,[110] and with the IR results shown above, where decreasing number of oxygen-containing functionalities (i.e. hydroxyl groups) were observed.
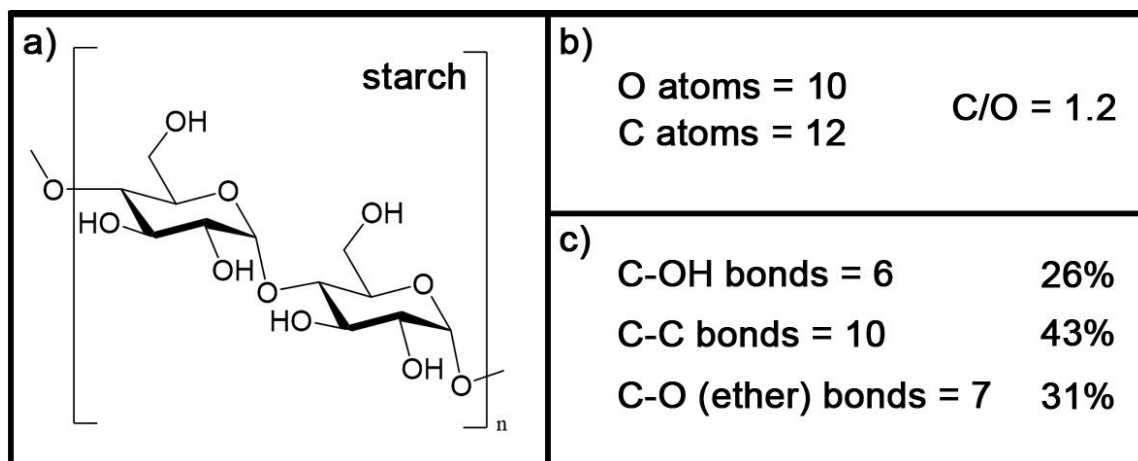
Figure 2.10 a) Diagram representing a starch chain, b) the C/O ratio of the starch chain and c) the types of carbon bonds contained in the starch chain.

Every type of bond appears at a specific binding energy in the XPS spectra which allows identification and quantification of the different functional groups present in a sample through deconvolution of the main peaks (i.e. C1s and O1s).

Deconvolution of C1s spectra of Starbon® exhibited six peaks corresponding to: double bonds between sp^2 carbons (C=C), single bonds between sp^3 carbons (C-C) and β carbons, hydroxyl groups (C-OH), ether groups (C-O-C), carbonyl functionalities (C=O) and carboxylic-type groups (O-C=O), as shown in Figure 2.11 and Table 2.3.[239] The number of double/aromatic bonds increased with the carbonisation temperature, reaching almost 20% at 800 °C, whilst aliphatic C-C bonds became less significant. This was in good agreement with previous work with Starbon®.[105]

The number of hydroxyl bonds at 300 °C was lower than the values for starch (27%, Figure 2.10) because of the dehydration reactions taking place at low carbonisation temperatures, where E_i elimination of -OH groups results in the formation of C=C double bonds or its tautomeric ketones, with subsequent elimination of water.[206] This was consistent with the presence of C=C double bonds and carbonyl groups in the S300 spectra. Hydroxyl functionalities increased for S450, which may be the result of chain scission reactions occurring between 300 and 450 °C during carbonisation.[206] Chain

scissions were consistent with the decrease in number of ether groups observed at S450. In close vicinity to hydroxyl or carboxyl groups, carbonyl functionalities may condense to lactone groups, which could explain the minor increase in carboxylic-type groups observed for S800.[240]

Deconvolution of O1s presented five peaks corresponding to: carbonyl groups (C=O), the carbonyl groups in esters, anhydrides or single carbon-oxygen bonds (C-O) in hydroxyl and ether groups, ether bonds in esters and anhydrides (O-C=O), carboxylic acid groups (-COOH) and O_2 adsorbed in the porous surface.[237] Theoretically, starch aerogels only contain the hydroxyl and ether groups. In contrast, S300 and S450 showed ketone groups, resulting from the E_i reactions occurring at low carbonisation temperatures. Peaks showing O-C=O and C-O bonds were significantly smaller for S800 because of the decreasing number of hydroxyl and ether groups at high temperatures of carbonisation. These observations were in good agreement with the deconvolution of C1s spectra discussed above.
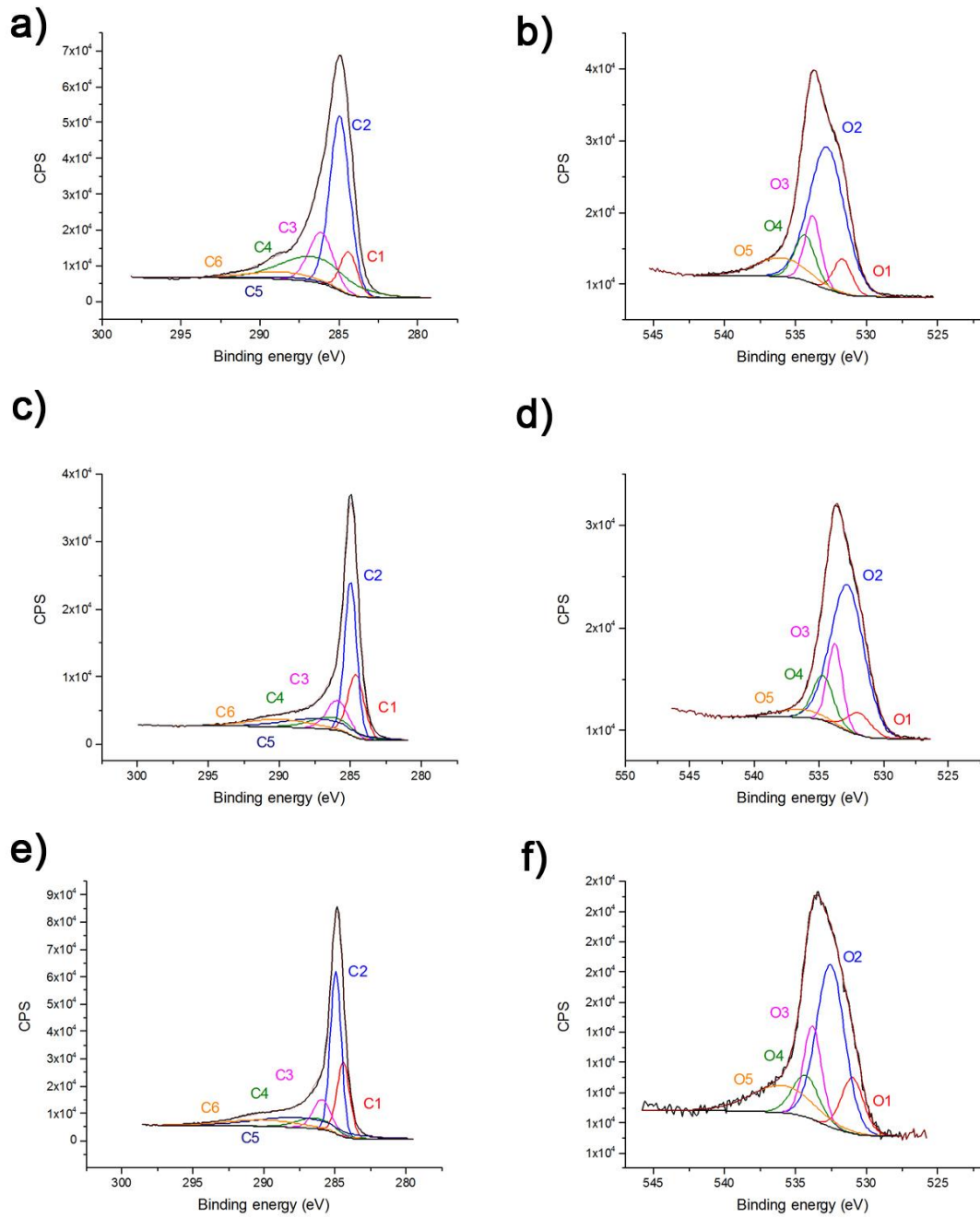
Figure 2.11 Deconvolution of the carbon C1s and oxygen O1s spectra for a-b) S300, c-d) S450 and e-f) S800.

Table 2.3 Quantification of the functional groups present in Starbon® at different temperatures of carbonisation, carried out by XPS.

Elements	Peaks	BE (eV)	Functional group	Fraction (%)		
				S300	S450	S800
Carbon	C1	284.3 ± 0.3	C=C	8	10	18
	C2	284.8 ± 0.2	C-C	45	43	37
	C3	286.1 ± 0.2	C-OH	15	21	12
	C4	286.6 ± 0.3	C-O-C	23	15	11
	C5	287.4 ± 0.2	C=O	5	6	12
	C6	289.0 ± 1.0	O-C=O	4	5	10
Oxygen	O1	531.5 ± 0.5	C=O	11	8	13
	O2	532.5 ± 0.3	C-O	56	59	48
	O3	533.4 ± 0.4	O-C=O	13	18	13
	O4	534.9 ± 0.5	HO-C=O	10	11	10
	O5	536.3 ± 0.3	ads O_2	10	5	15

2.2.3.4 Point of zero charge (pzc)

The point of zero charge is the specific pH at which the surface of a material is neither positive nor negatively charged.[241] In acidic aqueous solutions (pH < pzc) the surface of a solid gets positively charged, whereas basic conditions (pH > pzc) yield negatively charged surfaces.[242]

Pzc has become an essential parameter for adsorption studies, as positively charged surfaces attract negative ions and vice versa. Pzc of carbonised Starbon® were quantified applying the experimental work described in Section 7.1.8, and are summarised in Table 2.4.

Table 2.4 Point of zero charge values of carbonised Starbon®.

Material	S300	S450	S800
pzc	5.1	5.8	5.3

The presence of acidic functionalities (i.e. certain oxygen-containing groups such as anhydrides, carboxylic acid or lactones) have been associated to lower pzc. [240, 241, 243] On the other hand, basic functionalities like pyrones and resonating π-electrons from carbon aromatic rings are capable of attracting protons and therefore, have been related to higher values of pzc.[241, 243, 244] According to this, it was expected to obtain increasing pzc at higher carbonisation temperature. However, S800 presented lower pzc. This phenomenon can be explained by the condensation of basic carbonyl and hydroxyl- type functionalities to yield acidic lactones, occurring at high temperatures of carbonisation.[240]

The characterisation of carbonised Starbon® showed that materials with varying surface chemistry and textural properties were obtained by changing preparation temperature. Low temperatures yielded materials with relatively high oxygen content, rich in oxygen functionalities and with low fraction of microporosity. In contrast, carbonisation at high temperatures offered highly microporous materials with low oxygen content in which aromatic groups were more abundant. Understanding these variations was key to finding the optimal type of Starbon® for the adsorption of precious metals.

2.2.4 Metal adsorption

To investigate the ability of Starbon® to adsorb precious metals, carbonised Starbon® (S300, S450 and S800) were used to adsorb gold, palladium and platinum from acidic (pH=0) single-metal solutions. Experiments were carried out at very low pH to try to mimic real waste conditions[25]. Monoliths were ground to obtain a homogenous powder, with particle size < 300 μm, that could be applied to batch experiments. The amount of metal in solution was measured by ICP-MS and ICP-OES. Some of the samples were analysed by Dr. Lorna Eades at the School of Chemistry of the University of Edinburgh.

All three materials showed higher adsorption of gold compared to palladium and platinum (see Figure 2.12 and Table 2.5). Interestingly, Starbon® adsorption capacity significantly improved with the temperature of carbonisation, with S800 being the best adsorbent for

all three precious metals. The superior affinity for gold was directly related to the adsorption mechanism, which will be discussed in detail in the following sections.
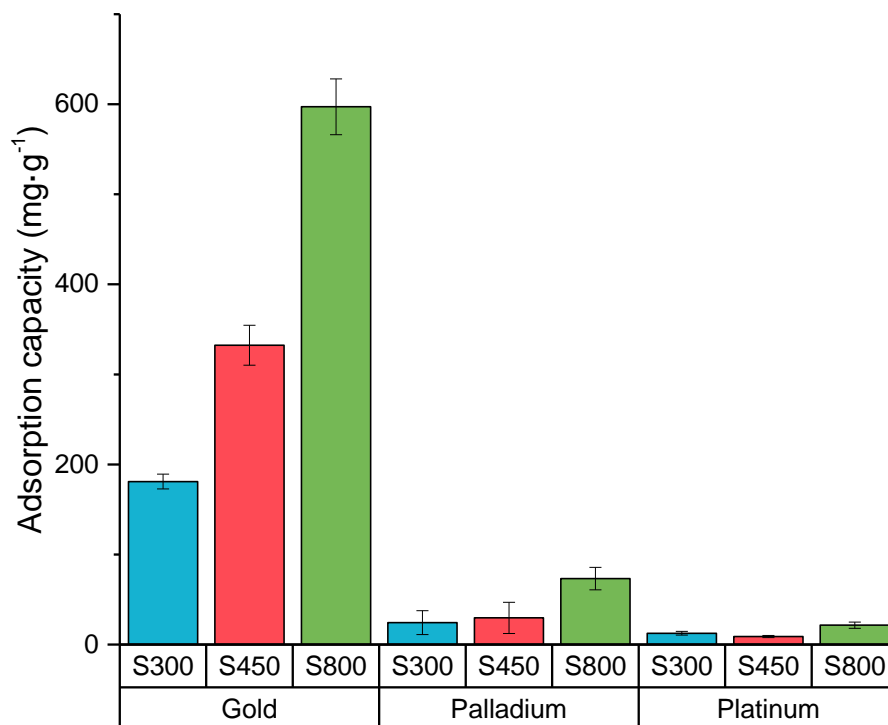
Figure 2.12 Comparison of the adsorption capacities displayed by three types of Starbon® for the adsorption of gold, palladium and platinum after 24 h of constant stirring at room temperature and pH 0.

Table 2.5 Adsorption capacity presented by S300, S450 and S800 for gold, palladium and platinum after 24 h of constant stirring at room temperature and pH 0.

Material	Adsorption capacity (mg·g^{-1})		
	Au	Pd	Pt
S300	181.0 ± 8.2	24.4 ±13.3	12.5 ± 2.1
S450	332.4 ± 22.1	29.6 ± 17.4	8.9 ± 1.1
S800	597.2 ± 31.0	73.2 ± 12.5	21.5 ± 3.5

A few examples of polysaccharide-derived carbon materials used for the adsorption of gold could be found in the literature.[82, 83, 87] As shown in Table 2.6, the adsorption capacity of Starbon®, and in particular S800, compares well with other bio-adsorbents. A more detailed list of polysaccharide derived adsorbents for precious metals can be found in Table 1.2 of Chapter 1.

Table 2.6 Adsorption capacity of gold displayed by other polysaccharide derived carbonaceous materials described in the literature.

Material	Adsorption capacity (mg·g^{-1})	Reference
Banana peel carbon	802	82
Rice husk carbon	150	83
Barley straw carbon	289	83
Starch-based hydrothermal carbon spherules	591	87

2.2.4.1 Mechanism for gold adsorption

The adsorption mechanism of gold involved a chemisorption process comprising the adsorption and subsequent reduction of Au^{3+} ions to its metallic form yielding gold NPs. Many authors in previous studies have suggested this redox mechanism, and it responds to the relatively high reduction potential displayed by AuCl$_4$$^-$, the predominant anionic species of Au^{3+} in acidic solution.[79, 85, 245] The reduction potential for Au^{3+} to metallic gold is higher than those for the conversion of PtCl$_4$$^{2-}$ and PdCl$_4$$^{2-}$ to their metallic forms (Scheme 2.1-3).[246]

Scheme 2.1 $$AuCl_4^- + 3e^- \rightarrow Au^0 + 4Cl^- \qquad (1.00\ V)$$

Scheme 2.2 $$PdCl_4^{2-} + 2e^- \rightarrow Pd^0 + 4Cl^- \qquad (0.62\ V)$$

Scheme 2.3 $$PtCl_4^{2-} + 2e^- \rightarrow Pt^0 + 4Cl^- \qquad (0.78\ V)$$
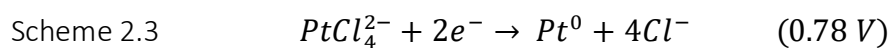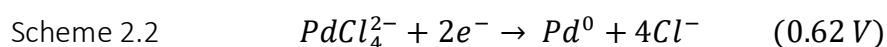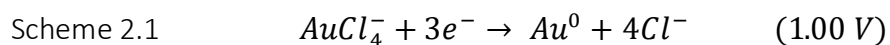
The reduction potential for the conversion of Au^{3+} to Au$^+$ and subsequent reduction of Au$^+$ to metallic gold are also higher than the above-mentioned for Pd and Pt, revealing a more favourable reaction between gold species and the carbonaceous surface.[246]

Scheme 2.4 $\qquad AuCl_4^- + 2e^- \rightarrow AuCl^- + 3Cl^- \qquad (0.93\,V)$

Scheme 2.5 $\qquad AuCl^- + e^- \rightarrow Au^0 + Cl^- \qquad (1.15\,V)$
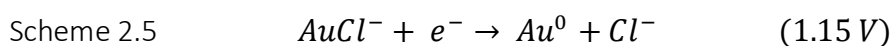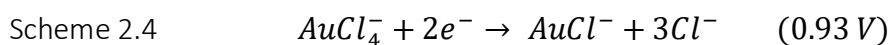
The reduction of Au^{3+} ions to metallic gold was confirmed through Transmission Electron Microscopy (TEM) and XPS analysis. Figure 2.13 shows TEM micrographs of the S800 surface before and after the adsorption of gold. TEM analysis was conducted in collaboration with Ms Meg Stark at the Technology Facility in the Department of Biology of the University of York, UK.
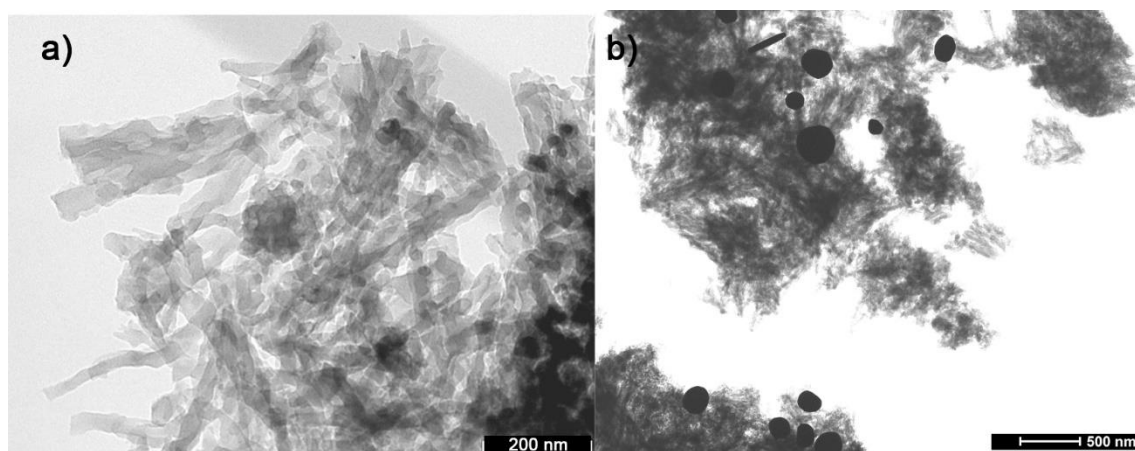

Figure 2.13 TEM micrographs of Starbon® carbonised at 800 ºC a) before and b) after adsorption of gold.

Spherical and hexagonal gold nanoparticles can clearly be observed after adsorption. The nanoparticles present had a large size (100-400 nm). A plausible explanation for such large nanoparticles was the formation of nanoshells, which consist of the aggregation of small nanoparticles around a core atom or molecule.[247] These nanoshells are usually formed using silica as core.[247] However, Shi et al. described the formation of nanoshells around a core of sulfur modified polystyrene.[248] Therefore, the traces of sulfur from p-

TSA may act as a core for the formation of nanoshells in Starbon®. Other studies showed that the formation of nanoshells was dependent on the concentration of gold in solution [249] This was in good agreement with the results observed in Chapter 3, where the concentration of gold in solution was significantly lower and unfinished nanoshells were observed.

XPS clearly showed the presence of gold at the material's surface (see Figure 2.14). The Au4f spectra could be deconvoluted into three sets of doublets. In agreement with the literature describing XPS analysis of Au, the two peaks within the doublet were 3.7 eV apart, presented identical full width at half maximum (FWHM) and the relative intensity was 4:3 for the 7/2 and 5/2 spin orbits respectively. The main doublet was found at 84.6 eV (7/2) which corresponds to the characteristic binding energy of Au^0 confirming the reduction of $AuCl_4^-$.[250, 251] The other two doublets at 86.1 and 86.6 eV corresponded to the characteristic binding energies of Au^+ and Au^{3+} respectively[251]. Such peaks indicated that small fractions of gold were only partially reduced or electrostatically adsorbed onto the material's surface. Interestingly, the amount of reduced gold varied with the carbonisation temperature; this will be discussed in detail in Section 2.2.4.4.
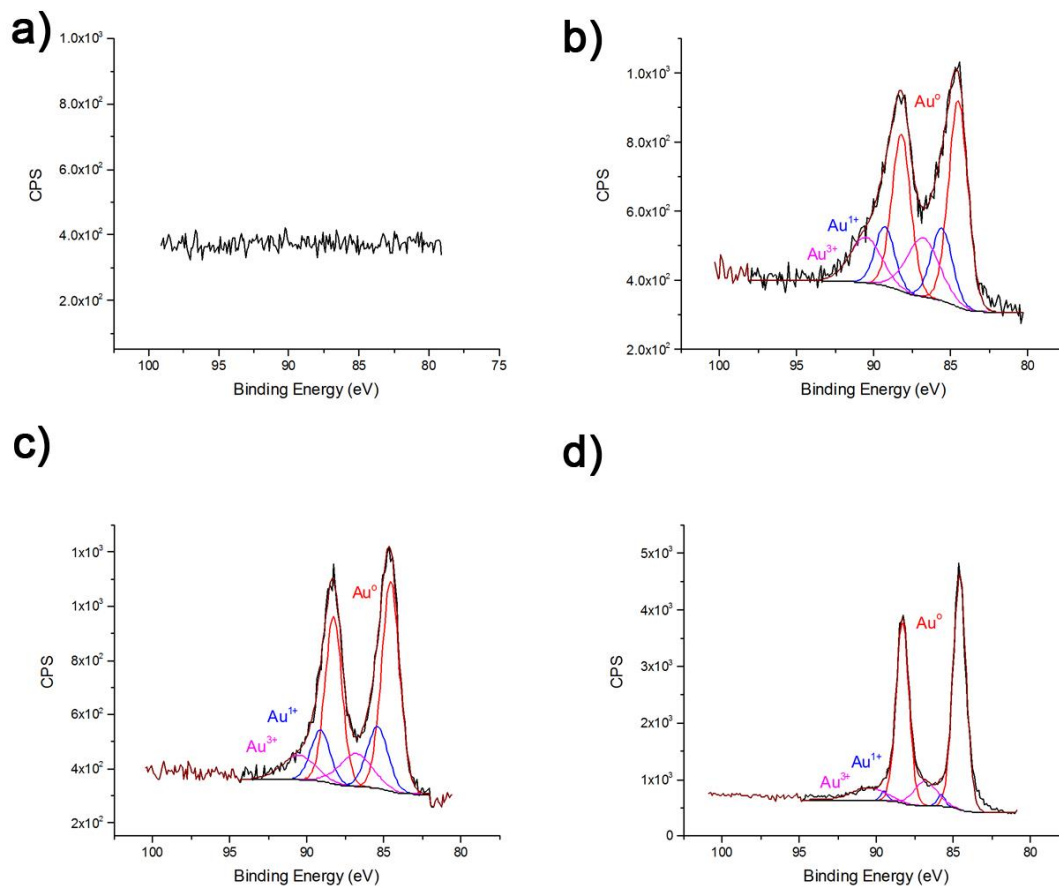
Figure 2.14 Deconvolution of gold Au4f XPS spectra for a) Starbon® before adsorption and b) S300, c) S450 and d) S800 after adsorption from a gold solution subjected to constant stirring for 24 h, at room temperature and pH 0.

Reduction of gold ions unavoidably caused an oxidation reaction on the surface. Several functional groups present on the Starbon® surface can be potentially oxidised (i.e. hydroxyl groups, carbonyl groups). Three possible mechanisms for surface oxidation have been suggested in the literature and are described below.[71, 87, 252, 253] Data from the characterisation of Starbon® after adsorption was compared against these three hypotheses to try to determine the mechanism taking place during the adsorption of gold.

- *Oxidation of hydroxyl groups to carbonyl groups*. Several authors described an adsorption-reduction mechanism in which $AuCl_4^-$ was first adsorbed onto the material by forming a chelating complex with oxygen atoms of hydroxyl an ether groups.[71, 87] Hydroxyl groups were then reduced to ketones, as described in Figure

2.15. As the number of hydroxyl groups decreased, the concentration of C=O groups rises. This hypothetical transformation suggest that the C/O ratio does not change after adsorption.
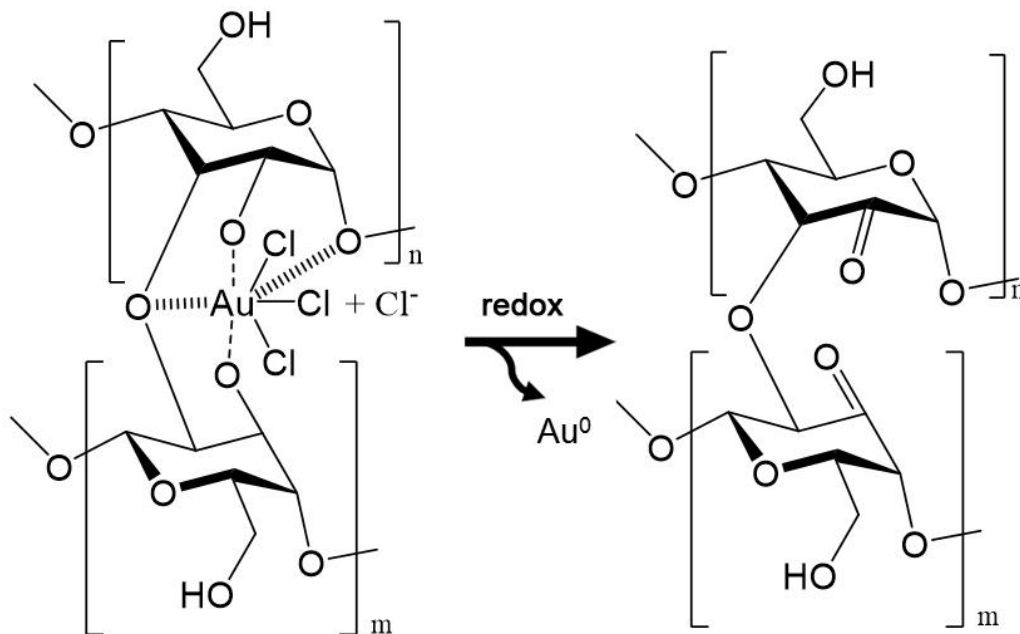
Figure 2.15 Scheme showing the adsorption of gold onto crosslinked cellulose.[71]

- *Decomposition of the carbon surface*. Bystrzejewski *et al.* suggested the oxidation of carboxylic groups to form CO_2, with the subsequent decomposition of the surface.[252] As a result, the C/O ratio was expected to increase after adsorption.

- *Formation of carboxylate groups*. Cox *et al.* suggested a similar oxidation-decomposition mechanism when studying the adsorption of Hg^{2+} onto carbonaceous flax shive.[253] However, the amount of CO_2 produced was lower than the fraction of mercury reduced. Consequently, it was suggested that the adsorption mechanism also involved transformation of other functional groups present in the surface, such as carbonyl into carboxylic groups.[253] The formation of carboxylate functionalities was expected to lower the C/O ratio after adsorption. In addition, oxidation of carbonyl groups to form carboxylic functionalities presented a standard reduction potential of -0.5 V.[254] This was

lower than those for the equivalent processes to form carbonyl and hydroxyl groups from hydroxyl (-0.2 V) and hydrocarbon groups (0.1 V) respectively, being therefore the most favourable option for oxidation.[254]

The elemental analysis carried out by XPS after adsorption showed lower C/O ratios for all three materials (Table 2.7). This phenomenon could only be caused by the formation of new carboxylic groups, as suggested by Cox *et al.*[253] Whereas, for S300 and S450 the reduction of C/O was low (< 1.3%), a significant drop could be observed for S800 (7.5%). The small variations of C/O observed for S300 and S450 could be the result of a combined oxidation where not only carbonyl groups were involved, and hydroxyl functionalities were also oxidised to carbonyl groups, as these transformations would not alter the amount of oxygen in the sample but contribute to the adsorption.

Table 2.7 Comparison of Starbon® C/O ratio before and after adsorption of gold from a solution subjected to constant stirring for 24 h, at room temperature and pH 0.

Material	C/O ratio (%)		
	Before adsorption	After adsorption	Variation
S300	4.3	3.6	-0.7
S450	6.6	5.3	-1.3
S800	19.8	12.3	-7.5

Deconvolution of C1s spectra after adsorption, according to the peaks described in Section 2.2.3.3, showed that carbonyl peak had significantly decreased for S800 (see Figure 2.16 and Table 2.8). This reduction was accompanied by analogous growth of the carboxylate peak. Even though, similar patterns could be observed for S300 and S450, decreasing hydroxyl groups were detected in these cases too, which is consistent with the hypothesis that multiple functional groups contribute to the oxidation of S300 and S450 surface.
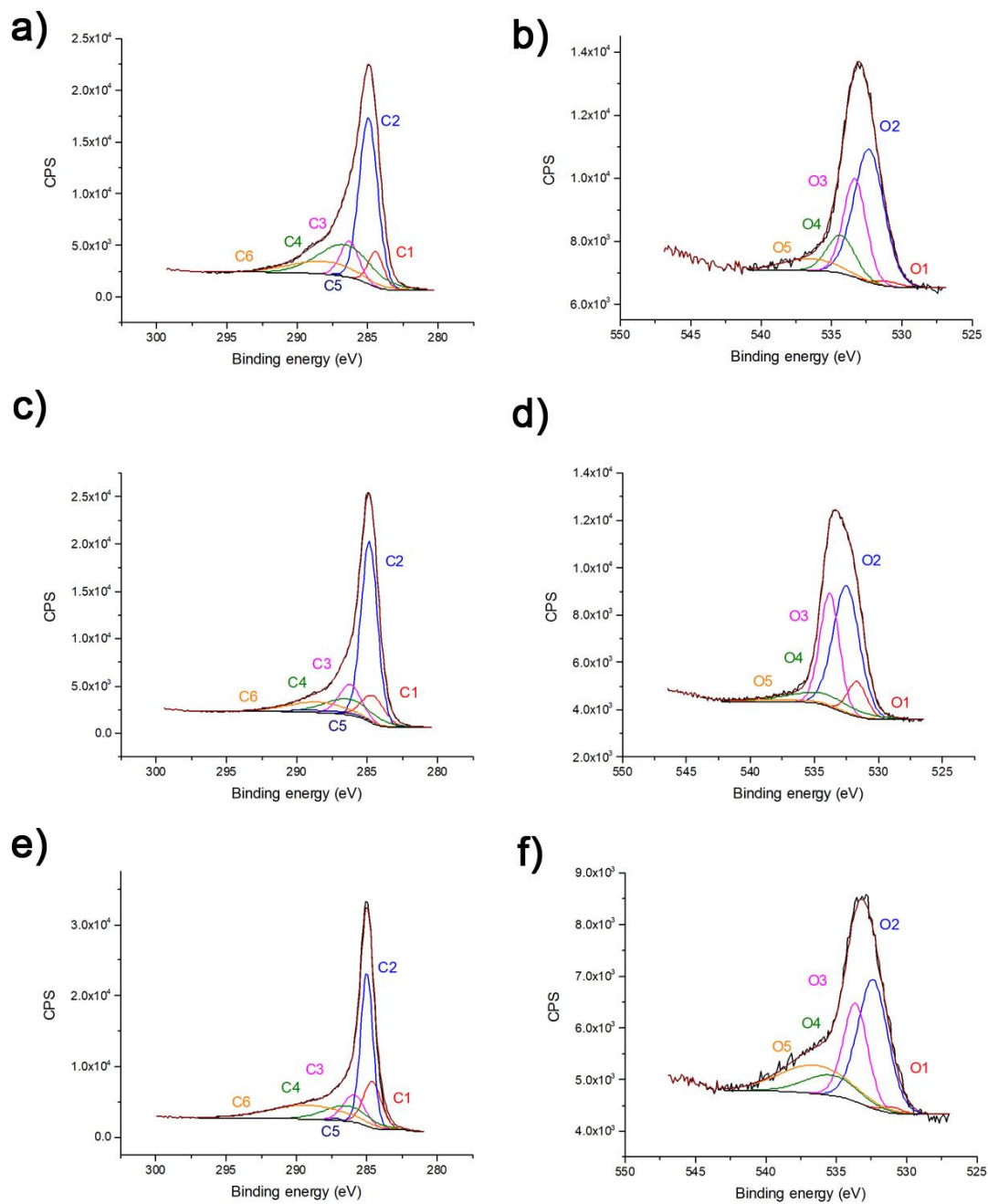
Figure 2.16 Deconvolution of C1s XPS spectra for a) S300, b) S450 and c) S800 and of O1s XPS spectra for d) S300, e) S450 and f) S800 after the adsorption of gold from a solution subjected to constant stirring for 24 h, at room temperature at pH 0.

Table 2.8 Quantification of functional groups present in Starbon® at different temperatures of carbonisation after adsorption of gold from a solution subjected to constant stirring for 24 h, at room temperature and pH 0.

Element	Peaks	BE (eV)	Functional group	Fraction (%)		
				S300	S450	S800
C	C1	284.3±0.3	C=C	8	12	17
	C2	284.8±0.2	C-C	45	51	39
	C3	286.1±0.2	C-OH	9	13	12
	C4	286.6±0.3	C-O-C	26	14	12
	C5	287.4±0.2	C=O	0	4	0
	C6	289.0±1.0	COO	12	7	19
O	O1	531.5±0.5	C=O	2	10	2
	O2	532.5±0.3	C-O	53	48	41
	O3	533.4±0.4	O-C=O	22	27	25
	O4	534.9±0.5	HO-C-O	15	13	11
	O5	536.3±0.3	ads O_2	8	3	20
Au	Au^0	84.2 ± 0.4	Au^0 (7/2)	33	42	48
	Au^0	87.9 ± 0.4	Au^0 (5/2)	25	32	35
	Au^+	85.8 ± 0.4	Au^+ (7/2)	12	7	2
	Au^+	86.2 ± 0.4	Au^+ (5/2)	9	5	1
	Au^{3+}	86.4 ± 0.2	Au^{3+} (7/2)	12	8	8
	Au^{3+}	90.1 ± 0.2	Au^{3+} (5/2)	9	6	6

Data from the C1s spectra was in good agreement with the deconvolution of the oxygen O1s spectra which, according to the peaks described in Section 2.2.3.3, indicated a decreasing number of carbonyl groups, and substantial increased in carboxylate groups for all three materials. As expected from C1s, lower number of hydroxyl groups were detected in S300 and S450 after deconvolution of O1s spectra.

S300 and S450 were also analysed by IR after adsorption to verify the observations made by XPS. As seen in Figure 2.17, the -OH band was significantly broader after adsorption. Broader bands have been associated to carboxylic compounds instead of hydroxyl groups.[238] The presence of carboxylic groups is in good agreement with the hypothesised oxidation of carbonyl to carboxylic groups as a result of the adsorption process. Before

adsorption, a C=O band appeared at 1716 and 1718 cm^{-1} for S300 and S450 respectively, a wavelength characteristic of ketones. These peaks were shifted to lower wavelengths after adsorption (1711 and 1706 cm^{-1} respectively), which was typical of carboxylic acids.[238]
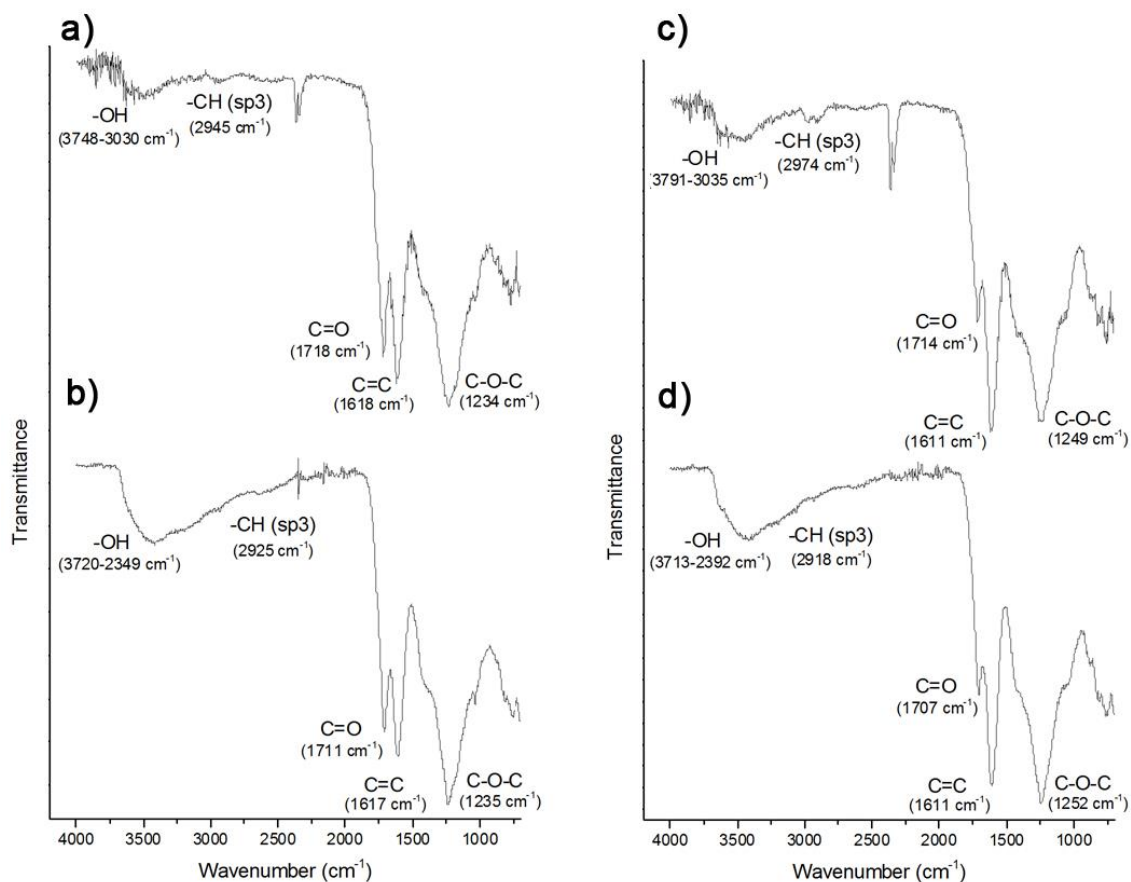
Figure 2.17 Infrared spectra of S300 a) before and b) after adsorption of gold; and IR spectra of S450 c) before and d) after adsorption of gold.

Results of XPS and IR were consistent with the *formation of carboxylate groups* as the mechanism for the surface oxidation. Therefore, adsorption of gold by Starbon® occurs via reduction of Au^{3+} to Au^{0} yielding nanoparticles and subsequent oxidation of the carbonyl groups to form carboxylic-type functionalities. S300 and S450 displayed evidence for both carbonyl and hydroxyl oxidation to carboxylic and carbonyl groups, respectively.

It has been suggested that the adsorption of gold onto carbonaceous surfaces occurs in three consecutive steps: adsorption, reduction and aggregation.[52] Initially, $AuCl_4^-$ gets electrostatically attracted to the positively charged surface of the material. As the working pH<pzc, metal ions are reduced due to electron-donor groups in the surface, which ultimately oxidise. Finally, nanoparticles were released from the surface and agglomerate to form clusters of gold nanoparticles, leaving free active sites for further adsorption. This three-stage mechanism fits the data obtained by XPS and IR and is also consistent with the agglomeration of nanoparticles observed by TEM. However, in the present work, nanoparticles were not released to solution, but stayed onto the porous network (as shown by TEM). Therefore, it is possible to suggest that Starbon® chemically adsorb gold onto its surface in a three-step process including electrostatic adsorption, reduction and agglomeration.

2.2.4.2 Palladium and platinum adsorption mechanism

The lower selectivity observed for platinum and palladium may be related to their standard reduction potentials (Scheme 2.2 and Scheme 2.3).[245, 246] The reduction potential of the carbonaceous solid varies from one material to another; however, the approximate value is close to those for Pd^{2+} and Pt^{2+} and therefore, it can significantly affect the adsorption mechanism.[254, 255] Different authors suggested different mechanisms for the adsorption of $PdCl_4^{2-}$ and $PtCl_4^{2-}$:[79, 245, 256]

- *Adsorption by ion exchange*. Zalupski *et al.* and Parajuli *et al.* suggested that the adsorption of $PdCl_4^{2-}$ occurred entirely via ion exchange because the reduction potential of the adsorbent was higher than those for $PdCl_4^{2-}$ and $PtCl_4^{2-}$, making the redox reaction non-favourable.[79, 245]
- *Combined adsorption and reduction*. Simonov proposed that the adsorption of $PdCl_4^{2-}$ occurred through two parallel mechanisms; reduction of Pd^{2+} and subsequent oxidation of the surface, and formation of stable π-complexes of $PdCl_2$ with the carbon double bonds present in the solid.[256] According to this hypothesis,

palladium nanoparticles resulting from reduction were found in the exterior surface of the carbonaceous material. On the other hand, π-complexes were formed on the whole surface of the material.[256]

Deconvolution of the Pd3d spectra after adsorption of $PdCl_4^{2-}$ exhibited two doublets of peaks where the two peaks within the doublet were 5.3 eV apart, presented identical FWHM and the relative intensity was 2:1 for the 5/2 and 3/2 spin orbits respectively. The characteristic doublet for Pd^0 at 335 eV (5/2) was present (see Figure 2.18).[257] However, the main doublet was observed at 337 eV which has been assigned to Pd^{2+} ions.[257] The presence of both palladium species was in good agreement with the *combined adsorption reduction* mechanism. The fraction of Pd^0 was 20%, consistent with Simonov's observation that only a small portion of the Pd was reduced.[256]

S300 and S450 were not analysed by XPS after adsorption of $PdCl_4^{2-}$ and $PtCl_4^{2-}$ due to the very low values of adsorption capacities displayed (Figure 2.12). Furthermore, the presence of nanoparticles was not expected for those materials, as Simonov *et al.* observed that large fractions of oxygen-containing functionalities did not lead to Pd nanoparticles.[256]

As shown in Figure 2.18, deconvolution of Pt4f spectra showed three doublets at 71.4 eV (7/2), corresponding to Pt^0, 72.2 eV related to Pt^0 coordinated to C-O groups, and 73.6 eV assigned to Pt^{2+} with Cl^- ligands.[258,259] The two peaks within the doublet were 3.4 eV apart, presented identical FWHM and the relative intensity was 4:3 for the 7/2 and 5/2 spin orbits respectively. The doublet at 72.2 eV may be the result of metallic platinum formed by a reductive process that was still complexed to oxygen-containing groups.[258] Similar to palladium, only 20% of Pt^{2+} was reduced to Pt^0 also suggesting a *combined adsorption-reduction* mechanism for this element.
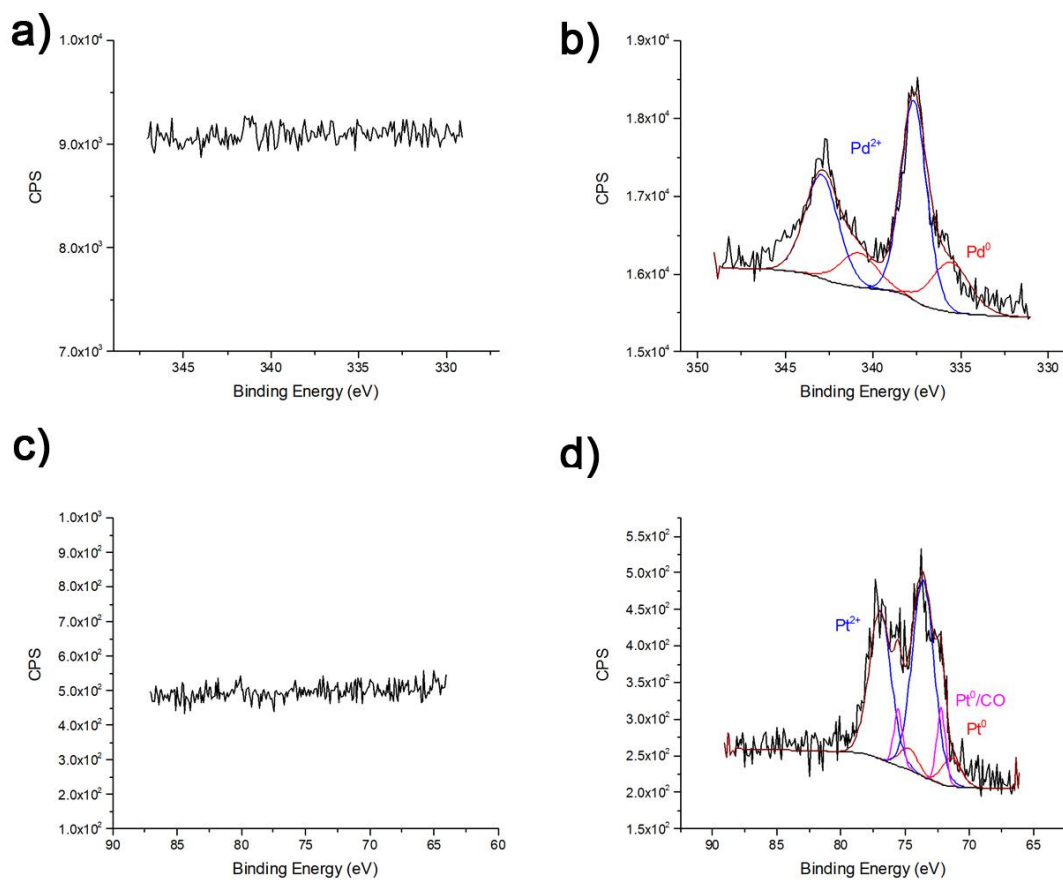
Figure 2.18 Deconvolution of Pd3d XPS spectra of S800 a) before and b) after adsorption of palladium; and deconvolution of Pt4f XPS spectra of S800 c) before and d) after adsorption of platinum. The experimental conditions were constant stirring for 24 h, room temperature and pH 0.

As for gold, the formation Pt^0 and Pd^0 caused the oxidation of the adsorbent surface. C/O ratio decreased after adsorption (Table 2.9). Nevertheless, this reduction was less pronounced than for gold, which is consistent with the lower amount of reduced palladium and platinum observed.

Table 2.9 Comparison of S800 C/O ratio before and after adsorption of platinum and palladium from respective solutions subjected to constant stirring for 24 h, at room temperature and pH 0.

Material	Metal	C/O ratio (%)		
		Before ads.	After ads.	Variation
S800	Pd	19.8	15.5	-4.3
S800	Pt	19.8	16.2	-3.6

101

The deconvolution of C1s spectra showed larger number of carboxylic groups to the detriment of carbonyl functionalities (Figure 2.19). As for the C/O ratio, the variations in these functional groups were not as noticeable as they were for gold. Deconvoluted O1s spectra showed lower fraction of C=O groups and increasing portions of carboxylic and carboxylate groups, which was in good agreement with the observations made for C1s.
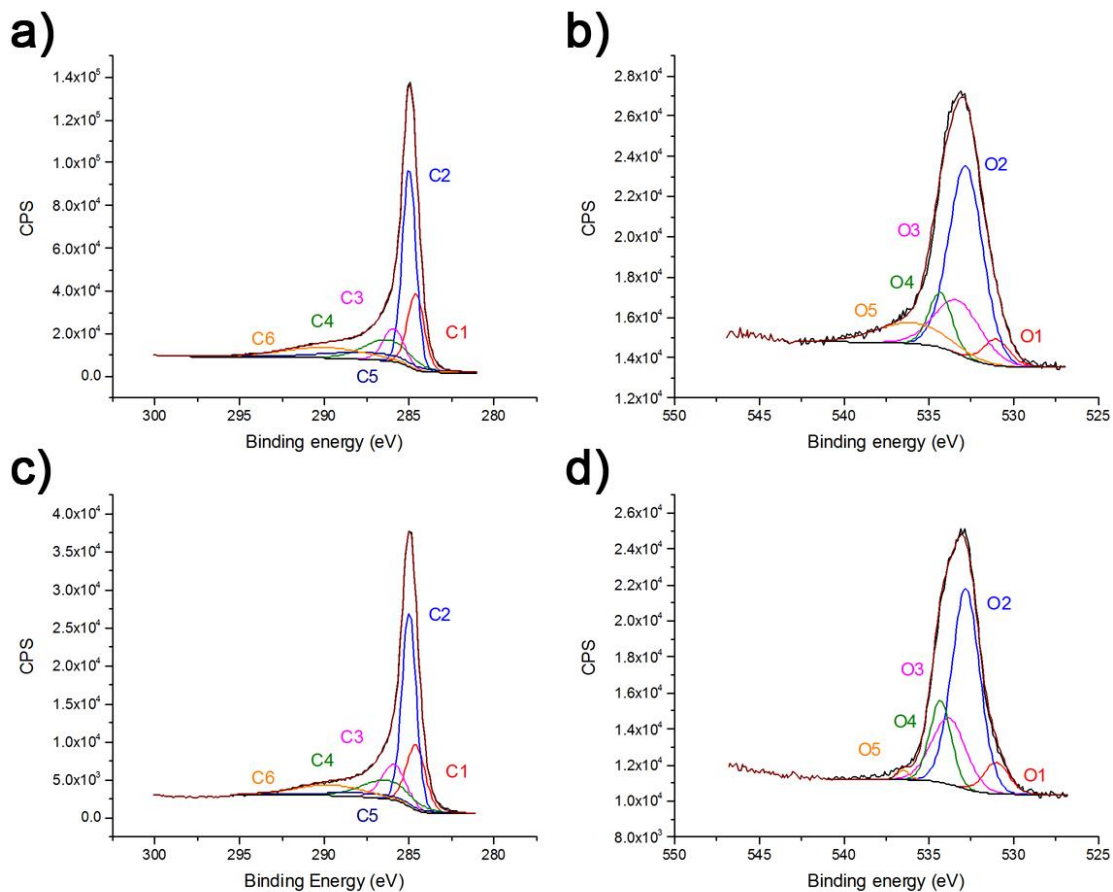
Figure 2.19 Deconvolution of XPS C1s and O1s spectra of S800 after adsorption of a-b) palladium and c-d) platinum. The experimental conditions were constant stirring for 24 h, room temperature and pH 0.

Table 2.10 Quantification of functional groups present in S800 after adsorption of palladium and platinum from respective solutions subjected to constant stirring for 24 h, at room temperature and at pH 0.

Element	Peak	BE (eV)	Chem.	Fraction (%)	
				S800-Pd	S800-Pt
C	C1	284.3 ± 0.3	C=C	18	20
	C2	284.8 ± 0.2	C-C	38	38
	C3	286.1 ± 0.2	C-OH	11	13
	C4	286.6 ± 0.3	C-O-C	14	11
	C5	287.4 ± 0.2	C=O	8	7
	C6	289.0 ± 1.0	COO	12	11
O	O1	531.5 ± 0.5	C=O	6	3
	O2	532.5 ± 0.3	C-O	50	59
	O3	533.4 ± 0.4	O-C=O	19	14
	O4	534.9 ± 0.5	COOH	9	17
	O5	536.3 ± 0.3	ads O_2	16	8
Pt	Pt^0	71.1 ± 0.4	Pt^0 (7/2)	-	5
	Pt^0	74.4 ± 0.4	Pt^0 (5/2)	-	4
	Pt^0/CO	72.8 ± 0.8	Pt^0/CO (7/2)	-	46
	Pt^0/CO	76.1 ± 0.8	Pt^0/CO (5/2)	-	34
	Pt^{2+}	72.0 ± 0.4	Pt^{2+} (7/2)	-	6
	Pt^{2+}	75.3 ± 0.4	Pt^{2+} (5/2)	-	5
Pd	Pd^0	335.6 ± 0.3	Pd^0 (5/2)	8	-
	Pd^0	340.9 ± 0.3	Pd^0 (3/2)	12	-
	Pd^{2+}	337.9 ± 0.4	Pd^{2+} (5/2)	32	-
	Pd^{2+}	343.2 ± 0.4	Pd^{2+} (3/2)	48	-

2.2.4.3 The role of chlorine atoms

The presence of Au^{3+}, Au^+, Pd^{2+} and Pt^{2+} on the surface of Starbon® was in good agreement with the appearance of chlorine in the elemental analysis done by XPS, as Cl^- were ligands in the complex species $AuCl_4^-$, $AuCl^-$, $PdCl_4^{2-}$ and $PtCl_4^{2-}$ in acidic solutions. As seen in Table 2.11, the amount of chlorine was within the range 0.3-0.6% of the total for Pt and Pd. The larger fraction of chlorine detected after adsorption of palladium compared to platinum was consistent with the higher uptake observed for this metal.

The deconvolution of Au4f discussed above, showed that S300 and S450 presented larger amounts of electrostatically adsorbed gold ions (Au^{3+}). Such adsorbed gold ions have Cl^- as ligands and therefore, it was expected that S300 and S450 presented larger concentrations of Cl^- in the surface. However, the highest fraction of chloride ions was detected in S800-Au. Further work is therefore needed to understand the role of chloride ions in the adsorption of precious metals onto Starbon®, however, this was out of the scope of the present work and it will be briefly discussed in the future work section (Chapter 6).

Table 2.11 Elemental composition of Starbon® materials after adsorption of precious metals from metal solutions subjected to constant stirring for 24 h, at room temperature and at pH 0.

Material	Elemental analysis (%)						
	C	O	S	Cl	Pt	Pd	Au
S800 - Pd	93.1	6.0	0.2	0.6	-	0.1	-
S800 - Pt	93.7	5.8	0.1	0.4	-	-	-
S300 - Au	78.0	21.4	0.1	0.4	-		0.1
S450 - Au	83.8	15.8	-	0.3	-		0.1
S800 - Au	91.3	7.4	0.2	0.7	-	0.2	0.2

Figure 2.20 shows deconvolution of Cl2p spectra, which exhibited two doublets at 198.2 and 200.7 eV, that were assigned to Cl^- and chlorine atoms bonded to carbon atoms respectively (C-Cl).[250] The two peaks within the doublet were 1.6 eV apart, presented identical FWHM and the relative intensity was 2:1 for the 5/2 and 3/2 spin orbits respectively.[260] Deconvolution of Cl2p spectra showed very low fraction of Cl^- groups in favour of the alleged C-Cl bonds.[250] Thus, further work is needed to understand whether some chlorine atoms may have been incorporated into the carbon backbone or were just adsorbed onto the surface during adsorption.
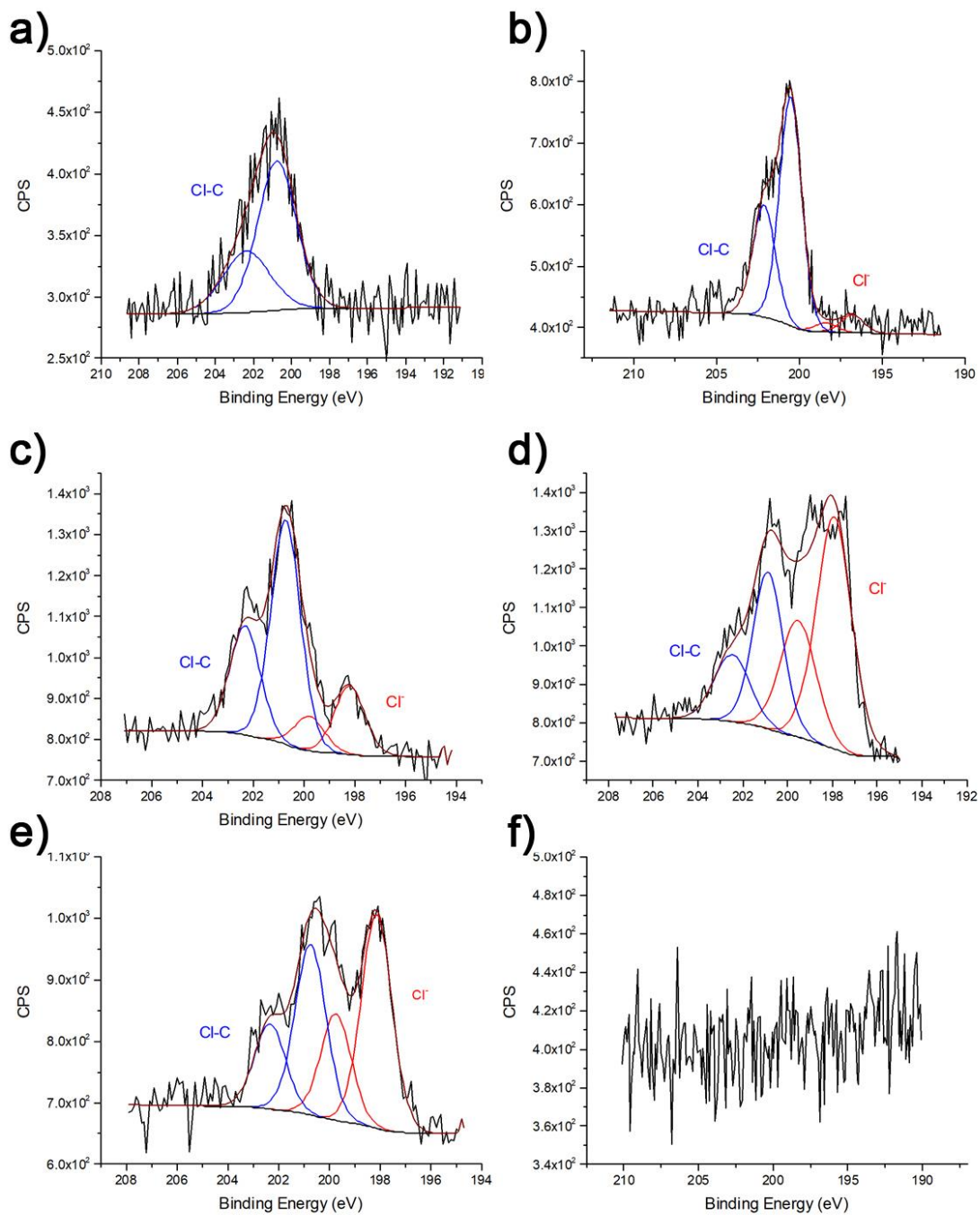
Figure 2.20 Deconvolution of Cl2p XPS spectra for a) S300, b) S450 and c) S800 after adsorption of gold; S800 after adsorption of d) palladium and e) platinum; f) S800 before adsorption. The experimental conditions of the adsorption experiments were constant stirring for 24 h, room temperature and pH 0.

Some studies have shown that low pH and therefore, higher concentrations of Cl⁻ (when HCl (aq) used to acidify), lower the adsorption of precious metals in favour of Cl⁻.[71, 76, 77]

This agrees with the results of this study, where experiments conducted at pH=3 led to significantly higher adsorption (over 3000 mg·g^{-1}) of gold than at pH=0 (600 mg·g^{-1}).[134] Nevertheless, mechanistic and kinetic studies concerning the adsorption of precious metals onto Starbon® were carried out at low pH (i.e. pH=0) to mimic the conditions of real metal waste streams (i.e. metal leaching solutions from discarded devices), which are generally highly acidic.[19]

2.2.4.4 The effect of carbonisation temperature in adsorption

S800 offered the highest adsorption efficiency for all three precious metals, displaying adsorption capacities at least twice or three times larger than the other two adsorbents (see Figure 2.12 and Table 2.5). Such significant differences may be caused by variations in the adsorption mechanism occurring with each material.

As shown in Figure 2.14, deconvolution of Au4f spectra showed three doublets corresponding to different oxidation states of gold. The fractions of gold species varied with the preparation temperature of Starbon®. Interestingly, the fraction of Au^0 was significantly lower for S300 (58%) and S450 (74%) compared to S800 (83%). This trend was similar to that displayed by adsorption capacities which suggested a direct correlation between adsorption capacity and adsorption mechanism, where the latter is, in turn, closely related to the surface characteristics of the solid. Some of the surface characteristics that can affect the adsorption of metals are detailed below:

- *Aromaticity*. Aromatic groups were twice as abundant in S800 compared to the other two adsorbents. As aromatic rings are rich in electrons, S800 had the ability to reduce higher number of Au^{3+} to its metallic form, and therefore removing larger amounts of gold from solution. Conductivity measurements showed that S800 presents some degree of conductivity (7 mS·cm^{-1}). Thus, electrons from aromatic rings could be transported to the adsorption sites, where metals were reduced.[256]

- *Microporosity and surface energy.* The presence of micropores has been related to higher values of surface energy, due to the proximity of pore walls.[130] High surface energies have, in turn, been associated to stronger adsorption processes in which the adsorbate can be adsorbed but cannot be desorbed.[130] As observed in Table 2.1, microporosity and surface energy increased with the carbonisation temperature of Starbon®. Thus, S800, with the largest number of micropores and the highest surface energy, presented the best characteristics to achieve the greatest adsorption capacity. Additionally, S800 showed the largest surface area and therefore, had more available surface for adsorption.

- *Point of zero charge.* Pzc for S300, S450 and S800 was 5.1, 5.8 and 5.3 respectively, confirming that all three materials displayed positively charged surface under the acidic working conditions. In contrast, precious metals were present as negatively charged ions in acidic solutions: $AuCl_4^-$, $PdCl_4^{2-}$ and $PtCl_4^{2-}$.[71, 77] Thus, the positive surface of Starbon® initially attracted the negative ions close to its surface and later reduced these ions to their elemental form.[71, 85] Interestingly, as stated by Asad 2015 *et al.*, low pzc may have detrimental effect for adsorption of metals, as the active sites suffer a dissociative reaction becoming negatively charged:[85]

$$RC\text{-}H + H_2O \rightarrow RC^- + H_3O^+$$
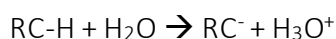
Therefore, the lower pzc displayed by S300 compared to S450 and S800 may be related to its lower adsorption capacity for gold.

2.2.4.5 Adsorption isotherms

The curve describing the retention of a substrate onto a solid surface within a range of concentrations is known as adsorption isotherm.[261] These curves are extremely informative and key to understand the adsorption mechanism of certain substances onto solid surfaces. Giles *et al.* classified adsorption isotherms into four categories, depending on their shape:[262]

- *'C type' isotherm.* Represented by a straight line passing through the origin, symbolises the constant relation between the adsorbed solute and the sorbate still in solution. It has been commonly applied to low or narrow ranges of concentration.

- *'L type' isotherm*. Characterised by a concave curve in which the ratio between the solute adsorbed and the remaining in solution decreased at increasing initial concentrations. It can generally be found in metal adsorption studies.[76, 245] 'L' isotherm can be sub-categorised depending on the presence or lack of plateau. The latter could indicate no apparent limit on the adsorption capacity of the solid or it could also be related to the orientation of the ions adsorbed.

- *'H type' isotherm*. It can be considered as a particular case of 'L type' isotherms, as their shapes are almost identical. However, 'H' displays a nearly vertical line at low concentrations, suggesting high affinity between the solute and the adsorbent.

- *'S type' isotherm*. Represented by a sigmoidal curved is caused by two opposite mechanism having place during the adsorption.

Figure 2.21 shows the adsorption isotherms for carbonised Starbon® obtained at room temperature. Adsorption of gold was well-represented by the 'H' indicating high affinity between Starbon® and gold. This was in good agreement with the redox mechanism suggested in previous sections and with other gold adsorption studies found in the literature.[71] On the other hand, platinum adsorption gave a straight line, 'C-type', isotherm at low initial concentrations. The limited solubility of platinum chloride in aqueous media required the usage of a narrow range of low concentrations to study adsorption isotherms, conditions that can lead to 'C type' isotherms.[261] Palladium adsorption displayed the characteristic 'L' isotherm, some of which presented a clear plateau, and therefore limited adsorption capacity, such as S300-Pd and S800-Pd.
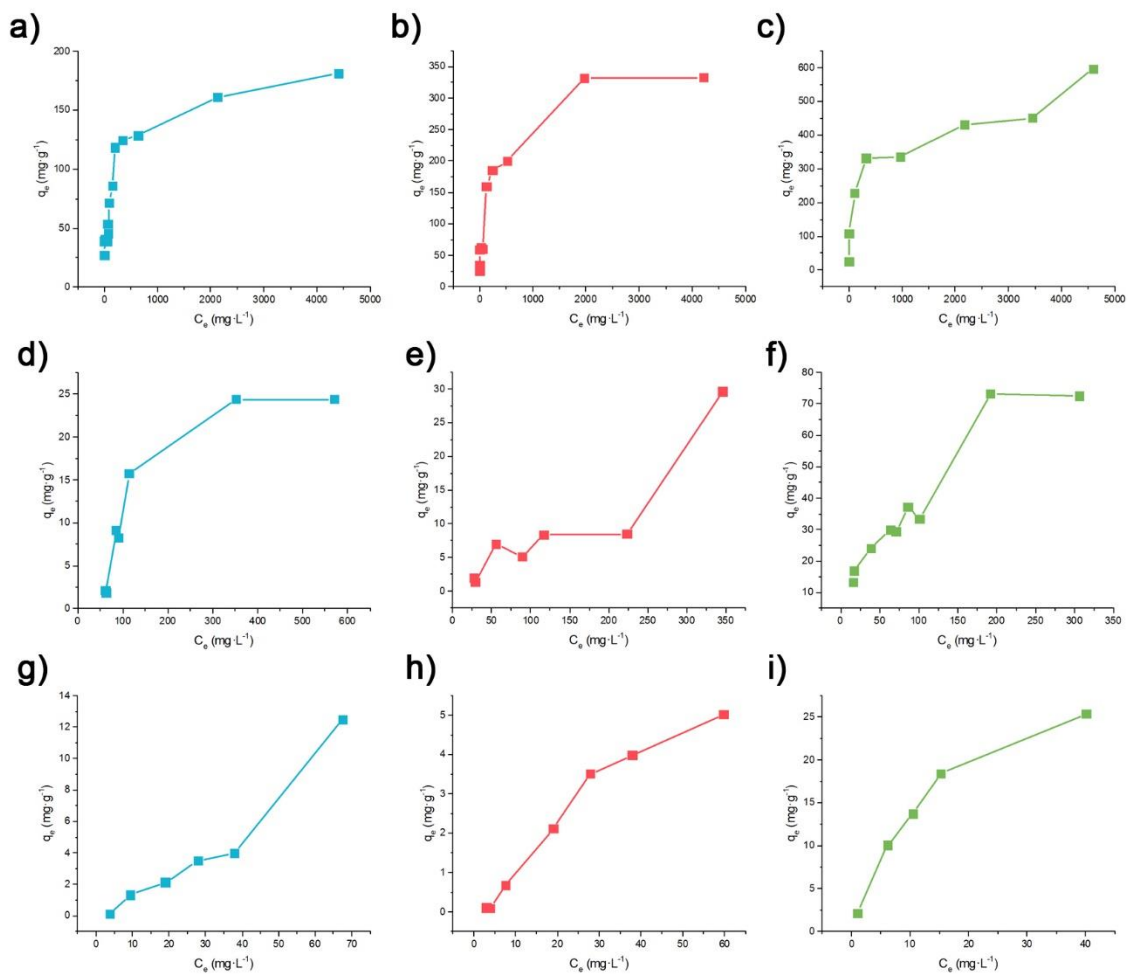
Figure 2.21 Adsorption isotherms for a) S300, b) S450 and c) S800 after the adsorption of gold; adsorption isotherms for d) S300, e) S450 and f) S800 after the adsorption of palladium; adsorption isotherms for g) S300, h) S450 and i) S800 after the adsorption of platinum. The experimental conditions were constant stirring for 24 h at room temperature and pH 0

As showed by XPS in the Section 2.2.4.1, the mechanism of Starbon® to adsorb gold included both oxidation/reduction to yield NPs, and electrostatic interactions between the ions and the material's surface. The formation of nanoparticles can be considered as an irreversible process as the NPs cannot be re-dissolved under the experimental conditions. On the other hand, the electrostatic interactions are a reversible process. Adsorption isotherm models can only be applied to reversible adsorption processes. Thus, the following section, which discuss some of these models in detail, will use the data related to the reversible adsorption only. Irreversible adsorption can be observed in the

adsorption isotherms plots (Figure 2.21), as it was represented by a vertical line at low concentrations which quickly flattens to yield a rectangular isotherm. A few points in the gold isotherms displayed a vertical line and therefore, those will be disregarded when applying the adsorption models. Nevertheless, the isotherm does not flatten following that vertical line, but keep increasing, which was indicative of certain degree of physisorption. The vertical line could only be observed for Au, as Pd and Pt did not form a significant number of nanoparticles during adsorption, as were electrostatically adsorbed instead.

Three different isotherm equations were employed to fit the experimental data shown above: Langmuir, Freundlich and Dubinin-Radushkevich (D-R), to achieve a better understanding of the adsorption mechanism (i.e. monolayer vs multilayer adsorption).

- *Langmuir isotherm.* It assumes that as metal ions get adsorbed the form a monolayer.[263] Once this first layer is completed, no more adsorption takes place and a plateau can be observed.[264] Langmuir isotherm also presumes adsorption onto homogenous surfaces.[264] Its linearized form can be expressed as follow:[264]

$$\frac{C_e}{q_e} = \frac{1}{Q_o} \cdot C_e + \frac{1}{K_L \cdot Q_o}$$

   where C_e and q_e are the concentration ($mg \cdot L^{-1}$) and adsorption capacity ($mg \cdot g^{-1}$) at equilibrium respectively. Q_0 represents the adsorption capacity of the monolayer ($mg \cdot g^{-1}$). [264]

   By plotting C_e/q_e against C_e a linear plot is obtained with $1/K_L$ as intercept and a_L/K_L as gradient.

   The dimensionless factor R_L shows favourable adsorption when falls within the range 0-1 and can be calculated from the following formula:[81, 265]

$$R_L = \frac{1}{1 + K_L \cdot C_0}$$

- *Freundlich isotherm*. It presumes that adsorption on heterogenous surfaces can lead to the formation of several layers of adsorbed material.[266] The linearized form of the Freundlich isotherm is:[105]

$$\ln q_e = \ln k_f + \frac{1}{n} \ln C_e$$

Where 'n' is the heterogeneity factor and indicates favourable adsorption at values close or greater than 1.[267] K_f is a Freundlich constant related to the adsorption capacity of the material.[266]

A straight line with $\ln(k_f)$ as intercept and $1/n$ as slope is obtained after plotting $\ln(q_e)$ against $\ln(c_e)$.

- Dubinin-Radushkevich (D-R) isotherm. This isotherm is based on the postulate that the mechanism of adsorption in micropores is pore filling rather than layer-by-layer surface coverage.[268] Through D-R it is possible to calculate the energy of adsorption if monolayer adsorption is assumed.[269] Values within the range of 8-16 kJ·mol^{-1} indicate physisorption,[270] whereas energies above 16 kJ·mol^{-1} suggest chemisorption processes. The linear equation can be expressed as:

$$\ln q_e = \ln q_m - K' \cdot \varepsilon^2$$

where ε (Polanyi potential), expressed in J^2·mol^{-2}, can be calculated from:

$$\varepsilon = RT \cdot \ln\left(1 + \frac{1}{C_e}\right)$$

q_m is the saturation capacity of the monolayer, expressed in mg·g^{-1}, R is the gas constant (J·K^{-1}·mol^{-1}), T is the temperature (K) and K' (mol^2·J^{-2}) is a D-R constant related to the adsorption energy (E_{ads}) in kJ·mol^{-1}, which can be calculated from the following formula:[271]

$$E_{ads} = \frac{1}{\sqrt{2K'}}$$

Representation of $\ln(q_e)$ against ε^2 gives a linear fit with K' as gradient and $\ln(q_m)$ as intercept.

Gold experimental data fit well to the Langmuir isotherm, displaying r^2 values over 0.99 for S300 and S450 and 0.91 for S800 (Figure 2.22, Table 2.12). Interestingly, the monolayer adsorption capacity represented by Q_0, were in good agreement with the adsorption capacities calculated experimentally (Table 2.5). The concentration range used to obtain the isotherms was 25-5000 mg·L^{-1}. The R_L values fell within the 0-1 interval throughout this concentration range for all three Starbon® materials, indicating favourable adsorption in all cases. K_L, which is related to the rate of adsorption, decreased with increasing temperatures of carbonisation. Therefore, although S800 was capable of forming more gold NPs (as shown before in this chapter), physisorption occurred faster for S300 and S450. This could be explained by the larger number of oxygen-containing groups in those two materials. Such oxygen groups get positively charged at the low pH values of the experiments and thus electrostatically adsorbed the PM anions.

Data was also fitted well to Freundlich and D-R isotherms. However, fittings were not as good as with Langmuir's model. This indicated that the reversible process of adsorption occurred via monolayer coverage of the adsorption sites. This results were in good agreement with some other polysaccharide-derived carbon materials found in the literature.[83, 87] For example, Wang et al., who studied the adsorption of gold onto carbon porous spherules, also observed good fittings for both Langmuir and Freundlich models.[87] However, Langmuir r^2 values were superior. On the other hand, Soleimani et al., who used AC from apricot stones for the adsorption of gold, obtained better fitting with the Freundlich isotherm.[84] This suggested that the mechanism of adsorption strongly depend on the material's physical and chemical properties.
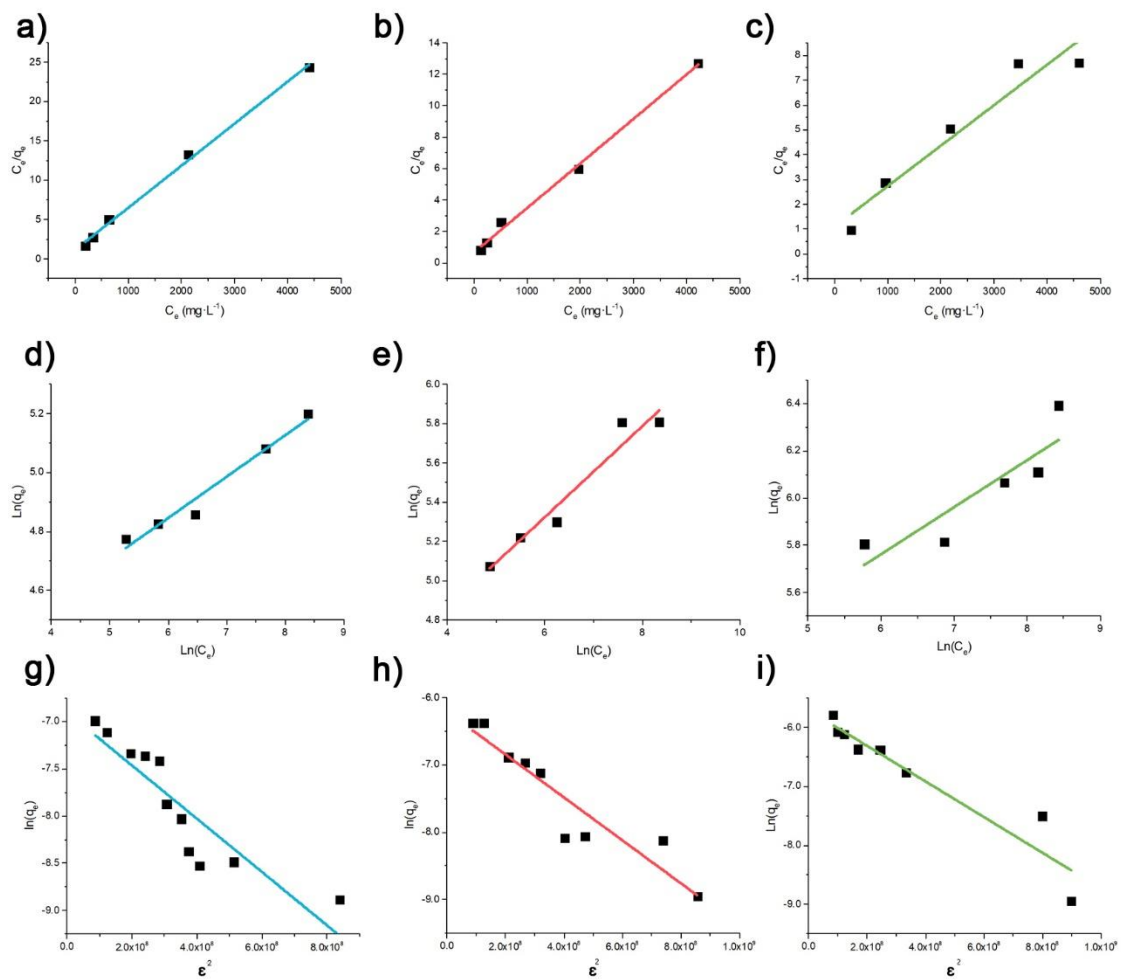
Figure 2.22 Langmuir isotherm fitting graphs for a) S300, b) S450 and c) S800; Freundlich isotherm fitting graph for d) S300, e) S450 and f) S800; D-R isotherm fitting graphs for g) S300, h) S450 and i) S800 after adsorption of gold.

Table 2.12 Langmuir, Freundlich and D-R isotherm parameters after adsorption of gold. Fittings with r^2 values < 0.7 have not been included in the Table.

	S300	S450	S800
Langmuir			
K_L (L·mg^{-1})	4.7×10^{-3}	4.3×10^{-3}	1.5×10^{-3}
Q_0 (mg·g^{-1})	186.9	353.4	613.5
R_L	0.89-0.04	0.89-0.05	0.96-0.12
r^2	0.9958	0.9951	0.9120
Freundlich			
K_f	54.81	51.25	96.09
n	7.13	4.33	5.014
r^2	0.9689	0.9337	0.7127
D-R			
$q_m\times10^{-3}$ (mg·g^{-1})	197.0	394.0	650.1
K' (mol^2·J^{-2})	2.8×10^{-9}	3.2×10^{-9}	3.0×10^{-9}
E_{ads} (kJ·mol^{-1})	13.3	6.3	6.4
r^2	0.7949	0.8676	0.8856

Regarding adsorption of Pd, S300 could not be fit by any of the models adequately, and further work is required to elucidate the adsorption mechanism. Only S800 could be adequately fitted to the Langmuir isotherm (Figure 2.23 and Table 2.13). However, this fitting was poorer than Freundlich. A good fitting was also obtained with the D-R model for both S450 and S800. However, the monolayer capacities calculated by this model did not agree well with the experimentally calculated values. This could be due to the fact that Starbon® are not completely microporous, as assumed by the D-R model.

Both S450 and S800 experimental data fit well to Freundlich isotherm. The equilibrium constant K_f, which is related to the adsorption capacity, was much larger for S800 than for S450, in good agreement with the adsorption capacity values obtained experimentally.[105] The heterogeneity factor indicated favourable adsorption in both cases.

These results suggested that the adsorption of Pd led to multilayer adsorption when S450 and S800 were employed.
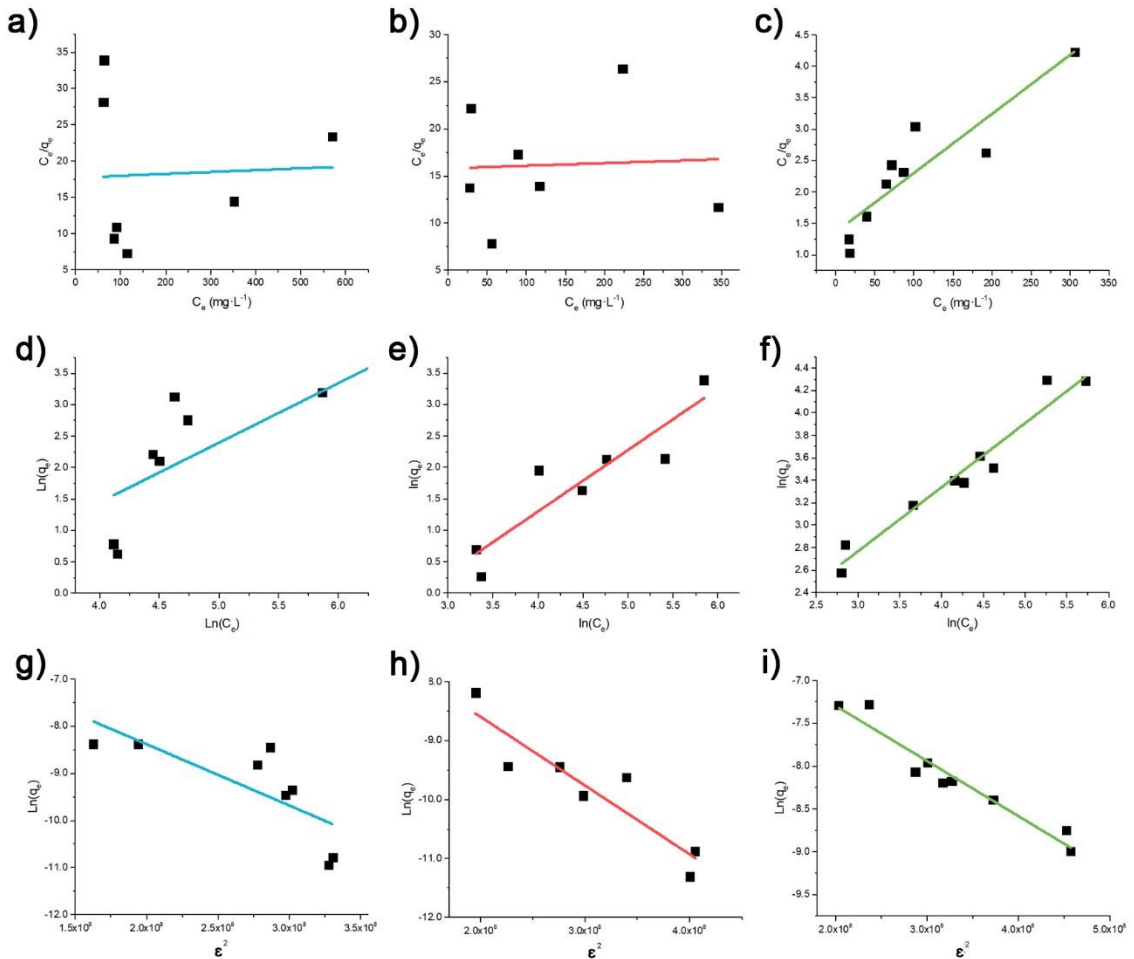
Figure 2.23 Langmuir isotherm fitting graphs for a) S300, b) S450 and c) S800; Freundlich isotherm fitting graph for d) S300, e) S450 and f) S800; D-R isotherm fitting graphs for g) S300, h) S450 and i) S800 after adsorption of palladium.

Table 2.13 Isotherm parameters after adsorption of palladium. Fittings with r^2 values < 0.7 have not been included in the Table.

	S300	S450	S800
Langmuir			
K_L (L·mg^{-1})	-	-	6.9×10^{-3}
Q_0 (mg·g^{-1})	-	-	106.6
R_L	-	-	0.83-0.36
r^2	-	-	0.7948
Freundlich			
K_f	-	7.4×10^{-2}	2.8
n	-	1.02	1.75
r^2	-	0.8146	0.9432
D-R			
q_m (mg·g^{-1})	-	201.1	260.7
K' (mol^2·J^{-2})	-	1.2×10^{-8}	6.4×10^{-9}
E_{ads} (kJ·mol^{-1})	-	6.5	8.8
r^2	-	0.8168	0.9295

Only S800 could be adequately fitted to the Langmuir isotherm when platinum was adsorbed. The r^2 values were 0.99 and the adsorption capacity was very similar to the experimentally calculated. In addition, R_L values showed favourable adsorption of platinum in the range of concentrations used in the experiment. Although good fittings were also observed with the Freundlich and D-R models, Langmuir r^2 value was closer to 1, indicative of monolayer adsorption.

D-R model gave good fittings ($r^2>0.92$) for S300 and S450. However, the monolayer adsorption capacities obtained by this model disagreed well with those calculated experimentally. S300 and S450 fit well to the Freundlich model. The heterogeneity factor indicated non-favourable adsorption for both materials which was in good agreement with the low platinum adsorption capacities observed for those materials.

These results indicated that platinum was adsorbed onto S300 and S450 through a multilayer mechanism.

The mechanistic differences observed between Pd and Pt for S800 are interesting and are supported by the Pt^0(CO) group observed by XPS. The Langmuir model assumes that one active site can adsorb one molecule. A reduction mechanism requires a reaction between a metal ion and an active site of the adsorbent. Therefore, the larger fraction of reduced Pt compared to Pd could explain the monolayer mechanism observed for Pt 800, in opposition to the multilayer adsorption of Pd by the same material. This is in good agreement with the reduction potential of Pt, which is higher than that of Pd and thus, more likeable to be reduced.

To the authors knowledge, no studies with carbonised polysaccharide adsorbents have been carried out for the adsorption of palladium and platinum. Other polysaccharide-derived materials described in the literature displayed good correlation with the Langmuir model.[76, 77]
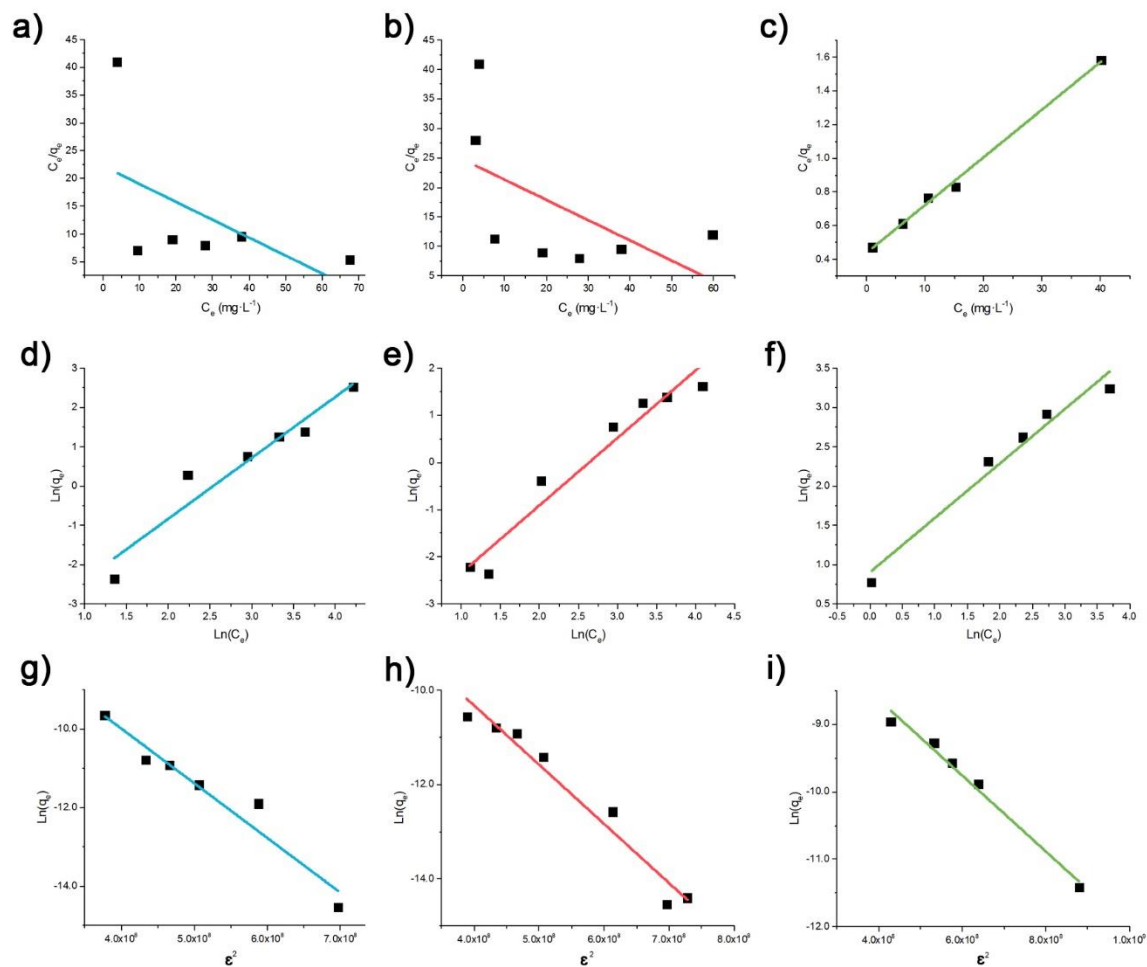
Figure 2.24 Langmuir isotherm fitting graphs for a) S300, b) S450 and c) S800; Freundlich isotherm fitting graph for d) S300, e) S450 and f) S800; D-R isotherm fitting graphs for g) S300, h) S450 and i) S800 after adsorption of palladium.

Table 2.14 Isotherm parameters after adsorption of platinum. Fittings with r^2 values < 0.7 have not been included in the Table.

	S300	S450	S800
Langmuir			
a_L (L·mg^{-1})	-	-	2.1×10^{-2}
Q_0 (mg·g^{-1})	-	-	35.3
R_L	-	-	0.94-0.42
r^2	-	-	0.9952
Freundlich			
K_f	2.0×10^{-2}	2.3×10^{-2}	2.4×10^{-2}
n	0.6	0.7	1.4
r^2	0.9122	0.9379	0.9575
D-R			
q_m (mg·g^{-1})	2320.5	963.3	330.5
K' (mol^2·J^{-2})	1.4×10^{-8}	1.3×10^{-8}	-5.6×10^{-9}
E_{ads} (kJ·mol^{-1})	6.0	6.3	4.7
r^2	0.9277	0.9530	0.9801

In summary, Langmuir isotherm fit well data for the adsorption of gold onto the three materials and platinum onto S800, displaying R_L values within the favourable adsorption and Q_0 similar to the adsorption capacities experimentally calculated, suggesting monolayer adsorption. On the other hand, S450 was best described by Freundlich isotherm for the adsorption of both platinum and palladium, indicative of multilayer coverage. The literature showed examples of good fitting to both Langmuir and Freundlich depending on the bio-adsorbent employed, which indicated that the mechanism of adsorption was highly dependent on the material employed.[83, 84, 87]

2.2.4.6 Kinetic studies of precious metals adsorption onto Starbon® surface.

Kinetic studies help to understand the adsorption process, indicating the rate-limiting steps and the time after which equilibrium is achieved.[272]

In order to study the kinetics of metal adsorption on Starbon®, the reactions were monitored for 24 h and samples were taken and analysed at regular intervals. By plotting the fraction of metal removed against time, it was possible to compare the rate of adsorption of the three types of Starbon® (Figure 2.25).
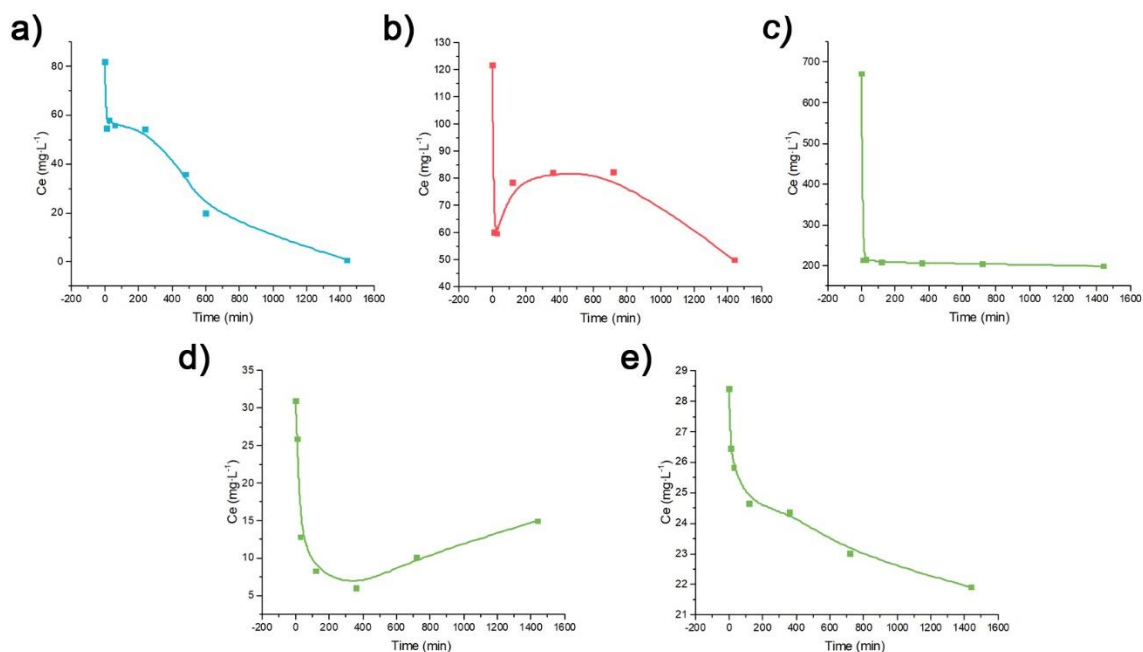
Figure 2.25 Rate of gold removal from solution by a) S300, b) S450 and c) S800; d) of palladium by S800 and e) of platinum by S800.

Gold showed the fastest rate of adsorption. Remarkably, equilibrium was reached after only 10 min of mixing the metal solution with S450 and S800. This phenomenon of rapid adsorption of gold has also been observed by other authors employing carbonaceous materials.[83, 84]

Desorption rate was higher than adsorption in the range of 120 and 720 min for S450. It was not clear why this phenomenon occurred, and further work is needed to elucidate the causes. Nevertheless, the literature showed that the oxygen containing functionalities could be modified in the presence of oxidative HNO_3.[273] As the gold interacts with oxygen functional groups during the adsorption, a plausible explanation for the desorption observed could be the degradation of some of the functional groups of the carbon due to

120

the strong acidic media, which would return some of the adsorbed gold ions back into solution.

S300 showed a very different pattern of adsorption where a pseudo-equilibrium stage was reached after 10 min and lasted up to 240 min. At this point, concentration in solution progressively decreased until around 800 min, when a second equilibrium was achieved. These pseudo-equilibrium stage may be related to the different oxidation states of gold found in Starbon®, as seen previously by XPS (Figure 2.14). Nevertheless, further work is required to determine the nature of such adsorption rates.

When S800 was used to adsorb palladium, the equilibrium was reached after 360 min. However, after this time, the percentage of palladium in solution increased by 20% until the experiment was stopped. This phenomenon could be caused by partial re-dissolution of the Pd ions due to the strong acidity of the metal solution. This phenomenon was also observed by Argun *et al*. and Arrascue *et al*. who attributed it to instability of the adsorbent or weak interactions between the metal and the adsorbent, and the saturation of the material after which adsorption/desorption processes take place.[59, 274] In the present work the instability of the adsorbent was not plausible, as this effect was not observed during gold or platinum adsorption with S800 and further work is required to understand this phenomenon.

Regarding platinum, the rate of adsorption decreased significantly after 120 min, indicating proximity to the equilibrium.

To complete the mechanistic understanding developed throughout this chapter, kinetic data was fitted to different models that describe the reaction limiting step. A wide variety of kinetic models have been used in the literature to explain the adsorption of metals onto bio-adsorbents.[275] These kinetic models can be classified into: 1) adsorption reaction models and 2) diffusion models.[275]

2.2.4.6.1 Adsorption reaction models

Reaction models focuses on the 'reaction' between adsorbent and adsorbate, disregarding previous diffusion stages.[275] In turn, the order of an adsorption reaction can be described in terms of the concentration of metal in solution, or the material's adsorption capacity.[276] Most authors describe the order of adsorption in relation to the capacity of the material, using Langergren's or pseudo-first-order equation, pseudo-second-order-equation and Elovich model. This is also the approach that has been followed in the present work.[276] Nevertheless, some of the data was also fit using models based on the metal concentration in solution to corroborate the findings made by the abovementioned models (Figure A 1 and Figure A 2 of Appendix 1). The results from both methods were in good agreement.

- *Pseudo-first-order model.* This model assumes that the adsorption rate is proportional to the difference between the the adsorption capacity of the adsorbent and the adsorption capacity at a time 't'. It can be described by the following expression:[276]

$$\log(q_e - q_t) = -\frac{k_1}{2.303} \cdot t + \log q_e$$

Where q_e and q_t are the adsorption capacities (mg·g^{-1}) at equilibrium and at a time 't' (min) and K_1 is the pseudo-first-order rate constant (min^{-1}).

- *Pseudo-second-order model.* This model was first developed to describe the adsorption of divalent metals onto peat moss.[277] It assumes chemisorption involving exchange of electrons and can be expressed as follows:[278]

$$\frac{t}{q_t} = \frac{1}{k_2 \cdot q_e^2} + \frac{1}{q_e} \cdot t$$

Where k_2 is the pseudo-second-order rate constant (g·mg^{-1}·min^{-1})

The initial rate of adsorption, h (mg·g^{-1}·min^{-1}), can be calculated from q_e and K_2 using the following expression:

$$h = q_e^2 \cdot k_2$$

- *Elovich model*. This second-order model was initially used to described chemisorptive adsorption of gas onto solids. Nevertheless, it has been successfully applied to metal adsorption. It assumes that the rate of adsorption decreased exponentially with the amount of adsorbed material. It can be described as follows:[276]

$$q = \alpha \cdot \ln(a \cdot \alpha) + \alpha \cdot \ln(t)$$

Where α is the initial adsorption rate (mg·g^{-1}·min^{-1}) and a is the adsorption constant (g·mg^{-1}).

2.2.4.6.2 Diffusion models

These models presume that the process of adsorption includes three main steps: 1) film diffusion, in which the adsorbate moves through the liquid film wrapping the adsorbent particles; 2) Intraparticle diffusion, in which the adsorbate moves along the adsorbent surface towards the active sites; and 3) mass action, including the interactions between adsorbent and adsorbate.[275] As the step of mass action is disregarded in purely physisorptive processes, the two main diffusion models have been based on liquid film and intraparticle diffusion.[275]

- *Liquid film diffusion model*. This model assumes that the rate of adsorption is equal to the rate at which the adsorbate moves across the liquid film. It can be expressed with the following expression:[61]

$$\ln\left(1 - \frac{q_t}{q_e}\right) = -R' \cdot t$$

Where R' is the liquid film diffusion rate constant (min^{-1}).

- *Intraparticle diffusion* model (Weber-Morris equation). It assumes that the amount of adsorbate onto the solid surface is proportional to the square root of time, as it can be observed in the expression below:[275]

$$q_t = k_{int} \cdot t^{1/2} + C$$

123

where K^{int} ($mg \cdot g^{-1} \cdot min^{-1/2}$) represents the constant of intraparticle diffusion and C gives information about the layer thickness.

Experimental data for the adsorption of gold onto Starbon® was fit to the above-described models (Figure 2.26 and Figure 2.27) and constants of adsorption rate were calculated from the linear adjustment (Table 2.15).
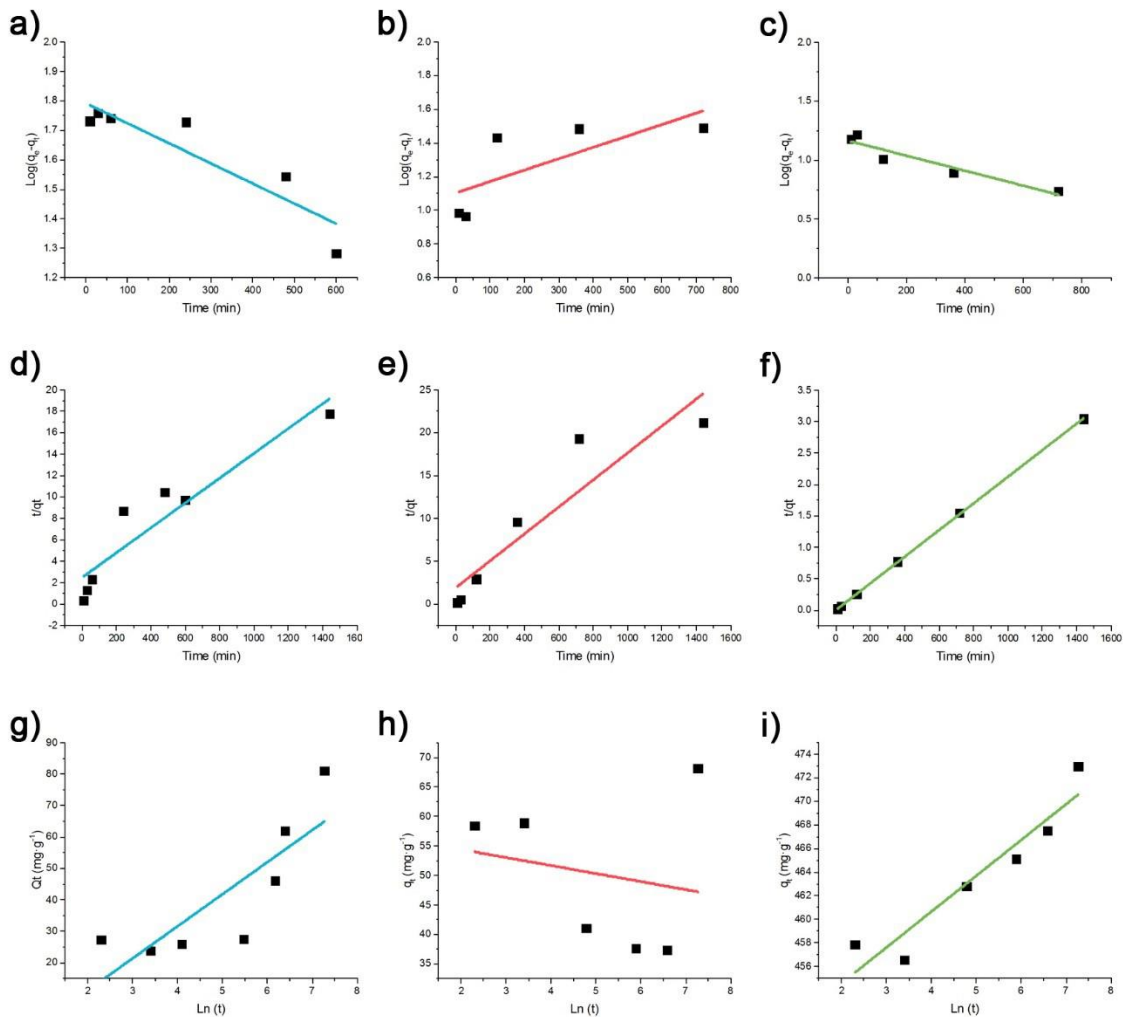
Figure 2.26 Pseudo-first order fitting graphs for a) S300, b) S450 and c) S800; pseudo-second order fitting graphs for d) S300, e) S450 and f) S800; Elovich fitting graphs for g) S300, h) S450 and i) S800 after gold adsorption.
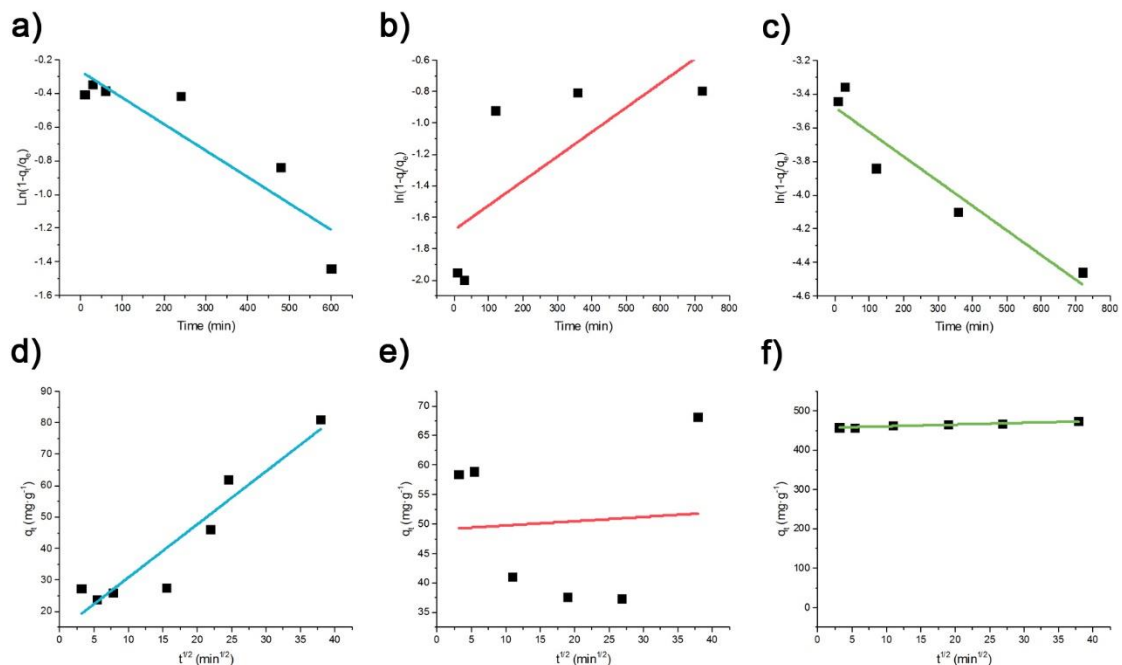
Figure 2.27 Film diffusion model fitting for a) S300, b) S450 and c) S800; Intraparticle diffusion model for d) S300, e) S450 and f) S800 after adsorption of gold.

The data of S300 fit best to the intraparticle diffusion model. The presence of an intercept that did not pass through the origin indicated that this model was not the only limiting step for the adsorption of gold onto S300.[279] The experimental data of S300 also fit well to the pseudo-second-order model. As this model is used to describe processes involving chemisorption,[278] these results were consistent with the redox mechanism suggested throughout this chapter.

Regarding S450, the data could only be fit successfully to the pseudo-second-order model, which is consistent with the redox mechanism of adsorption described earlier on this chapter. Nevertheless, the results should be taken successfully as the rate of removal of S450 displayed an unusual trend (Figure 2.25).

The experimental data of S800 fit very well (r^2=1) to the pseudo-second-order. This is in good agreement with the redox adsorption mechanism. However, adsorption occurred

so rapidly for S800 that more kinetic points within the initial 10 min would be required to fully understand the rate-limiting step.

Similar polysaccharide-derived carbonaceous materials described in the literature also displayed rapid adsorption of Au.[84, 87] Wang *et al.*, who describe polysaccharide derived spherules for gold adsorption, also observed good fitting with the pseudo-second order model.[87]

Table 2.15 Kinetic parameters after gold adsorption. Fittings with r^2 values < 0.7 have not been included in the Table.

	S300	S450	S800
Pseudo-first order			
Q_e (mg·g^{-1})	61.7	-	14.5
K_1 (min^{-1})	1.6×10^{-3}	-	1.5×10^{-3}
r^2	0.7911	-	0.8757
Pseudo-second-order			
Q_e (mg·g^{-1})	86.4	63.6	452.2
K_2 (g·mg^{-1}·min^{-1})	5.9×10^{-5}	1.3×10^{-4}	$7. \times 10^{-4}$
h (mg·g^{-1}·min^{-1})	0.44	0.53	159.5
r^2	0.8596	0.8296	1
Elovich model			
α (mg·g^{-1}·min^{-1})	-	-	3.0
a (g·mg^{-1})	-	-	131.9
r^2	-	-	0.8727
Liquid-film diffusion model			
R' (min^{-1})	1.6×10^{-3}	-	1.5×10^{-3}
r^2	0.7911	-	0.8756
Intraparticle-diffusion model			
K_{int} (mg·g^{-1}·min$^{-1/2}$)	0.53	-	1.68
r^2	0.8789	-	0.8783

Regarding adsorption of Pd with S800, it was only possible to fit the data to pseudo-second-order and intraparticle diffusion (Figure 2.28, Figure 2.29 and Table 2.16). This could be due to the unusual trend of removal rate observed on Figure 2.25. Q_e values

obtained from the pseudo-second order were very similar to the experimental results, showing the validity of the model. The intraparticle diffusion model displayed two linear sections, which can be attributed to the different pore sizes present in Starbon®; thus, the first linear section was attributed to diffusion into larger pores while the second segment was related to smaller pores.

Platinum adsorption data fit well to all reaction models described in Section 2.2.4.6.1 and Section 2.2.4.6.2 (Figure 2.28 Pseudo-first order fitting graphs for S800 after adsorption of a) Pd and b) Pt; pseudo-second order fitting graphs for S800 after adsorption of c) Pd and d) Pt; Elovich fitting graphs for S800 after adsorption of e) Pd and f) Pt. Figure 2.28, Figure 2.29 and Table 2.16). However, best r^2 values were obtained for pseudo-second-order. Comparing the 'h' values calculated from the pseudo-second-order model, it was possible to observe that the initial rate of adsorption was significantly slower than Au. This is in good agreement with the results displayed in Figure 2.25 where it was shown that S800 reached equilibrium after only 10 min into the experiment in the case of gold.

The intraparticle diffusion method showed a one stage linear fitting with intercept ≠ 0, indicating that intraparticle diffusion was not the only rate-limiting step, which could suggest a combination of chemisorption and intraparticle diffusion as rate-limiting steps.

Similar polysaccharide-derived materials described in the literature for the adsorption of Pd and Pt also showed best fittings for the pseudo-second order model.[61, 62] Regarding diffusion models, Fujiwara *et al.* observed best fittings with liquid film diffusion, opposite to the observations in the present work.[61] This suggested that the type of diffusion and therefore the limiting step for the adsorption depend on the structure of the material and the adsorption mechanism taking place. The rate of adsorption constants calculated from pseudo-second-order and the intraparticle-diffusion method were comparable to those shown by similar studies in the literature for all three Starbon®.[61, 62]

Figure 2.28 Pseudo-first order fitting graphs for S800 after adsorption of a) Pd and b) Pt; pseudo-second order fitting graphs for S800 after adsorption of c) Pd and d) Pt; Elovich fitting graphs for S800 after adsorption of e) Pd and f) Pt.

128
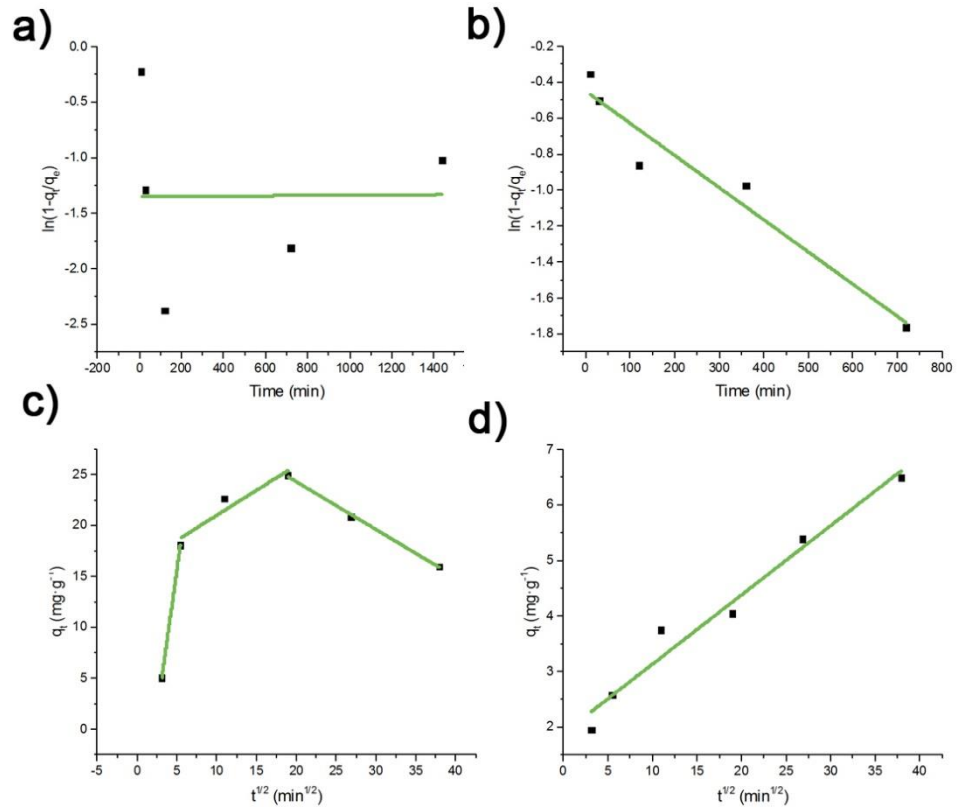
Figure 2.29 Film diffusion model fitting for S800 after adsorption of a) Pd and b) Pt; Intra-particle diffusion model fitting for S800 after adsorption of c) Pd and d) Pt.

Table 2.16 Kinetic parameters after adsorption of Pd and Pt. Fittings with r^2 below 0.7 are not displayed.

	S800-Pd	S800-Pt
Pseudo-first order		
Q_e (mg·g^{-1})	-	4.1
K_1 (min^{-1})	-	1.8×10^{-2}
r^2	-	0.9264
Pseudo-second-order		
Q_e (mg·g^{-1})	16.3	6.5
K_2 (g·mg^{-1}·min^{-1})	-1.4×10^{-3}	1.6×10^{-3}
h (mg·g^{-1}·min^{-1})	-0.37	0.07
r^2	0.9754	0.9723
Elovich model		
α (mg·g^{-1}·min^{-1})	-	0.9
a (g·mg^{-1})	-	0.8
r^2	-	0.9242
Liquid-film diffusion model		
R' (min^{-1})	-	1.8×10^{-3}
r^2	-	0.9264
Intraparticle-diffusion model		
K_{int} (mg·g^{-1}·min$^{-1/2}$)	5.6; 0.5; -0.5	0.12
r^2	1; 0.8326; 0.9953	0.9614

In summary, kinetic data generally fit well to pseudo-second-order and intraparticle diffusion models suggesting a combination of chemisorption and diffusion of the adsorbate along the material's surface as rate-limiting steps. Nevertheless, further work is required to corroborate these results, as it was only possible to carry out one repetition of the experiments due to the cost of metals and analytical techniques.

2.3 Conclusion

A method for the preparation of Starbon® monoliths has been developed. The monolithic shape could be potentially advantageous, and particularly for adsorption, as the packing of a column can be avoided. Although the general properties were similar to those of

powdered Starbon®, interesting differences in porosity (i.e. total pore volume and PSD) caused by the modifications in the preparation methods, were noted. Materials with very different surface chemistry and textural properties were obtained by varying the preparation temperature; low temperatures yielded materials with relatively high oxygen content, rich in oxygen functionalities and with a low fraction of microporosity. In contrast, carbonisation at high temperatures offered highly microporous materials with low oxygen content in which aromatic groups were more abundant.

The materials were used to adsorb precious metals from acidic environments, where platinum, palladium and gold were adsorbed to different extents. Starbon® S800 showed particularly good adsorption of gold. The mechanism of adsorption involved in this process included reduction of the Au^{3+} to its metallic form with the subsequent formation of gold NPs, and the oxidation of the carbonyl groups in Starbon®. The formation of gold NPs is very relevant as they find uses in many applications including catalysis and medical applications. The adsorption of gold, which led to monolayer coverage, was very rapid as equilibrium was reached after only 10 min of reaction. Palladium and platinum were mostly electrostatically adsorbed, with a small fraction being reduced to its metallic form. The adsorption process in this case was slower and led to multilayer coverage of Starbon® in the case of palladium and monolayer for platinum. For all three metals, a combination of chemisorption and intraparticle diffusion of the adsorbate along the material's surface were considered the rate-limiting steps.

Starbon®, and in particular S800, showed very good potential to be used for the recovery of precious metals from aqueous waste streams. Metal recovery from secondary sources is a hot topic nowadays due to the increasing demand of PMs for applications such as electronics, which is putting high pressure on the metal ores and leading to price rises. Further work to prove this potential would need to elucidate the selectivity of Starbon® towards precious metals when the solution contains a mixture of elements, as it occurs in real waste solutions. This is discussed in Chapter 3. It would also be interesting to look at the application of the metal-loaded Starbon® materials as catalyst in relevant organic

reactions. Alternatively, desorption of metals and reusability of Starbon® for further adsorption processes needs to be studied in order to determine the lifetime of these materials when used for metal adsorption.

Towards real life applications of Starbon®

Chapter 3

3 Towards real life applications of Starbon®

3.1   Aims of the work

The work described in this chapter aims to apply the knowledge about precious metal adsorption by Starbon® discussed in Chapter 2 to more 'realistic' cases, including:

- Recovery from synthetic solutions containing a mixture of metals
- Recovery from a complex 'real waste' solution obtained from electronic scrap.
- Recovery from a single metal solution using a continuous system.

The experiments described above provided useful information about the potential applicability of Starbon® in real-life scenarios.

3.2   Introduction

In order to reduce pressure on metal ores, secondary sources of PMs have been investigated among which WEEE stands out due to the increasing amounts of such waste.[36, 42] Several techniques can be used to retrieve precious metals from WEEE, with the leaching by strong acids and subsequent adsorption by bio-derived materials the focus of much research nowadays.[43, 113] Although a significant effort has been made towards the identification of potential polysaccharide-derived adsorbents for PMs, very few studies have explored the selective adsorption of a specific metal from a mixture.[45, 66, 71] Selectivity during adsorption is important because the treatment of WEEE with strong acids brings many metals into solution besides PMs.[280] Similarly, many studies suggest potential bio-adsorbents for WEEE treatment, but only a few carried out experiments with 'real' waste solutions to determine the actual applicability of these materials.[50, 120] Flow adsorption is another key factor that needs to be accounted for when

assessing applicability since industrial scale processes are generally carried out in continuous regimes. A limited number of studies regarding the flow adsorption of PMs have been reported.[60, 76, 281]

Recovering the metals from the bio-adsorbent once the adsorption has been completed is almost as important as the adsorption process itself. The utilisation of the metal-loaded bio-adsorbents as catalysts has been recently suggested.[122, 123, 282, 283] Supported metals are required to catalyse numerous reactions and several methods have been developed to support PM NPs onto carbon supports.[8, 284] Therefore, the in-situ utilization of metal-loaded bio-adsorbents could be doubly advantageous by saving energy and minimising waste generation that occur during both the retrieval of metals from the bio-adsorbent and the supported-catalyst production.

The selectivity and applicability of Starbon® have been assessed in the present chapter by performing adsorption experiments with synthetic and real E-waste solutions. Starbon® monoliths were used to assess the potential applicability of these new materials in the adsorption of precious metals in flow regime.

3.3 Results and discussion

3.3.1 Selectivity of Starbon® towards precious metals

Starbon® were added to an acidic solution (pH 3) containing a mixture of base and precious metals in order to understand the selectivity of these materials towards PMs. Cu, Ni, Zn, Pd, Pt and Au were selected as the group of elements for recovery based on two key factors: 1) these elements make up the metal composition of mine tailing samples from North American Palladium, Lac des Iles mine in Ontario Canada and 2) these elements are extensively utilized in consumer electronics, and thus end up in significant concentrations in WEEE.[6, 31, 285] Based on findings of the Phytocat project, a model solution of Cu^{2+}, Ni^{2+}, Zn^{2+}, Pd^{2+}, Pt^{2+} and Au^{3+} with an approximate concentration was 100 mg·L^{-1} created (Table 3.1).[285] The concentration of Pt^{2+} was significantly lower due to the

poor solubility of the Pt^{2+} salt at the working pH. This led to lower concentrations of Pt^{2+} and in the model solution, which is also in good correlation with the concentrations of these elements in the mine tailings.[285] Starbon® S300, S450 and S800 were added to this solution and results can be found in Figure 3.1.

Table 3.1 Initial concentration of the metals contained in the solution. The values are expressed in both mass and molar concentration units.

Metal	Initial concentration	
	$mg \cdot L^{-1}$	$mmol \cdot L^{-1}$
Nickel	105.0	1.79
Copper	105.0	1.65
Zinc	105.0	1.61
Palladium	115.0	1.08
Platinum	10	0.05
Gold	132	0.67
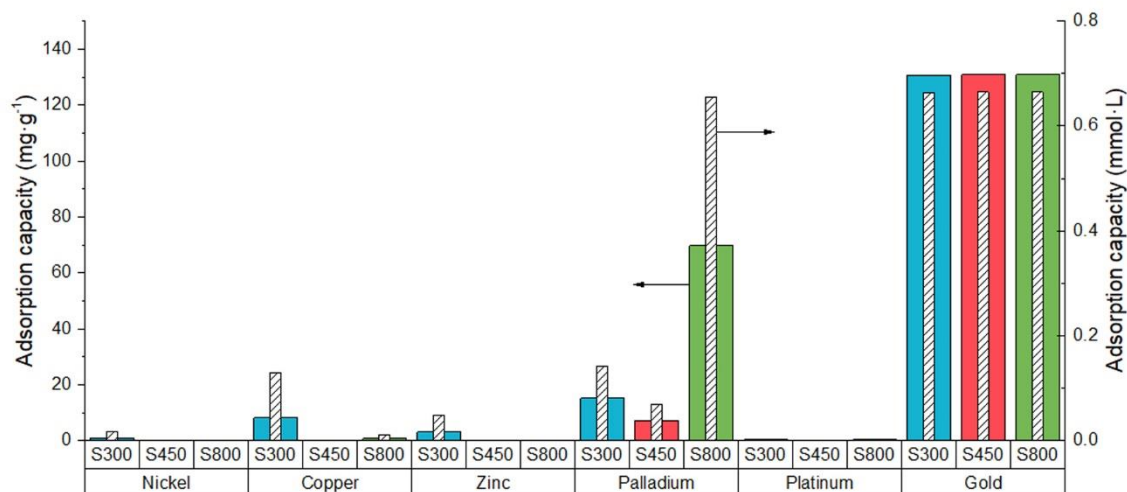
Figure 3.1 Comparison of the mass adsorption capacities ($mg \cdot g^{-1}$) for a range of metals of S300 (blue), S450 (red) and S800 (green). The molar adsorption capacities ($mmol \cdot L^{-1}$) are shown by the black dashed columns. The experimental conditions were constant stirring for 24 h at room temperature and pH 3.

Gold was completely removed from solution by all three Starbon®. On the other hand, none of the base metals were significantly adsorbed (<10%). Palladium and platinum were

partially removed from solution. However, the low concentration of platinum in the initial solution made it difficult to appreciate this in Figure 3.1. Although the molar concentrations shown in Table 3.1 were not the exactly the same for all metals due to the molar weight of each element, the concentration of base metals was higher and therefore the results showed that the adsorption of PMs by Starbon® was selective and preferential. These results were in good agreement with other studies performed in the literature. For example, Pangeni *et al*. tested crosslinked cellulose aerogels for the adsorption metals from a complex solution.[71] They observed that gold was selectively adsorbed whereas base metals were left in solution, and only traces of palladium were aadsorbed at pH 1.[71] Pangeni *et al.* attributed the selective adsorption of gold to the adsorption-reduction mechanism involved, which is consistent with the findings of Chapter 2.[71] Chassary *et al*. used chitosan derivates to adsorb Pd and Pt from solutions containing both metals and observed higher selectivity towards Pd, in agreement with the results of the present work.[66]

Considering the maximum adsorption capacities obtained in Chapter 2 and the results displayed in Figure 3.1, S450 was the most selective material towards a single element, as it removed the gold, leaving all the other metals in solution. Only traces (<10%) of palladium were also adsorbed, whereas S300 and S800 adsorbed larger concentrations of this metal. S800 presented the best selectivity towards PMs as a group, taking up all the gold, 70% of palladium and >50% of platinum, but none of the base metals. S300 did not display as good adsorption capacity for palladium as the other two Starbon® and it also adsorbed small amounts of Ni^{2+}, Cu^{2+} and Zn^{2+}.

TEM analysis was undertaken to understand whether the presence of other metals in solution affected the mechanism of adsorption and therefore the formation of NPs discussed in Chapter 2. The TEM images displayed throughout this chapter were taken in collaboration with Ms Meg Stark at the Technology Facility in the Department of Biology of the University of York, UK. Interestingly, the NPs observed were not homogeneously distributed but gathered in specific regions forming circular aggregates. These aggregates

had a similar size to the large particles observed in Chapter 2, which suggested that the present aggregations were incomplete nanoshells. A plausible reason for the presence of unfinished nanoshells was the lower concentration of gold in solution, compared to the experiments in Chapter 2.[249] The size of the individual NPs was 30 nm, similar to those seen in the literature.[248] Therefore, the presence of other ions in solution did not affect the formation of NPs. However, the gold concentration of the initial solution seemed to be an important factor in the formation of NPs.
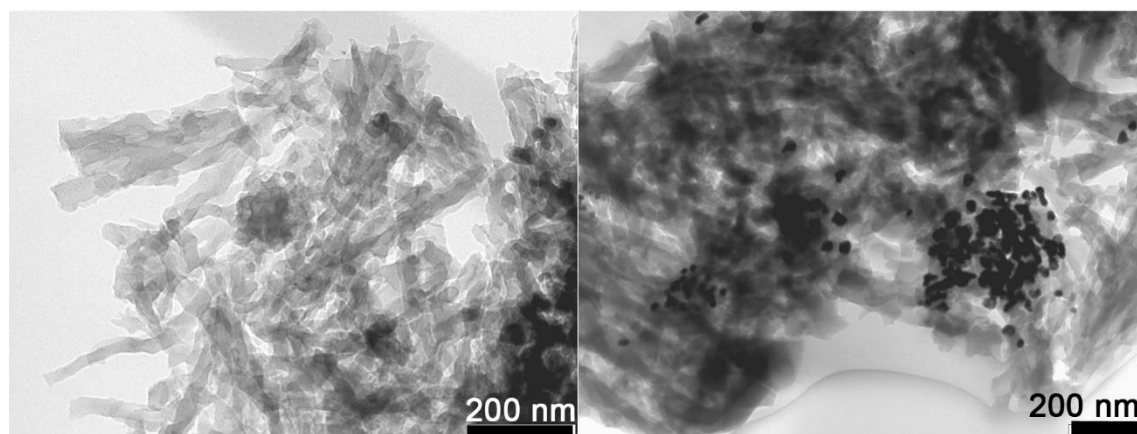
Figure 3.2 TEM of S800 a) before and b) after adsorption from a mixture metal solution containing Ni^{2+}, Cu^{2+}, Zn^{2+}, Pd^{2+}, Pt^{2+} and Au^{3+} after 24 h of constant stirring at room temperature and pH 3.

Further studies were conducted in which the mass concentration of precious metals in solution was lowered 100 times in relation to the base metals, to better represent certain types of metal waste (i.e. E-waste).[113] Results showed that S800 removed >90% of PMs, leaving the other metals in solution despite this vast difference in concentration (Figure 3.3). Small amounts of copper were adsorbed onto the Starbon® surface (10%). Although the copper adsorbed represented only a small fraction of the total mass of copper in solution, the amount of copper in Starbon® exceeded that of PMs. Therefore, even though preferential adsorption of PMs was independent of the initial concentration, selective adsorption was best achieved when the initial concentration of PMs was similar to that of the other metals in solution.
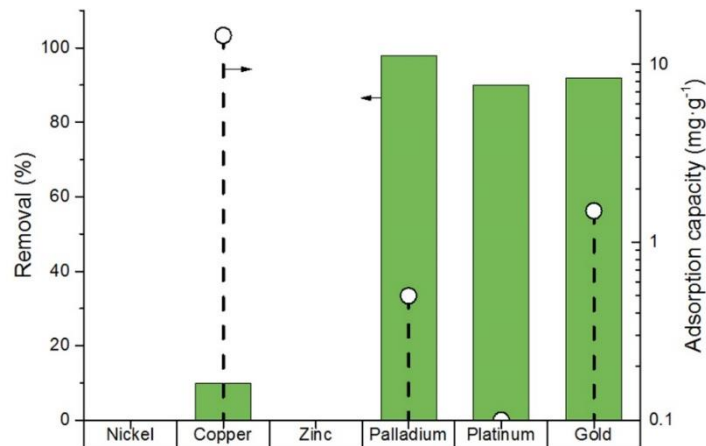
Figure 3.3 Amount of metals recovered by S800 expressed in percentage (bars) and in mg·g^{-1} (dashed lines) after 24 h of constant stirring at room temperature and pH 3.

3.3.2 Case study: using Starbon® to recover precious metals from 'real' waste

Taym Ltd, an industrial collaborator specialising in treating a wide variety of wastes, provided two complex metal solutions after hydrometallurgical treatment of E-waste.[286] S300 and S800 were used as adsorbents to recover valuable metals from these solutions, in order to study the applicability of Starbon® in the treatment of real waste.

Before the adsorption experiments, the metal solutions were characterised by ICP-MS and results showed that most metals were present as traces (<10 ppm) with the exception of cobalt, iron, copper, tin, nickel and gold (Table 3.2).

Table 3.2 Composition and concentration (mg·L^{-1}) of the E-waste solutions supplied by Tyam Ltd, obtained from ICP-MS analysis.

Metals	Concentration (mg·L^{-1})	
	Solution 1	Solution 2
Cr, Mn, Zn, Mo, Ag, Pd	< 1	< 1
Na, Pb, Ti	1 – 10	1 - 10
Co	12	19
Fe	41	58
Cu	56	63
Sn	60	80
Ni	142	102
Au	199	116

Regarding the metals present in large concentrations (>10 ppm), only gold and tin were significantly adsorbed (Figure 3.4); 100% of Au was adsorbed by S800 reaching an adsorption capacity of 214 mg of gold per g of Starbon®. The complete removal of gold from solution indicated that S800 was not saturated and could uptake more gold. This was in good agreement with the results shown in Chapter 2 which shown an adsorption capacity of ~600 mg·g^{-1}. S300 only adsorbed 54% of the available gold, which equated to 119 mg·g^{-1} and indicated proximity to the saturation point, which agreed well with the maximum adsorption capacity calculated in Chapter 2 (180 mg·g^{-1}). S300 and S800 adsorbed 2 and 12% of the Sn respectively, which translated into adsorption capacities of 1.5 and 8.5 mg·g^{-1}. Wasewar *et al.* studied the adsorption of tin onto granulated activated carbon and obtained significantly higher adsorption capacities (85-120 mg·g^{-1}).[287] Interestingly, they observed a strong relation between the initial concentration of tin in solution and the amount of tin adsorbed. Considering that the initial concentration of tin in the study of Wasewar *et al.* was 6-8 times higher than in the present work, the adsorption capacities displayed by Starbon® materials agreed well with those in the literature.[287] The partial adsorption of Sn by Starbon® can be attributed to the main tin species in solution, $SnCl_6^{2-}$.[288] As seen in Chapter 2 for gold, the negatively charged ions were attracted to the positively charged surface of Starbon® at low pH. Nevertheless,

further work is needed to elucidate the adsorption mechanism of Sn by Starbon®. However, this was out of the scope of the present work.

Mo and Pb, which were found in trace concentrations in the metal solutions, were also partially adsorbed by Starbon®. Both S300 and S800 recovered 9% of Pb, and 25 and 49% of Mo respectively. However, the concentration of these metals in solution was very low (<10 ppm) and therefore no significant amounts of Pb and Mo can be found in the surface of Starbon® (<1 mg·g^{-1}). As shown by the literature, ACs presented high adsorption capacities for these two metals. Nevertheless, the selectivity of Starbon® towards gold observed in the present study was considered more beneficial for the recovery process than high adsorption capacity for several elements. Interestingly, Pagnanelli *et al.*, who studied the adsorption of molybdenum by AC, suggested a mechanism of adsorption in which Mo was reduced and the carbon surface oxidised.[289] This could be a plausible mechanism for the adsorption of molybdenum onto Starbon®, however, it was outside of the scope of the present project to carry out the necessary further work.

The results discussed above and displayed in Figure 3.4 refer to solution 1. Reproducible trends were obtained for the other solution provided by Taym (solution 2).
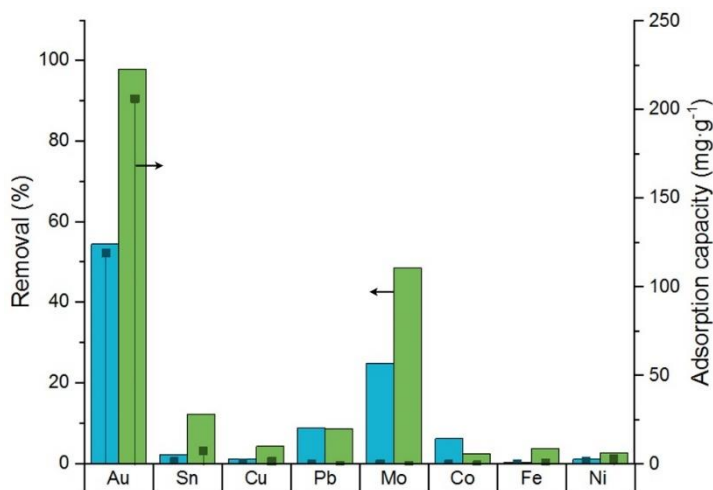
Figure 3.4 Amount of metals removed from solution 1 by S300 (blue) and S800 (green) expressed as percentage (bars) and as adsorption capacity (mg·g^{-1}) (lines) after 24 h of constant stirring at room temperature.

As discussed in Chapter 2, gold was adsorbed onto the Starbon® surface through a reduction mechanism in which Au NPs were formed. TEM analysis was performed to study whether the presence of a broad range of other elements in solution may have an influence on the adsorption mechanism. NPs could be clearly observed on the surface of S800. Interestingly, these NPs were radically different to those observed in Chapter 2 and the synthetic metal mixture experiments. These NPs were homogeneously distributed and presented relatively small size, with diameters below 10 nm (Figure 3.5), indicating no aggregation and therefore no formation of gold nanoshells. A plausible explanation for this phenomenon could be the presence of capping agents in the metal solution, which limit the aggregation of Au NPs.[290] Capping agents are generally organic molecules such as long chain hydrocarbons, polycarboxylic acids or cationic surfactants.[290] Nevertheless, Nag *et al*. showed that inorganic elements, such as SH^-, OH^-, S^{2-}, could also act as capping agents in the preparation of nanocrystals due to the formation of an electrical double layer around each nanocrystal.[291] As Taym did not fully disclose their preparation method of the solutions in order to protect IP, it is possible that such solutions contain sulfur compounds that can act as capping agents. On the other hand, it was not possible to observe NPs on S300.
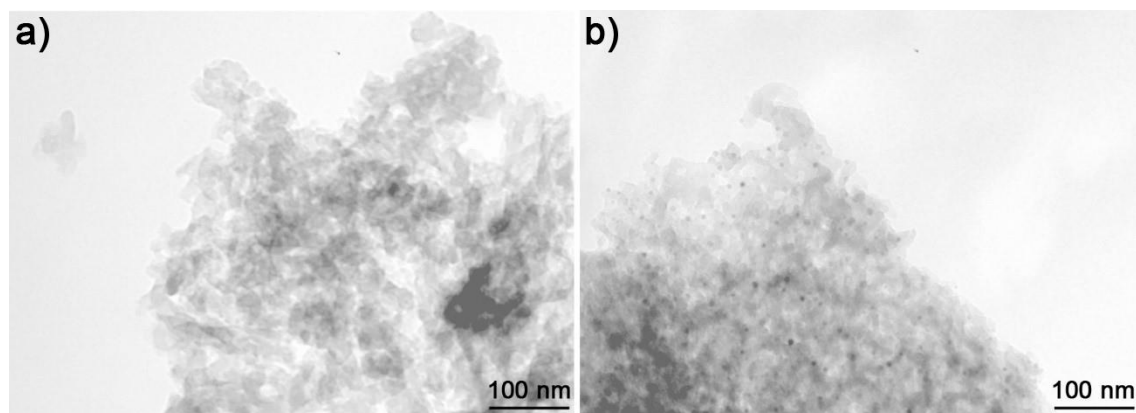
Figure 3.5 TEM images of S800 a) before and b) after treatment of E-waste solutions.

XPS analysis was carried out to investigate the lack of NPs in S300. The XPS analysis was carried by the team of the National EPSRC XPS Users' Service facility at Newcastle

University (UK). The elemental analysis showed that S300 C/O ratio was lower (3.6 vs 4.3) following adsorption, which indicated a certain degree of oxidation of the Starbon® surface. In turn, the XPS signal for gold was small, suggesting that only very little amount of gold could be detected on the surface of Starbon®. The slight decrease in the C/O ratio could be caused by the reduction of the traces of gold detected in solution. Unfortunately, it was not possible to deconvolute the Au4f peaks due to the low signal observed. Therefore, further work is needed to understand the differences observed between ICP, TEM and XPS.

On the other hand, the deconvolution of the Au4f peaks of S800 showed that 83% of the gold recovered was reduced to its metallic form (Figure 3.6). In addition, the carbon surface was oxidised (the C/O ratio decreased from 19.8 to 10.2) producing more carboxylic groups, which was consistent with the results observed in Chapter 2. XPS also displayed a doublet of peaks at 487.5 and 496 eV (Figure 3.6). These binding energies and distance between peaks were characteristic of tin compounds.[250] The position of the peaks, towards higher binding energies compared to metallic Sn, may be associated to the presence of SnX_6^{2-} where X is a halogen species.[250] This was in good agreement with the main tin species found in solution at acidic pH as shown above,[288] and would indicate that tin was electrostatically adsorbed to the surface of S800. Nevertheless, further work is needed to unambiguously determine the adsorption mechanism of tin onto Starbon® materials.
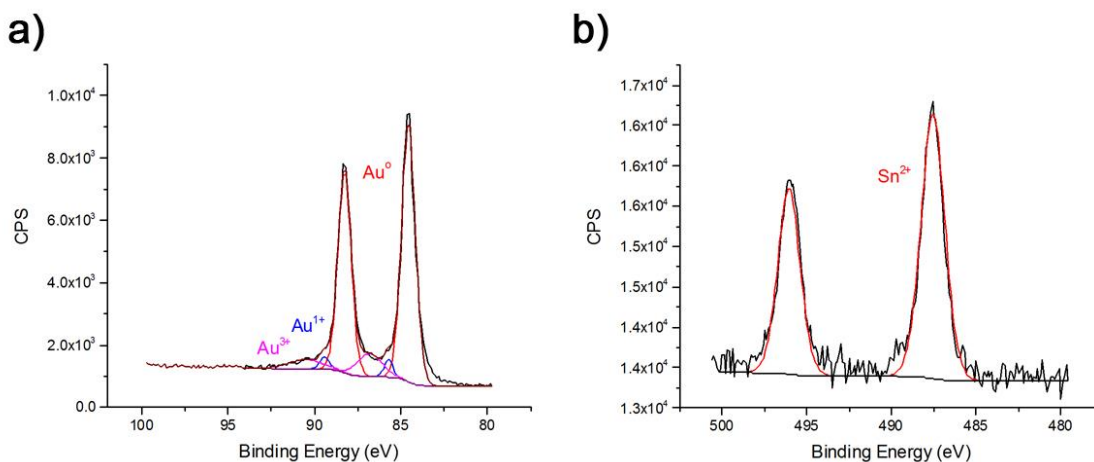
Figure 3.6 Deconvolution of Au4f (a) and Sn3d (b) XPS spectra of S800 after adsorption from an E-waste solution provided by Taym Ltd. The adsorption experimental conditions were constant stirring for 24 h, at room temperature and pH 0.

3.3.3 Adsorption in flow

The aim of the flow experiments was to perform a proof of concept experiment to demonstrate the feasibility of applying Starbon® monoliths to continuous processing. In accordance to this, a single metal solution (only containing gold) was passed through a column of Starbon® (S800). Optimisation of the process was out the scope of this thesis and main steps towards an optimal process are discussed in the future work section in Chapter 7.

3.3.3.1 Description of the set up

An S800 monolith was fixed inside a Swagelok tubing with the aid of an epoxy resin to obtain a monolith reactor which could be used to carry out flow adsorption experiments (Figure 3.7). The monolith reactor was manufactured in collaboration with Chris Mortimer, Stuart Murray and Mark Roper from the Chemistry mechanical workshops of the University of York.

144
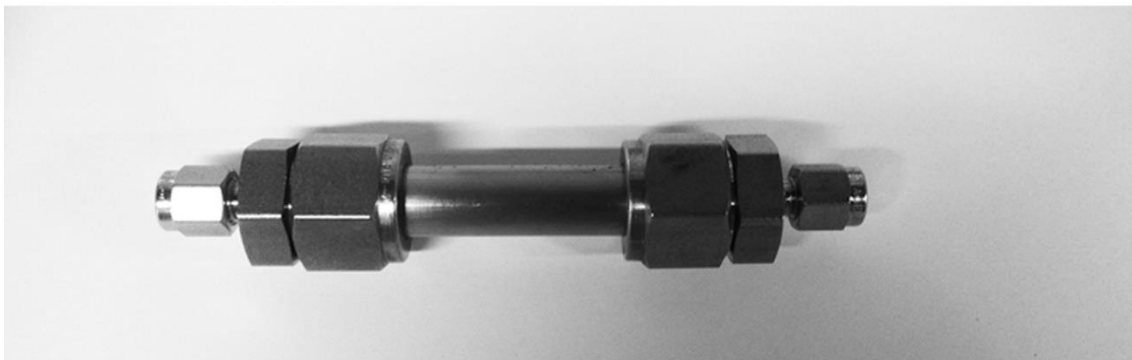
Figure 3.7 Monolith reactor containing an S800 Starbon® monolith fixed to the walls of Swagelok tubing with the aid of epoxy resin.

The monolith reactor was attached to an HPLC pump able to transport the gold solution from the initial reservoir, through the monolith reactor, to the end point where the purified solution was collected (Figure 3.8).
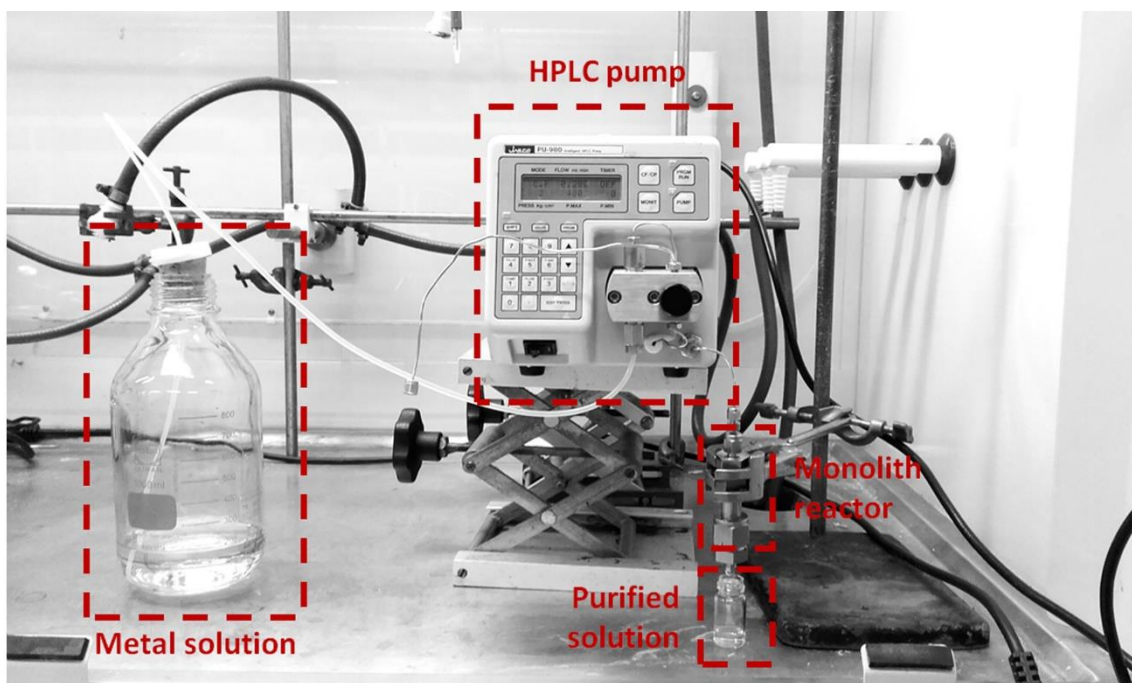
Figure 3.8 Laboratory set up for the continuous flow adsorption experiments to recover gold with an S800 monolith.

In order to reach the breakthrough point in a reasonable timeframe (~95 h), the initial concentration of the metal solution (100 mg·L^{-1}) and the flow rate (0.2 mL·min^{-1}) were

increased compared to that described in other studies in the literature.[76] The calculations to estimate the breakthrough point are shown in Figure 3.9. Note that the data obtained experimentally did not allow the calculation of the residence time.

• **Gold adsorption capacity of S800*** = 600 mg·L^{-1}	600 mg·L^{-1} x 0.19 g = <u>120 mg</u> required to 'saturate' the monolith
• **Mass of the monolith** = 0.2 g	114 mg / 100 mg·L^{-1} = <u>1.14 L</u> of initial solution required to reach breakthrough
• **Concentration of initial gold solution** = 100 mg·L^{-1}	1.14 L / 0.2 mL·min^{-1} = <u>5700 min</u> required to reach breakthrough
• **Flow rate of solution through the system** = 0.2 mL·min^{-1}	5700 min / 60 min·h^{-1} = <u>95 h</u> required to reach breakthrough
*Calculated in Chapter 2	

Figure 3.9 Calculations to predict the breakthrough time of the flow adsorption experiments.

The pH of the solution was adjusted to 3 in order to ensure gold solubilisation and prevent corrosion of the HPLC pump.

3.3.3.2 Results

Having passed through the monolith reactor, the solution was collected at different time intervals, enabling the observation of changes in the collected solution over time. The variations in colour of the output solution were noteworthy:

- The initial solution presented a light-yellow shade before entering the system, which was caused by the $AuCl_3$.

146

- This solution turned completely clear after getting in contact with the monolith for the first few minutes. However, the solution collected after 30 min displayed a pink shade and this colouration became more apparent during the coming hours (up to 3 h).

- Such colour vanished after 6h.

- The pink colour reappeared in the samples collected after 11 h. The pink colour intensified at increasing times, and a closer look also showed a yellowish shade after 24 h (Figure 3.10).

Figure 3.10 Colour change of the output solution at different time intervals after passing a gold solution of pH 3 through the monolith reactor.

Each of these colour changes gave indications of the processes occurring inside the monolith reactor during adsorption and are discussed below in detail.

Pink colour of the output solution from 30 min to 6 h

Pink colour in relation to gold solutions has been commonly associated with the presence of Au NPs. In order to confirm the presence of NPs, the solutions were analysed by TEM, as discussed in detailed later in this section (Figure 3.11). However, Au NPs were not expected in solution at any stage of the experiment, as the batch test showed that the nanoparticles stayed 'attached' to the surface of Starbon®.

The presence of Au NPs in the output solution between 30 min and 6 h could be explained by the existence of some unattached molecules inside the Starbon® structure, which led

to the formation of NPs. During carbonisation, starch undergoes a series of chemical transformations, as explained in Chapter 2. As part of these transformations, a variety of molecules were generated in the form of gases, liquid tar and solid char (Starbon®).[206] These liquid tar molecules may be trapped in the porous structure and remain there after carbonisation unless the material is thoroughly washed. When the monolith reactor was connected to the flow system and the gold solution was passed through, these molecules were able to reduce some of the gold ions and both the organic molecules and the corresponding gold nanoparticles were 'washed out' of the monolith by the flowing solution. Once all these molecules were flushed out after 6 h, the solution did not contain neither organic matter nor NPs as seen in the TEM images displayed in Figure 3.11 and in the total organic content (TOC) results presented in Table 3.3. TEM showed other compounds besides Au NPs in the 1-3 h sample which could be the 'flushed' organic particles mentioned above (Figure 3.11). On the other hand, no NPs could be observed in the interval of 8 to 11 h, when the solution was colourless (Figure 3.11).
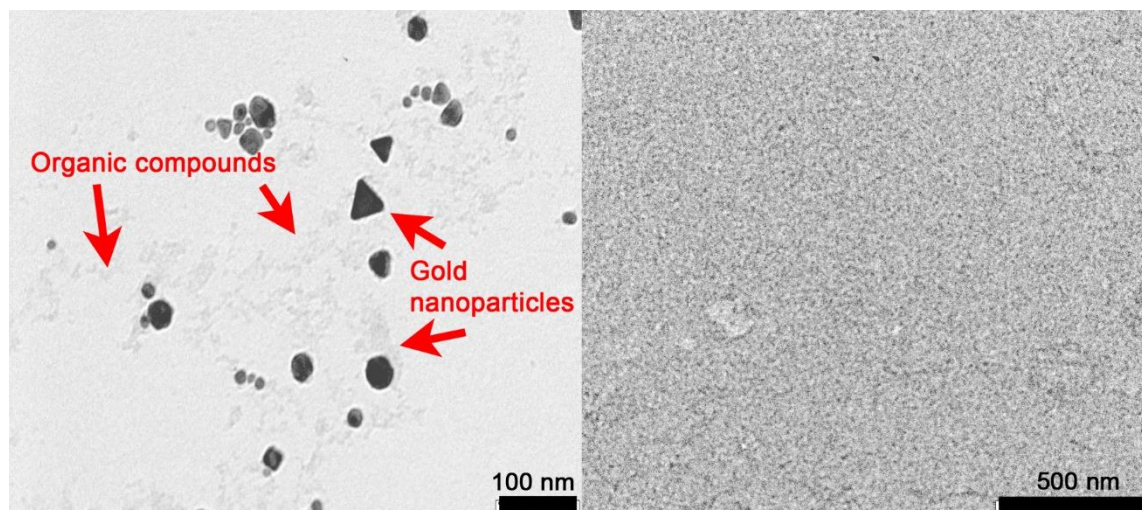
Figure 3.11 TEM of the output solution collected from the interval a) 1-3 h and b) 6-8 h after passing a gold solution of pH 3 through the monolith reactor.

In addition, TOC analysis was performed in order to corroborate the presence of organic molecules in solution. TOC was carried out in collaboration with Dr. Javier Remón Nuñez. Table 3.3 displays the results from the TOC analysis. The deionized water used as a blank

displayed a TOC value of 6.9 mg·L^{-1} and such value was used as detection limit and subtracted from the results obtained for the other samples. The negative values are very close to 0 and it can be considered that the concentration of organic components, if any, was too low to be detected.

The results showed that the fraction collected between 1 and 3 h, which displayed a characteristic pink colour and therefore contained Au NPs, also contained 12.3 mg·L^{-1} of organic matter. On the other hand, the colourless sample taken between 6 and 8 h only showed traces of organic matter (1 mg·L^{-1}).

Table 3.3 Total organic content analysis of fractions collected after the continuous flow experiments at different time intervals.

Time interval	Washing time of the monolith	Total organic content (mg·L^{-1})
1 to 3h	2h H$_2$0 + 2 h acid	12.3
1 to 3h	12h H$_2$0 + 12 h acid	-0.3
HCl (pH 3) wash	12h H$_2$0 + 12 h acid	-0.4
Deionised H$_2$O wash	12h H$_2$0 + 12 h acid	-0.2
6 to 8h	2h H$_2$0 + 2 h acid	1.0
34 to 48h	2h H$_2$0 + 2 h acid	6.5

The presence of unattached organic molecules inside the column was undesirable, as part of the gold in solution was 'lost' in the output solution rather than kept supported in the monolithic surface. In order to overcome this problem, the process was repeated using a new monolith reactor which was washed for 24 h prior the experiment, by passing ~150 mL of deionised water for 12 h followed by ~150 mL of an HCl solution (pH=3) for another 12 h.

The results of this second experiment showed a completely transparent solution during the first 6 h hours of the experiment, suggesting that the unattached organic molecules had been flushed out during the washing. TOC analysis did not detect organic matter in

the end-point water and acid washing solutions (Table 3.3). This was not conclusive to state that there was no organic matter in those solutions, as it could be due to low concentration of the organic compounds in solution, below the TOC detection limit of the machine. This was plausible, as all the 150 mL of washing solution were collected in the same vessel (no interval collection).

Colourless solution between 6 h and 11 h

The colourless solution observed between 6 and 11 h shown in Figure 3.10 suggested that the ions in solution were being reduced and deposited onto the Starbon® surface.

The experiment was monitored by ultraviolet-visible spectroscopy (UV-vis). A UV-vis spectrum was recorded for every fraction of solution collected. Two main peaks were observed at 299.8 and 545.8 nm. The peak at 299.8 nm corresponded to gold ions Au^{3+} in solution, whereas the peak at 544.7 nm was characteristic of Au NPs.[292, 293] No Au^{3+} nor Au NPs were detected between the 8-11 h in the output solution (Figure 3.12). The lack of these species in the output solution indicated that neither the monolith nor the interface with the epoxy were significantly damaged, thus letting the gold solution through (the possible damage of interfaces is discussed below in this section). The absence of NPs and organic matter was confirmed by TEM and TOC as shown in Figure 3.11 and Table 3.3 respectively.
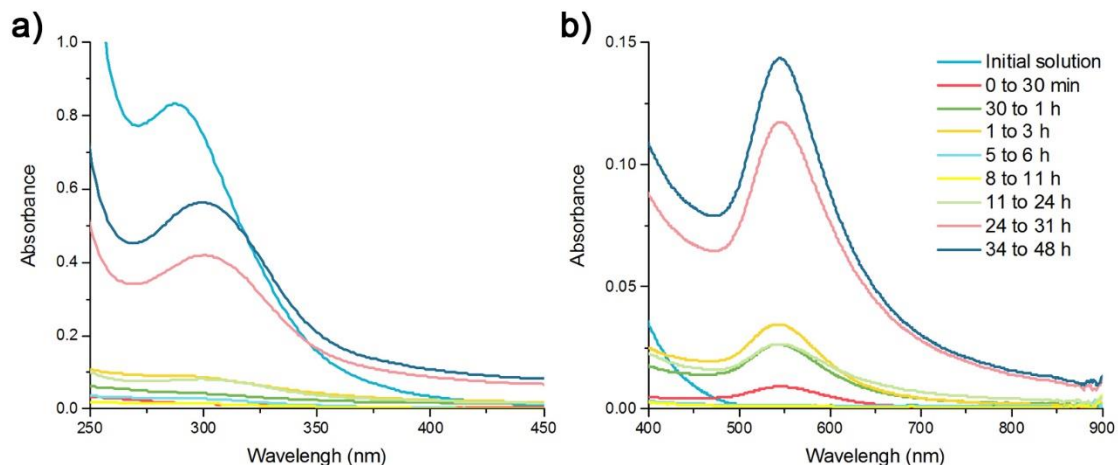
Figure 3.12 UV-vis spectra of the different fractions collected overtime at a) short wavelengths (250 to 450 nm) and b) long wavelengths (400 to 900 nm). This UV-vis correspond to the experiment in which short pre-washing with deionised water (2h) and acidic aqueous solution (2h) was applied prior passing the gold solution (pH 3) through the monolith reactor.

Pink and yellow colour observed after 11 h into the experiment

UV-vis spectra shown in Figure 3.12 showed that the peak for Au^{3+} became increasingly prominent after 24 h. The increasing concentration of Au^{3+} ions in the output solution could reveal different scenarios:

1. The monolith was reaching its breakthrough point and some of the Au^{3+} ions in solution could not be adsorbed by the material. According to this hypothesis, the output solution should present yellow colour. No NP leaching, and therefore no pink colour, was expected (Figure 3.13a).

2. The interface between the epoxy resin and the monolith was damaged overtime. This allowed adsorption at early stages of the experiment, but also let some of the Au^{3+} to pass through the system without being reduced at later times (Figure 3.13b). Adsorption would occur on the top horizontal surface, and the lateral side of the monolith. The depth at which the horizontal adsorption occurred entirely depended on the time required to produce significant damage on the interface. Such damage allows the gold solution to get in contact with the epoxy resin, which can reduce the gold as discussed below in this section. The Au NPs formed by this

151

means did not get attached to epoxy and reached the output solution through the damage interface, giving pink colour to solution.

3. Damages on the interface between the epoxy resin and the Swagelok tubing (Figure 3.13c). Similar to the previous case, however in this case, only adsorption in the horizontal top surface of the monolith would occur, and no adsorption in the lateral of the monolith would be observed.

4. Localised decomposition of the Starbon® monolith (Figure 3.13d). This localised decomposition may be the result of a non-homogenous carbonisation of the monolith; Before carbonisation, the monoliths were introduced in a solution of p-TSA (as shown in Chapter 2). Due to the monolithic shape, the p-TSA must permeate from the outside towards the inside and therefore, if the monolith was not kept in solution for long enough, the p-TSA might not have reached the internal part of the monolith which may have resulted in chemical and structural differences. TGA discussed in Chapter 2 presented a peak around 300 °C which could be assigned to late starch decomposition of fractions that had not been in contact with the p-TSA. As for the previous cases, this would allow some degree of adsorption and reduction onto the Starbon® surface. However, some Au^{3+} ions would also be able to pass through the system without being reduced.

The results obtained by microscopy, TEM, TOC and XPS analysis are discussed below and used to identify the most likely scenario of those described above.
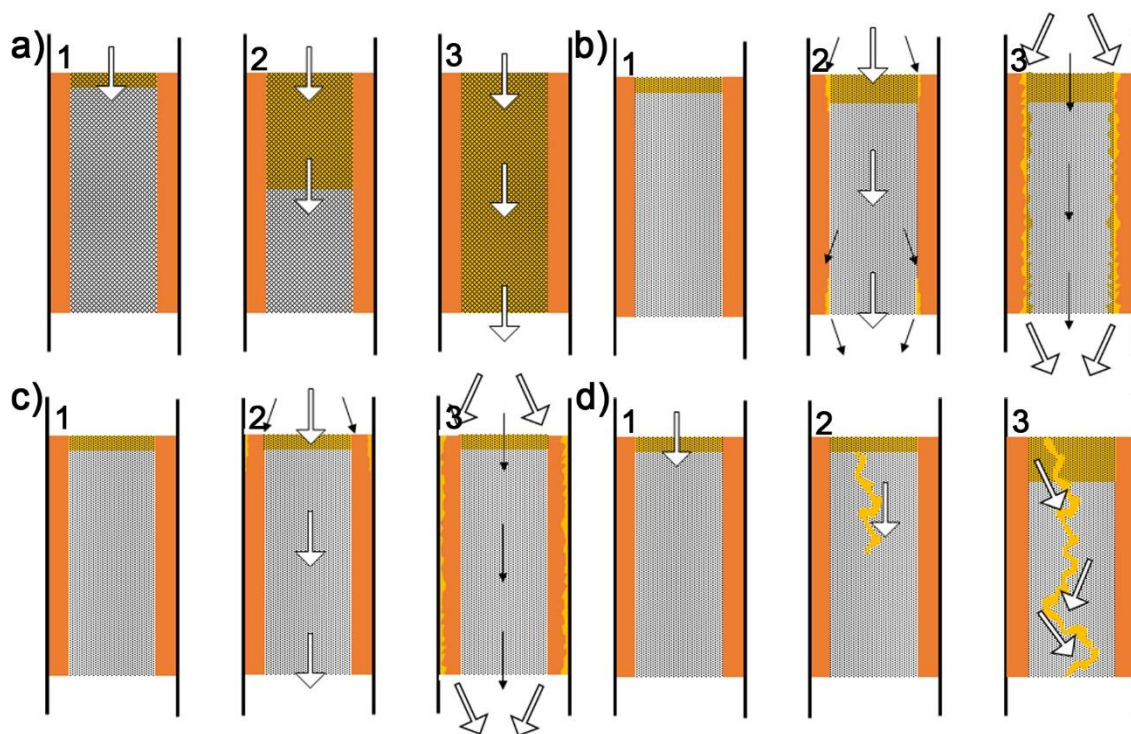
Figure 3.13 Possible processes occurring during the flow adsorption experiments where 1 symbolises the early stages, 2 the middle stage and 3 the final stage of the processes. a) breakthrough, b) degradation of the interface between the monolith and the epoxy resin, c) degradation of the interface between the epoxy resin and the Swagelok tubing and d) localised decomposition of the monolith. Wide arrows represent the main stream of the solution whereas thin arrows represent the flow of small fractions of solution.

As shown by the UV-vis spectra in Figure 3.12, the concentration of Au^{3+} started to become significant in the sample collected between 24 and 31 h, as the concentration increased from 10% at 24 h up to 51% at 31 h. The amount of Au^{3+} ions in solution kept increasing until the experiment was stopped at 48 h, point at which the solution contained 67% of Au^{3+}. The peak at 545.8 nm in the UV-vis spectra, characteristic of Au NPs was also observed after 8 h and its concentration increased over time. In addition, the Au^{3+} in the output solution was detected well before theoretically predicted in Figure 3.9. Although it has been shown that relatively fast flow rates could reduce the adsorption capacity of a material and therefore bring forward the breakthrough point,[294] the presence of NPs in the output solution indicated that the Au^{3+} found in solution were due to some sort of degradation/damage of the system, discarding option number 1.

The monolith reactor was opened after the adsorption experiment and both ends were observed under the microscope. On the top surface (the one through which the solution entered the system) it was possible to observe concentric circles covering the whole surface. This was in good agreement with the localised decomposition described in option number 4. The metal solution presented relatively strong acidity, which could have increasingly degraded the monolith structure towards the inner core.
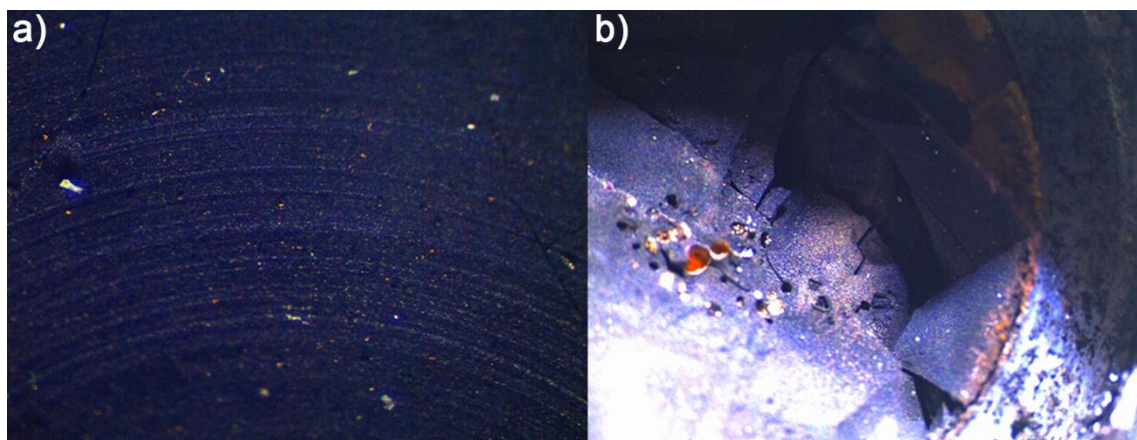
Figure 3.14 Microscopic view of a) the top surface of the monolith (entering point of solution) and b) the bottom surface of the monolith (exiting point of solution).

The bottom surface (the one through which the solution exited the system) showed fractures in the part in contact with the epoxy resin. This agreed well with the decomposition of the interface between the monolith and the epoxy described in option number 3, which can cause damage on the sides of the monolith. This damage could open a path for Au^{3+} and the Au NPs formed by contact with the epoxy resin, to reach the output solution. TOC analysis supported this hypothesis, as it showed the presence of organic matter in solution at the final stages of the experiment (Table 3.3), which could be fractions of the monolithic column. TEM also showed the presence of other components in solution apart from the Au NPs which could be Starbon® fractions due to decomposition (Figure 3.15).
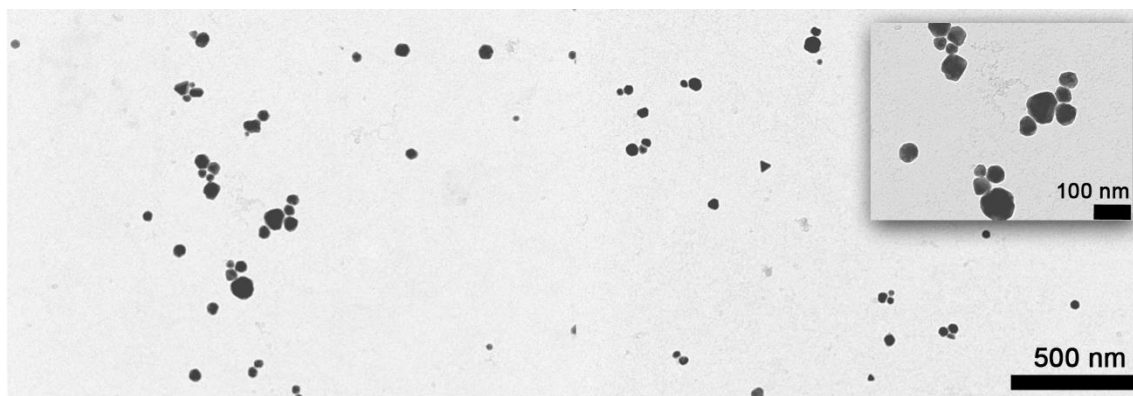
Figure 3.15 TEM image of the gold nanoparticles in solution in the interval of 34-48 h. The inset shows a region of the same sample at higher magnification.

The Starbon® monolith was analysed by XPS after the flow adsorption experiment, looking for Au NPs on the Starbon® surface. XPS analysis was carried out by Dr David Morgan at the School of Chemistry of the University of Cardiff. XPS did not detect gold. As the whole column was ground up and mixed before the analysis, a plausible explanation for the lack of Au could be the gradient between the top and the bottom of the monolith, where the top had adsorbed some gold, but the bottom had not. As a result, the XPS results displayed the average concentration of gold in the carbon sample, which was very low. The C/O ratio observed by XPS was 21.6 slightly higher than that observed for S800 in Chapter 2. This was in good agreement with 'flushing out' the oxygen-containing molecules trapped in the Starbon® pores.[206]

Finally, a small portion of the epoxy resin used to attach the monolith to the Swagelok tubing was added to a vial containing the initial solution of Au^{3+}, in order to determine if the epoxy resin could also be reducing some of the gold ions to NPs and releasing those into the solution. As shown in Figure 3.16, the epoxy resin was capable of reducing the gold ions.
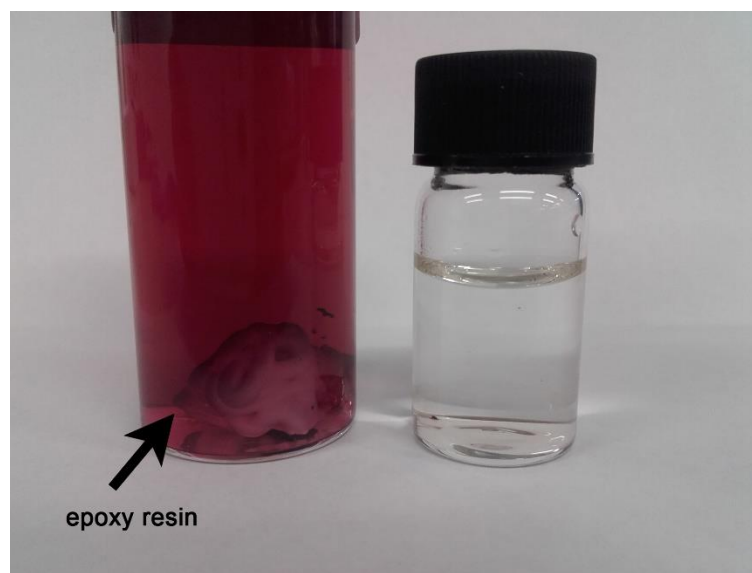
Figure 3.16 Appearance of the Au^{3+} solution after (left) and before (right) being in contact with the epoxy resin used to attach the Starbon® monolith to the Swagelok tubing.

All the evidence discussed above indicated that breakthrough (option number 1) was not reached during the experiment. The presence of Au^{3+} in the output solution was due to a combination of factors, including the degradation of the interface between the epoxy resin and the monolith (option number 2) as well as due to partial degradation of the material (option number 4). Degradation of the interface between the epoxy resin and the tubing (option number 3) can neither be confirmed nor denied with the current evidences. The continuous flow examples for the recovery of precious metals described in the literature did not encounter the above described problems because the material was a powder packed on a column.[60, 76] However, the development and use of monolithic structures is preferred as it has been shown that the surface area of monoliths was more accessible, leading to higher adsorption capacities.[295]

The aim of the present work was to proof the feasibility of the monoliths in flow systems for metal adsorption. The experiments described in this chapter showed that the Starbon® monoliths can be incorporated to a flow system through which a metal solution can be passed for 11 h without significant damage to the system. However, the system needs to be optimised as after 11 h some of the $AuCl_3$ solution passed through the system

without being absorbed, indicating some degradation of either the Starbon® monolith and the interfaces between the epoxy resin. In addition, the epoxy resin employed did react with the gold ions. As some of the main issues were related to the epoxy resin, this component will need to be replaced by another compound that can resist the backpressure and acidity of the system, whilst not leading to NP formation. Regarding the partial decomposition of the Starbon® monoliths, it could be solved by changing the application method of the p-TSA. Nevertheless, the optimisation of the process was out of the scope of the project and guidelines to improve the system are discussed in the future work section (Chapter 7).

Remarks about the NPs found in solution

The position of the Au NPs peak in the UV-vis spectrum has been related to the size of the NPs. This peak appeared at 542.2 nm in the solution collected between 1-3 h, and shifted to 544.7 nm for the solutions collected at 34-48 h. The peak at 542 nm was indicative of NP diameter of 60 nm, and a shift towards larger wavelengths suggested bigger NPs of approximately 70 nm. This was in good agreement with TEM, which showed Au NPs with an average diameter 50 nm during the 1-3 h interval (Figure 3.11), and average diameter of 70 nm NPs during the 34-48 h interval (Figure 3.15). In addition, the nanoparticles observed presented different shapes, including circular, square, triangular, hexagonal and irregular forms. NPs with similar size and shapes were observed by Gardea Torresdey *et al*. who study the formation of Au NPs using alfalfa biomass.[296] It has been suggested that the different shapes of NPs are related to the kinetics of the growth of such particles,[297] which agrees well with the experimental conditions, where the damage to the interface between the epoxy resin and the monolith would cause different speed pathways for the solution to pass through and would lead to different rates of NPs growth.

Further work to understand the conditions that favour a specific type of NPs is needed, as this could show new application routes for Starbon® materials.

3.4 Conclusion

The work described in this chapter showed that Starbon® present great potential to be used for precious metal recovery:

- The materials were highly selective towards precious metals when the mixture also contained base metals such as Ni, Cu and Zn. This selectivity was maintained even when the mass concentration of precious metals was 100 times lower than that of the base metals.

- The materials performed well when used to absorbed metals from a 'real waste' solution obtained from disposed electronics. The waste solution contained 15 different metals, 5 of which were in concentrations over 10 ppm (including gold). Starbon® preferentially adsorbed gold leaving all the other metals in solution. Only tin, molybdenum and lead were partially adsorbed as well. However, the adsorption capacities for these metals were very low compared to gold (8.5 mg·g^{-1} for tin and <1 mg·g^{-1} for Pd and Mo).

- Starbon® monoliths were incorporated to a flow system in which an acidic metal solution could be passed through for 11 h without significant damage to the system. During this time, Au^{3+} was adsorbed onto the monolith as shown by the colourless output solution. Although the method to attach the monolith to the Swagelok tubing needs to be optimised, the present work proofs the feasibility of applying Starbon® monoliths to flow systems.

Interestingly, the NPs obtained under different conditions varied. Therefore, further work towards understanding the conditions that favour a type of NPs over the others could be highly beneficial to open the way to new applications for Starbon®.

Preparation and characterisation of Starbon® composites

Chapter 4

4 Preparation and characterisation of Starbon® composites

4.1 Introduction

Electrochemical double layer capacitors are energy storage devices formed by two electrodes (usually carbon-based) and an electrolyte.[181] In EDLCs the energy is stored physically in the surface of a porous material which allows fast charge discharge cycles.[181] Research is currently focused on improving the properties of EDLCs to obtain materials capable of storing higher amounts of energy and in turn maintain the ability to deliver such energy rapidly.[298]

ACs are the most widely used material in commercial EDLCs due to advantageous properties including wide availability, relatively low cost and high surface area.[203, 207, 299] However, AC present three main drawbacks in regard to their utilisation for EDLCs: 1) poor conductivity due to their large surface area, 2) very low number of mesopores and 3) they are usually produced as powders, and a binding material is required to form the electrode discs.[194, 203, 300] The mesopores contained in materials such as Starbon® have been found to be necessary in EDLC materials as they contribute to improve the diffusion of the electrolyte throughout the materials porous structure.[131] Binding agents added to create the electrode disc usually increase the resistivity of the material which translates into lower capacitance.[301] In order to overcome these issues, other materials such as CNTs have been tested as potential EDLC materials as they present high conductivity and are readily accessible.[203] However, the effective surface area of CNTs is relatively low, which leads to low values of capacitance.[195]

The preparation of carbon-carbon composites to yield a material which combines high surface area, good conductivity and a significant number of mesopores has been recently

studied.[219, 225, 302] For example, highly dispersed CNTs were added to ACs to yield a composite with enhanced energy and power density compared to the untreated AC.[219] Graphene has also been trialled as a potential material for EDLC due to its very large surface area and good conductivity. Graphene was also used to enhance the conductivity and capacitance of AC.[225] Although the application of high-tech carbons such as CNTs and graphene can enhance the electrochemical properties of an EDLC device, it is important to consider that the production of these materials could be expensive and cumbersome which may increase the overall cost of the energy storage device.[303]

Graphite is a carbon allotrope consisting of a succession of staked graphene layers.[204] It presents very good electric properties, with a conductivity of 10^6 S·m^{-1}.[304] Graphite is also widely available and inexpensive which makes it a good candidate to be used in carbon-carbon composites.[305]

Herein, we present alternative carbon-carbon composites that combine the advantageous porosity of Starbon® with the high conductivity of graphite. In addition, the new materials can be prepared as monoliths without the use of binding agents. It is believed that the addition of the non-expensive and highly conductive graphite to mesoporous Starbon® can result in porous conductive carbons with potential to be used for EDLC.

4.1.1 Aims of the work

- Preparation of Starbon®-graphite composite materials to enhance the electrochemical properties of Starbon® in order to apply such materials for energy storage applications.
- Characterisation of the Starbon®-graphite composites materials.

4.2 Results and discussion

4.2.1 Preparation of the Starbon®-graphite composites

The method for the preparation of Starbon® was adapted to prepare the monolithic composite materials.[110]

As graphite is not easily dispersible in water, graphite must be thoroughly mixed with starch before gelation.[306] To overcome this challenge, ball milling (BM) was introduced at the beginning of the process. This step was essential to reduce the graphite particle size sufficiently to aid its dispersion within the polysaccharide matrix. Previous studies showed that BM of a mixture of cellulose and graphite resulted in exfoliated graphite particle size which adhered to the cellulose particles.[307] The reduction of the graphite particles was observed by XRD (see Section 4.2.3.4) and good dispersion was shown in the surface of the aerogel monoliths (material after drying) and SEM images (Figure 4.1). The SEM images were taken by Dr Peter Shuttleworth at the Instituto de Ciencia y Tecnología de Polímeros of the Consejo Superior de Investigaciones Científicas (Spain). A range of BM processing time was tested to assess its effect on the dispersion of graphite within the polysaccharide matrix; 10 minutes of treatment was found to be insufficient as the aerogel presented heterogeneous distribution. On the other hand, after 30 or 60 minutes, a more homogeneous interaction between the two materials was observed. It has been reported that long BM times can significantly damage the integrity of graphite crystals, and limit their desired conductivity properties.[308] Therefore, 30 min of BM were considered optimal to ensure good dispersion of graphite within the polysaccharide matrix without compromising the integrity of the graphite crystal.

Previous studies measured the electrical adsorption of a planetary ball mill, 350 W. Considering the usage time, the electrical yield and Watt price, using BM would increase the cost of the process by 4 cents and would be equivalent to the energy consumption of two TVs.[309, 310]
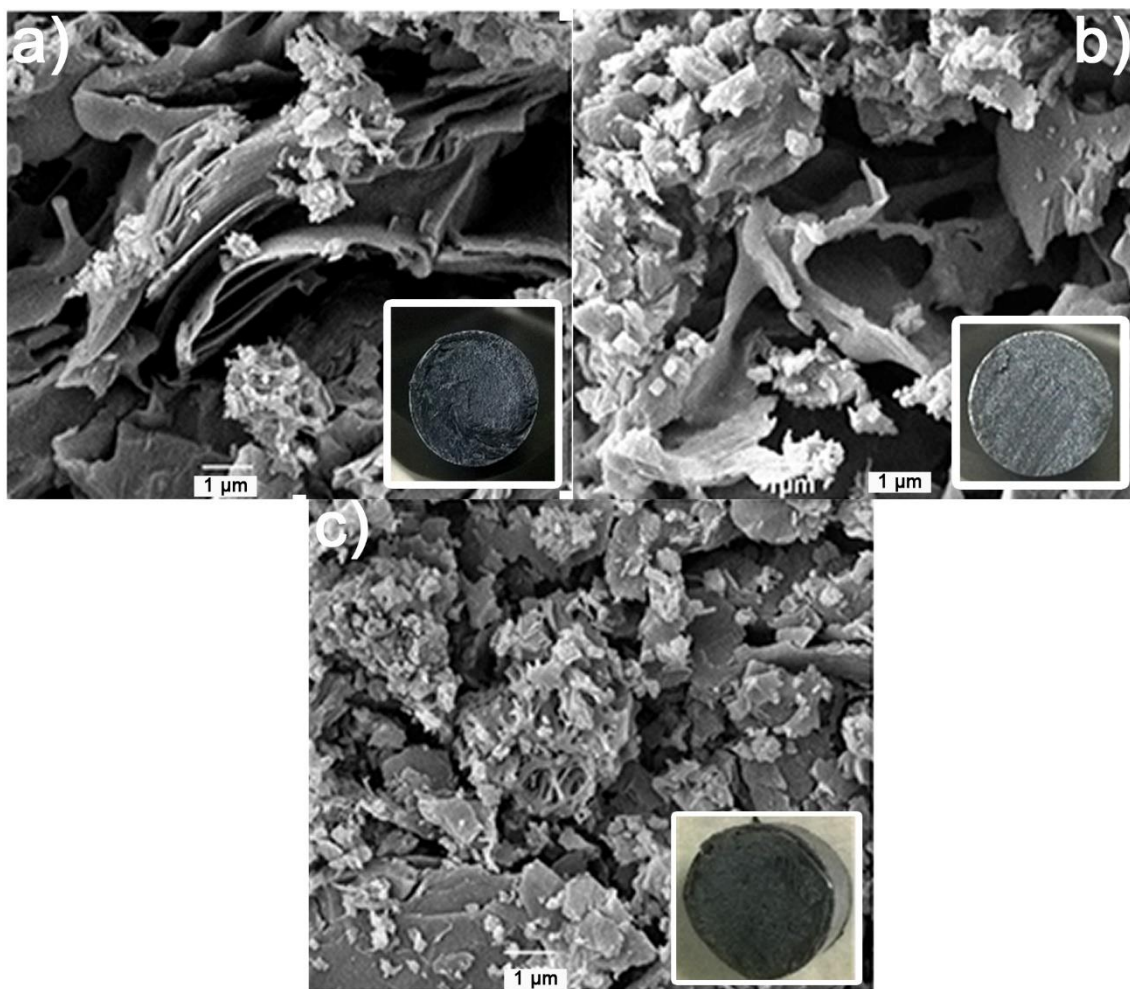
Figure 4.1 SEM images of the starch-graphite mixture after a) 10 min, b) 30 min and c) 60 min of ball milling treatment. The top surfaces of aerogel monolithic composites are shown in the insets.

The drying method was also modified to obtained a more hierarchical porous structure, which has been shown to improve the diffusion properties of the electrolyte in EDLC devices.[193] Monoliths were subjected to solvent exchange with tert-butanol (TBA) and subsequently freeze dried. Freeze drying (FD) generally involves two steps: 1) the freezing, in which the material is cooled down well below the triple point of the solvent, and 2) the sublimation, in which the solvent is removed as a vapour by lowering the pressure of the system.[311] FD tends to yield aerogels with porous structures containing a large amount of macropores but almost no mesopores.[312] However, Borisova *et al.* showed that using TBA in the solvent exchange step led to hierarchical aerogels

containing both meso- and macropores.[313] The mesopores were created by the crystals of TBA, which acted as porogens.[314] The rest of the process was kept the same as the one described in Chapter 2 for the preparation of Starbon® monoliths.

Six different materials with different initial concentrations of graphite were prepared. The names assigned to those materials, which will be consistently used through Chapter 4 and Chapter 5, are detailed in Table 4.1.

Table 4.1 Initial concentration of graphite (%) of the materials discussed throughout the chapter and their assigned names.

Initial concentration of graphite (%)	0	0.5	1	3	10	20
Name of the material	GPT-0	GPT-0.5	GPT-1	GPT-3	GPT-10	GPT-20

4.2.2 Characterisation of the relevant properties for EDLC applications of Starbon®-graphite composites

The porosity and conductivity of the resulting materials were measured, as these are the most relevant properties regarding EDLC as potential application. The appearance of the composite materials throughout the production process is also discussed in this section, including important technical parameters such as mass loss and diameter reduction during the preparation process.

4.2.2.1 Appearance of the Starbon®-graphite composites

BM of starch and graphite yielded a grey powder, the colour of which did not visibly vary at increasing concentrations of graphite. However, the colour difference became apparent in the aerogels, which clearly presented darker colour as the amount of graphite increased. All samples turned completely black during carbonisation (Figure 4.2).
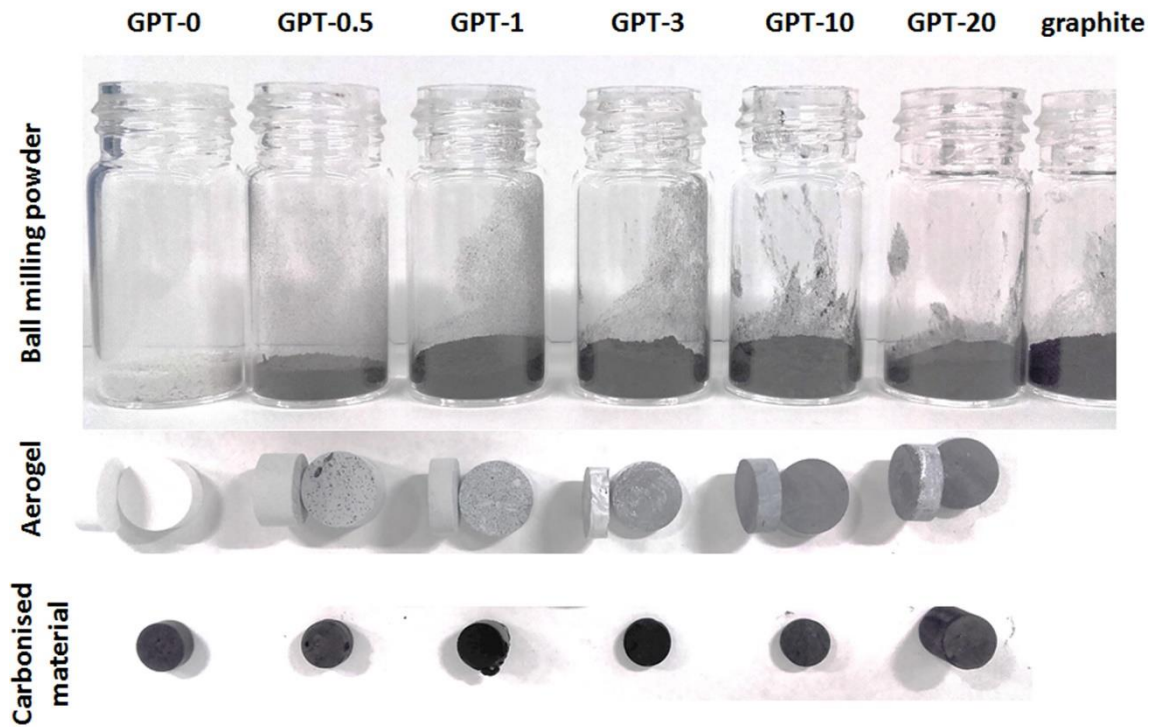
Figure 4.2 Starbon®-graphite composites at different stages of the preparation process; powder resulting after 30 min of BM (top row), aerogel composites (middle row) and carbonised composites (bottom row).

The composite gels were poured into a cylindrical mould (same as the one used in Chapter 2) after gelation (12.4 mm of diameter). In this case, the monoliths were cut down after retrogradation to yield small discs that could be tested in EDLCs. The diameter of the aerogel discs varied from 11.9-12.4 mm, but no obvious trend could be drawn regarding concentration of graphite. The concentration of graphite did not clearly affect the diameter of the carbonised materials either, which had diameters between 7.5 and 8.6 mm. Therefore, the diameter reduction occurring during carbonisation (30-40%) was similar for all composites and was independent of the concentration of graphite in the composite. The diameter of GPT-0 shrunk 4% less than the Starbon® monoliths described in Chapter 2 suggesting that the differences were due to the alterations in the preparation process.

On the other hand, increasing amounts of graphite led to lower mass loss during carbonisation (Table 4.2). This phenomenon can be explained by the thermal stability of

graphite at the temperatures of carbonisation; graphite was subjected to the same carbonisation programme and the results showed no significant decomposition during carbonisation (96% mass residue) and therefore, composites containing larger amounts of graphite presented lower mass reduction.

Table 4.2 Mass loss (%) occurred during carbonisation at 800 °C, measured by thermal gravimetric analysis.

Material	GPT-0	GPT-0.5	GPT-1	GPT-3	GPT-10	GPT-20
Mass loss during carbonisation (%)	70.8	69.8	69.2	67.3	64.9	61.0

The density of the aerogels was very similar for all the aerogel materials (Table 4.3). This suggested that the different properties observed in the carbonised materials with different concentrations of graphite were developed at a later stage of the production process (mostly during carbonisation).

After carbonisation, higher densities were observed for composites with larger concentrations of graphite (Table 4.3). This could be explained by the formula of density – the coefficient of mass over volume ($\rho=m/V$). As discussed above, the diameter of the monoliths was not affected by the amount of graphite. However, the concentration of graphite did influence the mass loss during carbonisation, which resulted in higher densities for composites rich in graphite. Interestingly, the density of GPT-0.5 and GPT-1 were lower than that for GPT-0®. Both GPT-0.5 and GPT-1 contained very low concentration of graphite and in consequence the mass loss observed after carbonisation was very similar to that for GPT-0. However, those materials presented significantly larger surface area (100-150 $m^2 \cdot g^{-1}$ more than Starbon®) which led to the lower density observed.

Table 4.3 Density of Starbon®-graphite composites (g·cm^{-3}) in the aerogel form and after carbonisation at 800 °C.

Material	GPT-0	GPT-0.5	GPT-1	GPT-3	GPT-10	GPT-20
Density of aerogels (g·cm^{-3})	0.32	0.35	0.32	0.35	0.35	0.32
Density of carbonised materials (g·cm^{-3})	0.35	0.23	0.25	0.40	0.46	0.49

4.2.2.2 Porosimetry

The aerogel composites were characterised by N_2 adsorption and their textural properties are summarised in Table 4.4. The materials were found to be consistently highly mesoporous with little microporosity (below 1%), high pore volumes (>0.7 cm^{3}g^{-1}) and high specific surface areas (> 150 m^{2}g^{-1}). Larger pore volumes, slightly lower surface areas and microporosity were observed compared to the Starbon® aerogels in Chapter 2, which could be due to the freeze-drying step.[312, 315].

As graphite does not disperse well in water, BM was used to achieve a good mixing between the starch and graphite prior gelation. BM's ability to reduce graphite particle size and favour good dispersion and exfoliation of graphite when performed in combination with polysaccharides,[307, 308] did not seem to have a detrimental effect on the material's porosity.

It was also observed that the surface area and microporosity of the materials were independent of the BM times, whereas the total and mesopore volume increased from 0.72 to 0.79 cm^{3}g^{-1} after processing times of 10 min and 60 min, respectively.

The high porosity displayed by the composite aerogels showed that graphite did not inhibit the formation of the characteristic mesopores found in Starbon® despite its low porosity and surface area (<48 m^{2}g^{-1}).

Table 4.4 Textural properties GPT-20 aerogels after being subjected to different BM times, analysed by N_2 adsorption porosimetry. BET model was applied to obtain the surface area. Total and mesopore volumes were calculated from the BJH model. D-R model was used to obtain the micropore volumes.

Ball milling time (min)	Starbon®-graphite aerogels containing 20% of graphite (GPT-20)				
	Surface area ($m^2 \cdot g^{-1}$)	V_{tot} ($cm^3 \cdot g^{-1}$)	V_{micro} ($cm^3 \cdot g^{-1}$)	V_{meso} ($cm^3 \cdot g^{-1}$)	Microporosity (%)
10	160.7	0.72	<0.01	0.72	0.42
30	160.8	0.76	<0.01	0.76	0.39
60	158.3	0.79	<0.01	0.80	0.38

The N_2 adsorption isotherm of the GPT-20 aerogel (Figure 4.3) showed a Type IV isotherm characteristic of mesoporous materials, which was consistent with previous work on Starbon® aerogels.[228] The isotherms displayed H3 hysteresis loop with no limitation of adsorption at high relative pressures.[232] The H3 hysteresis loop is characteristic of plate-like particles which leads to slit-shaped pores.[232] This was in good agreement with the SEM shown in Figure 4.1b.
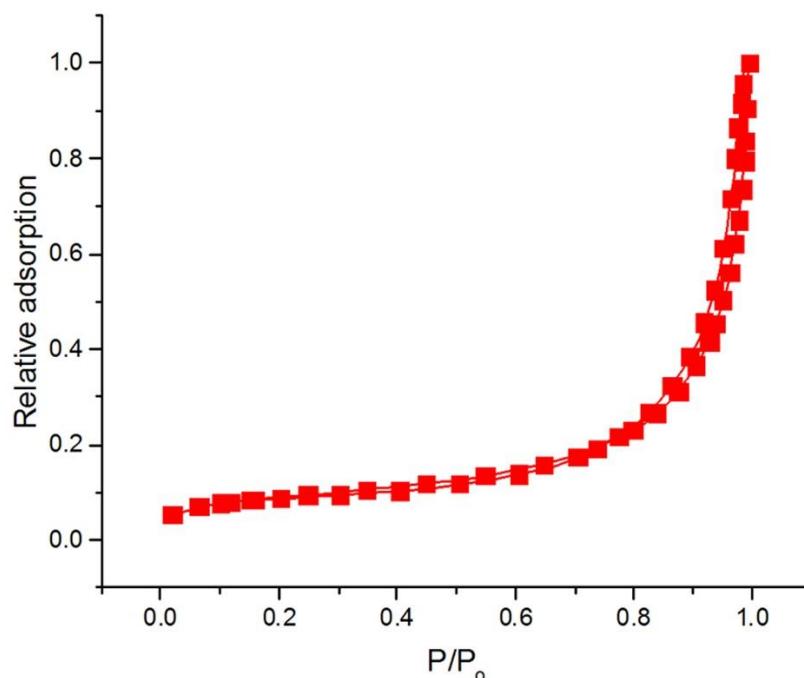
Figure 4.3 N$_2$ adsorption isotherm of GPT-20 aerogel after 30 min BM, measured by N$_2$ adsorption porosimetry.

The textural properties of the carbonised Starbon®-graphite composites were also analysed by N$_2$ adsorption (Table 4.5). Increasing amounts of graphite resulted in decreasing total pore volumes and surface areas, due to the intrinsic low porosity of graphite. Surprisingly, the addition of traces of graphite enhanced the number of micropores and consequently the surface area compared to GPT-0. This could be caused by structural disruption. Another plausible explanation for this is that the well-dispersed particles of graphite that do not intimately interact with starch could act as porogens when they decomposed during carbonisation. This phenomenon may also occur with higher concentrations of graphite. However, in those cases, the larger amounts of graphite may cause aggregation and when partially decomposed during carbonisation, led to bigger pores. This hypothesis was in agreement with the pore size distribution, where increasing concentrations of graphite led to larger pores (discussed below in this Section). Evidences of decomposition of graphite are shown below; nevertheless, graphite was not expected to significantly decompose at the carbonisation temperatures employed. Some possible reasons for such decomposition are:

- The volatile compounds produced during carbonisation (e.g. organic and sulphuric acids, CO, CO_2) may create an 'aggressive' environment that is capable of favouring partial decomposition of graphite. The sulfuric acids can be derived from the p-TSA added to catalyse the carbonisation. Sulfuric acid in combination with oxidising agents has been used for the preparation of graphite oxide from graphite.[316] Although the carbonisation conditions for the Starbon®-graphite composites cannot be considered oxidising because it was performed under vacuum, local oxidising environments may be created due to the high oxygen content of starch, and the CO and CO_2 released during carbonisation. Therefore, this acidic conditions could favour the transformation of some of the graphite in the composites to graphite oxide, which has been shown to decompose into H_2O, CO_2 and CO at the carbonisation temperatures of the present process.[317] Nevertheless, as the conditions described in the literature to obtain graphite oxide from graphite were different to those in this thesis, further work is needed to understand if transition to graphite oxide occurred.
- The contact with the starch molecules which are rich in oxygen atoms and become soft/molten and highly oxidative at high temperatures.

These would promote decomposition of the graphite particles that were not intimately interacting with the hydrophobic parts of the starch helixes. Only the graphite particles in intimate interaction with starch would remain in the composite after carbonisation.

Table 4.5 Textural properties of the Starbon®-graphite composites after carbonisation at 800 ºC.

Material	Starbon®-graphite composites carbonised at 800 °C, 30 min of BM				
	Surface area $(m^2 \cdot g^{-1})$	V_{tot} $(cm^3 \cdot g^{-1})$	V_{micro} $(cm^3 \cdot g^{-1})$	V_{meso} $(cm^3 \cdot g^{-1})$	Microporosity (%)
GPT-0	560.4	0.66	0.23	0.43	35
GPT-0.5	718.9	0.67	0.30	0.37	45
GPT-1	671.4	0.93	0.29	0.64	31
GPT-3	477.1	0.69	0.20	0.49	29
GPT-10	408.8	0.49	0.18	0.32	36
GPT-20	336.7	0.40	0.14	0.26	35
Graphite	47.8	0.11	0.02	0.09	18

Maximum total and mesopore volumes of 0.93 and 0.64 $cm^3 \cdot g^{-1}$ were reached with the sample GPT-1 and progressively decreased with increasing amounts of graphite due to the intrinsic non-porosity of graphite.

At increasing concentrations of graphite, the number of micropores decreased along with the total and mesopore volumes, which kept the microporosity almost unaltered (~30-35%).

Overall, in composites with low concentration of graphite, the high porosity of Starbon® prevailed, combining the high surface area of Starbon® with the more open porous structure of the composites. In composites with high concentration of graphite, the amount of Starbon® was lower and so was the surface area and pore volume of the composite.

Carbonised GPT-0 presented lower surface area and pore volume than the S800 material described in Chapter 2. This showed that alterations in the preparation process did affect the final properties of the materials. The main variations in the production process were, the addition of the BM step and the utilization of FD instead of scCO$_2$. It is noteworthy that the starch/water ratio employed during gelation was slightly lower for the

composites (0.25 instead of 0.33 g·cm^{-3}) in order to obtain a runnier gel that could be more easily poured in the mould. This could also affect the textural properties of the final material. However, previous studies about Starbon® showed that the surface area and pore volume of the materials increased with increasing starch/water ratios up to 0.05 g·cm^{-3} point at which the trend was inverted and the textural properties decreased with increasing concentrations of starch.[228] According to this, larger surface areas and pore volumes would have been expected for GPT-0. The results not showing such trend indicated that either the BM or FD steps caused the lower textural properties. This agreed well with previous publications, where it was shown that FD may lead to lower surface areas and poorer mesoporosity.[315]

The addition of graphite led to the formation of a more open structure as shown by SEM in later in this chapter, and as shown by the larger pore diameters displayed by the PSD in Figure 4.4. The presence of larger pores could improve the flow/mass transfer/diffusion properties of the material in, as these act as highways that direct and improve the 'traffic flow' to the minor roads, the micropores.[318] Therefore, larger meso- and macroporous channels that increase access to the micropores could be advantageous in EDLCs and facilitate ion diffusion within the electrodes.[319]
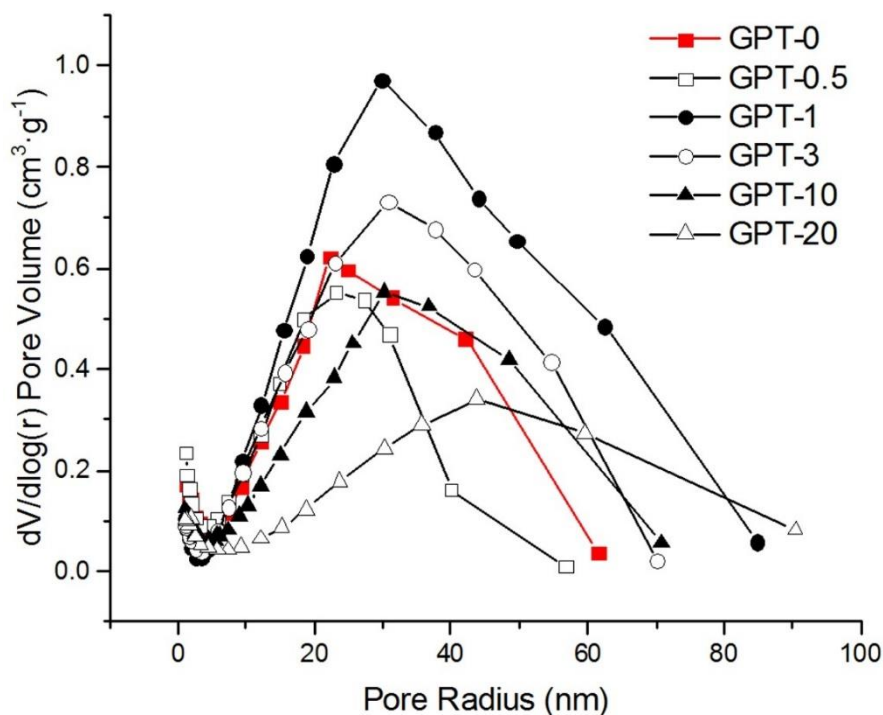
Figure 4.4 Pore size distribution of the carbonised Starbon®-graphite composites, measured by N_2 adsorption porosimetry.

The N_2 adsorption isotherms of the composites are displayed in Figure 4.5. All materials presented Type IV which was characteristic of Starbon®.[231] This was in good agreement with the results obtained for S800 in Chapter 2. As for the aerogels, the isotherm did not present finite adsorption at high relative pressures. The hysteresis loop corresponded to type H3 which is characteristic of slit-shaped pores.[232] This agreed well with the observations made by SEM later in this chapter.

In figure 4.5b point '*' indicates coverage of the monolayer and beginning of multilayer adsorption.[232]
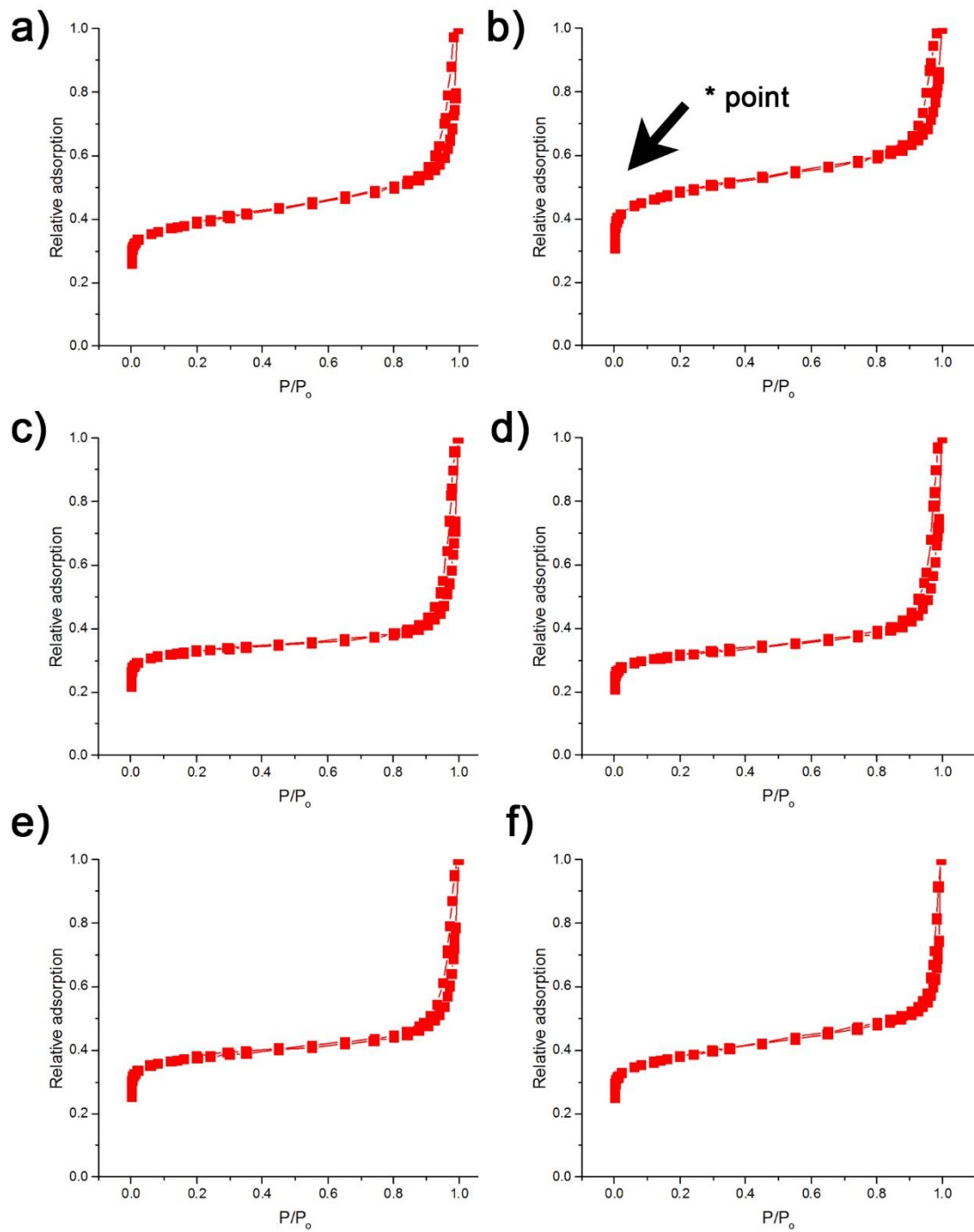
Figure 4.5 N$_2$ adsorption isotherms of the carbonised Starbon®-graphite composites, measured by N$_2$ adsorption porosimetry. The '*' point indicates the starting point of multilayer coverage.

4.2.2.3 Conductivity

The conductivity of starch has been shown to improve up to 10 times when 10% of expanded graphite was added.[304] Therefore, an increase in the electrical conductivity of the composites compared to that of pure Starbon® was expected. As a reference, the electrical conductivity of graphite described elsewhere reached 10^6 S·m^{-1}.[304] On the other hand, Starbon® showed certain degree of electrical conductivity, but the values were < 1 S·m^{-1}.

The values for the electrical conductivities of the Starbon®-graphite composites are displayed in Figure 4.6 and Table 4.6 and showed that increasing amounts of graphite led to increasing values of conductivity, which reached 47.7 S·m^{-1} for GPT-10. Conductivity slightly decreased at concentrations over 10%. This phenomenon could be explained by the aggregation of the graphite particles, which resulted in a decrease of the electrical percolation. This phenomenon is hypothesised to be related to structural changes affecting conductivity. As error bars for these measurements could not be recorded, further work is needed to corroborate this hypothesis.

The obtained values were several orders of magnitude higher than those described by Pradhan *et al.* for similar graphite-starch bio-composites.[304] The measurements of conductivity were carried out by Dr. Peter Shuttleworth at the Instituto de Ciencia y Tecnología de Polímeros of the Consejo Superior de Investigaciones Científicas (Spain).

Table 4.6 Conductivity values of the Starbon®-graphite composites, expressed in S·m^{-1}.

Material	GPT-0	GPT-1	GPT-3	GPT-10	GPT-20
Conductivity (S·m^{-1})	0.69	1.78	19.2	47.7	36.2
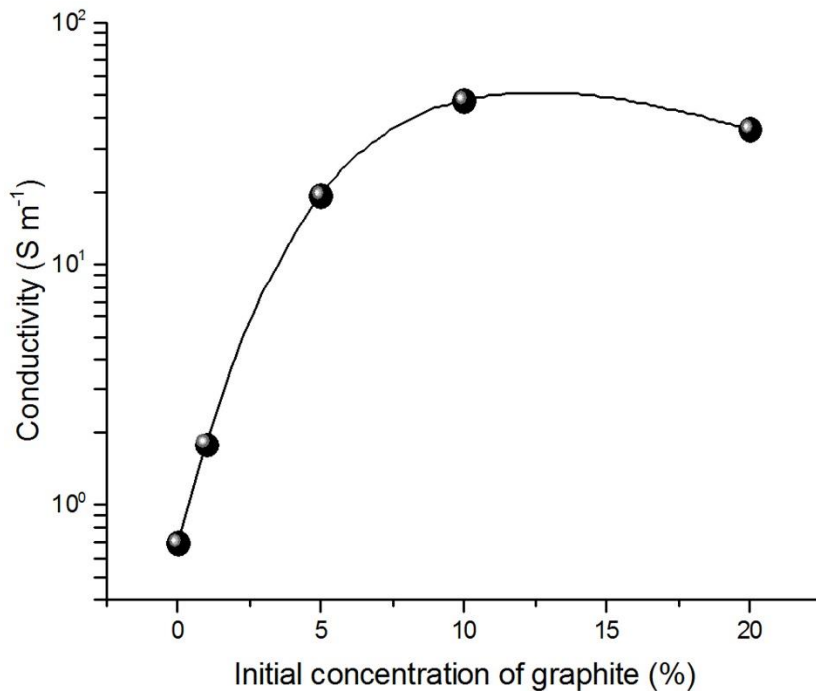
Figure 4.6 Effect of the initial concentration of graphite (%) in the electrical conductivity (S·m⁻¹) of the Starbon®-graphite composites.

4.2.3 Further characterisation to study the interaction between starch and graphite in the Starbon®-graphite composites

Further characterisation was carried out to gain a better understanding of the interaction between Starbon® and graphite.

4.2.3.1 SEM and TEM

SEM images of GPT-20 were taken at different stages of carbonisation. As shown in Figure 4.7, at low temperatures of carbonisation (200 °C) very large particles of graphite, with a diameter of up to 10 µm, were observed. However, at high temperatures of carbonisation (800 °C) it was not possible to observe these particles which suggested that they disappeared during carbonisation.
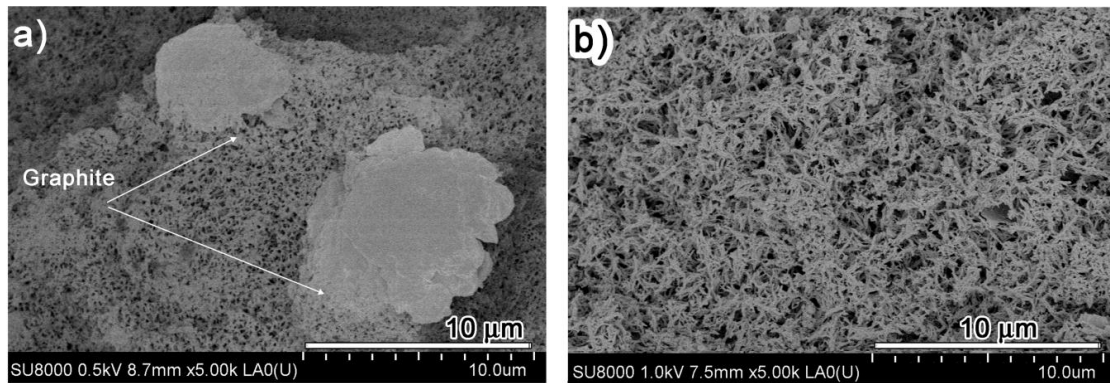
Figure 4.7 SEM images of GPT-20 after carbonization at a) 200 ºC and b) 800 ºC.

A closer maximisation of the SEM images showed that the structure of GPT-20 presented wider pores than that of GPT-0 (Figure 4.8). This phenomenon was consistent with the PSD discussed in Section 4.2.2.2. The bigger pores resulted from the aggregation of the fibres which yielded thicker pore walls. As shown in Figure 4.8, a pore wall was formed by several fibres. Those individual fibres were measured for GPT-0, GPT-3 and GPT-20. The width distribution showed that most of the fibres measured 25 or 35 nm in all three samples. Therefore, the width of the individual fibres was independent of the concentration of graphite.

In turn, the size of the graphite nanoparticles found in the carbonised GPT-20 were measured by high resolution TEM for which the obtained values were 24 and 37 nm. The graphite particles were therefore reduced from 10 µm down to 24 and 37 nm upon carbonisation at 800 ºC.
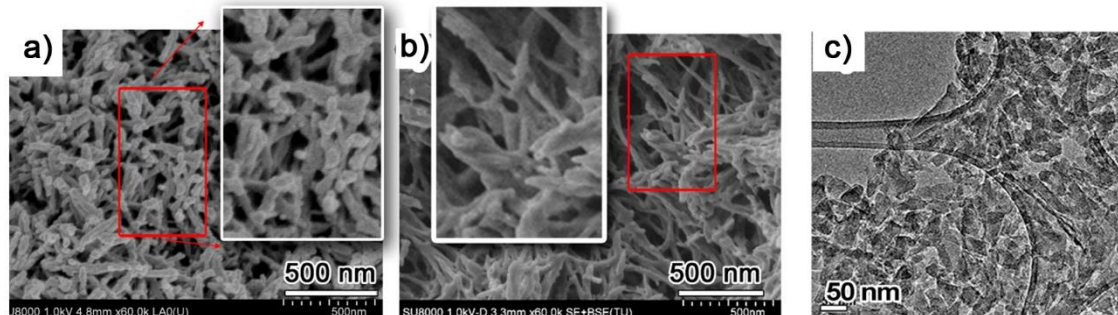
Figure 4.8 SEM images of a) GPT-O and b) GPT-20 after carbonization at 800 ºC; c) TEM of GPT-20 after carbonisation displaying the graphite nanoparticles. The inlets correspond to magnification of the areas framed by red squares.

Interestingly, the size of the graphite particles was almost identical to that observed for the structural fibres. This indicated an intimate interaction between graphite and starch. A plausible mechanism was the incorporation of graphite to the starch fibre causing the size restriction of the graphite particles, as shown in Figure 4.9. As an example of incorporation and size restriction, Star et al. showed that CNTs could be placed inside the helical chains of starch.[320] The possible causes for the size reduction of graphite nanoparticles during carbonisation have been discussed in Section 4.2.2.2.
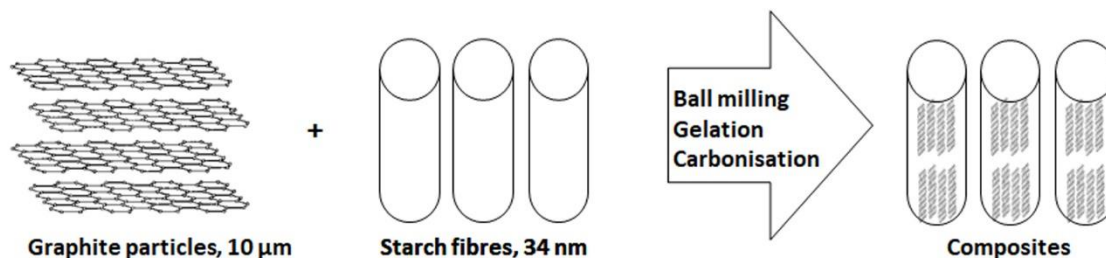
Figure 4.9 Hypothesised mechanism of interaction between graphite and starch in the Starbon®-graphite composites.

4.2.3.2 TGA

As shown in Table 4.2, increasing the concentration of graphite led to lower mass loss during carbonisation. Based on the mass residue after carbonisation, it was possible to estimate the final concentration of graphite in the composites (Table 4.7). The theoretical concentration of graphite was calculated according to the following formula:

178

$$T_g = \frac{m_{o,g} \cdot m_{r,g}}{m_{o,c} \cdot m_{r,c}} \cdot 100$$

Where T_g was the theoretical concentration of graphite, $m_{o,g}$ and $m_{o,c}$ were the initial mass of graphite and composite mixture respectively, expressed in g. $m_{r,g}$ and $m_{r,c}$ were the mass residue after carbonisation of graphite and the composite respectively, expressed as a fraction.

The actual concentration of graphite was calculated by subtracting the mass residue of GPT-0 to the composites´ residue. Surprisingly, the values obtained were significantly lower than the theoretically calculated (Table 4.7). These values agreed well with those obtained by XPS (Section 4.2.3.3). Such low experimental concentrations of graphite suggested decomposition of graphite during the carbonisation process, which was in good agreement with the observations made by SEM where the big graphite particles observed at 200 °C had disappeared at 800 °C. Plausible reasons for the unexpected decomposition of graphite were given in section 4.2.2.2. Nevertheless, further work is needed to explore how decomposition occurs.

Table 4.7 Final concentration of graphite (%) in the Starbon®-graphite composites carbonised at 800 ºC, calculated from TGA and XPS.

Material	Initial concentration of graphite (%)	Final concentration of graphite in the composites (%)		
		Theoretical	From TGA	From XPS
GPT-0	0	0	0	0
GPT-0.5	0.5	2	1	3
GPT-1	1	3	2	4
GPT-3	3	15	4	6
GPT-10	10	27	6	10
GPT-20	20	49	10	12

TGA spectra of GPT-0 and GPT-20 were further processed in order to understand whether the presence of graphite affected the decomposition pathway occurring during carbonisation. To achieve this, spectra were normalised to the actual starch content of

the materials and the derivatives were used to obtain the main points of decomposition, and finally the spectra of GPT-0 was subtracted to that of GPT-20 (Figure 4.10); negative values showed temperature ranges at which the decomposition of GPT-20 was slower than that of GPT-0; positive values indicated points at which the decomposition was accelerated due to the presence of graphite. Two main changes in the decomposition pathway could be observed:

- At ~200 °C the decomposition of GPT-20 was significantly slower than that of GPT-0, suggesting that the addition of graphite reduced the degree of decomposition at low temperatures. At this range of temperatures, the main process occurring was the crosslinking/dehydration of C-OH groups to form ether and carbonyl groups.[132] Pradhan *et al.* studied the interactions between starch and expanded graphite in composite materials, and showed that the C-OH groups of starch could be interacting with the expanded graphite. [304] These interactions may be occurring in the present work and could help anchoring some of the oxygen to the structure. The reduction of mass loss at this stage of the process was in good agreement with the suggested interaction between the C-OH functional groups of starch, and graphite as such interaction would decrease the C-OH available for decomposition.
- At 274 °C decomposition was accelerated, but the difference with GPT-0 was significantly lower than observed at 200 °C.

Minor increases in decomposition rates were observed at higher temperatures (420, 600 and 690 °C). These points, in addition to 274 °C, corresponded to the molecular transitions occurring during starch decomposition.[321, 322] Therefore, these results suggested that the presence of graphite may accelerate certain molecular transitions. This could be related to the good thermal conductivity of graphite, which would enhance heat distribution, and therefore decomposition, across the monolith.
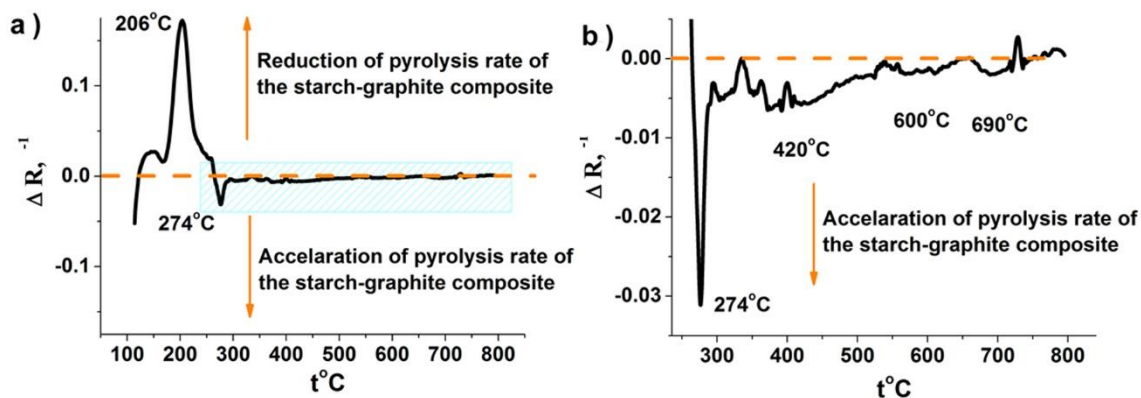
Figure 4.10 a) Subtraction of the GPT-0 1st derivate TGA pattern to the 1st derived GPT-20 TGA pattern, and b) zoom in the region of 300 -800 °C (figure was produced by Dr Peter Shuttleworth, at the Centro the Ciencia y Tecnología de Polímeros of the Consejo Superior de Investigaciones Científicas).

4.2.3.3 XPS

Deconvolution of C1s region of Starbon®-graphite composites exhibited six peaks corresponding to: double bonds between sp^2 carbons (C=C), single bonds between sp^3 carbons (C-C) and β carbons, hydroxyl groups (C-OH), ether groups (C-O-C), carbonyl functionalities (C=O) and carboxylic-type groups (O-C=O),[239] as shown in Table 4.8 and Figure 4.11.

Table 4.8 Quantification (%) of the carbon-carbon functional groups present in the Starbon®-graphite composites after carbonisation at 800 °C.

			Composite					
Peak	BE (eV)	Functional group	GPT-0	GPT-0.5	GPT-1	GPT-3	GPT-10	GPT-20
C1	284.6 ± 0.3	C=C	19	22	23	25	29	31
C2	285.0 ± 0.3	C-C	42	38	37	36	36	32
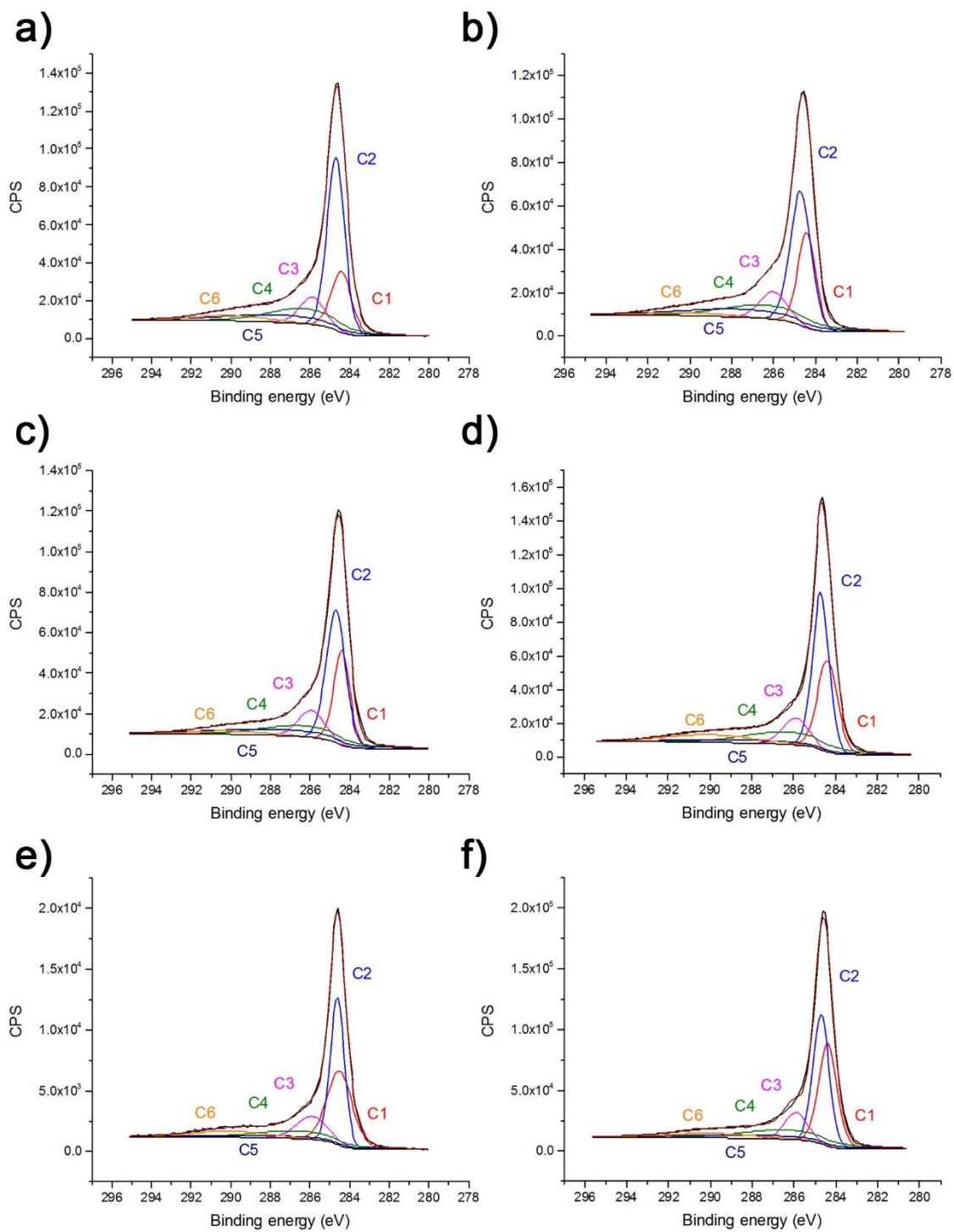
Figure 4.11 Deconvolution of C1s XPS spectra of a) GPT-0, b) GPT-0.5, c) GPT-1, d) GPT-3, e) GPT-10 and f) GPT-20 after carbonisation at 800 °C. C3, C4, C5 and C6 corresponded to C-OH, C-O-C, C=O and O-C=O groups respectively but their discussion was out of the scope of the project.

It was observed that the C1 peak corresponding to C-C (sp^2) bonds augmented with increasing amounts of graphite to the detriment of the C-C (sp^3) peak. This was expected due to the chemical configuration of graphite. However, the amount of graphite observed by XPS was significantly lower than predicted theoretically (Table 4.7). The final concentrations of graphite obtained by XPS were in good agreement with the ones calculated from TGA. The position and intensity of the carbon-oxygen peaks were very similar for all materials.

The elemental composition of the carbonised composites was measured by XPS (Table 4.9). It was expected that increasing amounts of graphite led to decreasing concentration of oxygen groups in the composites, as the added graphite did not contain oxygen functionalities. As expected, large concentrations of graphite led to lower number of oxygen groups. However, low concentrations of graphite favoured an increase in the concentration of oxygen atoms compared to original Starbon®. This phenomenon may be explained by the chemical interactions established between graphite and starch. Pradhan *et al.* studied the interactions between starch and expanded graphite in composite materials, and showed that the -C-OH groups of starch could be interacting with the expanded graphite.[304] These interactions may be occurring in the present work, and could help anchor some of the oxygen to the structure. This hypothesis was in good agreement with the delayed decomposition of the composites at low temperatures of carbonisation. In composites with high concentrations of graphite this effect could not be observed due to the large concentrations of graphite 'diluting' the concentration of the oxygen.

Table 4.9 Elemental composition (%) of the Starbon®-graphite composites calculated by XPS.

Element	GPT-0	GPT-0.5	GPT-1	GPT-3	GPT-10	GPT-20
C	91.8	86.0	82.6	95.6	97.3	96.0
O	7.2	10.4	11.4	3.9	2.5	3.5
S	0.6	2.0	2.4	0.2	0.2	0.2
Other	0.4	1.6	3.6	0.3	0.0	0.3

The presence of sulphur was also observed in the Starbon® monoliths prepared in Chapter 2 and its origin was attributed to the p-TSA added to catalyse the carbonisation. It was observed that the amount of S was lower for composites rich in graphite. This suggested that higher graphite concentrations interacted more with the sulfuric groups in the manner described in Section 4.2.2.2, adding evidence in favour of the decomposition mechanism. GPT-0.5 and GPT-1 displayed 3 and 4 times more amount of sulphur than the material with no graphite and further work is needed to understand this phenomenon. Traces of other elements were detected by XPS including Na, Ca and B. Traces of Na were contained in the p-TSA added to the sample.[323] B was found in stainless steel and could have been transferred from the vessels used for BM.[324]

4.2.3.4 XRD

XRD analysis was used to determine the size of the graphite nanoparticles at different stages of the process (i.e. BM, carbonisation), in order to corroborate the results obtained from SEM and TEM.

The diffraction pattern of graphite presented two peaks corresponding to the (002) reflections at 26.6 ° and 54.8 ° 2Θ, which was in good agreement with the literature.[325, 326] The small peaks observed around 45 ° 2Θ represented the (100) and (101) reflections.[327] A rhombohedral phase which normally coexists with the characteristic hexagonal phase can also be found in this region represented by the (101) and (012) reflexions.[327] The out-of-plane (L_c) crystallite size of the graphite nanoparticles could be determined by the Scherrer equation from the half maximum values of (002) respectively.[327, 328]

$$L_c = \frac{K \cdot \lambda}{\beta \cdot \cos \Theta}$$

184

Where the dimensionless factor K = 0.89, β = 180/(π·fwhm) represents the line broadening at half the maximum intensity (rad), λ is the wavelength of the X-ray (nm) and Θ is Braggs angle (°).

XRD also allowed to calculate the distance between the graphene layers conforming the graphite particles (d_{002}), expressed in nm, and the number of graphene layers present in a graphite nanoparticles (N) using the following formulas respectively:[328]

$$d_{002} = \frac{\lambda}{2 \cdot \sin \Theta}$$

$$L_c = (N - 1) \cdot d_{002}$$

The graphite particles presented an out-of-plane thickness of 37 nm. 30 min of BM reduced the size of such graphite particles by 32%, down to 25 nm for GPT-20. This translated into a shorter and wider peak at 26.6 ° 2Θ in the spectra (Figure 4.12). Nevertheless, the peak kept its sharpness, indicating that the integrity of the crystal structure was not significantly disrupted during the process. The d_{002} obtained for both graphite (no BM) and GPT-20 after BM was 0.334 nm. This was in good agreement with the d_{002} observed for graphite by other authors,[329] and indicated that BM did not distort the organization of the graphene layers, as d_{002} was not altered. The number of layers for graphite (no BM) and the GPT-20 mixture after BM was 111 and 76 respectively.
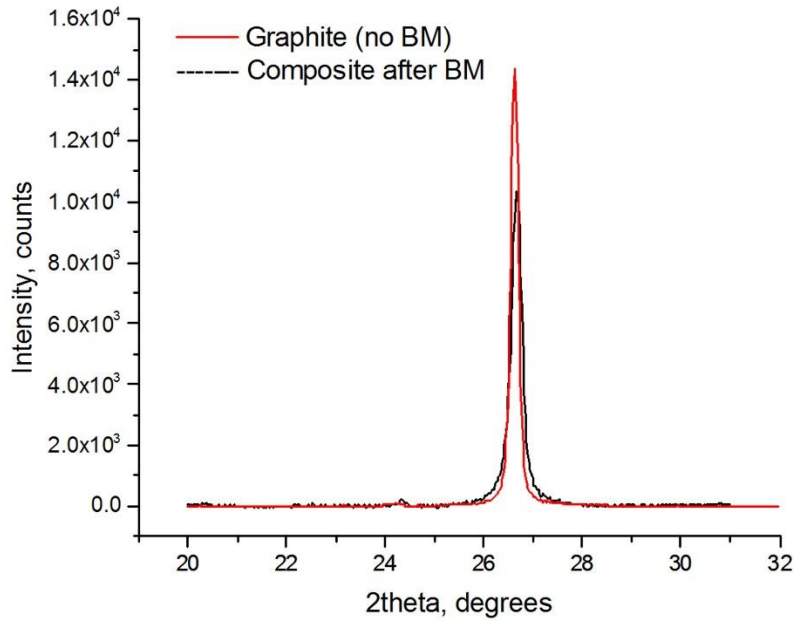
Figure 4.12 XRD patterns of graphite (no BM) and GPT-20 mixture after BM.

The carbonised Starbon®-graphite composites were also analysed by XRD. The diffraction pattern of GPT-0 showed a broad band between 20 and 25 ° 2Θ which has been associated to amorphous carbons.[308] The graphitic peak at 26.6 ° 2Θ was not present on the S diffraction pattern. On the other hand, the composites showed both the amorphous carbon band and the graphitic peak. The intensity of the amorphous band decreased, and the graphitic peak sharpened with increasing concentrations of graphite (Figure 4.13). MAGBON®, very similar materials to Starbon®, also presented the broad band between 20 and 25 ° 2Θ.[330]
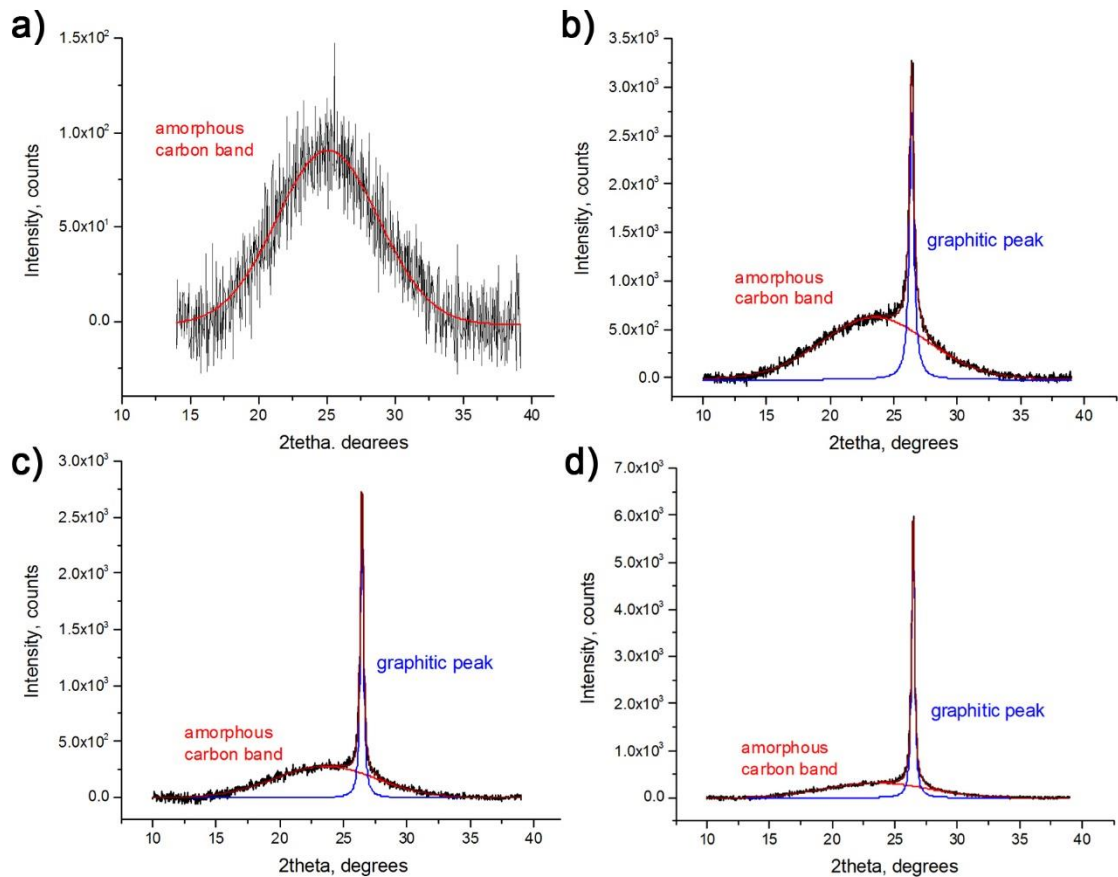
Figure 4.13 XRD patterns a) GPT-0, b) GPT-3, c) GPT-10 and d) GPT-20 after carbonisation at 800 ℃.

The out-of-plane size of the carbonised composites was calculated, and values are detailed in Table 4.10. It can be observed that the out-of-plane size was further reduced during carbonisation, from 25.2 nm to ~20 nm. Increasing amounts of graphite led to bigger graphite particles. However, the size reached a maximum for GPT-10 after which it was slightly reduced in GPT-20. The number of graphene layers found in the graphite particles for GPT-3, GPT-10 and GPT-20 after carbonisation was 57, 66 and 62 respectively, 18% lower than after BM and almost 50% lower than the initial graphite, which was in good agreement with the decomposition of graphite described in Section 4.2.2.2.

Carbonisation had a clear effect on the organisation of graphene layers. For example, increasing distance between layers at decreasing concentrations of graphite were

187

observed (Table 4.10). This trend was expected, as lower concentrations of graphite led to more turbostratic materials, in which the layers were not perfectly orientated and therefore the distance between them augment.

None of these values could be calculated for GPT-0 due to the lack of graphitic peak. However, the distance between graphene layers in ACs have been calculated elsewhere (0.36 nm).[331]

As seen in Section 4.2.3.1, TEM showed that the size of the graphite particles varied between 20 and 40 nm with maximum concentrations at 24 and 37 nm. The out-of-plane size of the graphite particles were in good agreement with these observations, as the obtained L_c values for the carbonised materials was just under 24 nm. Therefore, the results obtained by XRD added further evidence to the interaction mechanism shown in Figure 4.9.

Table 4.10 Size measurements of the graphite particles contained in the Starbon®-graphite composites, obtained by XRD analysis.

Material	GPT-0	GPT-3	GPT-10	GPT-20	GPT-20 (after BM)	Graphite (no BM)
L_c (nm)	-	18.8	22.0	20.4	25.2	36.9
N	-	57	66	62	76	111
d_{002} (nm)	-	0.337	0.336	0.336	0.334	0.334

4.3 Conclusion

Starbon®-graphite composites have been produced in the shape of discs by adapting the preparation method described in Chapter 2 for the formation of Starbon® monoliths. The composites combine the high mesoporosity of the Starbon® with the good electric conductivity of graphite. Two main alterations were introduced in the process:

- Ball milling was introduced as initial step of the process to enhance the interaction between starch and graphite. BM partially reduced the size of the graphite particles as shown by XRD, which improved its dispersion in the polysaccharide matrix and homogeneity of the composite.

- ScCO$_2$ drying was substituted by freeze-drying. Ethanol, which was used during the solvent-exchanging was also replaced by TBA as it has been shown that in combination with freeze drying this yields a hierarchical porous structure. Such structures have improved diffusion and mass transfer throughout the pores which has been shown to be advantageous for EDLC applications (intended for these materials).

The obtained materials were highly mesoporous with certain degree of macro- and microporosity. Increasing amounts of graphite favoured wider pores and higher conductivities.

Further characterisation was carried out in order to gain better understanding about the interaction established between graphite and starch. SEM showed that the thickness of the carbonaceous fibres found in the materials was almost identical to that of the graphite particles measured by TEM. This suggested inclusion of the graphite particles in the fibre and subsequent restriction of the size of such particles. This hypothesis was in good agreement with the findings from SEM, TGA and XPS, which indicated the decomposition during carbonisation of the graphite that was not closely interacting with the starch.

XPS showed a higher number of oxygen groups when low concentrations of graphite were used in to the composite. In addition, TGA showed a different decomposition pattern for composites rich in graphite and Starbon® in which the decomposition was slowed down at low temperatures (<250 ^{o}C). Both phenomena can be explained by the interaction of graphite with the C-OH bonds of starch, suggested in the literature for similar materials. Therefore, graphite and starch may be bonded through such functional groups.

The hierarchical porosity and the relatively high conductivity of the Starbon®-graphite composites in addition to the wide availability and low cost of the raw materials (starch and graphite) make these materials potentially good candidates to be used as electrodes for EDLC devices as well as other possible applications.

Power-full electrochemical double-layer capacitors based on Starbon® composites

Chapter 5

5 Power-full electrochemical double-layer capacitors based on Starbon® composites

5.1 Introduction

Renewables sources can fulfil many times the current energy requirements.[164] However, the main drawback of renewable sources is the lack of continuity in its generation, as production highly depends on the time of day and weather conditions.[169] Consequently, the development of energy storage devices that can accumulate the energy generated during off-peak times and released upon demand is vital to the success of renewable sources of energy.[170, 173] Energy storage is also beneficial for many other applications such as regulation of grid fluctuations, in transportation or to power portable electronic devices.[171] Much attention is being placed in small-scale storing devices such as batteries and EDLCs. A battery is capable of storing relatively high amounts of energy through a chemical process which can only be released slowly.[173] On the other hand, EDLCs store the energy physically by charge separation of an electrolyte which allows for rapid charge and discharge of the device.[181] However, EDLCs can only accumulate relatively low amounts of energy per gram.[181]

Due to the complementary properties of batteries and EDLCs regarding energy and power density, EDLCs are usually presented as auxiliary devices for batteries. For example, in hybrid and electric vehicles EDLCs provide energy for acceleration, hill climbing or starting in cold weather that batteries are not capable of supplying fast enough.[198] However, the numerous advantages of EDLCs including high cycle rate, environmental stability and safety have encouraged research on the development of EDLCs with larger capacitances that can compete with batteries.[179, 298]

The capacitance of an EDLC device is highly dependent on the porosity of the material that composes the electrode (i.e. surface area) and its conductivity.[181] Generally, large surface areas are found in highly microporous materials. However, very small micropores may not contribute to energy storage if they are not accessible to the electrolyte.[198] The presence of mesopores have shown to be advantageous as they facilitate the access to some micropores.[193, 332] On the other hand, large pores and contact between powder particles tends to increase the internal resistance of the material.[195] In order to develop EDLC devices with large capacity, composites containing a highly porous carbon doped with another conductive carbon are currently being developed. For example, CNTs and graphene enhanced the energy and power density when added to ACs.[219, 225] However, these conductive materials are expensive which increases the price of the final electrode.

The author believes that the Starbon®-graphite composites described in Chapter 4 could be excellent candidates for EDLC applications as they combine the relatively large and highly mesoporous surface area of Starbon® with the good conductivity and low cost of graphite. In addition, these composites can be produced in the monolithic form avoiding the use of binders that may deteriorate the performance of the EDLC.

5.1.1 Aims of the work

- Test the potential applicability of Starbon®-graphite composites as electrodes for EDLC devices by assessing their electrochemical properties using cyclic voltammetry, galvanostatic charge discharge and electrochemical impedance spectroscopy.
- Determination of the optimal amount of graphite in the composite to perform as EDLCs.

5.2 Results and discussion

Among all type of Starbon®, S800 presented the most suitable micro/mesoporous ratio (see Table 2.1 from Chapter 2) to produce electrodes for EDLC devices as highly

microporous materials with large surface areas are generally related to high storing capacitance when the majority of the micropores are accessible to the electrolyte.[333] This dependence on the surface area is due to the storing of the charge occurring at the interface between the electrode and the electrolyte, and not in the bulk of the material.[181] It has also been shown that the presence of larger pores (i.e. mesopores) improves the diffusion of the electrolyte, enhancing the capacitance of a material and accelerating the energy delivery rate.[333] Starbon® carbonised at lower temperatures (i.e. S300 and S450) present larger number of oxygen atoms in their structure (see Chapter 2). Although it has been shown that the occurrence of heteroatoms can enhance the capacitance of an electrode due to better wettability which improve the ion diffusion, and allow Faradaic redox reactions, it also increases the internal resistance and degradability of the electrolyte, lowering performance at fast scan rates and decreasing the number of cycles that the electrode can complete.[194, 334, 335] In accordance with all the above, S800 was chosen for the preparation of Starbon®-graphite composites which were used to produce electrodes for supercapacitor devices.

The physical and chemical properties of Starbon®-graphite composites were discussed in detail in Chapter 4 and the present chapter focuses on the determination of the electrochemical characteristics of these materials in order to assess their applicability as electrodes for EDLC devices.

Three electrochemical techniques are recurrently used in the literature to investigate the electrochemical properties of a material: cyclic voltammetry (CV), galvanostatic charge discharge (GCD) and electrochemical impedance spectroscopy (EIS).[333] Applying these techniques, it is possible to quantify essential parameters of a supercapacitor, including its energy and power density, capacitance, life-spam and internal resistance.[336] The experimental CV, GCD and EIS measurements were carried out in collaboration with Dr Enrique Morales Bergas at the Centro de Ciencia y Tecnología de Polímeros of the Consejo Superior de Investigaciones Científicas (Spain).

5.2.1 Cyclic voltammetry

5.2.1.1 Shape of the cyclic voltammogram

This voltammetric electrochemical technique measures the current generated after the application of an increasing voltage which cycles periodically.[337] It provides information about the permitted voltage window (the voltage range in which the electrolyte is stable) and the processes governing the energy storage.[333, 338-340] In an ideal supercapacitor the current is completely independent of the applied voltage as the storing process is purely electrostatic which is represented as a perfectly rectangular cyclic voltammogram.[181,333] The shape of the cyclic voltammogram can be altered by two main factors: Faradaic redox reactions that produce peaks of current at the characteristic voltage of the reaction, and the resistance to diffusion of the material which is responsible for diamond-like shaped cyclic voltammograms.[333] As the amount of oxygen in the composites was very low, as seen in Chapter 4, observation of current peaks derived from Faradaic reactions in the cyclic voltammogram were not expected. However, diamond-like shaped cyclic voltammograms are frequently observed for carbon electrodes at fast scan rates of analysis, when there is not enough time for the electrolyte to adequately diffuse in the porous structure of the electrode, lowering the surface area available.[341]

As observed in Figure 5.1a, Starbon®-graphite composites displayed rectangular cyclic voltammograms at slow scan rates (1 mV·s^{-1}). The lack of current peaks indicated that no Faradaic redox reactions contributed to the energy storing process. Nevertheless, the redox metal adsorption mechanism described in Chapter 2 suggested that Faradaic reactions may be occurring due to the oxygen containing functionalities present in S800. However, the small fraction of such groups (<5%) may have difficulted the observation of Faradaic reactions on the cyclic voltammograms. Further work is needed to elucidate the presence and role of Faradaic reactions. The increase in current observed at voltages close to 1 V was associated to the decomposition of the electrolyte, indicating that larger voltages should not be applied when working with an aqueous electrolyte.[342]

At fast scan rates (100 mV·s^{-1}), the presented a diamond-like cyclic shape. This phenomenon was more pronounced for GPT-0 and GPT-0.5, which could be explained by the presence of less accessible pores that difficult diffusion in which the electrolyte cannot easily penetrate, lowering the surface area available.[341] For instance, GPT-0.5 presented the highest fraction of micropores (45%), which have been shown to be less easily accessible to the electrolyte.[333] In addition, the pore size distribution of Starbon®-graphite composites discussed in Chapter 4 showed increasing pore sizes at high concentrations of graphite, which may facilitate the diffusion of the electrolyte in those materials. Other AC-carbon composites found in the literature also shown a diamond-like voltammogram at fast scan rates.[302, 343]
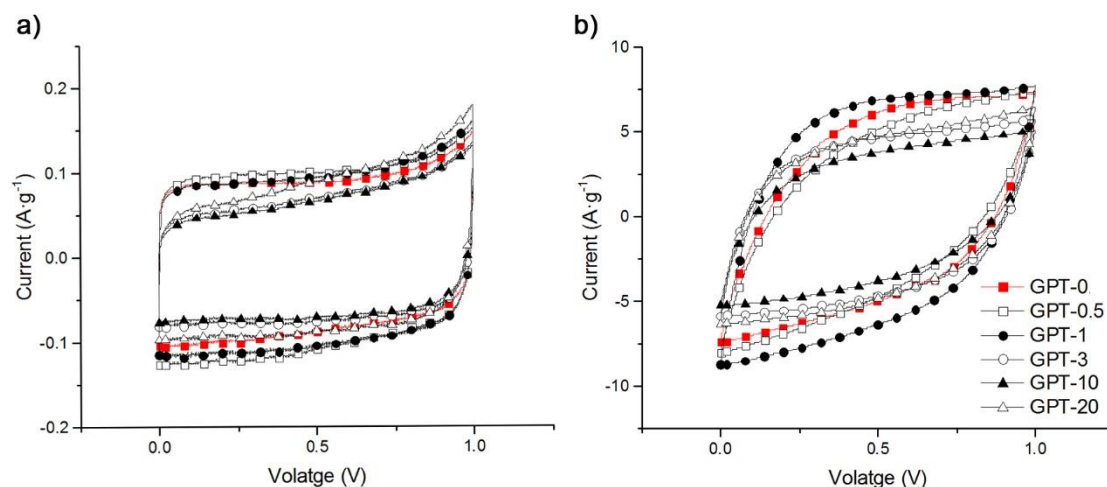
Figure 5.1 Cyclic voltammogram of GPT-0 (red) and the other Starbon®-graphite composites (black) at a) slow scan rates (1 mV·s^{-1}) and b) fast scan rates (100 mV·s^{-1}).

The capacitance of a material can be calculated from the area contained in the cyclic voltammogram. By comparing the curves of GPT-0 (red line) to the composites it was possible to observe that GPT-0.5 and GPT-1 presented larger capacitance than GPT-0 at slow scan rates. Similarly, GPT-1 showed larger area and therefore better capacitance than GPT-0 at fast scan rates. These observations were in good agreement with the capacitance values calculated in the following section.

5.2.1.2 Capacitance from the cyclic voltammogram

CV is generally used to determine the capacitance of an electrode using the following equation:[344]

$$C = \frac{(\int I\, dV) \cdot 2}{\Delta V \cdot m \cdot v}$$

where C is the electrode's capacitance, expressed in $F \cdot g^{-1}$, $\int I \cdot dV$ is the discharge part of the area contained in the cyclic voltammogram ($A \cdot V$), ΔV is the voltage window, expressed in V, v is the scan rate in $V \cdot s^{-1}$ and 'm' is the mass of active material (g) in one of the electrodes. The multiplier 2 is used to transform the capacitance of the system into the capacitance of the electrodes.

Capacitance is commonly measured in a wide range of scan rates, as this is important for practical applications.[345] Capacitance values closer to full performance can be obtained at slow scan rates.[338, 346] In this case, a range of scan rates from 1 to 100 $mV \cdot s^{-1}$ were screened (Table 5.1).

Table 5.1 Capacitance ($F \cdot g^{-1}$) values for Starbon®-graphite composites at different scan rates.

Material	Scan rate $mV \cdot s^{-1}$								
	1	2	5	10	20	40	60	80	100
GPT-0	176.1	167.2	163.0	143.1	125.0	105.3	97.2	85.7	76.8
GPT-0.5	200.0	187.7	175.4	154.1	130.9	105.9	89.3	77.6	67.5
GPT-1	198.4	192.0	187.4	167.7	147.8	126.2	112	102.0	93.0
GPT-3	158.3	148.0	145.9	130.6	115.5	99.3	88.9	81.1	74.0
GPT-10	157.8	144.2	136.2	119.8	102.9	84.5	72.5	64.2	57.2
GPT-20	205.4	185.1	176.0	154.1	132.3	109.8	95.6	86.2	78.1

Interestingly, at slow scan rates the highest capacitance was obtained with the composites that contained either very low (0.5 and 1%) or very large (20%) amounts of

graphite, displaying values close to 200 $F \cdot g^{-1}$ reaching a maximum value of 205.4 $F \cdot g^{-1}$ with GPT-20. These materials well exceeded the performance of the GPT-0, the material with no graphite (176.1 $F \cdot g^{-1}$), and a significant number of materials described in the literature which capacitances averagely varied between 75 and 175 $F \cdot g^{-1}$.[347] On the other hand, GPT-3 and GPT-10 presented significantly lower capacitance values. These materials exhibited low surface area compared to GPT-0, a parameter that has been shown to be closely related to capacitance.[181] Regarding GPT-3, its porosity was 15% lower than that of GPT-0. In turn, its capacitance at low scan rates was 10% lower than that of GPT-0. This suggested that the lower capacitance of GPT-3 was mostly caused by the reduction in surface area. GPT-10's surface area was 27% lower than that of GPT-0 and however, its capacitance only decreased 10%. To understand this phenomenon, it is necessary to clarify that the capacitance values were expressed per gram of active material (the Starbon® fraction, without including graphite mass) following the trend followed in the literature.[334, 344] GPT-10 contained almost twice as much theoretical graphite, and therefore less mass of active material. That is why, even though GPT-3 presented better absolute capacitance, the performance per gram of active material resulted almost identical for both materials. This effect was even more pronounced for GPT-20 where the amount of active material was halved compared to GPT-0. An explanation of why the theoretical amounts of graphite were chosen for the calculations, and a comparison with the capacitance values obtained from the experimental fractions can be found in later in this chapter, in Section 5.2.4.

The capacitance of all materials decreased with increasing scan rates. This phenomenon was commonly observed in the literature,[332, 343, 348] and it was due to the electrolyte not having enough time to penetrate in some of the smallest pores. At fast scan rates (100 $mV \cdot s^{-1}$), the largest capacitances were still given by composite materials with either very large (GPT-20) or very small (GPT-1) concentrations of graphite. In this case, the maximum capacitance of 93.0 $F \cdot g^{-1}$ was reached by GPT-1. The values obtained at fast scan rates were within the same range than those observed in the literature, and in some cases even higher.[332, 348]

A closer look showed that the capacitance was not lost at the same rate for all composites; for example, GPT-0.5 experimented the largest drop of capacitance, showing a 66% loss at 100 mV·s^{-1} compared to its performance at 1mV·s^{-1}. On the other hand, GPT-1 and GPT-3 were the most stable materials, losing 53% of their capacitance when the scan rate increased from 1 to 100 mV·s^{-1}. A similar phenomenon was also observed by Zheng et al. who compared the performance of micro and mesoporous materials.[332] They observed that the capacitance reduction was more pronounced for microporous materials.[332] This was in good agreement with the present work, where GPT-1 and GPT-3 presented the lowest fraction of microporosity and consequently a milder decrease of capacitance at increasing scan rates. The lower capacitance dependence on scan rates displayed by GPT-1 and GPT-3 was also favoured by the presence of short and homogeneous diffusion path lengths for the electrolyte in these materials.[349] This was in good agreement with the shorter Warburg regions observed for GPT-1 and GPT-3 (this is discussed in detailed later in this Chapter, in Section 5.2.3).[349] GPT-0 displayed an intermediate loss of capacitance (56%) which led to 76.8 F·g^{-1} at 100 mV·s^{-1}. This reduction was in good agreement with other commercial mesoporous carbons shown in the literature.[332] On the other hand, GPT-10 and GPT-20 experimented a sharp reduction of capacitance at increasing scan rates (64 and 62% respectively). Whereas the capacitance for GPT-20 was still high at 100 mV·s^{-1} due to its good performance at slow scan rates, GPT-10 was consistently the least capacitive material at both slow and fast scan rates, due to its low surface area and relatively large microporosity.
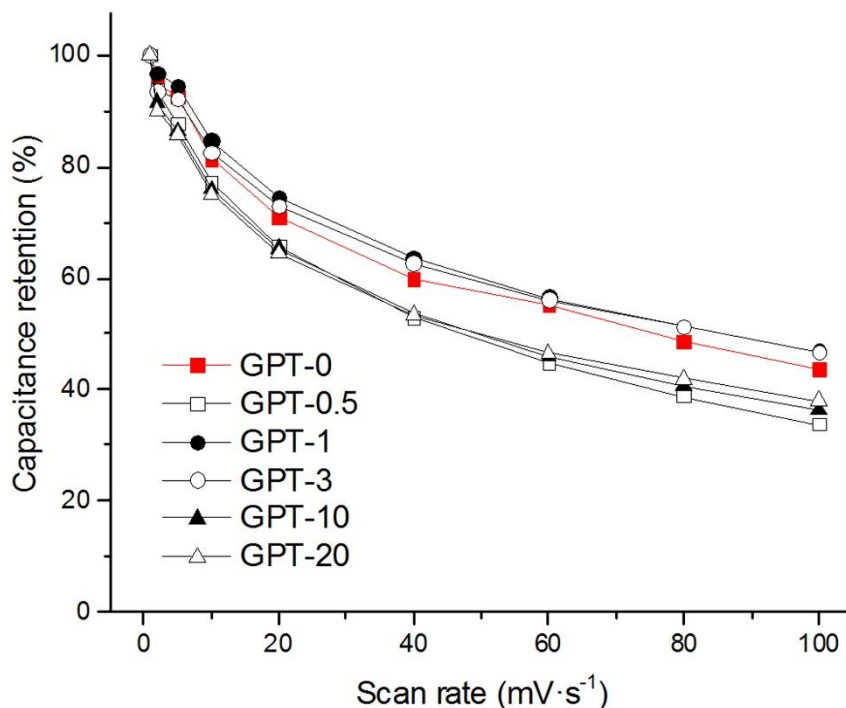
Figure 5.2 Capacitance retention (%) of GPT-0 (red) and the other Starbon®-graphite composites (black) at different scan rates (mV·s^{-1}).

The high values of capacitance shown by GPT-1 and GPT-20, two composites with very different composition and physicochemical properties, can be understood by looking at their surface area and conductivity:

- Surface area. As discussed in Chapter 4, graphite can be considered non-porous with a surface area of 47.8 m^2·g^{-1}. In consequence, the addition of graphite to Starbon® decreased the surface area of the composite with the exception of GPT-0.5 and GPT-1 in which small amounts of graphite led to slightly higher surface areas. When the majority of the pores are accessible to the electrolyte, a high surface area has been associated to better capacitive behaviour and thus,[333] the large values of capacitance observed for GPT-0.5 and GPT.1 can be explained by their good surface area (Figure 5.3).

- Conductivity/internal resistance. The conductivity of the composites significantly improved with increasing amounts of graphite. Therefore, the large capacitance

shown by GPT-20 was due to the good conductivity of these materials (Figure 5.3). From the data discussed in Chapter 4 it was noteworthy that GPT-10 presented higher conductivity and surface area than GPT-20 and however, it displayed lower capacitance. This phenomenon can be explained by the mass of active material contained in each composite; graphite is considered non-active due to its lack of porosity and therefore the amount of active material decreased with increasing concentrations of graphite being as low as 50% for GPT-20. Thus, although GPT-10 displayed higher absolute capacitance than GPT-20, the latter presented better performance per gram of active material.
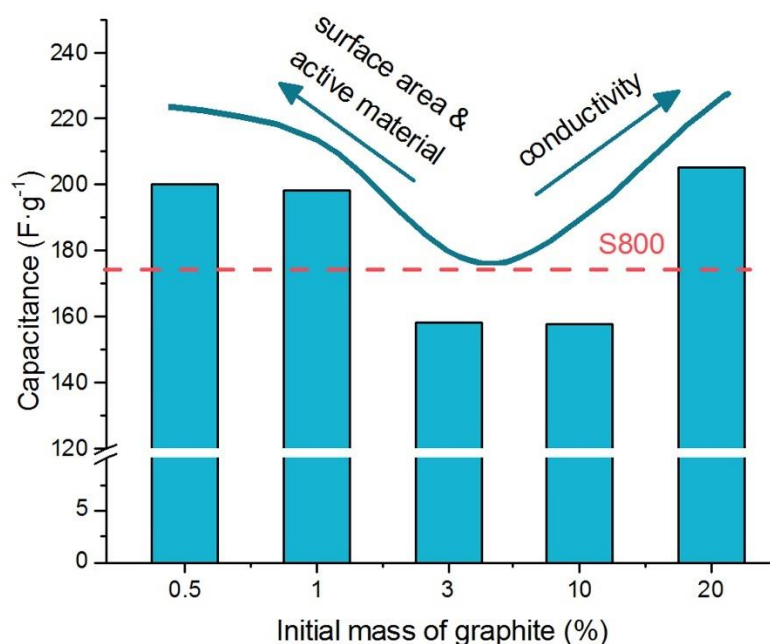
Figure 5.3 Schematic representation of the main factors affecting the capacitance of the Starbon®-graphite composites.

5.2.2 Galvanostatic charge discharge

5.2.2.1 Shape of the galvanostatic charge discharge curves

GCD is a static technique in which the variation of voltage with time is measured when a current pulse is applied.[350] This technique is used to assess the performance of the

supercapacitor, including its stability, capacitance, internal resistance and energy and power density.[351-353]

The triangular shape of the charge discharge curves observed in an ideal EDLC device indicates that the capacitance is mainly due to the double layer effect.[354] Faradaic reactions would distort the linearity of the discharge curve.[354] The equivalent series resistance (ESR) described below also affect the triangular shape, by creating an ohmic drop at the beginning of the discharge curve.[355]

As shown in Figure 5.4a, at low currents, the charge discharge curved for Starbon®-graphite composites were linear and triangular suggesting that the capacitive behaviour was mostly attributed to the double layer and no Faradaic reactions were taking place.[354] Nevertheless, as mention in Section 5.2.1, the oxygen-containing functionalities in S800 may be causing Faradaic reactions difficult to detect due to the low concentration of such groups (<5%). Both sides of the 'triangle' were symmetrical highlighting the good reversibility of all materials.[348] In addition, no ohmic drop was observed at low current densities which indicated good diffusion of the electrolyte into the materials' pores, as explained in detail later in this section. On the other hand, the galvanostatic curves obtained at high current densities presented ohmic drops for all materials (Figure 5.4b). Xu *et al*. who prepared similar composites of AC-CNT, also observed increasing ohmic drops at higher current densities.[348] GPT-0 and GPT-0.5 presented the largest ohmic drops reaching values of 0.89, in contrast to GPT-1 and GPT-3 with ohmic drops < 0.63. As the ohmic drop is related to the ESR, the differences observed can be explained by discussing the ESR which is the resistance of the system.[356] Several factors contribute to the ESR and such contributions can be grouped in two categories: electronic and ionic contributions.[353] The electronic contribution includes the intrinsic resistance of the active material, and the contact resistance between carbon particles, and between the electrode and the current collector.[357] The ionic contribution includes the ionic transport inside the pores, the double layer and the electrolytic solution.[353] In this work, the materials were built as monoliths and therefore the contact resistance between carbon

particles can be disregarded. In addition, the contact resistance between the electrode and the current collector, and the ionic transportation in the double layer and the electrolytic solution were common to all systems. Therefore, ESR provided information of the intrinsic resistance of the active material and the diffusion of the electrolyte in the pores. In accordance to this, higher ESR could be indicative of limited mobility of the electrolyte inside the porous structure.[358] Minimisation of all these factors can improve the performance of the system.[357]
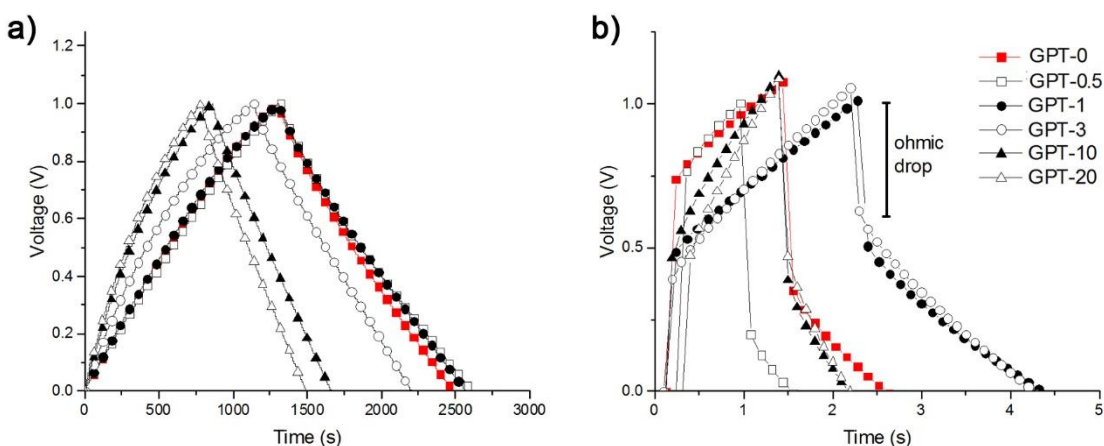
Figure 5.4 Galvanostatic charge discharge curves for GPT-0 (red) and the other Starbon®-graphite composites (black) at current values of a) 1 mA and b) 200 mA.

The ESR (Ω) can be calculated from the ohmic drop (V) observed in the galvanostatic charge discharge curves according to the follow equation:[354]

$$ESR = \frac{Ohmic\ drop}{I}$$

Where I was the applied current (A). Therefore, ESR values for the different materials were obtained from the slope of the plot representing the ohmic drop against current density shown in Figure 5.5 where higher slopes indicated larger values of ESR. Numeric values can be found in Table 5.2.
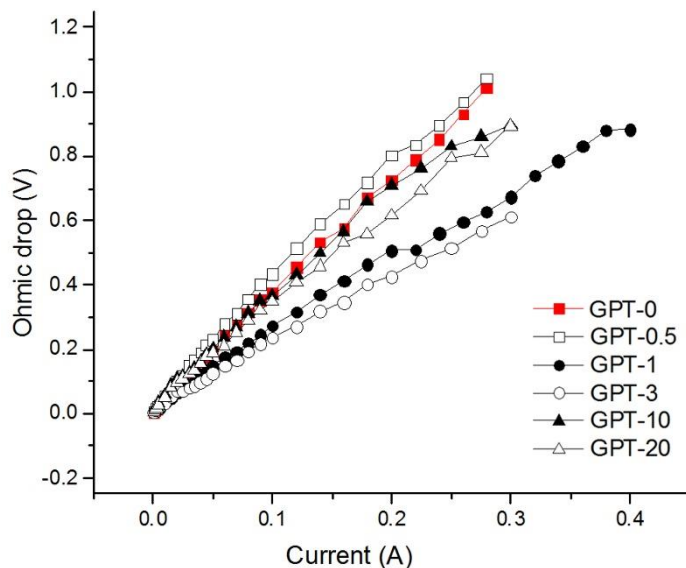
Figure 5.5 Relation between the ohmic drop (V) and the current density (A) of GPT-0 (red) and the other Starbon®-graphite composites (black).

As seen above and in Table 5.2, GPT-0 and GPT-0.5 showed the largest ohmic drops and therefore ESR (3.6 and 3.7 Ω respectively). This was indicative of high internal resistance and non-favourable distribution of the electrolyte. This was in good agreement with the low conductivity observed for GPT-0 in Chapter 4. In addition, those materials were highly microporous which has been previously associated to limited diffusion of the electrolyte.[332] On the other hand, GPT-1 and GPT-3 displayed the lowest ohmic drops, leading to ESR values of 2.2 and 2.0 Ω respectively. This was consistent with the lower microporosity and higher conductivity shown by these two materials compared to GPT-0, and indicated good diffusion of the electrolyte in their porous structure.[341] Consequently, despite its poor conductivity, the combination of high surface area, large pore volume and the presence of relatively large pores (d=11.4 mm) in GPT-1, favoured the diffusion of the electrolyte. Instead, GPT-3 displayed lower surface area and pore volume, but its good conductivity and relatively low concentration of small pores balanced this out, contributing to the good diffusion of the electrolyte. These results were in good agreement with the impedance results, discussed later in this chapter, in Section 5.2.3, where it was also possible to observe good electrolyte diffusion for GPT-1 and GPT-3. The microporous fraction of GPT-10 and GPT-20 was very similar to that of GPT-0. However,

the ESR values obtained for those materials were lower. This could be explained by the much higher conductivity displayed by this materials in comparison to GPT-0. Lu *et al.*, who prepared similar composite materials combining AC and CNTs, observed that the composites displayed lower ohmic drop compared to the AC, in good agreement with the results of the present work.[359]

Table 5.2 Equivalent series resistance (ESR) for Starbon®-graphite composites calculated from the galvanostatic charge discharge curves and expressed in Ω.

Amount of graphite (%)	0	0.5	1	3	10	20
ESR (Ω)	3.6	3.7	2.2	2.0	3.2	3.0

5.2.2.2 Coulombic efficiency

From the GCD curves was also possible to calculate the coulombic efficiency (CE) according to the equation described below.[360] CE shows how much of the energy stored during the charging process it is possible to recover during discharge.[353, 360]

$$CE = \frac{t_d}{t_c} \cdot 100$$

Where t_d and t_c are the times of discharge and charge respectively (s).

As seen in Table 5.3, the CE of the composites decreased with increasing concentrations of graphite when the measurements were performed at low current densities, reaching a maximum of 97.7% for GPT-0.5 and lowering to 89.0% for GPT-20. The CE for GPT-0 was comparable to that of GPT-20. This showed that low concentrations of graphite allowed to discharge almost all the energy stored during charging. However, in GPT-0 and high concentration composites, a loss of 10% was observed. The charge discharge efficiency has been shown to be between 0.85-0.98 and therefore the CE of Starbon®-graphite composites compared well with other electrochemical capacitors shown in the literature.[203] On the other hand, the opposite trend was expected, as increasing amounts

of graphite should favoured electron mobility in the network of the composite.[361] As values for comparison could not be found in the literature, future work is needed to understand this phenomenon.

The coulombic efficiency of some of the composites suffered a significant drop at high currents (24-47% variations) with the exception of GPT-1 and GPT-3 which CE only decreased 7.7 and 3.0% respectively. The enhanced performance of GPT-1 and GPT-3 could be attributed to better electron mobility which contributed to a more effective charging and discharging process and avoided energy loss as heat.[361]

Table 5.3 Coulombic efficiency (%) at low (1mA) and high (200 mA) working currents for Starbon®-graphite composites.

Graphite content (%)	CE at 1 mA (%)	CE at 200 mA (%)	CE variation (%)
0	90.9	66.7	24.2
0.5	97.7	50.0	47.7
1	96.6	88.9	7.7
3	93.5	90.5	3.0
10	92.6	46.2	46.4
20	89.0	54.5	34.5

5.2.2.3 Capacitance from the galvanostatic charge discharge curves

GCD can also be used to calculate capacitance applying the following equation:[362]

$$C = \frac{I \cdot \Delta t}{m \cdot \Delta V}$$

Where C is the specific capacitance (F·g^{-1}), I is the current during the discharge (A), Δt is the discharge time (s), m is the active mass of one of the electrodes (g) and ΔV is the voltage window applied (V).

The capacitance measured at low currents followed the same trend that the values obtained by CV, the composites with either very low or very large amounts of graphite are the ones showing the best capacitances (comparison between the different methods is displayed later in this chapter, in Figure 5.12). It is noteworthy that the absolute values are typically not comparable as both techniques are significantly different and therefore differences may occur.[363] The variations within the results generally arise from differences in the current density. According to Stoller *et al.*, who assessed the best practical methods to studied the electrochemical performance of supercapacitors, GCD was the preferred method to determine the capacitance of the system as this methodology correlated better on how a load is applied to supercapacitor devices.[354] Nevertheless, the obtained values were similar to those obtained by CV, and were found within or above the average performance displayed by other carbon materials used in EDLC devices (75-175 $F \cdot g^{-1}$).[347] The values of capacitance calculated from GCD at a current density of 1 mA are shown in Table 5.4.

Table 5.4 Capacitance ($F \cdot g^{-1}$) of Starbon®-graphite composites measured using the galvanostatic charge discharge curves.

Amount of graphite (%)	0	0.5	1	3	10	20
Capacitance ($F \cdot g^{-1}$)	177.4	212.7	204.5	148.5	137.6	172.4

GCD measurements were carried out within a range of currents from 1 mA to 280 mA in order to study the effect of increasing current in the capacitive behaviour. The capacitance values for different currents within a window between 2-280 mA ($\sim 0.2 - 25$ $A \cdot g^{-1}$) can be found in Appendix 2. Figure 5.6 displayed the relation between capacitance and current density. It showed that the capacitance of Starbon®-graphite composites was highly dependent on the current, especially at currents below 10 mA, as the capacitance decreased at least 15% in this region. The capacitance loss was similar for all materials at currents below up to 10 mA (current densities of ~ 1 $A \cdot g^{-1}$). However, at current values over 10 mA, GPT-1 and GPT-3 displayed lower dependency on current as the slope of

capacitance loss was less steep than that for the other materials. This can be attributed to a more favourable ion transportation of the electrolyte in these composites.[341] GPT-20 presented an intermediate slope, as its relatively high degree of microporosity may limit diffusion of the electrolyte, but its good conductivity can enhance the charge transport. Other carbon-carbon composites found in the literature also presented a steep slope at low current densities that turned less abrupt at higher energy densities. For example, Chen *et al*., who prepared AC-CNTs composites, also observed a steeper slope up to 1 A·g^{-1}, which progressively flattened.[361] In other cases, the capacitance dependence on current density was much lower and such phenomenon was ascribed to good porous network and god conductivity that allowed for enhanced diffusion.[341, 364] GPT-0, GPT-0.5 and GPT-1 were measured during the same experimental process, and therefore the peak observed at 13 A·g^{-1} it was likely caused by a defect during the experiment.
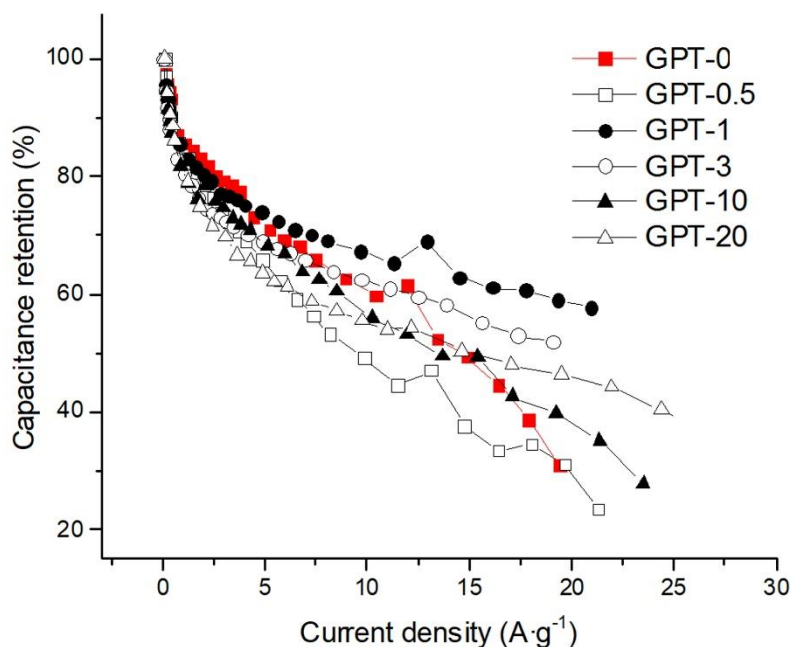
Figure 5.6 Effect of the current density on the capacitance of GPT-0 (red) and the other Starbon®-graphite composites (black).

5.2.2.4 Stability

10000 consecutive charge discharge cycles were performed to assess the stability of the materials over time. As shown in Figure 5.7a, all materials showed good retention of the initial capacitance, displaying over 86% of their original capacitance after 10000 cycles. In the inset of Figure 5.7a, it is possible to observe that the composites with larger concentrations of graphite (3, 10 and 20%) were more stable, showing over 95% of the initial capacitance after 10000 cycles. In contrast, GPT-0 showed the poorest stability, with a 14% decrease from its original capacitance (Table 5.5).
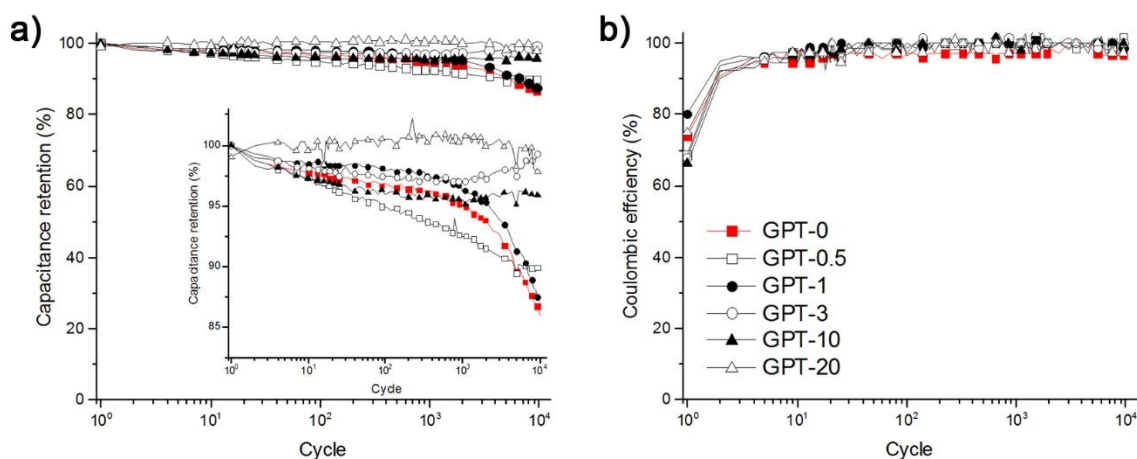
Figure 5.7 Performance of GPT-0 (red) and Starbon®-graphite composites (black) during the first 10000 cycles expressed as a) capacitance retention (%) and b) coulombic efficiency (%).

The enhanced stability of GPT-3, GPT-10 and GPT-20 may be attributed to the mechanical and textural properties of the composites resulting from the addition of graphite. For example, Noked *et al.* showed that the stability of AC was enhanced after the addition of CNTs.[365] Deng *et al.*, who observed that the addition of CNTs to AC nanofibers improved the cyclic stability of the materials, attributed this phenomenon to the fibrous-like structure of the composites, which prevented the exfoliation of the material.[341] As shown in Chapter 4, the sponge-like configuration observed in Starbon® changed to more fibrous-like structure for the Starbon®-graphite composites, which could explain the observed increased stability for the composites with higher concentrations of graphite.

Table 5.5 Capacitance retention (%) of Starbon®-graphite composites after 10000 galvanostatic charge discharge cycles measured at 25 mA.

Amount of graphite (%)	0	0.5	1	3	10	20
Capacitance retention (%)	86.0	89.9	87.1	99.5	95.9	98.0
Coulombic efficiency (%)	98.3	100	97.1	100	98.1	97.2

The coulombic efficiency is generally used to evaluate the stability of the electrodes over time.[354] As shown in Figure 5.7b, the CE of all materials was over 97% after 10000, which was indicative of good capacitive behaviour and cyclic stability.[366] Taking into consideration the current effects and allowing for the first scan difference, this was in good agreement with results observed in Section **Error! Reference source not found.**.

5.2.2.5 Energy and power density

Energy density is an important parameter for the characterisation of supercapacitors that measures the amounts of energy that can be stored by a specific material.[175] On the other hand, the power density determines how fast such energy can be released.[175] EDLC devices are characterised for showing rapid discharge rates (high power densities) but low energy densities when compared to batteries.[194] The reason for these differences lies on the way the energy is stored in each device; while batteries store the energy in the bulk of the material, EDLC accumulate the charge in the surface of the electrode.[181, 194] Therefore, EDLC are capable of much rapid deliveries as there is no ionic conduction limitation from the bulk of the electrode.[194] In addition, EDLCs do not present the kinetic limitations characteristic of the battery redox processes.[194] In turn, as EDLC devices can only store energy in the surface of the material, the amount of energy per mass of material accumulated by a battery is significantly higher.[194]

Energy (E), expressed in Wh·Kg^{-1}, and power density (P), in W·Kg^{-1} were calculated according to the following equation:[367-369]

$$E = \frac{1}{2} \cdot C \cdot (\Delta V)^2$$

$$P = \frac{E}{\Delta t}$$

Where C was the capacitance in $F \cdot g^{-1}$, ΔV represented the voltage of a full discharge disregarding the ohmic drop (V) and Δt was the discharge time in seconds disregarding the ohmic drop.

The Ragone plot of Starbon®-graphite composites is represented in Figure 5.8, from which it was possible to observe that power density significantly improved at increasing current values for all materials. This trend was also observed for other similar carbon composites materials in the literature.[348, 359, 370] Interestingly, the power densities of some of the materials stabilised and even decreased when the highest currents were applied. Highlighted in blue are the energy/power densities obtained at 280 mA (which was the highest current used in the experiment). As indicated by the blue markers, power density suffered a considerable drop for GPT-0, GPT-0.5, GPT-10 and GPT-20 in a lower extend, whereas the variation for GPT-1 and GPT-3 was minimal. This sudden decrease has been attributed by other authors to large values of internal resistance which caused dissipation of large amounts of energy during the charge discharge process.[370] This trend was in good agreement with the ESR values calculated above.

The highest power density was recorded with GPT-20, reaching 11.4 $kW \cdot kg^{-1}$ at a current of 180 mA. This was higher than the average power density observed in supercapacitor materials (1-10 $kW \cdot kg^{-1}$).[194] As an example, the AC-CNTs composites described by Xu *et al*. displayed a power density of 7.3 $kW \cdot kg^{-1}$ at similar current densities.[348] GPT-1 and GPT-3 showed maximum values of 9.9 and 10.4 $kW \cdot kg^{-1}$, at a current of 280 mA. Although the power densities observed for GPT-0, GPT-0.5 and GPT-10 were lower, these values were still in the same range than those for other carbon supercapacitors, being 5.7, 5.8 and 7.7 $kW \cdot kg^{-1}$ respectively, at current densities of 160, 160 and 180 mA.[194]

As seen in Figure 5.8, the energy density did not vary significantly at low current densities. In contrast, it drastically decreased at high currents for some of the electrodes. A similar trend was observed for similar materials in the literature. [348, 359, 370] This phenomenon responds to a significant amount of energy being dissipated as heat and can be explained through the energy density formula displayed above taking into account that the ohmic drop was subtracted from the voltage window. This formula showed that the energy density is proportional to the capacitance and the square of the voltage window, and therefore the ohmic drop.[369]

- At low current values, the ohmic drop was negligible and thus, the voltage window was close to 1 V. Therefore, the term of voltage window can be disregarded, and the energy density was proportional to the capacitance. According to this, the energy density followed the same trend than that observed for the capacitance values calculated by GCD, where GPT-0.5 and GPT-1 presented the highest values and GPT-3 and GPT-10 the lowest (Figure 5.9).

- On the other hand, at high currents the ohmic drop was more significant, lowering the value of the voltage window term (< 1 V). As the voltage factor was squared and lower than 1, it had more weight in the final result, and therefore the energy values decreased at high currents (Figure 5.9).

According to the above, materials with larger ohmic drops were expected to present a more significant drop in energy density. In agreement with the ohmic drops discussed in Section 5.2.2.1, where GPT-0 and GPT-0.5 presented the largest drops and GPT-1 and GPT-3 the smallest, GPT-0 and GPT-0.5 show the most noticeable reduction in energy density, by more than two orders of magnitude, at 280 mA. On the other hand, GPT-1 and GPT-3 showed a relatively small loss of energy density at the same current. As previously discussed, the ohmic drop represented the internal resistance and the resistance to the electrolyte's diffusion; the larger this resistance, the more energy was lost as heat, and therefore the less energy can be stored in a certain electrode.[358]
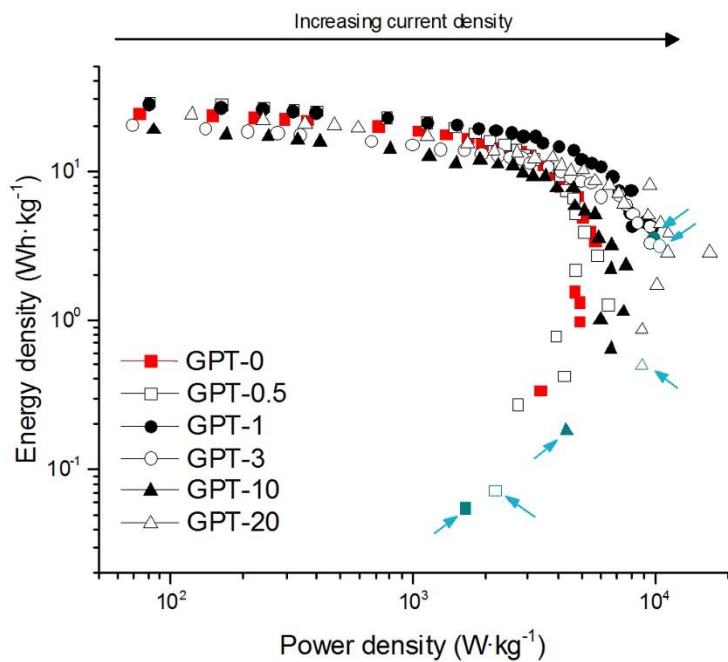
Figure 5.8 Ragone plot of GPT-0 (red) and the other Starbon®-graphite composites (black). The blue markers and the arrows represent the power and energy densities at the highest experimental current (280 mA).
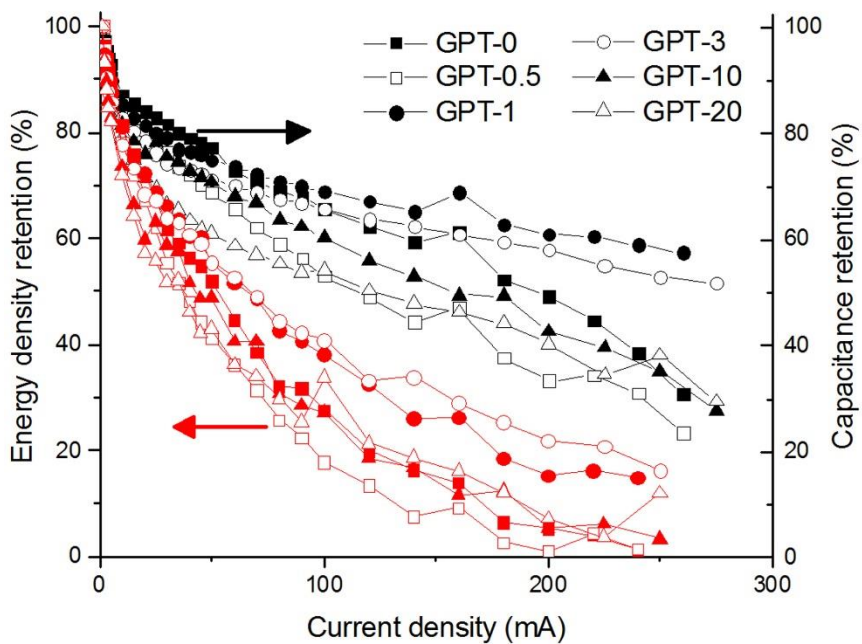
Figure 5.9 Comparison of capacitance (black) and energy density (red) retention of Starbon®-graphite composites.

5.2.3 Electrochemical Impedance Spectroscopy (EIS)

The term impedance refers to the opposition that a circuit presents to a passing current when certain alternating voltage is applied.[371] In an oversimplified manner, it can be described as the 'resistance' in an alternating current circuit.[372] Impedance also accounts for other phenomena that impede the current from flowing in a cell (e.g. capacitance, inductance, diffusion). Nevertheless, it is important to note that impedance is described in terms of both magnitude and phase, as opposed to a resistance that only presents magnitude.[372] Impedance can be, in turn, separated in two components: real and imaginary impedance, both measured in ohms. The real part of the impedance can be determined from the resistance, and the capacitance determines the imaginary part.[356]

EIS is a technique that allows one to measure the impedance of an electrode and allow to identify the different electrical properties of the material (i.e. capacitance).[372] To measure impedance, an alternating voltage is applied over a range of frequencies and the variations in magnitude and phase are analysed.[373] Data is usually represented in a Nyquist plot which shows the imaginary part of the impedance over the real impedance.[373] In an ideal capacitor, the Nyquist diagram displays a vertical line separated from the 'y' axis by the solution resistance (R_s).[374] However, a carbon supercapacitor generally displays three very differentiated regions in the Nyquist plot:[348, 349, 366, 370]

- At high frequencies, the current alternates very rapidly and the electrolyte has not enough time to diffuse inside the pores. Therefore, this region is characterised by a lack of mass transfer and the aggregation of the charge in the surface of the electrode which is directly in contact with the bulk of the electrolyte only.[375] At these frequencies, the device presents a dominant resistive nature.[358]
In the Nyquist plot this region is generally represented by a semicircle. The point at which this semicircle intercepts the 'x' axis is known as the R_s (Figure 5.10), which comprises the resistance of the electrolyte in contact with the current collector and the electrode.[358, 376] By extrapolation of the linear section at low

frequency regions and the 'x' axis it is possible to calculate the internal resistance of the material.[354, 376] The other extreme of the semicircle is known as the knee point, at which the capacitive behaviour starts.[370] The diameter of the semicircle provides the values of ESR (Figure 5.10) which gives information about the resistance to the electrolyte's diffusion in the porous structure.[358] Higher ESR are related to poor diffusion, whereas lower ESR indicates good distribution of the electrolyte through the porous structure.[358]

It is noteworthy that different interpretations of the Nyquist plot semicircle were found in the literature.[348, 349, 366, 376] The methodology followed in the present work was adopted following discussion consulted with the electrochemical expert who collaborated in the project.[363]

- The capacitive behaviour observed at medium frequencies is mainly derived from macro- and mesopores because the frequency alternates slower than at high frequencies and the electrolyte can diffuse in the large pores (i.e. meso- and macropores).[375]

In the Nyquist plot this region, also known as Warburg section (Figure 5.10), can be usually identified by a straight line at an angle of approximately 45° with the 'x' axis at the knee point.[349] It indicates that ion diffusion is frequency dependent.[349]

- At low frequencies, the current alternates slowly giving time for the electrolyte to penetrate even in the smallest pores, which now can contribute to the capacitance (Figure 5.10).[375] In the Nyquist plot appears as a vertical straight line after the Warburg region.[377]
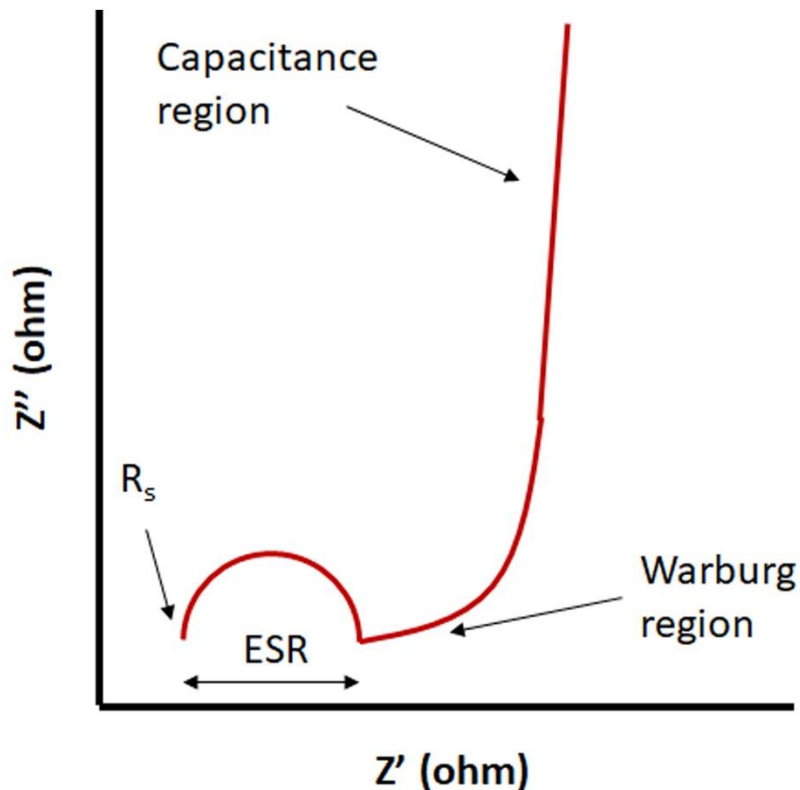
Figure 5.10 Schematic representations of the typical Nyquist plot of a carbon electrode.

To measure the impedance, an alternating voltage was applied at different frequencies within the range of 0.005 and 500000 Hz. Figure 5.11 shows the Nyquist plot of Starbon®-graphite composites in which it is possible to observe that all materials presented the characteristic shape given by carbon supercapacitors, with a straight and almost vertical line at low frequencies, a Warburg region in the middle area and a semicircle at high frequencies.

A closer look to the high frequency regions (inset of Figure 5.11) showed that the intercept of the semicircle with the 'x' axis, which represented the R_s of the system, slightly decreased at increasing concentrations of graphite (see Table 5.6). This could be indicative of a lower contact resistance between the electrode and the electrolyte. A similar phenomenon was observed by Yi *et al.*, which who prepared mesoporous carbons doped with CNTs. Yi *et al.* results showed lower R_s values for the composite materials

compared to the sample with no CNTs. This suggests that a higher degree of graphitization reduced the contact resistance between the electrode and the electrolyte.

The values of ESR were obtained from the diameter of the semicircle and are listed in Table 5.6. The semicircles with the largest diameter, and therefore the largest ESR values, were shown by GPT-0.5 and GPT-0. On the other hand, the smallest ESR was displayed by GPT-3 followed by GPT-1. Although the absolute values did not match those obtained by GCD, the trend observed was the same, and therefore the same reasons explained in Section 5.2.2.1 apply here. The absolute values calculated by EIS were smaller than those obtained by GCD, which has also been observed in previous studies.[358]

The knee point (Table 5.6), which shows the starting point of the capacitive behaviour, is marked by end of the semicircle.[370] As the R_s values (beginning of the semicircle) were very similar for all materials, the knee points followed the same trend observed for the ESR where GPT-3 displayed the earliest knee point. Its capacitive behaviour appeared at higher frequencies (540 Hz) than for the other materials, which was indicative of better rate performance.[370]

All six materials presented a Warburg region as seen by the angled lines appearing after the knee point in the inset of Figure 5.11. This phenomenon indicated that the diffusion in Starbon®-graphite composites was frequency dependent.[349] At low frequencies, all materials presented an almost vertical straight-line indicative of pure capacitive behaviour.[229] An ideal capacitor would present a vertical line parallel to the 'y' axis.[378] Gamby *et. al* suggested that deviations from the ideal model are due to the wide pore size distributions observed in carbon materials, as the penetration depth of the alternate signal decreased with frequency.[377] According to this, in carbons with wide pore size distribution the signal would only penetrate in the largest pores at a specific high frequency. At lower frequencies, the signal would be capable to penetrate in smaller pores, resulting in a deviation from the vertical line.[229] The present work was in good agreement with the results observed for other carbon and carbon-carbon composites

described in the literature; such materials also presented deviation from the ideal behaviour.[341, 343, 361, 379]
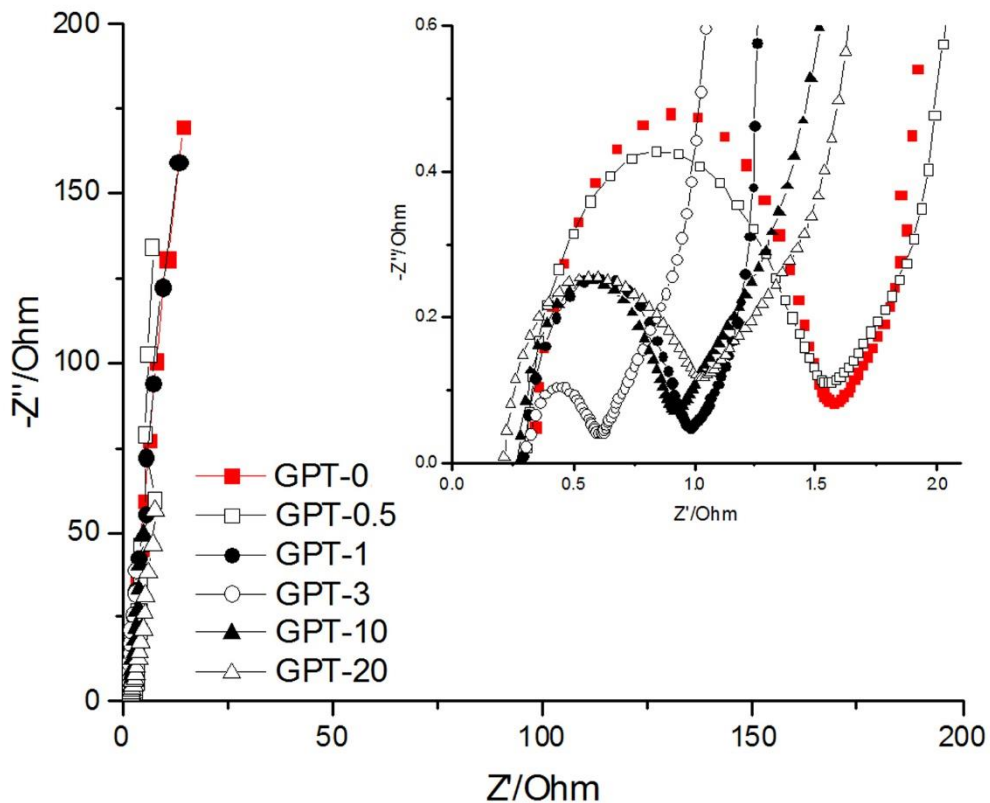
Figure 5.11 Nyquist plot of GPT-0 (red) and the other Starbon®-graphite composites, and the amplification of the high frequency region (inset).

Table 5.6 Parameters of the Starbon®-graphite composites, obtained from the high frequency region of the Nyquist plot.

Material (% GPT)	Rs (Ω)	Knee point (Ω)	Knee point frequency (Hz)	ESR (Ω)
0	0.35	1.57	113	1.22
0.5	0.31	1.55	87	1.24
1	0.30	0.99	149	0.69
3	0.31	0.61	540	0.30
10	0.28	0.92	439	0.64
20	0.22	1.03	236	0.81

The capacitance of the electrodes was calculated from the impedance data using the following equation:[335]

$$C = \frac{1}{\pi \cdot f \cdot Z'' \cdot m}$$

Where C was the capacitance in F·g^{-1}, f represented the frequency in Hz, Z'' was the imaginary part of the impedance in Ω and m the active mass of the electrode in grams. As discussed above, the absolute values of capacitance calculated from different techniques are typically not compared. However, the results obtained from EIS showed a similar trend to those obtained from CV and GCD (Figure 5.12), with very low or very high amounts of graphite leading to the best capacitance values. Nevertheless, the obtained values were similar to those obtained by CV, and were found within or above the average performance displayed by other carbon materials used in EDLC devices (75-175 F·g^{-1}).[347]
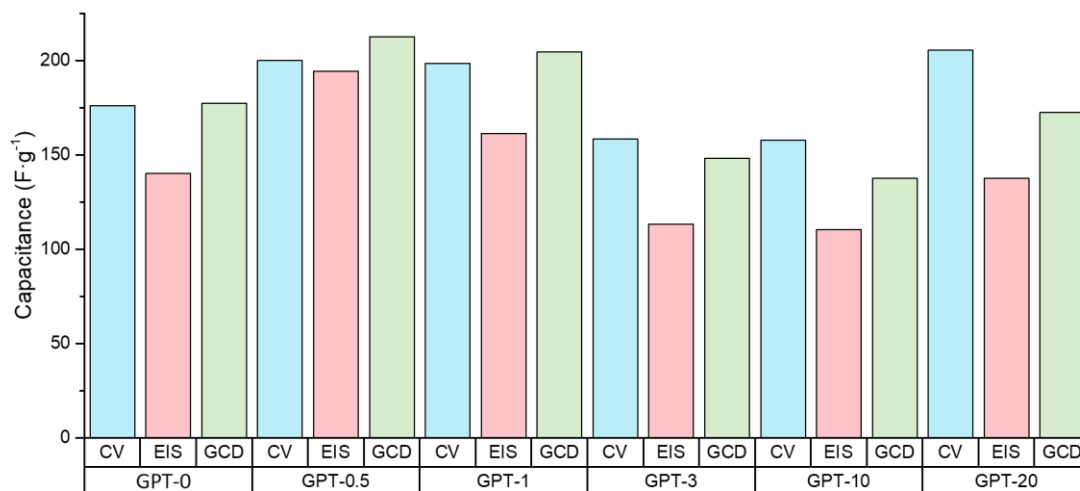
Figure 5.12 Capacitance (F·g^{-1}) of Starbon®-graphite composites calculated by CV (blue), EIS (red) and GCD (green).

The phase angle is the phase difference between voltage applied to impedance and the current driven through it.[372] The representation of this parameter over frequency is known as the Bode plot and gives information about the capacitive behaviour of an electrode.[372] Figure 5.13a, showed phase angles close to -90° at low frequencies for all samples which suggested good capacitive behaviour, as the phase angle for a pure capacitor is -90°.[372, 380, 381] On the other hand, pure resistors present a phase angle of 0°.[372]

GPT-0.5 followed by GPT-1 presented the closest values to -90° with 87.0 and 85.3° respectively indicating enhanced capacitive behaviour compared to the other composites. This was in good agreement with the lower ESR observed for GPT-1 and GPT-3 in Section 5.2.2.1. The peak observed at high frequencies of the Bode plot was related to the semicircle observed in the Nyquist plot.

The real (C') and imaginary (C'') parts of the capacitance, expressed in F, were calculated according to the following formulas:[378]

$$C'(\omega) = \frac{-Z''(\omega)}{\omega \cdot |Z(\omega)|^2}$$

$$C''(\omega) = \frac{Z'(\omega)}{\omega \cdot |Z(\omega)|^2}$$

Where Z' and Z'' are the real and imaginary parts of the impedance, ω is the angular frequency and $|Z(\omega)|$ is the modulus of the impedance.

C' was plotted against frequency as displayed in Figure 5.13b. This graph is good indicative of whether the maximum value of capacitance has been reached.[378] It was possible to observe that capacitance was highly dependent on frequency, as al low frequencies the capacitance increased dramatically. Although the values of capacitance observed at very low frequencies in the C' plot where in the same range to those calculated from the

constant current experiments, the maximum capacitance (shown at 0.005 Hz) were lower than those calculated by CV and GCD in previous sections. This phenomenon suggested that at such frequency not all the pores were filled with electrolyte and therefore the maximum capacitance was not reached.[378, 382]
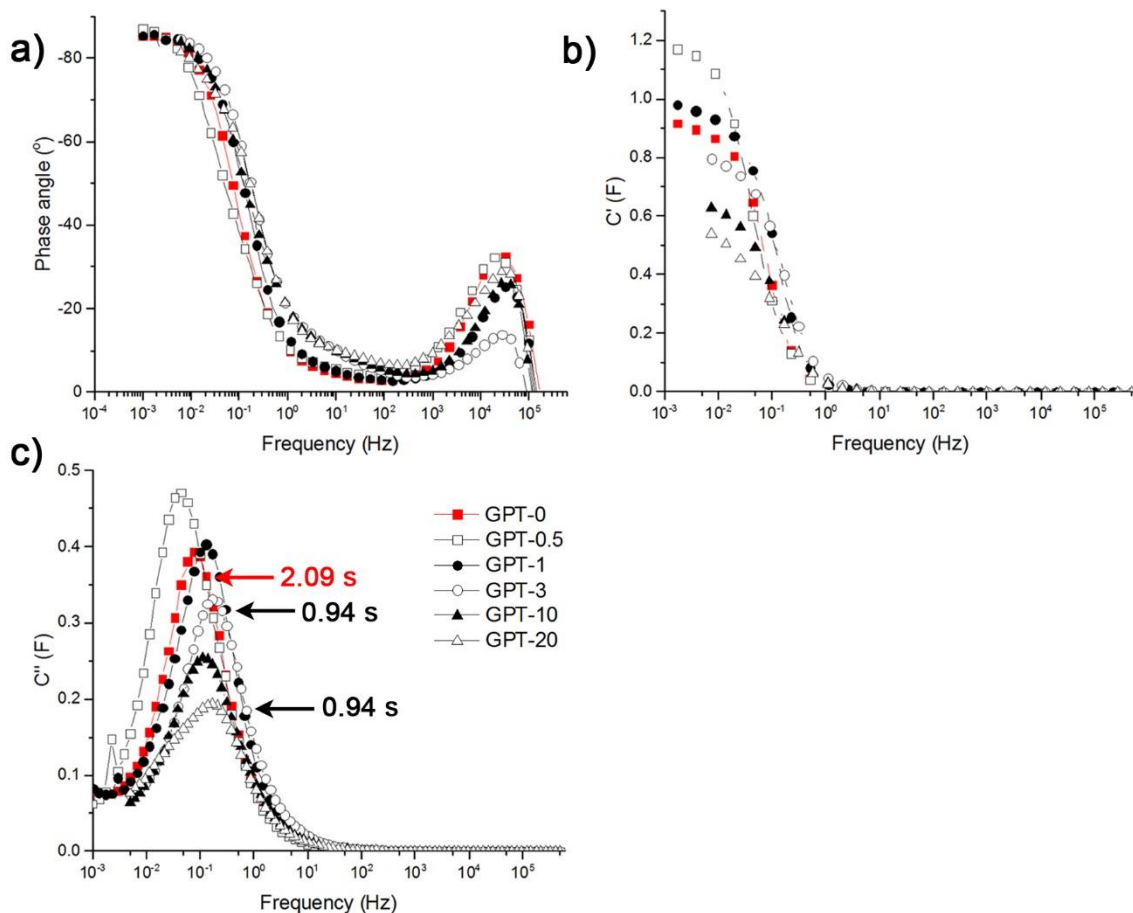
Figure 5.13 a) Phase angle (°), b) real (C') and c) imaginary (C'') capacitance (F) of Starbon®-graphite composites as a function of frequency.

Figure 5.13c displayed the imaginary capacitance over frequency. The peak observed at low frequencies in the C'' graph can provide with valuable information about the relaxation time (τ_0) of certain material, which indicates how fast the electrode can be charged or discharged. Fast relaxation times have been associated to better reversibility and efficiency.[344] Such a parameter can be calculated from the frequency at the peak's maximum (f_0 in Hz) through the following formula:[378]

$$\tau_0 = \frac{1}{f_0}$$

The results are listed in Table 5.7 where it was possible to observed that GPT-3 and GPT-20 offered the fastest discharge times with 0.94 s, followed by GPT-1 with a discharge time of 1.22 s. GPT-10 also presented a fast relaxation time (1.43 s). These short relaxation times can be explained by their relatively good conductivity, as seen in Chapter 4, and their good diffusion properties, as discussed in the present chapter. The enhanced relaxation time of GPT-3 was in good agreement with the low ESR obtain for this material. Although GPT-1 presented slightly better ESR and therefore better diffusion of the electrolyte, GPT-20 was more conductive, which resulted in slightly lower relaxation times compared to GPT-1. On the other hand, GPT-0 and GPT-0.5 presented the longest discharge time with 2.1 and 3.6 s respectively due to their poor conductivity and larger resistance to diffusion of the electrolyte. The relaxation times described in the present work were within the range of those described for similar carbon and carbon-carbon materials.[344,383] For example, the ordered carbonaceous materials described by Feng *et al*. displayed relaxation times higher than most of the Starbon®-graphite composites (1.58 and 2.43 s).[344] On the other hand, Portet *et al*. showed that CNTs displayed faster relaxation times (0.7 s).[383] Nevertheless, this was partially attributed to the lower capacitance of the material and not entirely to an outstanding performance as supercapacitor.[383]

Table 5.7 Relaxation time (s) of Starbon®-graphite composites.

Composites	GPT-0	GPT-0.5	GPT-1	GPT-3	GPT-10	GPT-20
Discharge time (s)	2.09	3.60	1.22	0.94	1.43	0.94

5.2.4 Effect of the active material on capacitance

The capacitance values calculated in this chapter used the theoretical concentration of graphite after carbonisation to calculate the values of capacitance. It was noteworthy that

the real concentration of graphite calculated by TGA and XPS in Chapter 4 was lower that the theoretically calculated. The capacitance values using the experimental values obtained by XPS are displayed in Table 5.8.

Table 5.8 Comparison of the capacitance values (F·g⁻¹) calculated using experimental and theoretical concentrations of graphite in the material.

Technique	Capacitance (F·g⁻¹)					
	GPT-0	GPT-0.5	GPT-1	GPT-3	GPT-10	GPT-20
CV - Theoretical	176.2	200.0	198.4	158.2	157.8	205.4
CV - Experimental	176.2	202.9	200.2	143.6	127.3	118.5
GCD - Theoretical	176.2	212.7	204.5	148.5	137.6	172.4
GCD - Experimental	176.2	216.2	206.1	134.5	111.0	99.6
EIS - Theoretical	176.2	194.4	161.4	113.4	110.5	137.5
EIS - Experimental	176.2	197.6	162.8	102.7	89.1	79.4
Difference (%)	+0	+1.6	+0.9	+9.4	-19.4	-42.2

Composites with low concentrations of graphite presented almost identical values of capacitance to those described above. This can be explained by the very low variation in graphite content calculated from the theoretical and experimental method. On the other hand, significant changes were observed for GPT-10 and GPT-20 which capacitance calculated from the experimental values were up to 30 and 80 F·g⁻¹ lower. Such variation was due to the difference between the theoretical and experimental concentrations (17 and 37% lower for GPT-10 and GPT-20 respectively). The theoretical and experimental concentrations of graphite in GPT-3 differed in 10% and therefore the variations observed in capacitance were < 15%. Although the experimental values were lower, they still fell within the average values of capacitance observed for carbonaceous electrodes and in some cases were even higher than other materials described in the literature.[194, 343, 364] For example, the AC-CNTs composites developed by Azam *et al*. and the mesoporous carbon-CNTs composites described by Qian *et al*. displayed maximum capacitance values of 60 F·g⁻¹.[343, 364]

The theoretical values were chosen to carry out the electrochemical studies in order to study the maximum performance that could be achieved with Starbon®-graphite composites.

5.3   Conclusion

The results discussed in this chapter showed that Starbon®-graphite presented high capacitance values, displaying similar or higher values than other composite materials in the literature and reaching 177.4 and 212.7 F·g^{-1} respectively. In all cases, the capacitance was due to the double layer effect. It has been shown that the addition of graphite during Starbon® preparation can improve the performance of this material as an electrode for energy storage applications. Interestingly, different concentrations of graphite enhanced different electrochemical properties:

- Low concentration of graphite in the composites (GPT-0.5) led to values of capacitance over 200 F·g^{-1} at low current densities due to the enhanced surface area observed in this material. On the other hand, such capacitance was significantly reduced at increasing current densities. This type of material also presented large resistance to diffusion of the electrolyte symbolised by a high ohmic drop that led to substantial reductions of the energy density at high current values. The coulombic efficiency, although very high at low current densities, decreased drastically at high currents. This material also displayed a 10% reduction of its original capacitance after 10000 cycles.
- Medium concentrations of graphite (GPT-1 and GPT-3) presented the optimal porous network in terms of electrolyte diffusion which was indicated by low ohmic drops and small reduction of capacitance, power and energy density at increasing current densities. In addition, GPT-1 presented high values of capacitance, over 200 F·g^{-1} at low current densities and just below 100 F·g^{-1} at high values of current. On the contrary, due to its lower surface area, GPT-3 displayed much lower values

of capacitance. On the other hand, GPT-3 showed excellent capacitance retention (99.5%) after 10000 cycles while GPT-1 retained 87%.

- Large concentrations of graphite (GPT-20) led to relatively high values of capacitance (172 $F \cdot g^{-1}$) at low current densities. Nevertheless, these results were lower than those showed by GPT-0. This type of composite presented values of power density that exceed the average results found in the literature and can retain 98% of its initial capacitance after 10000 cycles. On the other hand, the capacitance was not well preserved with increasing current densities and the coulombic efficiency was also notably affected by increasing the current.

   GPT-10 also contained large amounts of graphite. However, it displayed the smallest value of capacitance due to its low surface area and the relatively low concentration of active material in comparison to GPT-20.

Overall, GPT-1 presented the optimal textural properties that allow for good diffusion of the electrolyte and high capacitance, energy and power density.

Concluding remarks and future prospects

Chapter 6

6 Conclusions and future work

6.1 Concluding remarks

6.1.1 Development of Starbon® monoliths and their application for precious metal adsorption

Chapter 1 showed that minor adjustments in the method to produce Starbon® enabling the preparation of these materials in the monolithic shape. The possibility to shape the materials opened a new range of potential applications for Starbon®, such as flow chemistry and energy storage where monoliths and disc shapes, respectively, are required.

The general properties of the monoliths were similar to those of powdered Starbon®, including large and mesoporous surface area, and tuneable surface chemistry, which can range from hydrophilic to hydrophobic by adjusting the temperature of carbonisation. Nevertheless, interesting differences in total pore volume and pore size distribution resulted by the modifications in the preparation method.

Starbon® powder first, and monoliths later, were tested for the adsorption of precious metals. Au^{3+}, Pd^{2+} and Pt^{2+} were adsorbed at different extend. Nevertheless, Starbon® (in particular S800), displayed much higher adsorption capacity for Au^{3+} (~ 600 mg·g^{-1}). The adsorption of gold was very rapid (equilibrium reached in ~10 min) and monolayered. The mechanism of adsorption consisted on the oxidation of the Starbon® surface and the reduction of the Au^{3+} ions to for Au NPs. This mechanism allowed for a green process, as the recovery of precious metals from waste streams was complemented by the *in-situ* formation of a high value-added product, supported Au NPs. This kind of nanoparticles have shown to play a significant role in today's chemical industry, from catalysis to medical applications. Therefore, Starbon® supported Au NPs could be potentially used as

catalysts in industrially relevant processes. In addition, the *in-situ* utilisation of the recovered metals avoided the need for metal desorption which could require significant amounts of solvent.

Starbon® selectivity adsorbed precious metals when synthetic and real waste mixtures containing a range of base metals including Zn^{2+}, Ni^{2+} and Cu^{2+} were employed, and even when the concentration of such base metals was 100 time higher than the precious metals.

Interestingly, the Au NPs observed were very different depending on the initial concentration of the metal solution or the presence of other components in solution. Whereas complex real waste mixtures led to small and homogeneously distributed NPs, single metal studies with a high initial concentration of gold in solution led to the formation of gold nanoshells, agglomerations of NPs with good optical and electrical properties and that can find application in cancer treatment.

Starbon® monoliths were incorporated to a flow system to test the potential of these materials in flow chemistry experiments. It was possible to continuously feed metal solution for up to 11 h. After that time, the interface between the monolith and the tubing surrounding it was damage and therefore optimisation of the system is still required. Nevertheless, this experimental work showed the potential of Starbon® monoliths for flow chemistry applications.

Overall, the present work showed the good potential applicability of Starbon® for the selective recovery of precious metals, with particular attention to gold, from complex waste solutions.

6.1.2 Preparation of Starbon®-graphite composites and their application for energy storage

Starbon®-graphite composites that combined the highly porous structure of Starbon® and the good electric conductivity of graphite were developed by adjusting the original preparation method of Starbon®. The introduction of ball milling, and the substitution of $scCO_2$ for freeze drying led to composites in which the starch and graphite were homogeneously mixed, leading to a hierarchical porous structure that contained macro-, meso- and micropores. The literature demonstrated that the presence of large pores can improve the diffusion through the pores, which can be beneficial for many applications including energy storage by electrochemical double layer capacitors. In addition, the composites were shaped as discs, without the need to use binding agents that could negatively affect the electric properties of the material.

Starbon®-graphite composites were tested as electrodes in energy storage devices. The electrochemical properties of the new materials were comparable to those shown in the literature for similar materials and reached capacitance values of 205.4 $F{\cdot}g^{-1}$. Both physical and electrochemical properties were highly dependent on the amount of graphite added to the composite. Whereas small concentrations of graphite maintained or even improved the high surface area of Starbon®, a larger fraction of graphite led to the formation of bigger pores but lower surface area; nevertheless, the high conductivity of graphite led to high values of capacitance. In addition, it was observed that composites with relatively small concentration of graphite presented the most favourable structure for electrolyte diffusion. Therefore, the optimal composition for energy storage applications was found to be 1% of graphite. This material was conductive, allowing for good diffusion of the electrolyte and its hierarchical structure did not decrease the available surface area nor the capacitance to store energy.

Overall, the new Starbon®-graphite composites and in particular those with 1% of graphite, presented favourable textural and electrochemical properties for their

applications in energy storage devices. In addition, the materials were produced in the required shape for the application without the need for binding agents which can worsen the final properties.

6.2 Future work

Regarding metal adsorption, the overall continuation of the project should be focus on moving the research towards the commercialisation stage by understanding the interaction of Starbon® with other elements contained in solution and improving the current flow system to resist the characteristic acidic media of waste metal solutions. In relation to the development of energy storage materials, the future work should aim to enhance the properties of the new materials in order to make them cost effectively compared to similar materials described in the literature. Specific actions are described in more detail below.

6.2.1 Techno-economic assessment of the potential scale-up of Starbon® as adsorbent and metal-loaded catalyst.

The work carried out in this thesis showed the potential of Starbon® to be used for the recovery of precious metals from waste solutions. Future work is now required to assess the scalability of the process including life cycle assessment, volume of demand and volume of PM-supported catalysts that could potentially be produced.

6.2.2 Understanding the partial desorption of gold at early stages of the kinetic studies.

The kinetic studies showed that some of the gold initially adsorbed by S450 was desorbed after 120 min into the experiment. The literature describes how the oxygen functionalities of carbonaceous materials could be affected by the presence of strong acids. As the experiments were carried at pH 0, it may be possible that some of these functional groups that interact with gold ions decompose and therefore the gold was returned to solution. Nevertheless, further work is needed to corroborate this hypothesis, including replicas of

the experiments; due to the cost of PMs and the ICP-MS analysis, it was not possible to repeat the kinetic experimental work. Replicas will also bring reassurance to the models applied in Section 2.2.4.6.2.

6.2.3 Understanding the interaction between Starbon® and other elements in solution

The XPS spectra of Starbon® materials after adsorption showed the presence of chlorine atoms. The deconvolution of the Cl2p region suggested that both chloride ions and chlorine atoms bonded to carbon were present on the Starbon® surface. Although the presence of chloride ions was expected due to the predominant electrostatic adsorption mechanism taking place for Pd and Pt, and partially observed for Au, the occurrence of C-Cl was not anticipated. Therefore, further work is required to verify the signal observed by XPS and to understand the mechanism for the formation of such C-Cl bonds during the adsorption process.

As demonstrated in Chapter 3, the use of Starbon® to recover precious metals from complex mixtures showed partial adsorption of some metals – tin, molybdenum and lead. Further work is required to calculate the maximum adsorption capacity for these metals, as well as a complete mechanistic study.

6.2.4 Experimental comparison with activated carbon

The adsorption capacity of Starbon® for precious metals have been compared to those of similar carbon materials found in the literature. This comparison showed that S800 perform similarly or superiorly than other bio-derived materials. The adsorption rate presented by Starbon® is expected to exceed that of AC, due to the larger pores of the former compared to the characteristic highly microporous surface of AC. If confirmed, this would be indicative of enhanced performance of Starbon® over activated carbon. An in-depth study of the kinetics of gold adsorption by ACs could corroborate such a hypothesis.

6.2.5 Investigate the lack of gold in the surface of S300 after adsorption from real waste

ICP showed good adsorption of gold by S300 from real waste solutions (~125 mg·g^{-1}). However, XPS did not detect gold at the surface of the material. From these ICP results and the XPS analysis performed in Chapter 2, it was expected to clearly observe gold by XPS. Therefore, further work is required to understand such discrepancies between techniques.

6.2.6 Optimise the design of the monolith reactor system to carry out continuous flow adsorption

A flow system that incorporated Starbon® monoliths was developed to carry out continuous adsorption experiments. The monoliths were fixed to a Swagelok tubing using epoxy resin. Although the system was functional during the first few hours, the constant supply of an acidic solution for a prolonged period of time damaged the interface between the epoxy resin and the monolith. The actions described below can help to improve the current system and should be explored:

- Washing the Starbon® monolith before attaching it to the Swagelok tubing would remove the impurities without shortening the lifespan of the flow system by prolonged washing times.
- Using an alternative material to attach the monolith to the tubing. This material should present higher resistance to acidic media and should not form nanoparticles in contact with the gold solution.
- Developing an entirely new approach to incorporate the monolith into a flow system. An alternative method could be using heating shrinkable tubing, which would fix the monolith by shrink to its diameter by application of heat. The heating shrinkable tube could be then incorporated to the flow system by shrinking its extremes to the relevant piece of tubing.

- In addition, connecting the system to a UV-vis detector is also advised for future experimental work, as it could help to understand the flow process and provide information about co-operative adsorption.

As mentioned above, studying the desorption of metals from the Starbon® surface was considered out of the scope of the present project because the long-term objective was to use the metal-loaded materials developed during adsorption as catalysts for flow chemical processes. Therefore, once the flow system is optimised, the metal-loaded Starbon® materials should be tested as catalysts in a range of flow chemical reactions including hydrochlorinations, Heck or Suzuki reactions.

6.2.7 Understanding the effect of the metal solution on the monolithic Starbon®

In Chapter 3, it was shown that some liquid tar residue from carbonisation could be trapped on the Starbon® pores. A solution passing through the monolith 'flushed-out' those molecules. To further corroborate those results, it would be very interesting to run N_2 adsorption porosimetry on Starbon® after the adsorption experiment, as larger pore volumes and surface areas are expected.

6.2.8 Investigating the effect of graphite on the coulombic efficiency

The coulombic efficiency of Starbon® composites displayed decreasing values with increasing amounts of graphite. This was opposite to the expected trend, as the presence of conductive graphite was predicted to enhance the electron mobility of the material and therefore the coulombic efficiency. Therefore, further work is needed to understand the effect of graphite on the coulombic efficiency of the composites when used as EDLC.

6.2.9 Investigating the evolution of graphite during carbonisation of the Starbon®-graphite composites

The results obtained by TGA and XPS, in combination with the literature suggested that graphite could be partially transform to graphite oxide during carbonisation. Unlike graphite, graphite oxide can be decomposed during carbonisation. In addition, it was suggested that the sulfur groups from p-TSA could lead to the formation of sulfuric acid vapours under the carbonisation conditions, which would favour the oxidation of graphite. Further work is needed to corroborate this hypothesis and get a more in-depth knowledge of the processes taking place during carbonisation. TG-IR could provide great insight in the process, as it would give information on the main functional groups present at the different stages of the carbonisation process. This could ultimately enable control over the amount of graphite lost during carbonisation and therefore tailor the electrochemical properties of the final material. In addition, this work could also provide insight on the evolution of conductivity with the concentration of graphite, to understand the plateau observed for GPT-20.

6.2.10 Developing and characterising new Starbon® composites

The good properties displayed by the Starbon®-graphite composites strongly suggest that the preparation of Starbon® composites with other materials could expand and further improve their properties. Reduced graphene oxide is an interesting option, as it presents high surface area, good electrical conductivity and has shown good capacitance and electrochemical properties in previous studies.

6.2.11 Understanding the role of oxygen-containing groups on the electrochemical properties of the materials.

S800 presents a small fraction of oxygen-containing functionalities (<5%) that may be responsible for certain Faradaic behaviour. However, such Faradaic effect was not clearly visible on the cyclic voltammograms nor the galvanostatic charge discharge curves.

Therefore, further work is needed to understand whether these reactions actually occur and their role in the capacitance of the materials. Starbon® materials carbonised at higher temperatures contain less oxygen groups (e.g. 1000 ^{0}C). Accounting for variations due to changes in porosity, a disparity in the capacitance values could indicate whether or not the oxygen-containing groups led to Faradaic reactions and therefore had an effect on the capacitance of the material.

6.2.12 Determination of the equivalent electric circuit of Starbon®-graphite composites

The main electrochemical properties of Starbon®-graphite composites have been determined in Chapter 5. In order to gain further knowledge about the electrochemical behaviour of such materials it would be useful to develop an equivalent circuit which models the system and allows predicting performance under different conditions.

6.2.13 Study the electrochemical properties of Starbon®-graphite supercapacitors using alternative electrolytes.

It has been shown that the use of non-aqueous electrolytes, such as organic compounds and ionic liquids, improve the electrochemical stability window at which a supercapacitor can operate. This enhances the amount of energy density that the material can store and therefore increasing the commercial applicability of these devices.

Experimental

Chapter 7

7 Experimental

7.1 Chapter 2: Preparation and characterisation of Starbon® monoliths and their application in precious metal adsorption.

7.1.1 Materials and chemicals

Purified high amylose starch was supplied and used as received from National Starch Food Innovation Plc. (UK) Analytical grade ethanol and acetone were purchased from VWR (UK). Monohydrate p-toluenesulfonic acid 98.5% pure was ordered to Sigma Aldrich (UK). Gold (III) chloride, Au 64.4% min, was acquired from Alfa Aesar (UK). Palladium (II) chloride 98% pure was purchased from FluoroChem (UK) and platinum (II) chloride 73% pure was received from Acros Chemicals (Belgium). TraceSELECT® 37% HCl and 69% HNO_3 were purchased from Fluka Analytical (UK). 0.1 M HCl and NaOH were bought from Fisher Chemical.

7.1.2 Preparation of Starbon® monoliths

4 g of high amylose corn starch were mixed with 12 mL of water and thoroughly stirred for 5 min. The mixture was subsequently gelatinised by heating at 140 °C for 10 min in a CEM II discover microwave by applying 150 W. After gelation, the obtained gel was poured into a cylindrical mould and subsequently cooled at 5 °C for 48 h. Water present in the gel was progressively exchanged with ethanol by plunging the gel in 12.5 mL of ethanol, which was refreshed every 24 h for a week. Monolith was dried using scCO₂ in a 500 mL SFE500 extractor at 40 °C and 150 bar with a flow rate of 30 g $CO_2 \cdot min^{-1}$ for 4 h. Ethanol was used as co-solvent in this process for the first 2 h. Then, the material was introduced in a solution of p-toluenesulfonic acid in acetone (5% w/v) for 2 days. The solvent was removed in a Heidolph rotary evaporator. The pressure in the rotary evaporator was reduced from atmospheric pressure to 14 mbar during the course of 4 hours. The material was subsequently heated under vacuum in a Barnstead Thermolyne

6000 furnace up to 300, 450 or 800 °C. The carbonisation programme followed is summarised in Table 7.1. The monoliths were grinded using a pestle and mortar and the particle size was homogenised to 300 μm with a sieve, prior the adsorption experiments.

Table 7.1 Carbonisation programme employed for the preparation of Starbon® monoliths.

Step	Initial temperature (°C)	Final temperature (°C)	Ramp rate (°C·min^{-1})
1	25	120	2
2	120	160	0.5
3	160	250	0.3
4	Hold for 3 h at 250 °C		
5	250	350	0.4
6	350	800	2

7.1.3 Scanning electron microscopy

SEM analysis was conducted in collaboration with Ms Meg Stark at the Technology Facility in the Department of Biology of the University of York, UK. SEM analysis was carried out using a JEOL JSM-6490LV. Samples were mounted on alumina plates and coated with a 7 nm layer of Au/Pd using a high-resolution sputter SC-7640 coating device prior to analysis.

7.1.4 N$_2$ adsorption porosimetry

N$_2$ adsorption porosimetry was used to determine surface area, micro- and mesopore volume of Starbon®. The analysis was carried out using an ASAP 2020 volumetric adsorption analyser from Micrometrics in which the measurements were performed at 77 K. Pre-carbonised and carbonised samples were degassed at 40 °C and 130 °C respectively for 6 h prior to analysis.

The Brunauer-Emmett-Teller (BET) theory was used to determine the surface area, and the Barret-Joyner-Halenda (BJH) equation was applied to calculate mesoporous volume

and pore size. The Dubinin-Radushkevich method was used to evaluate micropore volume.

7.1.5 Thermal gravimetric analysis

TGA was carried out using a Netsch 409 STA thermal analyser. Sample was loaded in a 3.5 ml ceramic crucible and heated to 800 $^{\circ}$C under N_2 flow (100 mL min^{-1}) at a constant rate of 1 $^{\circ}$C·min^{-1}. To identify the temperature regions in which significant mass loss occurred during heating, first derivate was applied to TGA curves.

7.1.6 Infrared spectroscopy

IR analysis was performed using a Perkin Elmer Spectrum 400 FT-IR/FT-NIR Spectrometer fitted with a Universal ATR Sampling Accessory. The spectrum was scanned from 4000 to 600 cm^{-1} with a resolution of 4 cm^{-1}.

7.1.7 X-ray photoelectron spectroscopy

XPS analysis was carried out by the team of the National EPSRC XPS Users' Service facility at Newcastle University (UK). The Thermo Scientific™ K-Alpha™+ X-ray Photoelectron Spectrometer fitted with a micro-focussed monochromatic Al Kα source. Samples were mounted on microscope glass covers using double-sided tape and were subsequently wrapped in aluminium foil to protect them during transportation to the analysis facility. Data analysis was performed with CasaXPS software and the binding energy of C 1s was calibrated to 284.6 eV.

7.1.8 Point of zero charge

0.01 M sodium chloride solution was prepared by dissolving 58.4 mg of solid chloride in 100 mL of deionised water. 5 mL of the stock solution were transferred to a sample vial where it was degassed by bubbling N_2 into the solution for several minutes. The pH was subsequently adjusted to 2 in an Jenway 3500 pH Meter fitted with Simple junction

universal pH electrode. The process was repeated to prepare a range of solutions with pH values between 2-8. The pH of the solution was adjusted using 0.1 M HCl and 0.1 M NaOH.

15 mg of Starbon® were added to each solution and vials were immediately sealed and subsequently stirred for 24 h. After this time, the solid was separated from solution by centrifugation for 3 min at 3500 rpm with a Heraeus Megafuge 40R Centrifuge from Thermo Scientific. The pH of the solution was measured (final pH). The final pH was plotted against the initial pH values, as shown in Figure 7.1. The point at which the experimental line cuts the 'initial pH = final pH' line is the point of zero charge.
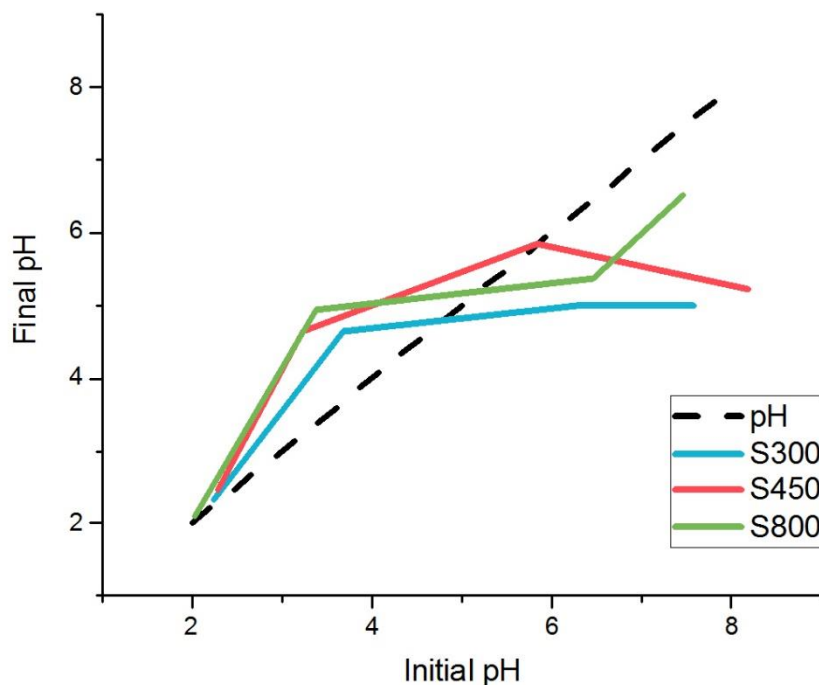
Figure 7.1 Influence of Starbon® in the pH of fixed pH solutions, and the corresponding point of zero charge of S300, S450 and S800.

7.1.9 Metal adsorption isotherms

An acidic stock solution of $AuCl_3$ was prepared by adding 0.37 g of $AuCl_3$ to 50 mL of 3M HCl. The concentration of the stocks solutions was 4000 mg·L^{-1} and was subsequently

diluted to prepare a range of lower concentrations (100-4000 ppm). In all cases pH was adjusted to 0 using TraceSELECT® 37% HCl. 10 mL of each solution were stirred with 10 mg of Starbon® for 24 h. Then, the adsorbent was separated from the solution by centrifugation for 10 min at 3500 rpm with a Heraeus Megafuge 40R Centrifuge from Thermo Scientific, and subsequent decantation. The same process was followed to prepare and carry out the experiments with $PdCl_2$ and $PtCl_2$. The stock concentration of these solutions was 500 mg·L^{-1}.

The concentration of metals in solution was measured by inductively coupled plasma-mass spectrometry (ICP-MS) and the adsorption capacity (q_e) was determined by:

$$q_e = \frac{(C_o - C_e) \cdot V}{m}$$

Where C_o is the initial concentration of the solution (mg·L^{-1}), C_e is the concentration of the sample solution (mg·L^{-1}), V is the volume of solution employed (L) and m the mass of adsorbent used (g).

All glassware was previously rinsed with aqua regia, a mixture of HCl (37%) and HNO_3 (70%) in a 3:1 molar ratio.

7.1.10 Metal adsorption kinetics

20 mL of 500 mg·mL^{-1} $AuCl_3$ solution (pH=0) were mixed with 20 mg of Starbon® and stirred for 24 h. 50 μL of the mixture were taken at regular intervals and added to 5 mL of 10% HCl solution. The same process was repeated for Pd and Pt, but in this case 50 μL were added to 5 mL of 1% HNO_3 solutions. Then, these solutions were centrifuged for 3 min at 3500 rpm with a Heraeus Megafuge 40R Centrifuge from Thermo Scientific and subsequently decanted to remove any traces of solids. Finally, the solutions were analysed by ICP-MS and or ICP-OES. Gold samples in 10% HCl were further diluted prior ICP analysis to yield samples with an acidity of 2%.

7.1.11 Inductively coupled plasma-mass spectrometry (ICP-MS) and inductively coupled plasma-optical emission spectrometry

ICP-MS was carried out to measure the metal concentration in solution. ICP-MS analysis was performed in an Agilent 7700x fitted with standard Ni sample and skimmer cones and coupled to a Mass Spectrometer (MS). The samples were run in He mode and the sample introduction line was rinsed for 60 s between samples using 5% HCl and 2% HNO_3 (30 sec with each compound). A calibration curve using certified multi-metal standard solutions was used to quantify the amount of metal in solution.

Samples were prepared by diluting metal-containing solutions down to concentrations within the range of 0.1-1 parts per million (ppm). 1% HCl (for Au) and 1% HNO_3 (for Pd and Pt), prepared from TRACE SELECT® HCl and HNO_3 concentrated acids, were used as solvent for the dilutions.

Some of the samples were carried out in the ICP-OES and ICP-MS of the School of Chemistry of the University of Edinburgh by Dr. Lorna Eades. The ICP-MS was an Agilent 7500ce and the ICP-OES, a Perkin Elmer Optima 5300 DV.

7.2   Chapter 3: Towards real-life applications of Starbon®

7.2.1   Materials and chemicals

Details of the materials used in this chapter, including starch, p-TSA, ethanol, acetone, the precious metals chloride salts, HCl and HNO_3 have been described in Section 7.1.1. $ZnCl_2$, 98% $NiCl_2$ 98% and $CuCl_2$ 97% were purchased from Aldrich. The electronic waste solutions containing a range of metals in acidic media were provided by Taym Ltd. The stainless-steel fittings and tubing used to build the monolith reactor were purchased from Swagelok.

7.2.2 Preparation of Starbon® and Starbon® monoliths

The method followed to prepare Starbon® was the same as that detailed in Section 7.1.2.

7.2.3 Preparation of the synthetic metal solution

The relevant amount of $AuCl_3$, $PdCl_2$, $PtCl_2$, $ZnCl_2$, $NiCl_2$ and $CuCl_2$ (~20 mg) was added to a 100 mL volumetric flask which was subsequently filled with ultrapure water. The pH was adjusted to 3 using HCl 0.1 M. The solution was thoroughly mixed. Then, it was introduced in an ultrasound bath for a few minutes (FB 15051 from Fisher Scientific). The solution was then centrifuged and decanted to remove the undissolved solids into a Duran glass bottle where it was stored. All the glassware in contact with the metal solution was previously rinsed with aqua regia, a mixture of HCl (37%) and HNO_3 (70%) in a 3:1 molar ratio, to avoid contamination.

7.2.4 Multi-metal adsorption studies with synthetic and real waste solutions

10 mL of the solution described in Section 7.2.3 were added to a glass vial containing 10 mg of Starbon® and stirred for 24 h. Then, the adsorbent was separated from the solution by centrifugation for 10 min at 3500 rpm with a Heraeus Megafuge 40R Centrifuge from Thermo Scientific, and subsequent decantation. The concentration of metals in solution was measured by ICP-MS and the adsorption capacity (q_e) was determined by:

$$q_e = \frac{(C_o - C_e) \cdot V}{m}$$

Where C_o is the initial concentration of the solution ($mg \cdot L^{-1}$), C_e is the concentration of the sample solution ($mg \cdot L^{-1}$), V is the volume of solution employed (L) and m the mass of adsorbent used (g).

The fraction of metal removed from solution (Rem) was calculated by the following expression:

$$Rem = \frac{(C_o - C_e)}{C_o} \cdot 100$$

7.2.5 ICP-MS

Details of the equipment and sample preparation were detailed in Section 7.1.11.

7.2.6 TEM

TEM analysis was conducted in collaboration with Ms Meg Stark at the Technology Facility in the Department of Biology of the University of York, UK. TEM images were taken by a Tecnai 12BioTwin made by FEI Eindhoven at 120 kV. Samples were soaked in ethanol and subsequently placed onto carbon grids via ethanol evaporation.

7.2.7 Total organic content analysis (TOC)

The analysis was carried out in collaboration with Dr Javier Remón Nuñez in a vario TOC cube from Elementar allocated in the Environment Department of the University of York. Deionised water was used as a blank which draw a detection limit of 6.9 mg·L^{-1}. Samples containing Au NPs were diluted by a factor of 1:2.

7.2.8 XPS

XPS analysis was carried out as described in Section 7.1.7. In addition, the monolith after the flow adsorption experiments was analysed by Dr David Morgan at the School of Chemistry of the University of Cardiff, using a Thermo Scientific™ K-Alpha™+ X-ray Photoelectron Spectrometer fitted with a micro-focussed monochromatic Al Kα source. Sample was mounted on microscope glass covers using double-sided tape and wrapped in aluminium foil to protect them during transportation to the analysis facility. Data analysis was performed with CasaXPS software and the binding energy of C 1s was calibrated to 284.6 eV.

7.2.9 Microscope images

Microscope images were taking with a Leica S6D microscope fitted with a Leica EC3 camera. The images were collected with Leica Suite software, version 1.7.0.

7.2.10 Construction of the monolith reactor for flow adsorption

Monoliths were attached to the inner part of a Swagelok tubing (3/8 in diameter) by using Araldite 2015 epoxy adhesive purchased from RS and left to dry for 24 h. Swagelok fittings were then added to both end of the tubing. This work was done in collaboration with Chris Mortimer, Stuart Murray and Mark Roper at the mechanical workshops of the Chemistry Department of the University of York.

7.2.11 Flow adsorption experiments

The monolith reactor was attached to a Jasco PU-980 HPLC pump. The inlet tubing of the HPLC pump was inserted in the $AuCl_3$ solution which left the system through the bottom end of the monolith reactor. The output solution was collected at regular intervals in glass vials. The concentration of the gold solution was ~100 mg·L^{-1} and the flow rate was adjusted to 0.2 mL·min^{-1}. Deionised water was passed through the system to wet the monolith before starting the experiment. After 2 h the deionised water substituted by diluted HCl (pH 3) to mimic the matrix of the gold solution. The acidic solution was allowed to flow for 2 h. In a second experiment, deionised water and diluted HCl were passed for 12 h each prior the experiment.

7.2.12 Ultraviolet-visible spectroscopy (UV-vis)

UV-vis analysis was carried out using a Jasco V-550 UV-visible spectrophotometer between 200 and 900 nm against a diluted HCl (pH 3) as a reference. Quartz cuvettes were used. The absorbance (A_o) of the gold stock solution was measured to calculate the fraction of gold chloride in every sample (F, %) using the following expression:

$$F = \frac{A_s}{A_o} \cdot 100$$

Where As was the absorbance of the sample at a specific time.

7.3 Chapter 4: Preparation and characterisation of Starbon® composites

7.3.1 Materials and chemicals

The starch, p-toluenesulfonic acid and acetone required for the preparation of the Starbon®-composite discs are the same than those described for the preparation of Starbon® monoliths in Section 7.1.1. Tert-butanol >98% was purchased from Flourochem. Graphite was purchased from Sigma Aldrich.

7.3.2 Preparation of Starbon® composites

Graphite was added to Hylon VII corn starch and subsequently ball milled in a Retsch Planetary Ball Mill PM 100, with a 250 mL capacity containing 5 stainless steel balls of 10 mm diameter. Samples were milled in three cycles of 10 min with a 15 min interval between each run to avoid overheating at a rate of 400 rpm. The resulting product was mixed with water in a ratio 1:4 and subsequently heated at 140 °C (90 W) for 10 min in a CEM II Discover microwave. The material was then poured into a cylindrical mould and retrograded at 5 °C for 48 h to yield a porous monolith gel block. This was subjected to three solvent exchanges with tert-butanol and then frozen using liquid N_2 (10 min) and subsequently freeze-dried (24 h). Then, the material was introduced in a solution of p-toluenesulfonic acid in acetone (5% w/v) for 2 days. The solvent was removed in a Heidolph rotary evaporator. The pressure in the rotary evaporator was reduced from atmospheric pressure to 14 mbar during the course of 4 hours. Finally, samples were carbonised under vacuum up to 800 °C in a Barnstead Thermolyne 6000 Furnace. The discs were sanded down to the required thickness (1 mm) with sand paper.

7.3.3 N$_2$ adsorption porosimetry

N$_2$ adsorption porosimetry was carried out as described in Section 7.1.4.

7.3.4 SEM

SEM micrographs were obtained using ultra-high field-emission scanning electron microscopy (FESEM) (SU8000, Hitachi Co., Japan). The images were taken by Dr Peter Shuttleworth at the Instituto de Ciencia y Tecnología de Polímeros of the Centro Superior de Investigaciones Científicas in Madrid, Spain.

7.3.5 TEM

TEM micrograph images were recorded using a Tecnai 12 BioTwin at 120kV. The images were taken by Dr Peter Shuttleworth at the Instituto de Ciencia y Tecnología de Polímeros of the Centro Superior de Investigaciones Científicas in Madrid, Spain.

7.3.6 TGA

TGA was carried out using a Netzsch STA 409 apparatus under constant N$_2$ flow and at a constant heating rate of 1 $^{\circ}$C·min^{-1}. The theoretical concentration of graphite after carbonisation was calculated from the values of mass residue recorded by TGA. To identify the temperature regions in which significant mass loss occurred during heating, first derivate was applied to TGA curves.

7.3.7 XPS

XPS analysis was carried out as described in Section 7.1.7.

7.3.8 X-ray powder diffraction (XRD)

The XRD analysis was carried out at the Instituto de Ciencia y Tecnología de Polímeros of the Centro Superior de Investigaciones Científicas in Madrid, Spain, using a JEOL 2010F

operating at 200kV. Data was processed using OriginPro 2016 using a Voight model for the deconvolution of the peaks.

7.4 Chapter 5: Power-full electrochemical double layer capacitors based on Starbon® composites

7.4.1 Preparation of Starbon®-graphite composites

Starbon®-graphite composite discs were prepared as detailed in Section 7.3.2.

7.4.2 Electrochemical experiments

Electrochemical experiments were conducted in collaboration with Dr. Enrique Morales at the Institute of Polymer Science and Technology of the Consejo Superior de Investigaciones Científicas in Madrid, Spain.

The electrodes used had a diameter of 8 mm and a thickness < 1mm. Symmetrical supercapacitors were assembled in SwagelokTM-type cells, using a glassy micro-fibre paper (Whatman 934AH) separator and a 2M H_2SO_4 aqueous solution as electrolyte. Two stainless steel (A20 alloy) rods acted as current collectors. Room temperature cyclic voltammetry and galvanostatic charge-discharge tests were performed by using a Solartron 1480 potentiostat/galvanostat instrument, in the potential range 0-1V. Prior to the analysis, samples were dried overnight at 100 °C under vacuum.

Appendices

Chapter 8

8 Appendices

Appendix 1: Kinetic data fit to models based on 'concentration of metal in solution'.
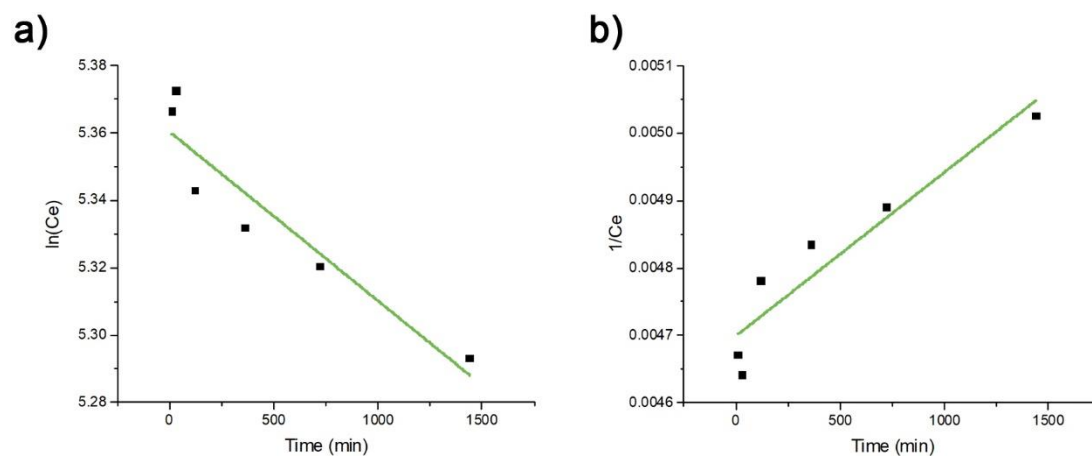
Figure A 1 Kinetic data of the adsorption of Au onto S800 fitted to the a) first and b) second order models based on concentration in solution.
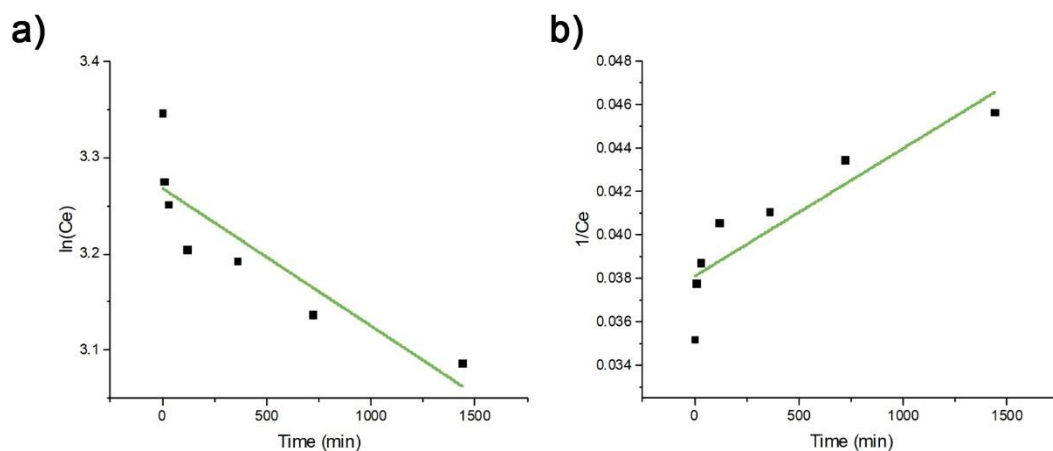
Figure A 2 Kinetic data of the adsorption of Pt onto S800 fitted to the a) first and b) second order models based on concentration in solution.

Appendix 2: Capacitance values at different currents

Table A 1 Capacitance values of Starbon® and Starbon® composites obtained from the galvanostatic charge discharge curves.

Current (A)	Capacitance (F·g⁻¹)					
	GPT-0	GPT-0.5	GPT-1	GPT-3	GPT-10	GPT-20
1	177.4	212.7	204.5	148.5	137.6	172.4
2	172.7	206.5	195.5	140.5	130.2	162.6
3	169.6	198.4	190.5	136.1	125.9	156.3
4	167.2	194.6	186.9	133.0	122.8	152.7
5	165.2	191.6	184.3	130.7	120.4	148.3
10	154.3	182.6	174.7	123.3	112.5	136.5
15	151.7	176.6	169.9	119.4	108.3	129.2
20	149.5	171.7	166.8	116.6	104.9	123.5
25	147.3	167.2	164.0	113.4	108.0	120.2
30	145.0	162.8	161.9	110.7	104.2	115.0
35	142.3	157.2	157.4	109.6	102.9	113.2
40	140.6	153.6	156.8	108.5	100.3	109.7
45	139.1	150.0	155.6	107.6	98.8	107.2
50	137.4	146.5	153.3	105.9	97.6	105.6
60	129.5	140.0	151.1	104.2	93.8	101.5
70	125.9	132.4	148.1	102.3	92.1	98.6
80	122.6	125.8	145.1	100.6	87.8	95.7
90	120.8	120.0	143.3	99.4	85.9	93.1
100	116.9	113.0	141.2	97.8	83.1	93.5
120	111.1	104.5	137.5	94.7	77.1	86.9
140	105.9	94.7	133.5	92.9	73.1	82.7
160	108.9	100.1	140.9	90.6	68.2	79.8
180	92.9	80.2	128.4	88.5	68.0	76.3
200	87.6	71.2	124.9	86.3	58.7	69.6
220	79.3	73.3	124.0	82.0	54.6	59.5
240	68.6	66.3	120.8	78.7	48.4	66.1
260	54.9	50.1	117.8	77.0	38.3	50.7
280	--	--	112.1	71.8	28.0	53.1

List of abbreviations

AC	Activated carbon
ACFs	Activated Carbon Fibres
a_e	Initial adsorption rate
a_L	Langmuir constant
A_o	Absorption of the gold stock solution
APR	Average Pore Diameter
A_s	Absorption of the gold sample
b_e	Elovich constant
BET	Brunauer–Emmett–Teller
BJH	Barrett-Joyner-Halenda
BM	Ball Milling
C	Capacitance
C'	Real part of capacitance
C''	Imaginary part of capacitance
CDCs	Carbide Derived Carbons
CE	Coulombic Efficiency
C_e	Concentration of metal in solution at equilibrium
CNTs	Carbon nanotubes
CO	Carbon monoxide
C_o	Initial concentration of metal in solution
CO_2	Carbon dioxide
CV	Cyclic Voltammetry
d_{002}	Distance between graphene layers
D-R	Dubinin-Radushkevitch

E	Energy density
E_{ads}	Energy of adsorption
EDLCs	Electrochemical Double Layer Capacitors
EIS	Electrochemical Impedance Spectroscopy
ES	Energy Storage
ESR	Equivalent Series Resistant
EU	European Union
E-waste	Electronic waste
ε	Polanyi potential
f	Frequency
FD	Freeze Drying
f_o	Frequency at peak's maximum
GCD	Galvanostatic Charge Discharge
GHGs	Greenhouse Gases
GPT-0	Starbon®-graphite composites with o% of initial graphite
GPT-0.5	Starbon®-graphite composites with o.5% of initial graphite
GPT-1	Starbon®-graphite composites with 1% of initial graphite
GPT-10	Starbon®-graphite composites with 1o% of initial graphite
GPT-20	Starbon®-graphite composites with 2o% of initial graphite
GPT-3	Starbon®-graphite composites with 3% of initial graphite
I	Current
ICP-MS	Inductively Coupled Plasma - Mass Spectrometry
ICP-OES	Inductively Coupled Plasma - Optical Emission Spectrometry
IR	Infrared spectroscopy
K	Scherrer constant
K'	D-R constant
k_1	Pseudo-first order constant rate

k_2	Pseudo-second order constant rate
k_f	Freundlich constant
k_{int}	Constant of intraparticle diffusion
K_L	Langmuir constant
L_c	Out-of-plane crystal size
m	Mass
MMA	Methyl ethacrylate
$m_{o,c}$	Initial mass of composite
$m_{o,g}$	Initial mass of graphite
$m_{r,c}$	Mass of composite after carbonisation
$m_{r,g}$	Mass of graphite after carbonisation
MSW	Municipal Solid Waste
n	Freundlich heterogeneity factor
N	Number of graphene layers
N_2	Nitrogen gas
NO_x	Nitrogen oxides
NPs	Nanoparticles
Θ	Bragg's angle
P	Power density
PCBs	Printed Circuit Boards
PCs	Personal Computers
PSD	Pore Size Distribution
p-TSA	p-toluenesulfonic acid
PVC	Polyvinyl chloride
PZC	Point of Zero Charge
q_e	Adsorption capacity at equilibrium
q_m	D-R saturation capacity of the monolayer

Q_o	Langmuir adsorption capacity of the monolayer
q_t	Adsorption capacity at a time 't'
R	Ideal gas constant
Rem	Percentage of removal
R'	Liquid film diffusion constant
R_L	Constant separation factor
R_s	Solution's resistance
S300	Starbon® carbonised at 300 °C
S450	Starbon® carbonised at 450 °C
S800	Starbon® carbonised at 800 °C
$scCO_2$	Supercritical carbon dioxide
SEM	Scanning Electron Microscopy
T	Temperature
TBA	Tert-butanol
t_c	time of charge
t_d	time of discharge
TEM	Transmission Electron Microscopy
T_g	Theoretical concentration of graphite
TGA	Thermal Gravimetric Analysis
TOC	Total Organic Content
USA	United States of America
UV-vis	Ultraviolet-visible spectrophotometry
V	Voltage
ν	Scan rate
VCM	Vinyl Chloride Monomer
WEEE	Waste Electrical and Electronic Equipment
XPS	X-ray Photoelectron Spectroscopy

XRD   X-Ray Powder Diffraction

Z'   Real component of the impedance

Z''   Imaginary part of the impedance

β   Full width of XRD peak

ΔI   Change in current applied

Δt   Discharge time

λ   Wavelength

τ_o Relaxation time

ω   Angular frequency

References

Chapter 9

9 References

1. P. T. Anastas and T. C. Williamson, *Green Chemistry: Designing Chemistry for the Environment*, ACS Publications, Washington DC, 1996.
2. P. T. Anastas and J. C. Warner, *Green chemistry: Theory and Practice*, Oxford University Press, Oxford, 1998.
3. P. T. Anastas and N. Eghbali, *Chemical Society Reviews*, 2010, **39**, 301-312.
4. D. Arapoglou, T. Varzakas, A. Vlyssides and C. Israilides, *Waste Management*, 2010, **30**, 1898-1902.
5. A. Cowley and B. Woodward, *Platinum Metals Review*, 2011, **55**, 98-107.
6. I. Bakas, M. Herczeg, E. B. Vea, A. Fråne, L. Youhanan and J. Baxter, *Critical metals in discarded electronics: Mapping recycling potentials from selected waste electronics in the Nordic region*, Nordic Council of Ministers, Copenhagen, 2016.
7. J. M. Thomas and W. J. Thomas, *Principles and practice of heterogeneous catalysis*, John Wiley & Sons, Weinheim, 2014.
8. T. Muroi, in *Noble metals*, ed. Y.-H. Su, InTech, Online, 2012, ch. 14, pp. 302-334.
9. G. J. Hutchings, *Journal of Catalysis*, 1985, **96**, 292-295.
10. *United States Pat.,* US2479110 A, 1949.
11. *United states Pat.,* US3415737 A, 1968.
12. *United States Pat.,* US4056373 A, 1977.
13. *United States Pat.,* US5925326 A, 1999.
14. Johnson Matthey, Precious Metals Management, http://www.platinum.matthey.com/about-pgm/applications#, (accessed May 2017).
15. C. W. Corti, R. J. Holliday and D. T. Thompson, *Applied Catalysis A: General*, 2005, **291**, 253-261.
16. C. W. Corti, R. J. Holliday and D. T. Thompson, *Topics in Catalysis*, 2007, **44**, 331-343.
17. P. Johnston, N. Carthey and G. J. Hutchings, *Journal of the American Chemical Society*, 2015, **137**, 14548-14557.
18. P. Goodman, *Gold Bulletin*, 2002, **35**, 21-26.
19. L. Barbieri, R. Giovanardi, I. Lancellotti and M. Michelazzi, *Environmental Chemistry Letters*, 2010, **8**, 171-178.
20. A. Reller, T. Bublies, T. Staudinger, I. Oswald, S. Meißner and M. Allen, *GAIA-Ecological Perspectives for Science and Society*, 2009, **18**, 127-135.
21. C. Meskers, Umicore precious metals refining, Delft, 2009.
22. A. J. Hunt, T. J. Farmer and J. H. Clark, in *Element Recovery and Sustainability*, ed. A. J. Hunt, The Royal Society of Chemistry, Cambridge, 2013, ch. 1, pp. 1-28.
23. C. Hagelüken, *Acta Metallurgica Slovaca*, 2006, **12**, 111-120.
24. UNEP, *E-Waste Management Manual*, United Nations Environment Programme, Osaka, 2007.

25. K. A. Hudson-Edwards, H. E. Jamieson and B. G. Lottermoser, *Elements*, 2011, **7**, 375-380.

26. B. G. Lottermoser, *Mine waste: Characterisation, Treatment and Environmetal Impacts*, Springer, Heidelberg, 2010.

27. W. Petruk, *Applied mineralogy in the mining industry*, Elsevier, Amsterdam, 2000.

28. D. Kossoff, W. E. Dubbin, M. Alfredsson, S. J. Edwards, M. G. Macklin and K. A. Hudson-Edwards, *Applied Geochemistry*, 2014, **51**, 229-245.

29. H. E. Jamieson, *Elements*, 2011, **7**, 381-386.

30. European Commision, Waste Electrical & Electronic Equipment (WEEE), http://ec.europa.eu/environment/waste/weee/index_en.htm, (accessed May 2017).

31. B. H. Robinson, *Science of the Total Environment*, 2009, **408**, 183-191.

32. T. E. Graedel, J. Allwood, J. P. Birat, M. Buchert, C. Hagelüken, B. K. Reck, S. F. Sibley and G. Sonnemann, *Journal of Industrial Ecology*, 2011, **15**, 355-366.

33. B. K. Reck and T. E. Graedel, *Science*, 2012, **337**, 690-695.

34. C. Hagelüken, *Platinum Metals Review*, 2012, **56**, 29-35.

35. *Science and Technology Committee, Strategically important metals Volume I: Report*, House of Commons, 2010.

36. J. R. Dodson, A. J. Hunt, H. L. Parker, Y. Yang and J. H. Clark, *Chemical Engineering and Processing: Process Intensification*, 2012, **51**, 69-78.

37. D. E. Rawlings, D. Dew and C. du Plessis, *Trends in Biotechnology*, 2003, **21**, 38-44.

38. J. P. Parfitt, *A study of the composition of collected household waste in the UK~ with particular reference to packaging waste*, University of East Anglia, 2000.

39. Eurostat Statistics Explained, Municipal waste statistics, http://ec.europa.eu/eurostat/statistics-explained/index.php/Municipal_waste_statistics, (accessed May 2017).

40. K. Halada, K. Ijima, M. Shimada and N. Katagiri, *Journal of the Japan Institute of Metals*, 2009, **73**, 151-160.

41. R. Widmer, H. Oswald-Krapf, D. Sinha-Khetriwal, M. Schnellmann and H. Böni, *Environmental Impact Assessment Review*, 2005, **25**, 436-458.

42. J. Huisman, F. Magalini, R. Kuehr, C. Maurer, S. Ogilvie, J. Poll, C. Delgado, E. Artim, J. Szlezak and A. Stevels, *Review of directive 2002/96 on waste electrical and electronic equipment (WEEE)*, United Nations University, 2008.

43. S. Syed, *Hydrometallurgy*, 2012, **115**, 30-51.

44. K. Liddell, T. Newton, M. Adams and B. Muller, *Journal of the Southern African Institute of Mining and Metallurgy*, 2011, **111**, 127-132.

45. K. F. Lam, C. M. Fong and K. L. Yeung, *Gold Bulletin*, 2007, **40**, 192-198.

46. D. Aderhold, C. J. Williams and R. G. J. Edyvean, *Bioresource Technology*, 1996, **58**, 1-6.

47. J. Radjenovic and D. L. Sedlak, *Environmental Science & Technology*, 2015, **49**, 11292-11302.

48. S. Babel and T. A. Kurniawan, *Journal of Hazardous Materials*, 2003, **97**, 219-243.

49. G. Crini, *Progress in Polymer Science*, 2005, **30**, 38-70.

50. J. R. Dodson, H. L. Parker, A. Muñoz García, A. Hicken, K. Asemave, T. J. Farmer, H. He, J. H. Clark and A. J. Hunt, *Green Chemistry*, 2015, **17**, 1951-1965.

51. D. Kratochvil and B. Volesky, *Trends in Biotechnology*, 1998, **16**, 291-300.

52. M. Gurung, B. B. Adhikari, H. Kawakita, K. Ohto, K. Inoue and S. Alam, *Chemical Engineering Journal*, 2011, **174**, 556-563.

53. N. Balasundram, K. Sundram and S. Samman, *Food Chemistry*, 2006, **99**, 191-203.

54. J. He and J. P. Chen, *Bioresource Technology*, 2014, **160**, 67-78.

55. C. K. Jain, D. S. Malik and A. K. Yadav, *Environmental Processes*, 2016, **3**, 495-523.

56. L. Zhang, Y. Zeng and Z. Cheng, *Journal of Molecular Liquids*, 2016, **214**, 175-191.

57. Johnson Matthey Precious Metals Management, http://www.platinum.matthey.com/prices/price-charts, (accessed January 2018).

58. Money Metals Exchange, https://www.moneymetals.com/precious-metals-charts, (accessed January 2018).

59. M. L. Arrascue, H. M. Garcia, O. Horna and E. Guibal, *Hydrometallurgy*, 2003, **71**, 191-200.

60. A. M. Donia, A. A. Atia and K. Z. Elwakeel, *Hydrometallurgy*, 2007, **87**, 197-206.

61. K. Fujiwara, A. Ramesh, T. Maki, H. Hasegawa and K. Ueda, *Journal of Hazardous Materials*, 2007, **146**, 39-50.

62. A. Ramesh, H. Hasegawa, W. Sugimoto, T. Maki and K. Ueda, *Bioresource Technology*, 2008, **99**, 3801-3809.

63. H. Wang, C. Bao, F. Li, X. Kong and J. Xu, *Microchimica Acta*, 2010, **168**, 99-105.

64. X. Chen, K. F. Lam, S. F. Mak and K. L. Yeung, *Journal of Hazardous Materials*, 2011, **186**, 902-910.

65. E. Guibal, A. Larkin, T. Vincent and J. M. Tobin, *Industrial & Engineering Chemistry Research*, 1999, **38**, 4011-4022.

66. P. Chassary, T. Vincent, J. S. Marcano, L. E. Macaskie and E. Guibal, *Hydrometallurgy*, 2005, **76**, 131-147.

67. E. Guibal, N. V. O. Sweeney, T. Vincent and J. M. Tobin, *Reactive and Functional Polymers*, 2002, **50**, 149-163.

68. D. W. Darnall, B. Greene, M. T. Henzl, J. M. Hosea, R. A. McPherson, J. Sneddon and M. D. Alexander, *Environmental Science & Technology*, 1986, **20**, 206-208.

69. N. Kuyucak and B. Volesky, *Biotechnology Letters*, 1988, **10**, 137-142.

70. Y. N. Mata, E. Torres, M. L. Blazquez, A. Ballester, F. M. J. A. González and J. A. Munoz, *Journal of Hazardous Materials*, 2009, **166**, 612-618.

71. B. Pangeni, H. Paudyal, M. Abe, K. Inoue, H. Kawakita, K. Ohto, B. B. Adhikari and S. Alam, *Green Chemistry*, 2012, **14**, 1917-1927.

72. E. Torres, Y. N. Mata, M. L. Blazquez, J. A. Munoz, F. Gonzalez and A. Ballester, *Langmuir*, 2005, **21**, 7951-7958.

73. M. E. Romero-González, C. J. Williams, P. H. E. Gardiner, S. J. Gurman and S. Habesh, *Environmental Science & Technology*, 2003, **37**, 4163-4169.

74. B. Pangeni, H. Paudyal, K. Inoue, H. Kawakita, K. Ohto and S. Alam, *Cellulose*, 2012, **19**, 381-391.

75. B. Pangeni, H. Paudyal, K. Inoue, H. Kawakita, K. Ohto and S. Alam, *Journal of Chemical & Engineering Data*, 2012, **57**, 796-804.

76. M. Gurung, B. B. Adhikari, X. Gao, S. Alam and K. Inoue, *Industrial & Engineering Chemistry Research*, 2014, **53**, 8565-8576.

77. C. R. Adhikari, D. Parajuli, K. Inoue, K. Ohto, H. Kawakita and H. Harada, *New Journal of Chemistry*, 2008, **32**, 1634-1641.

78. G. Gamez, J. L. Gardea-Torresdey, K. J. Tiemann, J. Parsons, K. Dokken and M. J. Yacaman, *Advances in Environmental Research*, 2003, **7**, 563-571.

79. D. Parajuli, C. R. Adhikari, H. Kawakita, S. Yamada, K. Ohto and K. Inoue, *Bioresource technology*, 2009, **100**, 1000-1002.

80. K. Deng, P. Yin, X. Liu, Q. Tang and R. Qu, *Journal of Industrial and Engineering Chemistry*, 2014, **20**, 2428-2438.

81. M. A. Z. Abidin, A. A. Jalil, S. Triwahyono, S. H. Adam and N. H. N. Kamarudin, *Biochemical Engineering Journal*, 2011, **54**, 124-131.

82. H. Zheng and L. Wang, *Soft Nanoscience Letters*, 2013, **3**, 29-36.

83. R. Chand, T. Watari, K. Inoue, H. Kawakita, H. N. Luitel, D. Parajuli, T. Torikai and M. Yada, *Minerals Engineering*, 2009, **22**, 1277-1282.

84. M. Soleimani and T. Kaghazchi, *Bioresource Technology*, 2008, **99**, 5374-5383.

85. R. Asadi-Kesheh, S.-A. Mohtashami, T. Kaghazchi, N. Asasian and M. Soleimani, *Separation Science and Technology*, 2015, **50**, 223-232.

86. A. Sari, D. Mendil, M. Tuzen and M. Soylak, *Journal of Hazardous Materials*, 2009, **162**, 874-879.

87. S. Wang, L. Liu, X. Sun and T.-K. Sham, *Journal of Materials Chemistry A*, 2015, **17**, 1666-1674.

88. S. Kamel, E. M. Hassan and M. El-Sakhawy, *Journal of Applied Polymer Science*, 2006, **100**, 329-334.

89. H. A. Krässig, *Cellolose: structure, accesibility and reactivity*, Gordon and Breach Science Publishers, Philadelphia, 1993.

90. G. Güçlü, G. Gürdağ and S. Özgümüş, *Journal of Applied Polymer Science*, 2003, **90**, 2034-2039.

91. L. Khezami, A. Chetouani, B. Taouk and R. Capart, *Powder Technology*, 2005, **157**, 48-56.

92. M. Rafatullah, O. Sulaiman, R. Hashim and A. Ahmad, *Journal of Hazardous Materials*, 2010, **177**, 70-80.

93. C. K. S. Pillai, W. Paul and C. P. Sharma, *Progress in Polymer Science*, 2009, **34**, 641-678.

94. A. Haug, B. Larsen and O. Smidsrod, *Acta Chemica Scandinavica*, 1966, **20**, 183-190.

95. A. I. Usov, G. P. Smirnova and N. G. Klochkova, *Russian Journal of Bioorganic Chemistry*, 2001, **27**, 395-399.

96. P. Fasahati, H. C. Woo and J. J. Liu, *Applied Energy*, 2015, **139**, 175-187.

97. S. Hartley, N. J. G. Pearce, W. T. Perkins, E. Dinelli, R. G. J. Edyvean, G. Priestman, L. Sandlands and R. Bachmann, Dealginated seaweed as a bioadsorption medium for treating metal mine drainage: issues surrounding its pre-treatment and use in small scale treatment plants in the EU LIFE "BIOMAN" project, Cagliari, 2007.

98. P. Sriamornsak, *Silpakorn University International Journal*, 2003, **3**, 206-228.

99.   C. D. May, *Carbohydrate Polymers*, 1990, **12**, 79-99.
100.   B. M. Yapo, C. Robert, I. Etienne, B. Wathelet and M. Paquot, *Food Chemistry*, 2007, **100**, 1356-1364.
101.   A. J. F. Carvalho, *Starch: major sources, properties and applications as thermoplastic materials*, Elsevier, Amsterdam, 2008.
102.   A. J. F. Carvalho, in *Handbook of Biopolymers and Biodegradable Plastics: Properties, Processing and Applications*, ed. S. Ebnesajjad, ElSevier, Waltham, 2012, ch. 7, pp. 129-145.
103.   Starch Europe, European Starch industry, http://www.starch.eu/european-starch-industry/, (accessed May 2017).
104.   *S. K. Patil & Associates, Global modified starch products & carbohydrates functional foods derivatives & markets-A strategic review*, Patil, S. K. & Associates, 2012.
105.   H. L. Parker, PhD, University of York, 2013.
106.   M. J. Miles, V. J. Morris, P. D. Orford and S. G. Ring, *Carbohydrate Research*, 1985, **135**, 271-281.
107.   J. O. B. Carioca, H. L. Arora, P. V. Selvam, F. C. A. Tavares, J. F. Kennedy and C. J. Knill, *Starch*, 1996, **48**, 322-326.
108.   Y.-C. Shi, T. Capitani, P. Trzasko and R. Jeffcoat, *Journal of Cereal Science*, 1998, **27**, 289-299.
109.   S. E. Case, T. Capitani, J. K. Whaley, Y. C. Shi, P. Trzasko, R. Jeffcoat and H. B. Goldfarb, *Journal of Cereal Science*, 1998, **27**, 301-314.
110.   V. L. Budarin, J. H. Clark, J. J. E. Hardy, R. Luque, K. Milkowski, S. J. Tavener and A. J. Wilson, *Angewandte Chemie International Edition*, 2006, **118**, 3866-3870.
111.   H. L. Parker, A. J. Hunt, V. L. Budarin, P. S. Shuttleworth, K. L. Miller and J. H. Clark, *RSC Advances*, 2012, **2**, 8992-8997.
112.   H. L. Parker, V. L. Budarin, J. H. Clark and A. J. Hunt, *ACS Sustainable Chemistry & Engineering*, 2013, **1**, 1311-1318.
113.   J. Cui and L. Zhang, *Journal of Hazardous Materials*, 2008, **158**, 228-256.
114.   E. Guibal, *Separation and Purification Technology*, 2004, **38**, 43-74.
115.   A. Albert and E. P. Serjeant, in *The Determination of Ionization Constants*, eds. A. Albert and E. P. Serjeant, Springer, New York, 1984, ch. 10, pp. 176-191.
116.   P. Somasundaran and D. R. Nagaraj, Chemistry and applications of chelating agents in flotation and flocculation, London, 1984.
117.   S. Kumar and S. Jain, *Journal of Chemistry*, 2013, **2013**, 1-13.
118.   C. Mack, B. Wilhelmi, J. R. Duncan and J. E. Burgess, *Biotechnology Advances*, 2007, **25**, 264-271.
119.   G. M. Gadd, *Journal of Chemical Technology and Biotechnology*, 2009, **84**, 13-28.
120.   N. Das, *Hydrometallurgy*, 2010, **103**, 180-189.
121.   L. Järup, *British medical bulletin*, 2003, **68**, 167-182.
122.   W. Ma, P. Zong, Z. Cheng, B. Wang and Q. Sun, *Journal of Hazardous Materials*, 2014, **266**, 19-25.
123.   W.-J. Liu, K. Tian, H. Jiang, X.-S. Zhang, H.-S. Ding and H.-Q. Yu, *Environmental Science & Technology*, 2012, **46**, 7849-7856.

124. W. K. O'Keefe, F. T. T. Ng and G. L. Rempel, *Industrial & Engineering Chemistry Research*, 2007, **46**, 716-725.
125. N. Yoneda, S. Kusano, M. Yasui, P. Pujado and S. Wilcher, *Applied Catalysis A: General*, 2001, **221**, 253-265.
126. D. A. Bulushev, I. Yuranov, E. I. Suvorova, P. A. Buffat and L. Kiwi-Minsker, *Journal of Catalysis*, 2004, **224**, 8-17.
127. W. Zhu, R. Michalsky, Ö. Metin, H. Lv, S. Guo, C. J. Wright, X. Sun, A. A. Peterson and S. Sun, *Journal of the American Chemical Society*, 2013, **135**, 16833-16836.
128. C.-H. C. Zhou, J. N. Beltramini, Y.-X. Fan and G. Q. M. Lu, *Chemical Society Reviews*, 2008, **37**, 527-549.
129. *United Kingdom Pat.,* EP20070726967, 2008.
130. C. F. Poole, *The Essence of Chromatography*, Elsevier, Amsterdam, 2003.
131. D. Qu and H. Shi, *Journal of Power Sources*, 1998, **74**, 99-107.
132. P. S. Shuttleworth, V. Budarin, R. J. White, V. M. Gun'ko, R. Luque and J. H. Clark, *Chemistry–A European Journal*, 2013, **19**, 9351-9357.
133. Z. Q. Li, C. J. Lu, Z. P. Xia, Y. Zhou and Z. Luo, *Carbon*, 2007, **45**, 1686-1695.
134. A. Muñoz-García, A. J. Hunt, V. L. Budarin, H. L. Parker, P. S. Shuttleworth, G. J. Ellis and J. H. Clark, *Green Chemistry*, 2015, **17**, 2146-2149.
135. J. H. Clark, V. Budarin, T. Dugmore, R. Luque, D. J. Macquarrie and V. Strelko, *Catalysis Communications*, 2008, **9**, 1709-1714.
136. V. L. Budarin, J. H. Clark, R. Luque, D. J. Macquarrie, A. Koutinas and C. Webb, *Green Chemistry*, 2007, **9**, 992-995.
137. V. Budarin, R. Luque, D. J. Macquarrie and J. H. Clark, *Chemistry–A European Journal*, 2007, **13**, 6914-6919.
138. A. Corma, S. Iborra and A. Velty, *Chemical Reviews*, 2007, **107**, 2411-2502.
139. J. S. Carey, D. Laffan, C. Thomson and M. T. Williams, *Organic & Biomolecular Chemistry*, 2006, **4**, 2337-2347.
140. R. Luque, V. Budarin, J. H. Clark and D. J. Macquarrie, *Green Chemistry*, 2009, **11**, 459-461.
141. L. M. M. Mesquita, R. M. A. Pinto, J. A. R. Salvador, J. H. Clark and V. L. Budarin, *Catalysis Communications*, 2015, **69**, 170-173.
142. R. Luque, V. L. Budarin, J. H. Clark, P. S. Shuttleworth and R. J. White, *Catalysis Communications*, 2011, **12**, 1471-1476.
143. N. Bhatt and A. Patel, *Journal of Molecular Catalysis A: Chemical*, 2007, **264**, 214-219.
144. J. M. Campelo, D. Luna, R. Luque, J. M. Marinas and A. A. Romero, *ChemSusChem*, 2009, **2**, 18-45.
145. B. Karimi, S. Abedi, J. H. Clark and V. Budarin, *Angewandte Chemie International Edition*, 2006, **45**, 4776-4779.
146. R. Luque, J. H. Clark, K. Yoshida and P. L. Gai, *Chemical Communications*, 2009, **0**, 5305-5307.
147. L. A. Oro, D. Carmona and J. M. Fraile, in *Metal-catalysis in Industrial Organic Processes*, eds. G. P. Chiusoli and P. M. Maitlis, Royal Society of Chemistry, Cambridge, 2006, ch. 3, pp. 79-113.

148. J. M. Bermudez, J. A. l. Menéndez, A. A. Romero, E. Serrano, J. Garcia-Martinez and R. Luque, *Green Chemistry*, 2013, **15**, 2786-2792.

149. *United States Pat.,* US6309430 B1, 2001.

150. V. Pace, P. Hoyos, M. Fernández, J. V. Sinisterra and A. R. Alcántara, *Green Chemistry*, 2010, **12**, 1380-1382.

151. R. Luque, V. Budarin, J. H. Clark and D. J. Macquarrie, *Applied Catalysis B: Environmental*, 2008, **82**, 157-162.

152. J. A. Melero, R. Van Grieken, G. Morales and M. Paniagua, *Energy & Fuels*, 2007, **21**, 1782-1791.

153. S. N. D. Lal, C. J. O'Connor and L. Eyres, *Advances in Colloid and Interface Science*, 2006, **123**, 433-437.

154. H. Baumann, M. Bühler, H. Fochem, F. Hirsinger, H. Zoebelein and J. Falbe, *Angewandte Chemie International Edition*, 1988, **27**, 41-62.

155. M. Ojeda, V. L. Budarin, P. S. Shuttleworth, J. H. Clark, A. Pineda, A. M. Balu, A. A. Romero and R. Luque, *Materials*, 2013, **6**, 1891-1902.

156. G. Durá, V. L. Budarin, J. A. Castro-Osma, P. S. Shuttleworth, S. C. Z. Quek, J. H. Clark and M. North, *Angewandte Chemie International Edition*, 2016, **128**, 9319-9323.

157. M. Doğan, Y. Özdemir and M. Alkan, *Dyes and Pigments*, 2007, **75**, 701-713.

158. N. Puvaneswari, J. Muthukrishnan and P. Gunasekaran, *Indian Journal of Experimental Biology*, 2006, **44**, 618-626.

159. Eurostat Statistics Explained, Energy Production and imports, http://ec.europa.eu/eurostat/statistics-explained/index.php/Energy_production_and_imports, (accessed May 2017).

160. J. Mohtasham, *Energy Procedia*, 2015, **74**, 1289-1297.

161. D. Gielen, F. Boshell and D. Saygin, *Nature Materials*, 2016, **15**, 117-120.

162. N. N. C. f. E. Information, *Journal*, 2015.

163. Enerdata, Global Energy Statistical Yearbook 2016, https://yearbook.enerdata.net/, (accessed June 2017).

164. O. Ellabban, H. Abu-Rub and F. Blaabjerg, *Renewable and Sustainable Energy Reviews*, 2014, **39**, 748-764.

165. A. Brown, S. Müller and Z. Dobrotkova, *Renewable energy: Markets and prospects by technology*, International Energy Agency, 2011.

166. L. P. Rosa, M. A. Dos Santos, B. Matvienko, E. O. Dos Santos and E. Sikar, *Climatic Change*, 2004, **66**, 9-21.

167. A. Zervos, C. Lins and J. Muth, *RE-thinking 2050: a 100% renewable energy vision for the European Union*, European Renewable Energy Council, 2010.

168. BP Global, Renewable energy - 2015 in review, http://www.bp.com/en/global/corporate/energy-economics/statistical-review-of-world-energy/renewable-energy.html, (accessed June 2017).

169. T. Kousksou, P. Bruel, A. Jamil, T. El Rhafiki and Y. Zeraouli, *Solar Energy Materials and Solar Cells*, 2014, **120**, 59-80.

170. T. U. Daim, X. Li, J. Kim and S. Simms, *Environmental Innovation and Societal Transitions*, 2012, **3**, 29-49.

171.   R. M. Dell and D. A. J. Rand, *Journal of Power Sources*, 2001, **100**, 2-17.
172.   H. Ibrahim, A. Ilinca and J. Perron, *Renewable and Sustainable Energy Reviews*, 2008, **12**, 1221-1250.
173.   I. Hadjipaschalis, A. Poullikkas and V. Efthimiou, *Renewable and Sustainable Energy Reviews*, 2009, **13**, 1513-1522.
174.   H. L. Ferreira, R. Garde, G. Fulli, W. Kling and J. P. Lopes, *Energy*, 2013, **53**, 288-298.
175.   University of Calgary, Energy density vs power density, http://energyeducation.ca/encyclopedia/Energy_density_vs_power_density, (accessed August 2017).
176.   Mitsui & Co, Dinorwig Power Station, http://www.fhc.co.uk/dinorwig.htm, (accessed June 2017).
177.   I. Dincer, *Energy and Buildings*, 2002, **34**, 377-388.
178.   M. Aneke and M. Wang, *Applied Energy*, 2016, **179**, 350-377.
179.   M. Winter and R. J. Brodd, *Chemical Reviews*, 2004, **104**, 4245-4269.
180.   D. Kundu, E. Talaie, V. Duffort and L. F. Nazar, *Angewandte Chemie International Edition*, 2015, **54**, 3431-3448.
181.   J. Garche, C. K. Dyer, P. T. Moseley, Z. Ogumi, D. A. J. Rand and B. Scrosati, *Encyclopedia of Electrochemical Power Sources*, Elsevier, Amsterdam, 2013.
182.   X. Tan, Q. Li and H. Wang, *International Journal of Electrical Power & Energy Systems*, 2013, **44**, 179-191.
183.   P. Alotto, M. Guarnieri and F. Moro, *Renewable and Sustainable Energy Reviews*, 2014, **29**, 325-335.
184.   D. Bresser, S. Passerini and B. Scrosati, *Chemical Communications*, 2013, **49**, 10545-10562.
185.   C. D. Parker, *Journal of Power Sources*, 2001, **100**, 18-28.
186.   F. Schipper and D. Aurbach, *Russian Journal of Electrochemistry*, 2016, **52**, 1095-1121.
187.   Y. V. Makarov, B. Yang, J. G. DeSteese, S. Lu, C. H. Miller, P. Nyeng, J. Ma, D. J. Hammerstrom and V. V. Vishwanathan, *Wide-area energy storage and management system to balance intermittent resources in the Bonneville Power Administration and California ISO control areas*, Pacific Northwest National Laboratory, 2008.
188.   T. M. I. Mahlia, T. J. Saktisahdan, A. Jannifar, M. H. Hasan and H. S. C. Matseelar, *Renewable and Sustainable Energy Reviews*, 2014, **33**, 532-545.
189.   M. S. Dresselhaus and I. L. Thomas, *Nature*, 2001, **414**, 332-337.
190.   B. L. Ellis and L. F. Nazar, *Current Opinion in Solid State and Materials Science*, 2012, **16**, 168-177.
191.   J. Wen, Y. Yu and C. Chen, *Materials Express*, 2012, **2**, 197-212.
192.   M. Jayalakshmi and K. Balasubramanian, *International Journal of Electrochemical Science*, 2008, **3**, 1196-1217.
193.   C. Largeot, C. Portet, J. Chmiola, P.-L. Taberna, Y. Gogotsi and P. Simon, *Journal of the American Chemical Society*, 2008, **130**, 2730-2731.
194.   G. Wang, L. Zhang and J. Zhang, *Chemical Society Reviews*, 2012, **41**, 797-828.

195.   L. L. Zhang and X. S. Zhao, *Chemical Society Reviews*, 2009, **38**, 2520-2531.

196.   P. P. Barker, Ultracapacitors for use in power quality and distributed resource applications, Chicago, 2002.

197.   A. Von Jouanne, P. N. Enjeti and B. Banerjee, *IEEE Transactions on Industry Applications*, 1999, **35**, 908-916.

198.   P. Sharma and T. S. Bhatti, *Energy Conversion and Management*, 2010, **51**, 2901-2912.

199.   S. Butterbach, B. Vulturescu, G. Coquery, C. Forgez and G. Friedrich, Design of a supercapacitor-battery storage system for a waste collection vehicle, Lille, 2010.

200.   X. Andrieu and J. F. Fauvarque, Supercapacitors for telecommunication applications, Paris, 1993.

201.   S. McCluer and J.-F. Christin, *Comparing data center batteries, flywheels, and ultracapacitors*, Schneider Electric, 2008.

202.   A. González, E. Goikolea, J. A. Barrena and R. Mysyk, *Renewable and Sustainable Energy Reviews*, 2016, **58**, 1189-1206.

203.   A. G. Pandolfo and A. F. Hollenkamp, *Journal of Power Sources*, 2006, **157**, 11-27.

204.   E. J. Bottani and J. M. D. Tascón, *Adsorption by carbons*, Elsevier, Amsterdam, 2011.

205.   H. O. Pierson, *Handbook of Carbon, Graphite, Diamond and Fullerenes*, Noyes Publications, Park Ridge, 1993.

206.   S. C. Moldoveanu, *Analytical pyrolysis of natural organic polymers*, Elsevier, Amsterdam, 1998.

207.   P. Simon and Y. Gogotsi, *Nature materials*, 2008, **7**, 845-854.

208.   E. Frackowiak, K. Jurewicz, K. Szostak, S. Delpeux and F. Beguin, *Fuel Processing Technology*, 2002, **77**, 213-219.

209.   M. J. Allen, V. C. Tung and R. B. Kaner, *Chemical Reviews*, 2009, **110**, 132-145.

210.   V. L. Budarin, J. H. Clark, R. Luque and R. J. White, *Material Matters*, 2009, **4**, 19-22.

211.   L. Bonnefoi, P. Simon, J. F. Fauvarque, C. Sarrazin and A. Dugast, *Journal of Power Sources*, 1999, **79**, 37-42.

212.   Y. Gogotsi, *Nanomaterials Handbook*, CRC press, Boca Raton, 2006.

213.   Y. Gogotsi, A. Nikitin, H. Ye, W. Zhou, J. E. Fischer, B. Yi, H. C. Foley and M. W. Barsoum, *Nature Materials*, 2003, **2**, 591-594.

214.   J. Chmiola, G. Yushin, Y. Gogotsi, C. Portet, P. Simon and P.-L. Taberna, *Science*, 2006, **313**, 1760-1763.

215.   J. R. Miller and P. Simon, *Science Magazine*, 2008, **321**, 651-652.

216.   X. Jian, S. Liu, Y. Gao, W. Tian, Z. Jiang, X. Xiao, H. Tang and L. Yin, *Journal of Electrical Engineering*, 2016, **4**, 75-87.

217.   *United States Pat.,* US6356433 B1, 2002.

218.   G. A. Snook and G. Z. Chen, *Journal of Electroanalytical Chemistry*, 2008, **612**, 140-146.

219.   C. Lei and C. Lekakou, *Surface and Coatings Technology*, 2013, **232**, 326-330.

220.   T. Bordjiba, M. Mohamedi and L. H. Dao, *Advanced Materials*, 2008, **20**, 815-819.

221. G. Lv, D. Wu, R. Fu, Z. Zhang and Z. Su, *Journal of Non-Crystalline Solids*, 2008, **354**, 4567-4571.
222. D. Yu and L. Dai, *The Journal of Physical Chemistry Letters*, 2009, **1**, 467-470.
223. Z. Fan, J. Yan, L. Zhi, Q. Zhang, T. Wei, J. Feng, M. Zhang, W. Qian and F. Wei, *Advanced Materials*, 2010, **22**, 3723-3728.
224. X. Huang, X. Qi, F. Boey and H. Zhang, *Chemical Society Reviews*, 2012, **41**, 666-686.
225. S. Yu, Y. Li and N. Pan, *RSC Advances*, 2014, **4**, 48758-48764.
226. Macrotrends.net, Gold Prices - 100 Year Historical Chart, http://www.macrotrends.net/1333/historical-gold-prices-100-year-chart, (accessed June 2017).
227. S. Karabulut, A. Karabakan, A. Denizli and Y. Yürüm, *Separation and Purification Technology*, 2000, **18**, 177-184.
228. R. J. White, PhD, University of York, 2008.
229. E. Taer, M. Deraman, I. A. Talib, A. Awitdrus, S. A. Hashmi and A. A. Umar, *International Journal of Electrochemical Science*, 2011, **6**, 3301-3315.
230. R. J. White, V. L. Budarin and J. H. Clark, *ChemSusChem*, 2008, **1**, 408-411.
231. V. Budarin, J. H. Clark, F. E. I. Deswarte, J. J. E. Hardy, A. J. Hunt and F. M. Kerton, *Chemical Communications*, 2005, 2903-2905.
232. K. S. W. Sing, *Pure and Applied Chemistry*, 1985, **57**, 603-619.
233. C. A. García-González, M. C. Camino-Rey, M. Alnaief, C. Zetzl and I. Smirnova, *The Journal of Supercritical Fluids*, 2012, **66**, 297-306.
234. D. Li, R. Tang, Y. Tian, Y. Qiao and J. Li, *BioResources*, 2014, **9**, 1246-1254.
235. L. Liu, Z. Liu, J. Yang, Z. Huang and Z. Liu, *Carbon*, 2007, **45**, 2836-2842.
236. J. Zhou, J. Song and R. Parker, *Carbohydrate Polymers*, 2007, **69**, 445-454.
237. U. Zielke, K. J. Hüttinger and W. P. Hoffman, *Carbon*, 1996, **34**, 983-998.
238. E. Pretsch, *Structure Determination of Organic Compunds*, Springer, Verlag, 2002.
239. E. Desimoni, G. I. Casella, A. Morone and A. M. Salvi, *Surface and Interface Analysis*, 1990, **15**, 627-634.
240. H. P. Boehm, *Carbon*, 1994, **32**, 759-769.
241. P. Chingombe, B. Saha and R. J. Wakeman, *Carbon*, 2005, **43**, 3132-3143.
242. J. S. Noh and J. A. Schwarz, *Journal of Colloid and Interface Science*, 1989, **130**, 157-164.
243. H. P. Boehm, *Carbon*, 2002, **40**, 145-149.
244. C. A. Leon y Leon, J. M. Solar, V. Calemma and L. R. Radovic, *Carbon*, 1992, **30**, 797-811.
245. P. R. Zalupski, R. McDowell and G. Dutech, *Solvent Extraction and Ion Exchange*, 2014, **32**, 737-748.
246. A. J. Bard, R. Parsons and J. Jordan, *Standard Potentials in Aqueous Solution*, CRC press, New York, 1985.
247. S. J. Oldenburg, R. D. Averitt, S. L. Westcott and N. J. Halas, *Chemical Physics Letters*, 1998, **288**, 243-247.
248. W. Shi, Y. Sahoo, M. T. Swihart and P. N. Prasad, *Langmuir*, 2005, **21**, 1610-1617.

249. Y. T. Lim, O. O. Park and H.-T. Jung, *Journal of Colloid and Interface Science*, 2003, **263**, 449-453.

250. C. D. Wagner, *Handbook of x-ray photoelectron spectroscopy: a reference book of standard data for use in x-ray photoelectron spectroscopy*, Perkin-Elmer Corporation, Eden Prairie, 1979.

251. M. P. Casaletto, A. Longo, A. Martorana, A. Prestianni and A. M. Venezia, *Surface and Interface Analysis*, 2006, **38**, 215-218.

252. M. Bystrzejewski and K. Pyrzyńska, *Materials Chemistry and Physics*, 2013, **141**, 454-460.

253. M. Cox, A. A. Pichugin, E. I. El-Shafey and Q. Appleton, *Hydrometallurgy*, 2005, **78**, 137-144.

254. A. Bar-Even, A. Flamholz, E. Noor and R. Milo, *Nature Chemical Biology*, 2012, **8**, 509-517.

255. M. Gurung, B. B. Adhikari, S. Morisada, H. Kawakita, K. Ohto, K. Inoue and S. Alam, *Bioresource Technology*, 2013, **129**, 108-117.

256. P. A. Simonov, A. V. Romanenko, I. P. Prosvirin, E. M. Moroz, A. L. Boronin, A. L. Chuvilin and V. A. Likholobov, *Carbon*, 1997, **35**, 73-82.

257. G. Kumar, J. R. Blackburn, R. G. Albridge, W. E. Moddeman and M. M. Jones, *Inorganic Chemistry*, 1972, **11**, 296-300.

258. O. Björneholm, A. Nilsson, H. Tillborg, P. Bennich, A. Sandell, B. Hernnäs, C. Puglia and N. Mårtensson, *Surface Science*, 1994, **315**, L983-L989.

259. C. Battistoni, A. M. Giuliani, E. Paparazzo and F. Tarli, *Journal of the Chemical Society, Dalton Transactions*, 1984, **7**, 1293-1299.

260. Surface Science Western - University of Ontario, X-ray Photoelectron Spectroscopy (XPS) Reference Pages, http://www.xpsfitting.com/2012/08/spin-orbit-splitting.html, (accessed July 2017).

261. G. Limousin, J.-P. Gaudet, L. Charlet, S. Szenknect, V. Barthes and M. Krimissa, *Applied Geochemistry*, 2007, **22**, 249-275.

262. C. H. Giles, T. H. MacEwan, S. N. Nakhwa and D. Smith, *Journal of the Chemical Society*, 1960, **0**, 3973-3993.

263. I. Langmuir, *Journal of the American Chemical Society*, 1918, **40**, 1361-1403.

264. S. J. Allen, G. Mckay and J. F. Porter, *Journal of Colloid and Interface Science*, 2004, **280**, 322-333.

265. G. B. H. S. Mckay, H. S. Blair and J. R. Gardner, *Journal of Applied Polymer Science*, 1982, **27**, 3043-3057.

266. Y. C. Wong, Y. S. Szeto, W. H. Cheung and G. McKay, *Langmuir*, 2003, **19**, 7888-7894.

267. S. D. Faust and O. M. Aly, *Adsorption Processes for Water Treatment*, Elsevier, Stoneham, 2013.

268. B. Acemioğlu, *Journal of Colloid and Interface Science*, 2004, **274**, 371-379.

269. C.-T. Hsieh and H. Teng, *Journal of Colloid and Interface Science*, 2000, **230**, 171-175.

270. A. Benhammou, A. Yaacoubi, L. Nibou and B. Tanouti, *Journal of Colloid and Interface Science*, 2005, **282**, 320-326.

271. Y. Kim, C. Kim, I. Choi, S. Rengaraj and J. Yi, *Environmental Science & Technology*, 2004, **38**, 924-931.
272. Y. S. Ho and G. McKay, *Process Safety and Environmental Protection*, 1998, **76**, 332-340.
273. L. A. Langley and D. H. Fairbrother, *Carbon*, 2007, **45**, 47-54.
274. M. E. Argun, S. Dursun, C. Ozdemir and M. Karatas, *Journal of Hazardous Materials*, 2007, **141**, 77-85.
275. H. Qiu, L. Lv, B.-C. Pan, Q.-J. Zhang, W.-M. Zhang and Q.-X. Zhang, *Journal of Zhejiang University-Science A*, 2009, **10**, 716-724.
276. Y.-S. Ho, *Journal of Hazardous Materials*, 2006, **136**, 681-689.
277. Y. S. Ho and G. McKay, *The Canadian Journal of Chemical Engineering*, 1998, **76**, 822-827.
278. Y.-S. Ho and G. McKay, *Process Biochemistry*, 1999, **34**, 451-465.
279. S. M. Yakout and E. Elsherif, *Carbon - Science and Technology*, 2010, **1**, 144-153.
280. M. Gurung, B. B. Adhikari, H. Kawakita, K. Ohto, K. Inoue and S. Alam, *Industrial & Engineering Chemistry Research*, 2012, **51**, 11901-11913.
281. H.-W. Ma, X.-P. Liao, X. Liu and B. Shi, *Journal of Membrane Science*, 2006, **278**, 373-380.
282. Y. Wu, H. Luo, H. Wang, L. Zhang, P. Liu and L. Feng, *Journal of Colloid and Interface Science*, 2014, **436**, 90-98.
283. Y. Ge, D. Xiao, Z. Li and X. Cui, *Journal of Materials Chemistry A*, 2014, **2**, 2136-2145.
284. A. Corma and H. Garcia, *Chemical Society Reviews*, 2008, **37**, 2096-2126.
285. G8-2012 Catalysing the Growth in Metal Recovery (PHYTOCAT), http://gtr.rcuk.ac.uk/projects?ref=EP%2FK022482%2F1, (accessed August 2017).
286. Taym Ltd., Company website, http://www.taym.com.ar/Spanish/default.aspx, (accessed July 2017).
287. K. L. Wasewar, S. Kumar and B. Prasad, *Journal of Environmental Protection*, 2009, **3**, 41-52.
288. T. Gajda, P. Sipos and H. Gamsjäger, *Monatshefte für Chemie-Chemical Monthly*, 2009, **140**, 1293-1303.
289. F. Pagnanelli, F. Ferella, I. De Michelis and F. Vegliò, *Hydrometallurgy*, 2011, **110**, 67-72.
290. Z. Niu and Y. Li, *Chemistry of Materials*, 2013, **26**, 72-83.
291. A. Nag, M. V. Kovalenko, J.-S. Lee, W. Liu, B. Spokoyny and D. V. Talapin, *Journal of the American Chemical Society*, 2011, **133**, 10612-10620.
292. A. V. Gaikwad, P. Verschuren, S. Kinge, G. Rothenberg and E. Eiser, *Physical Chemistry Chemical Physics*, 2008, **10**, 951-956.
293. Sigma Aldrich, Gold Nanoparticles: Properties and Applications, http://www.sigmaaldrich.com/technical-documents/articles/materials-science/nanomaterials/gold-nanoparticles.html, (accessed July 2017).
294. K. Vijayaraghavan, J. Jegan, K. Palanivelu and M. Velan, *Journal of Hazardous Materials*, 2004, **113**, 223-230.

295. F. Gritti, W. Piatkowski and G. Guiochon, *Journal of Chromatography A*, 2002, **978**, 81-107.

296. J. L. Gardea-Torresdey, K. J. Tiemann, G. Gamez, K. Dokken, S. Tehuacanero and M. Jose-Yacaman, *Journal of Nanoparticle Research*, 1999, **1**, 397-404.

297. J. M. Petroski, Z. L. Wang, T. C. Green and M. A. El-Sayed, *The Journal of Physical Chemistry B*, 1998, **102**, 3316-3320.

298. A. S. Aricò, P. Bruce, B. Scrosati, J.-M. Tarascon and W. Van Schalkwijk, *Nature Materials*, 2005, **4**, 366-377.

299. E. Frackowiak, *Physical Chemistry Chemical Physics*, 2007, **9**, 1774-1785.

300. P. K. T. Liu, *Industrial & Engineering Chemistry Research*, 1992, **31**, 2216-2222.

301. J. Smithyman, A. Moench, R. Liang, J. P. Zheng, B. Wang and C. Zhang, *Applied Physics A*, 2012, **107**, 723-731.

302. C. Lei and C. Lekakou, *Nanotechnology 2010: Advanced Materials, CNTs, Particles, Films and Composites*, 2010, **1**, 176-179.

303. D. Vairavapandian, P. Vichchulada and M. D. Lay, *Analytica Chimica Acta*, 2008, **626**, 119-129.

304. G. C. Pradhan and S. K. Swain, *Polymer Composites*, 2016, **37**, 2083-2091.

305. N. Liu, F. Luo, H. Wu, Y. Liu, C. Zhang and J. Chen, *Advanced Functional Materials*, 2008, **18**, 1518-1525.

306. P. M. Visakh, K. Srikaeo, M. Ghasemlou, J. Sahari, V. Calado, A. J. F. de Carvalho, A. Pereira, X. Luo, C. R. Bernal and H. Yang, *Starch-based blends, composites and nanocomposites*, Royal Society of Chemistry, Cambridge, 2015.

307. P. Sun, S. Kuga, M. Wu and Y. Huang, *Cellulose*, 2014, **21**, 2469-2478.

308. N. J. Welham and J. S. Williams, *Carbon*, 1998, **36**, 1309-1315.

309. M. Magini and A. Iasonna, *Materials Transactions, JIM*, 1995, **36**, 123-133.

310. SaveOnEnergy, Estimating Electricity Usage, https://www.saveonenergy.com/energy-consumption/, (accessed July 2017).

311. E. W. Flosdorf, *Freeze-drying.[Drying by sublimation.]*, Reinhold Publishing Corporation, New York, 1949.

312. X. Zhang, Z. Sui, B. Xu, S. Yue, Y. Luo, W. Zhan and B. Liu, *Journal of Materials Chemistry*, 2011, **21**, 6494-6497.

313. A. Borisova, M. De Bruyn, V. L. Budarin, P. S. Shuttleworth, J. R. Dodson, M. L. Segatto and J. H. Clark, *Macromolecular Rapid Communications*, 2015, **36**, 774-779.

314. A. Borisova, PhD, University of York, 2015.

315. A. C. Pierre and G. M. Pajonk, *Chemical Reviews*, 2002, **102**, 4243-4266.

316. M. Ciszewski and A. Mianowski, *Chemik*, 2013, **67**, 267-274.

317. M. Naebe, J. Wang, A. Amini, H. Khayyam, N. Hameed, L. H. Li, Y. Chen and B. Fox, *Scientific Reports*, 2014, **4**, 4375.

318. Y. Zhai, Y. Dou, D. Zhao, P. F. Fulvio, R. T. Mayes and S. Dai, *Advanced Materials*, 2011, **23**, 4828-4850.

319. W. Li, D. Chen, Z. Li, Y. Shi, Y. Wan, G. Wang, Z. Jiang and D. Zhao, *Carbon*, 2007, **45**, 1757-1763.

320. A. Star, D. W. Steuerman, J. R. Heath and J. F. Stoddart, *Angewandte Chemie International Edition*, 2002, **41**, 2508-2512.

321. P. S. Shuttleworth, V. Budarin and J. H. Clark, *Journal of Thermal Analysis and Calorimetry*, 2011, **105**, 577-581.

322. P. S. Shuttleworth, V. Budarin and J. H. Clark, *Journal of Materials Chemistry*, 2009, **19**, 8589-8593.

323. Sigma Aldrich, Product Specification Sheet of p-toluenesulfonic acid monohydrate - ACS reagent, >98.5%, http://www.sigmaaldrich.com/catalog/product/sial/402885?lang=en&region=GB , (accessed July 2017).

324. J. Jang, Y. B. Lee, K. T. Kim, Y. K. Kim and W. S. Ryu, Boron Content in Type 316 L Stainless Steel by Neutron Induced Autoradiography, Tsukuba, 2003.

325. B. Manoj and A. G. Kunjomana, *International Journal of Electrochemical Science*, 2012, **7**, 3127-3134.

326. R. B. Mathur, O. P. Bahl, T. L. Dhami and S. K. Chauhan, *Carbon Letters*, 2003, **4**, 111-116.

327. A. Milev, M. Wilson, G. S. K. Kannangara and N. Tran, *Materials Chemistry and Physics*, 2008, **111**, 346-350.

328. A. Sharma, T. Kyotani and A. Tomita, *Carbon*, 2000, **38**, 1977-1984.

329. G. E. Bacon, *Acta Crystallographica*, 1951, **4**, 558-561.

330. M. Ojeda, A. M. Balu, A. A. Romero, P. Esquinazi, J. Ruokolainen, H. Sixta and R. Luque, *ChemCatChem*, 2014, **6**, 2847-2853.

331. D. Prahas, Y. Kartika, N. Indraswati and S. Ismadji, *Chemical Engineering Journal*, 2008, **140**, 32-42.

332. C. Zheng, L. Qi, M. Yoshio and H. Wang, *Journal of Power Sources*, 2010, **195**, 4406-4409.

333. E. Frackowiak and F. Beguin, *Carbon*, 2001, **39**, 937-950.

334. E. Raymundo-Piñero, F. Leroux and F. Béguin, *Advanced Materials*, 2006, **18**, 1877-1882.

335. R. Kötz and M. Carlen, *Electrochimica Acta*, 2000, **45**, 2483-2498.

336. C. Zhong, Y. Deng, W. Hu, J. Qiao, L. Zhang and J. Zhang, *Chemical Society Reviews*, 2015, **44**, 7484-7539.

337. G. A. Mabbott, *Journal of Chemical Education*, 1983, **60**, 697-702.

338. H. Wang and L. Pilon, *Electrochimica Acta*, 2012, **64**, 130-139.

339. R. Lin, P. Huang, J. Segalini, C. Largeot, P.-L. Taberna, J. Chmiola, Y. Gogotsi and P. Simon, *Electrochimica Acta*, 2009, **54**, 7025-7032.

340. J. Chmiola, C. Largeot, P. L. Taberna, P. Simon and Y. Gogotsi, *Angewandte Chemie International Edition*, 2008, **120**, 3440-3443.

341. L. Deng, R. J. Young, I. A. Kinloch, A. M. Abdelkader, S. M. Holmes, D. A. De Haro-Del Rio and S. J. Eichhorn, *ACS Applied Materials & Interfaces*, 2013, **5**, 9983-9990.

342. H. Zhou, S. Zhu, M. Hibino and I. Honma, *Journal of Power Sources*, 2003, **122**, 219-223.

343. M. A. Azam, N. H. Jantan, N. Dorah, R. N. A. R. Seman, N. S. A. Manaf, T. I. T. Kudin and M. Z. A. Yahya, *Materials Research Bulletin*, 2015, **69**, 20-23.

344. H. Feng, M. Zheng, H. Dong, Y. Xiao, H. Hu, Z. Sun, C. Long, Y. Cai, X. Zhao and H. Zhang, *Journal of Materials Chemistry A*, 2015, **3**, 15225-15234.

345. S. M. Oh and K. B. Kim, *Chemical Communications*, 1999, **21**, 2177-2178.

346. R. Shah, X. Zhang and S. Talapatra, *Nanotechnology*, 2009, **20**, 395202.

347. A. Burke, *Journal of Power Sources*, 2000, **91**, 37-50.

348. G. Xu, C. Zheng, Q. Zhang, J. Huang, M. Zhao, J. Nie, X. Wang and F. Wei, *Nano Research*, 2011, **4**, 870-881.

349. M. D. Stoller, S. Park, Y. Zhu, J. An and R. S. Ruoff, *Nano Letters*, 2008, **8**, 3498-3502.

350. S.-I. Pyun, H.-C. Shin, J.-W. Lee and J.-Y. Go, *Electrochemistry of insertion materials for hydrogen and lithium*, Springer Science & Business Media, Verlag, 2012.

351. S.-M. Chen, R. Ramachandran, V. Mani and R. Saraswathi, *International Journal of Electrochemical Science*, 2014, **9**, 4072-4085.

352. B. O. Agboola and K. I. Ozoemena, *Journal of Power Sources*, 2010, **195**, 3841-3848.

353. S. M. Roldán Luna, PhD, Universidad de Oviedo, 2013.

354. M. D. Stoller and R. S. Ruoff, *Energy & Environmental Science*, 2010, **3**, 1294-1301.

355. A. Burke and M. Miller, *Electrochimica Acta*, 2010, **55**, 7538-7548.

356. I. Aldama Amado, PhD, Universidad Autónoma de Madrid, 2015.

357. A. Celzard, F. Collas, J. F. Mareche, G. Furdin and I. Rey, *Journal of Power Sources*, 2002, **108**, 153-162.

358. N. H. Basri and B. N. M. Dolah, *International Journal of Electrochemical Science*, 2013, **8**, 257-273.

359. W. Lu, R. Hartman, L. Qu and L. Dai, *The Journal of Physical Chemistry Letters*, 2011, **2**, 655-660.

360. M. Rajkumar, C.-T. Hsu, T.-H. Wu, M.-G. Chen and C.-C. Hu, *Progress in Natural Science: Materials International*, 2015, **25**, 527-544.

361. H. Chen, J. Di, Y. Jin, M. Chen, J. Tian and Q. Li, *Journal of Power Sources*, 2013, **237**, 325-331.

362. D. E. Pacheco-Catalán, M. A. Smit and E. Morales, *International Journal of Electrochemical Science*, 2011, **6**, 78-90.

363. Interview, Dr. Enrique Morales Vergas, Instituto de Ciencia y Technologia de Polimeros (Spain), August 2017.

364. X. Qian, Y. Lv, W. Li, Y. Xia and D. Zhao, *Journal of Materials Chemistry*, 2011, **21**, 13025-13031.

365. M. Noked, S. Okashy, T. Zimrin and D. Aurbach, *Angewandte Chemie International Edition*, 2012, **124**, 1600-1603.

366. B. Yi, X. Chen, K. Guo, L. Xu, C. Chen, H. Yan and J. Chen, *Materials Research Bulletin*, 2011, **46**, 2168-2172.

367. Y. Wang, Y. Song and Y. Xia, *Chemical Society Reviews*, 2016, **45**, 5925-5950.

368. Q. Lu, M. W. Lattanzi, Y. Chen, X. Kou, W. Li, X. Fan, K. M. Unruh, J. G. Chen and J. Q. Xiao, *Angewandte Chemie International Edition*, 2011, **123**, 6979-6982.

369. B. Fang and L. Binder, *The Journal of Physical Chemistry B*, 2006, **110**, 7877-7882.

370. Q. Zhou, J. Gao, C. Li, J. Chen and G. Shi, *Journal of Materials Chemistry A*, 2013, **1**, 9196-9201.
371. J. R. Macdonald, *Annals of Biomedical Engineering*, 1992, **20**, 289-305.
372. E. Barsoukov and J. R. Macdonald, *Impedance Spectroscopy: Theory, Experiment, and Applications*, John Wiley & Sons, Hoboken, 2005.
373. M. Inagaki, H. Konno and O. Tanaike, *Journal of Power Sources*, 2010, **195**, 7880-7903.
374. Y. H. Lin, T. Y. Wei, H. C. Chien and S. Y. Lu, *Advanced Energy Materials*, 2011, **1**, 901-907.
375. D.-W. Wang, F. Li, H.-T. Fang, M. Liu, G.-Q. Lu and H.-M. Cheng, *The Journal of Physical Chemistry B*, 2006, **110**, 8570-8575.
376. C. Lei, F. Markoulidis, Z. Ashitaka and C. Lekakou, *Electrochimica Acta*, 2013, **92**, 183-187.
377. J. Gamby, P. L. Taberna, P. Simon, J. F. Fauvarque and M. Chesneau, *Journal of Power Sources*, 2001, **101**, 109-116.
378. P. L. Taberna, P. Simon and J.-F. Fauvarque, *Journal of The Electrochemical Society*, 2003, **150**, A292-A300.
379. Z. Feng, R. Xue and X. Shao, *Electrochimica Acta*, 2010, **55**, 7334-7340.
380. T. Hiraoka, A. Izadi-Najafabadi, T. Yamada, D. N. Futaba, S. Yasuda, O. Tanaike, H. Hatori, M. Yumura, S. Iijima and K. Hata, *Advanced Functional Materials*, 2010, **20**, 422-428.
381. S. H. Aboutalebi, A. T. Chidembo, M. Salari, K. Konstantinov, D. Wexler, H. K. Liu and S. X. Dou, *Energy & Environmental Science*, 2011, **4**, 1855-1865.
382. E. Morales, F. Pico, T. A. Centeno and J. M. Rojo, Frequency Response Analysis of Mesoporous Carbon/RuO2 composites as supercapacitor electrodes, Zaragoza, 2011.
383. C. Portet, G. Yushin and Y. Gogotsi, *Carbon*, 2007, **45**, 2511-2518.